

# **Formation and Characterisation of Nanostructured Polypyrrole Films: Their Growth on Membrane Supports and Application in Heavy Metal Remediation**



NUI MAYNOOTH

Ollscoil na hÉireann Má Nuad

A thesis submitted to the National University of Ireland in fulfilment of the  
requirements for the degree of

**Doctor of Philosophy**

by

**Orla Power, B.Sc.**

Department of Chemistry

National University of Ireland Maynooth

October 2013

**Supervisor:** Dr. Denise Rooney

**Head of Department:** Dr. John C. Stephens

---

## Table of Contents

Declaration of Authorship.....	i
Acknowledgements.....	ii
Abstract.....	vi
<b>Chapter 1</b>	
<b>Introduction and Literature Review</b>	
1.1 Introduction.....	2
1.2 Conducting Polymers.....	3
1.3 Polypyrrole.....	6
1.3.1 Structural Properties of Polypyrrole.....	6
1.3.2 Electronic Properties of Polypyrrole.....	7
1.3.3 Redox Properties of Polypyrrole.....	9
1.3.4 Polymerisation of Polypyrrole.....	11
1.4 Polypyrrole Nanostructures.....	13
1.4.1 Hard Template Approach.....	13
1.4.2 Soft Template Approach.....	14
1.4.3 Template-Less Approach.....	15
1.5 Polypyrrole on Porous Membrane Supports.....	18
1.6 Sulfonated Calixarenes.....	20
1.6.1 Structural Properties of Sulfonated Calixarenes.....	21
1.6.2 Electrochemical Activity of Sulfonated Calixarenes.....	22
1.6.3 Inclusion Complexes of Sulfonated Calixarenes.....	23
1.6.4 Immobilisation of Sulfonated Calixarenes in Polypyrrole.....	24
1.7 Remediation of Heavy Metals.....	25
1.7.1 Common Heavy Metal Pollutants – Toxicity and Sources.....	25
1.7.2 Current Remediation Techniques for Heavy Metal Pollutants.....	27
1.7.3 Chromium – Toxicity, Sources and Regulatory Directives.....	28
1.7.4 Current Remediation Techniques for Chromium.....	29

---

---

1.7.5 Remediation by Conducting Polymers .....	30
1.8 References .....	32

## Chapter 2

### Experimental

2.1 Introduction .....	45
2.2 Experimental Procedures .....	46
2.2.1 Chemicals .....	46
2.2.2 Chemical Polymerisation on a Polyamide Porous Membrane.....	46
2.2.2.1 Using Anthraquinone-2-sulfonic Acid Sodium Salt (AQSA) as the Dopant.....	46
2.2.2.2 Using Methyl Orange as the Dopant.....	46
2.2.2.3 Combined Chemical Polymerisation Method.....	47
2.2.3 Preparation of Polypyrrole-Sodium Alginate (PpySA) Particles.....	48
2.2.4 The Electrochemical Set-up.....	48
2.2.4.1 Electrode Materials and Preparation.....	50
2.2.5 Electrochemical Polymerisation of Pyrrole .....	51
2.2.5.1 Electropolymerisation of Bulk Polypyrrole and Nanowires on a Conventional Electrode.....	51
2.2.5.2 Coating of Polypyrrole Nanowires with Ppy-Immobilised Dopant Films.....	52
2.2.5.3 Electropolymerisation of Polypyrrole Nanowires on a Porous Membrane .....	52
2.2.6 Cyclic Voltammetry.....	53
2.2.7 Polymer Characterisation.....	53
2.2.7.1 Microscopy .....	53
2.2.7.2 Spectroscopy.....	54
2.2.7.3 Water Contact Angle .....	55
2.2.8 Analysis of Cr(VI) Remediation by Polypyrrole Nanowires.....	55
2.2.8.1 Concentration of Sodium Dichromate in Solution.....	55
2.2.8.2 Colorimetric Tests .....	57
2.2.8.2(i) Colorimetric Test based on Hydrogen Peroxide / Potassium Peroxydisulfate Oxidation of Cr(III) .....	57

---

---

2.2.8.2(ii) Formation of a Chromophore Complex of Cr(VI) and 1,5-diphenylcarbazine	58
2.3 Experimental Techniques	60
2.3.1 Electrochemistry	60
2.3.1.1 Open Circuit Potential Measurements	60
2.3.1.2 Potentiostatic Amperometry	60
2.3.1.3 Cyclic Voltammetry	61
2.3.1.4 Electrochemical Quartz Crystal Microbalance	64
2.3.2 Surface Analysis	66
2.3.2.1 Scanning Electron Microscopy	66
2.3.2.2 Water Contact Angle	68
2.3.3 Spectroscopy	70
2.3.3.1 Energy Dispersive X-Ray Spectroscopy	70
2.3.3.2 Fourier Transform Infrared Spectroscopy	71
2.3.3.3 Raman Spectroscopy	72
2.3.3.4 UV-Visible Spectroscopy	73
2.4 References	75

## Chapter 3

### Growth and Characterisation of Polypyrrole Nanostructures

3.1 Introduction	79
3.2 Chemical Approach	80
3.2.1 Functional Dopants	80
3.2.1.1 Using Anthraquinone-2-sulfonic Acid Sodium Salt (AQSA) as the Dopant	80
3.2.1.1(i) Influence of Polymerisation Duration	81
3.2.1.1(ii) Influence of Monomer Concentration	81
3.2.1.1(iii) Influence of Reaction Volume	82
3.2.1.2 Using Methyl Orange as the Dopant	83
3.2.1.3 Combined Chemical Polymerisation Methods	84
3.2.2 Using Sodium Alginate as a Soft Template	85

---

---

3.2.2.1 Preparation of Polypyrrole-Sodium Alginate Particles.....	85
3.2.2.2 Characterisation of the PpySA Particles .....	86
3.3 Electrochemical Approach .....	87
3.3.1 Electropolymerisation of Ppy Nanowires on a Conventional Electrode.....	87
3.3.1.1 Influence of Applied Potential .....	89
3.3.1.2 Polymerisation Charge Density .....	90
3.3.1.3 Influence of Dopant Concentration.....	94
3.3.1.4 Effect of Seed Dopant Anion.....	100
3.3.1.5 Effect of Seed Dopant Cation .....	103
3.3.1.6 Investigation of the Polymer Base Layer.....	105
3.3.2 Formation of Polypyrrole Nanowires Doped with an Immobile Dopant.....	109
3.3.2.1 Coating Polypyrrole Nanowires with PpyC4S and PpyPSS films.....	110
3.3.2.2 SEM Characterisation of the PpyNW Coated with PpyC4S and PpyPSS Films	113
3.3.3 Characterisation of Polypyrrole Nanowires.....	116
3.3.3.1 Infrared Spectroscopy .....	116
3.3.3.2 Raman Spectroscopy .....	122
3.3.3.3 Water Contact Angle .....	127
3.3.4 Polymerisation of PpyNW on a Porous Membrane.....	129
3.3.4.1 Resistance Across the Gold Sputter Coated Membranes.....	129
3.3.4.2 Flow Rate Through the Gold Sputter Coated Membranes.....	130
3.3.4.3 Polymerisation of PpyNW on the Gold Sputter Coated Membranes.....	133
3.4 Summary and Conclusions.....	137
3.5 References .....	139

## Chapter 4

### Investigation of the Ion-Exchange Properties of *p*-Sulfonatocalix[4]arene-Polypyrrole and Polypyrrole-Polystyrene Sulfonate Films using EQCM

4.1 Introduction.....	146
4.2 Results and Discussion.....	150

---

---

4.2.1 Electropolymerisation of Polymer Films .....	150
4.2.1.1 Electropolymerisation of p-Sulfonatocalix[4]arene-Polypyrrole Film .....	150
4.2.1.2 Electropolymerisation of Polypyrrole-Polystyrene Sulfonate Film .....	152
4.2.1.3 Doping Level and Theoretical Film Thickness .....	155
4.2.2 Cyclic Voltammetry and Ion Exchange Properties of PpyC4S .....	158
4.2.2.1 Equilibration of PpyC4S Films .....	160
4.2.2.2 Effect of Film Thickness on the Redox Properties of PpyC4S .....	162
4.2.2.3 Effect of Dopant Concentration .....	166
4.2.2.4 Effect of Scan Rate .....	169
4.2.2.5 Metal Cation Exchange Properties of PpyC4S .....	176
4.2.2.6 Anion Exchange Properties of PpyC4S .....	184
4.2.3 Cyclic Voltammetry and Ion Exchange Properties of PpyPSS .....	187
4.2.3.1 Effect of Applied Growth Potential .....	187
4.2.3.2 Effect of Dopant Concentration .....	190
4.2.3.3 Effect of Scan Rate .....	192
4.2.4 Influence of Potential Window on Ion Exchange Properties of PpyC4S .....	195
4.3 Conclusions .....	199
4.4 References .....	201

## Chapter 5

### Remediation of Hexavalent Chromium using Polypyrrole Nanowires on Conventional Electrodes and Polyamide Membranes; and Polypyrrole-Sodium Alginate Particles

5.1 Introduction .....	206
5.2 Polypyrrole Nanowires – Preliminary Studies .....	208
5.2.1 Cr(VI) Speciation .....	208
5.2.2 Removal of Cr(VI) by Polypyrrole Nanowires .....	209
5.3 Mechanism of Chromium Remediation .....	212
5.3.1 Adsorption of Cr(VI) onto Polypyrrole – Anion Exchange .....	213
5.3.2 Protonation of Polypyrrole .....	215

---

---

5.3.3 Oxidation of Polypyrrole: Cr(VI) → Cr(III).....	218
5.3.3.1 Open Circuit Potential of Bulk Polypyrrole (PpyCl).....	220
5.3.3.2 Open Circuit Potential of Polypyrrole Nanowires (PpyNW) .....	223
5.3.4 Fate of Chromium.....	228
5.3.4.1 Hydrogen Peroxide / Potassium Peroxydisulfate Oxidation of Cr(III).....	229
5.3.4.2 Formation of a Chromophore Complex of Cr(VI) and 1,5-diphenylcarbazide ..	230
5.4 Removal Efficiency: Pre-reduction of the Polymer .....	234
5.4.1 Rate of Chromium Removal .....	234
5.4.2 Recyclability of the PpyNW films .....	236
5.5 Applications of PPyNW on a Porous Support .....	239
5.5.1 Nanowire Formation on Polyamide Membranes .....	239
5.5.2 Rate of Chromium Removal at a PPyNW Modified Membrane .....	240
5.5.3 Recyclability of Membranes .....	241
5.5.4 Electrochemically Enhanced Chromium Remediation – Pulse technique.....	243
5.5.5 Chromium Remediation in a Stirred Filtration Cell .....	246
5.6 Summary of Polypyrrole Nanowires.....	248
5.7 Polypyrrole-Sodium Alginate Particles .....	251
5.7.1 Preliminary Investigation of the Cr(VI) Removal by PpySA Particles .....	252
5.7.2 Effect of Solution pH.....	254
5.7.3 Effect of Solution Temperature .....	255
5.7.4 Effect of Initial Cr(VI) Concentration .....	257
5.7.5 Adsorption Kinetics .....	258
5.8 Summary of PpySA Particles.....	262
5.9 References .....	264

## Chapter 6

### Conclusions

6.1 Conclusions .....	269
6.2 References .....	275

---

---

Appendix

Conference Presentations and Publications ..... 278

---

## Declaration of Authorship

I hereby certify that this thesis has not been submitted before, in whole or in part, to this or any other university for any degree and is, except where stated, the original work of the author.

Signed: \_\_\_\_\_

Orla Power, B.Sc.

---

## Acknowledgements

A traditional African proverb says “It takes a village to raise a child”, and I believe the same sentiment can be applied to this thesis. I have many people to thank, without whom I don’t think I would have gotten this far.

Firstly, I would like to thank my supervisor Dr. Denise Rooney, your advice, guidance and friendship over the years has been invaluable; you’ve taught me to be a better scientist, to question everything and to always triple check! I would also like to thank Professor Carmel Breslin for support and encouragement and for the use of her lab and equipment.

Sincere thanks are also due to Dr. John Stephens, the current Head of Department and also to Professor John Lowry, the former Head of Department for giving me the opportunity to pursue my Ph.D. in such a welcoming department. During this research I was supported financially by the Department of the Environment, Community and Local Government and the Environmental Protection Agency. I would like to thank the EPA steering committee; Professor John Cassidy, Darragh Page, Darren Byrne and Lisa Sheils for their advice & direction throughout.

A special thanks to Dr. Anne Shanahan in DIT and Paul Tierney in ITT for allowing me to use the Raman and Water Contact Angle equipment. Thanks also to Patrick Carolan and Vince Lodge at the Tyndall National Institute Cork, for the SEM analysis which was conducted as part of the National Access Programme.

Particular thanks go to Dr. Johnny Colleran, your knowledge of electrochemistry is boundless and your enthusiasm and willingness to share that knowledge is so appreciated. The lab just isn’t the same without you. Also to Dr. Valeria Annibaldi, thank you for your time, energy and kindness. You were always on hand to explain the tricky bits.

To the technical staff of the Chemistry Department, without you the place would fall down! Thank you to Ken Maddock, Anne Cleary, Ollie Fenelon, Ria Walsh, Orla Joyce, Maryanne Ryan, Barbara Woods and Walter Walsh for your time, patience and support. Thanks also to Donna Nicholson, Carol Berigan and Niamh Kelly who are always happy to help. An extra special thanks to Noel Williams. Noel, your patience and generosity when faced with the most ridiculous of requests are wonderful. Thank you for your help in developing the various electrochemical cells, for answering all my computer related questions and for our shared love of cake sales.

---

Thank you to all the postgrads and postdocs, both past and present - from crash courses in computer programs and showing me the perfect thickness of a KBr disk, to the very welcome cups of tea and brilliant nights out, you are a lovely bunch of people and I wish you all happiness in whatever you do in the future. The proof-reading by Emer P., Adelaide and Louise was especially appreciated!

A big thank you is due to all of the official and unofficial members of “Team Denise”. Richard Doyle, Louise Gallagher, Conor McCarthy, Lynn Garry, Wayne Fogarty, Niall McGuinness and Ciaran O’Carroll, thank you for the assistance, guidance and proof-reading! Thank you also to my lab colleagues, Adelaide, Anita, Catherine, Gama, Paul, Samantha and Ursula. A special thanks to Karen and David, and of course Mr. Plant! You guys bring a real sense of happiness to the lab, and your friendship and ‘choons’ over the last few months helped no end. Thank you both (and Aidan) for proof-reading too!

There are two people in particular, without whom I don’t think I would have stuck it out. Wayne, you are the Philip to my Terrance, a man who knows good coffee and who will dance like a lunatic on every night out. Emer, you are my chemistry sounding board and a lady who knows the importance of hugs; I think the ‘real life’ we speak of is just around the corner. In you both I feel I’ve made friends for life, thank you for the laughs and the lunch dates.

A heartfelt thank you to my friends outside of the lab; Julie and Barry, Rob and Zara, and Will and Sorcha. Thank you guys for the holiday escapades, the wine and the shenanigans. Leonie, Emma and all the girls, thanks for the distractions of tea, biscuits and dancing, you are the best! Thanks also to all my friends from home, I love our Christmas get-togethers.

The support I received from my extended family was so important. Love and thanks to Nana Bowe, Angela, Yvonne and all the Bowes, Campbells, Doorlys and Powers!

To Mam and Dad, you have always been there to offer love, support and reassurance to your “perpetual student”. Words cannot describe how much you guys mean to me, and I’m dedicating this thesis to you. To my darling siblings, Michael, Caroline and Peter, thank you for the road trips to the shops, the board games, the books and for keeping me sane (I think?!).

Thank you to Mary, James and Sarah, for your encouragement and always making me feel at home.

Finally, I would like to thank Shane, for your unfailing love and support, you’ve been there for me from day one, and for that I thank you. We did it!

---

Dedicated with love to my Mam and Dad,

Thank you.

---

The most exciting phrase to hear in science, the one that heralds new discoveries,  
is not 'Eureka!' but 'That's funny...'

*Isaac Asimov*

If we knew what it was we were doing, it would not be called research, would it?

*Albert Einstein*

---

## Abstract

The Millennium Development Goal to halve, by 2015, the proportion of the population without sustainable access to safe drinking water, was met in 2010, with an additional two billion people gaining access to improved sources of drinking water since 1990. However in 2013, the United Nations Year of Water Cooperation, almost one in nine people worldwide still do not have access to a secure supply of clean, contaminant free drinking water. Although the EPA 2010 Report “Water Quality in Ireland 2007-2009” classes 84.7% of water bodies as good, the protection of Ireland’s water resources is paramount as an ever-increasing population requires a continuous supply of clean, safe drinking water. The Water Quality (Dangerous Substances) Regulations, 2001, were introduced to regulate dangerous substances, including heavy metals. These include chromium, nickel, lead, zinc and arsenic. The natural concentrations of these metals in water vary depending on the metal content of the surroundings, but they may also enter the environment from a range of anthropogenic sources. Chromium for instance is often released as a by-product of electroplating, leather tanning and pigment manufacturing processes.

In the research described herein, a number of polypyrrole based nanomaterials were developed and their potential for heavy metal removal was investigated. The polypyrrole nanomaterials formed were polypyrrole nanowires on conventional electrodes and on porous polyamide membranes; polypyrrole nanowires coated with polypyrrole-immobile dopant films and polypyrrole-sodium alginate particles.

Characterisation of the polypyrrole nanowires indicated that these films are more hydrophilic than polypyrrole formed in the bulk morphology. The removal of chromium by polypyrrole nanowires polymerised on conventional electrodes and on porous membranes was found to be initially enhanced by the application of a pre-reduction step which ensured that the polypyrrole was in its reduced state. After one hour immersion in an acidified chromium solution, little difference was observed between the rate of removal of the reduced polypyrrole nanowires and the non-reduced polypyrrole nanowires. Adsorption and spontaneous electron transport at the polymer interface were found to be the dominant processes in the removal process. The application of a reduction potential was found to improve the recyclability of the polypyrrole nanowires.

---

Polypyrrole nanowires were successfully coated with films of *p*-sulfonatocalix[4]arene-polypyrrole and polypyrrole doped with poly(sodium 4-styrenesulfonate). Characterisation of the thus coated nanowires suggested that the polypyrrole-immobile dopant films improved the conjugation of the polymer. The ion exchange properties of these coatings were examined using an electrochemical quartz crystal microbalance. It was found that polypyrrole doped with poly(sodium 4-styrenesulfonate) exhibited cation exchange behaviour, whereas the *p*-sulfonatocalix[4]arene-polypyrrole films exhibited mixed cation-anion exchange behaviour. The pre-dominance of cation or anion exchange of the *p*-sulfonatocalix[4]arene-polypyrrole films was dependent on the dopant concentration, the scan rate, and the nature of anion and cation in solution.

Chromium removal by the polypyrrole-sodium alginate particles was examined over a range of solution pHs and was found to be most effective at a solution pH of 1.0. While this material was designed primarily as an adsorbent, preliminary studies at pH 1.0 indicate that  $67 \pm 2$  percent of the Cr(VI) is reduced to Cr(III) and released back into solution. This suggests that spontaneous electron transfer between the conducting polymer and the Cr(VI) may be occurring. The kinetics of the adsorption process was best described by the *pseudo*-second-order kinetic model and fitting to the Morris-Weber model indicated that intraparticle diffusion may also play a role in the adsorption process.

# Chapter 1

---

## Introduction and Literature Review

---

## 1.1 Introduction

The work presented in this thesis is concerned with the formation of polypyrrole particles and nanowires and the adhesion of the nanowires onto a membrane support. The nanostructured polypyrrole materials and the polymer coating of the nanowires are characterised using a range of surface analysis and electrochemical techniques and their applications in the remediation of heavy metals are investigated.

The development of nanostructured conducting polymers is of great current interest, due to the unique electrical, chemical and optical properties exhibited by conducting polymers.<sup>1-5</sup> It is believed that nanostructured conducting polymers not only retain these qualities, but also exhibit unique properties, such as a large specific surface area and shorter path lengths for ion transport.<sup>6, 7</sup> This has led to the successful application of conducting polymer nanowires in a range of areas including electrochemical sensors,<sup>7, 8</sup> heavy metal remediation,<sup>9</sup> batteries,<sup>10</sup> supercapacitors<sup>11</sup> and actuators.<sup>12</sup> In the current research the polypyrrole nanostructures were employed for the removal of hexavalent chromium from aqueous solutions. The use of conducting polymers in the bulk and nanowire/nanotube/nanoparticle morphologies for the remediation of Cr(VI) have been extensively studied in recent years.<sup>13-20</sup> The removal strategy employed in this study may have advantages over existing methodologies as nanowire formation on a large porous electroactive membrane offers the potential for electrochemical regeneration of the polymer for further Cr(VI) remediation.<sup>13</sup> Polypyrrole has also been used for the removal of heavy metals such as gold, palladium, mercury, lead and silver from aqueous solutions.<sup>21-23</sup> This thesis also investigates the ion-exchange properties of polypyrrole films doped with large immobile dopants, for the removal of metal cations from solution.

In this Introduction, the fundamental processes involved in the polymerisation of pyrrole are discussed in terms of the structural and electronic properties of polypyrrole. This is followed by a review of current literature accounts of the formation of nanostructured polypyrrole and conducting polymers on porous supports. Sulfonated calixarenes and their incorporation into polypyrrole films are then detailed. Finally, the applications of conducting polymers for the removal of heavy metals from water are discussed with reference to the most significant literature reports.

## 1.2 Conducting Polymers

Conducting polymers are a class of functional polymers made of conjugated macromolecules which allow them to carry an electric current. Often called organic polymeric conductors or synthetic metals, they combine some of the mechanical features of plastics with electrical properties usually associated with metals.<sup>24</sup> Polyacetylene was the first to be fully characterised and developed, by Heeger, MacDiarmid and Shirakawa, and this research led to them being awarded a Nobel Prize in Chemistry in 2000.<sup>25-27</sup> Since then, heteroatom containing polymers such as polyaniline (PANI), polypyrrole (Ppy) and polyethylenedioxythiophene (PEDOT) have become more widely researched (Figure 1.1).<sup>28-31</sup>

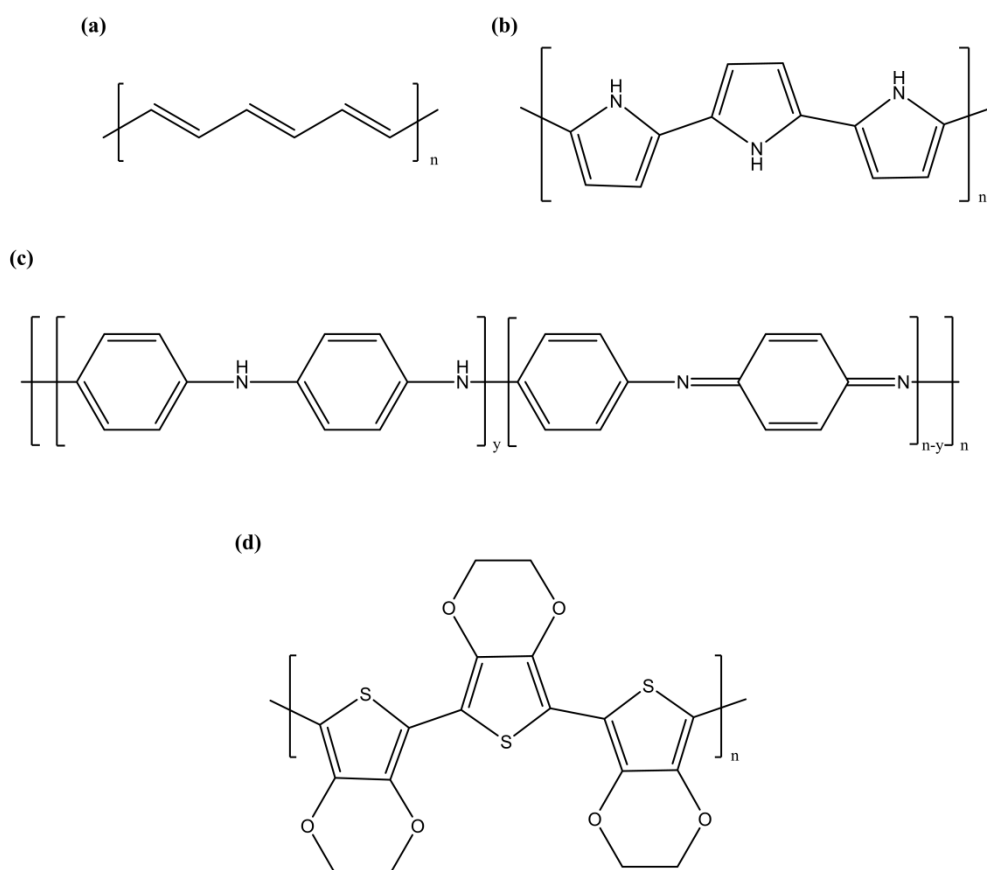


**Figure 1.1:** Chemical structures of conducting polymers in their de-doped state; a) polyacetylene, b) polypyrrole, c) polyaniline and d) polyethylenedioxythiophene.

All materials, including polymers, can be classified as insulators, semi-conductors or conductors, based on the degree of electrical conductivity they possess (Figure 1.2).

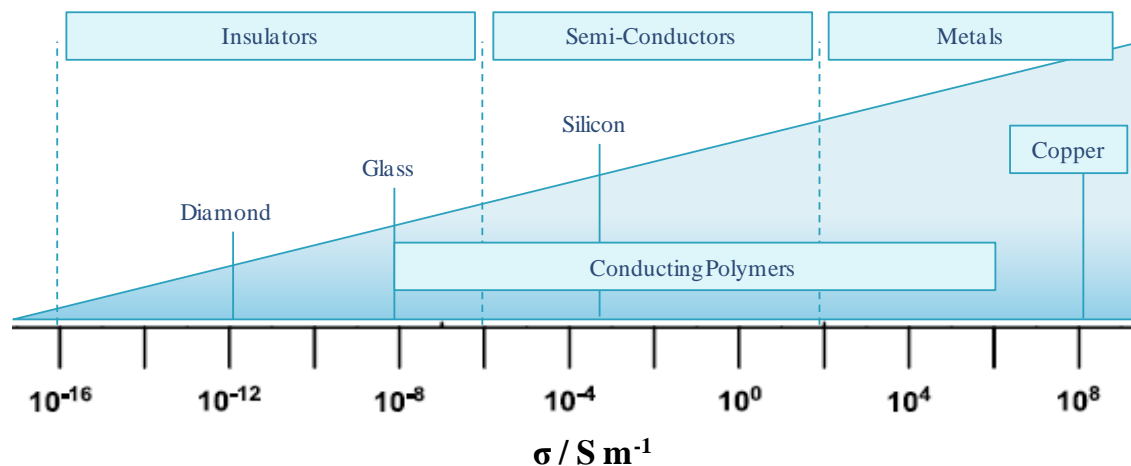


Figure 1.2: Classification of materials according to their electrical conductivity,  $\sigma$ .

This conductivity was described in 1985 by Bredas and Street, in terms of the band gap theory of solids.<sup>32</sup> This theory relates to the band gap ( $\Delta E$ ) between the highest occupied molecular orbital (HOMO) and the lowest unoccupied molecular orbital (LUMO), which constitute the valence band (VB) and conductance band (CB). Electrical insulators, such as glass or paper, have a large band gap, which inhibits the excitation of electrons from the VB to the CB. Thus, they do not have free flowing electrons, resulting in little or no conductivity ( $\sigma = 10^{-8} \text{ S m}^{-1}$ ). Electrical conductors such as copper, possess freely flowing electric charges, as the VB and CB overlap to form a single diffuse band described as an electron cloud ( $\sigma = 10^2 \text{ S m}^{-1}$ ).

The band gap theory cannot alone explain the conductivity associated with conducting polymers. Conducting polymers consist of chains of alternating double and single bonded  $\text{sp}^2$  hybridised atoms, which result in a delocalized conjugate system due to the overlap of  $\pi$ -electrons. This  $\pi$ -conjugated system allows for the generation and movement of charge carriers, known as polarons and bipolarons, along the polymer backbone.<sup>29</sup> The generation of these mobile charge carriers will be discussed in more detail in Section 1.3.2.

Conducting polymers can be synthesised either chemically or electrochemically in varying morphologies. For example, by varying the synthetic parameters during the oxidation of aniline, polyaniline can be formed as nanofibres,<sup>33</sup> nanodiscs or nanoplates and in morphologies reminiscent of roses, leaves or seashells.<sup>34</sup> Similarly, the oxidation

of pyrrole under varying conditions can result in a cauliflower, fibrillar or tapered morphology.<sup>35</sup>

Conducting polymers have generated interest due to their range of potential applications. These include sensors,<sup>8, 36</sup> actuators,<sup>12</sup> electronics and devices used in the generation and storage of renewable energy.<sup>37, 38</sup> Doping of a conducting polymer results in a change in the electronic band structure which is often accompanied by a change in the conducting polymers optical properties in the UV-Vis and NIR regions. This forms the basis for the use of conducting polymers in electrochromic devices and optical sensors.<sup>1</sup> Both polypyrrole and polyaniline have been utilised in devices employing electrochromic displays.<sup>37</sup> The electroluminescent properties of polythiophene and poly(paraphenylene) have been exploited in the development of organic light-emitting diodes.<sup>1, 37</sup> Doping of conducting polymers can also result in the generation of an overall charge along the polymer backbone. This results in the release or uptake of ions such that electroneutrality is maintained. This property of conducting polymers is widely used in systems based on an ion-exchange technique; such as ion-exchange membranes,<sup>1</sup> artificial muscles or actuators,<sup>12</sup> drug delivery systems,<sup>39</sup> and metal ion transport or remediation.<sup>40, 41</sup> Dependant on the size of the dopant used, conducting polymers can often be designed as electrochemically switchable anion or cation exchange materials.<sup>42-44</sup>

## 1.3 Polypyrrole

Polypyrrole is the most popularly studied conducting polymer due to its facile preparation, good conductivity and environmental stability<sup>45</sup> as well as its switchable redox activity,<sup>46, 47</sup> ion exchange abilities<sup>48-51</sup> and biocompatibility.<sup>52</sup> It can be prepared either by chemical or electrochemical methods and can exhibit conductivities of up to  $100 \text{ S m}^{-1}$ .<sup>53, 54</sup> Of particular interest to the current study is the electrochemical switching of Ppy, which is accompanied by ion exchange for the purposes of maintaining the electroneutrality of the polymer matrix. The possibility of using Ppy membranes for the uptake and release of ions was first posited by Burgmayer and Murray.<sup>55</sup> Ppy can be employed as an anion or cation exchange material, depending on the polymerisation conditions and the size of the incorporated dopant.<sup>49</sup>

### 1.3.1 Structural Properties of Polypyrrole

Polypyrrole is a black, insoluble, amorphous material which was first synthesised in 1969 by Dall'Olio *et al.* by the oxidation of pyrrole in sulfuric acid.<sup>56</sup> The first electrochemical polymerisation of a Ppy film was achieved by Diaz *et al.* at IBM, who showed that the Ppy films could be electrochemically cycled between a conducting and an insulating state.<sup>57, 58</sup> Ppy consists of repeating pyrrole monomer units; five-membered heterocyclic rings of a nitrogen and four carbon atoms, all with  $sp^2$  hybridisation. This generates a delocalised  $\pi$ -electron system made from four carbon and two nitrogen  $2p_z$  electrons. During oxidative polymerisation, the monomer units bind through carbon-carbon  $\sigma$  bonds. Good electrical conductivity in the polymer occurs when bond formation takes place at the 2 and 5 positions on the pyrrole ring (Figure 1.3). This is called  $\alpha$ -coupling which results in coplanar pyrrole rings, ensuring overlap of the  $\pi$ -systems and extending the conjugation along the Ppy chain. However,  $\beta$ -coupling can also arise when bond formation occurs at the 3 and 4 positions. During polymer propagation, up to one pyrrole ring in every three may be linked by  $\beta$ -coupling.<sup>59</sup> This results in branching,<sup>60</sup> which can decrease the conductivity of the polymer by breaking the linearity and planarity of the Ppy chains.<sup>61</sup> Oxidation side reactions with water may also cause defects in the polymer, interrupting the conjugation and thus the conductivity of the Ppy.<sup>62</sup>

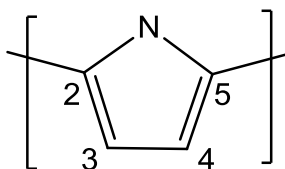


Figure 1.3: The numbering of the carbon atoms of a pyrrole unit within a polypyrrole chain.

### 1.3.2 Electronic Properties of Polypyrrole

Polypyrrole, and conducting polymers in general, demonstrate conductivity due to their extended conjugated  $\pi$ -system. This conductivity is classed in terms of the band gap theory of solids.<sup>32</sup> The interaction of a polymer unit with its neighbouring units leads to the formation of electronic bands. The highest occupied electronic level, or molecular orbital (HOMO) is equivalent to the valence band (VB) while the lowest unoccupied molecular orbital (LUMO) constitutes the conducting band (CB). The width of the band gap ( $\Delta E$ ) between the VB and CB determines the electronic properties of a material (Figure 1.4). Within this band gap, there are no energy states available for an electron to occupy. Therefore, electrons will move along the polymer chain only if they are promoted to a higher energy state. This will only happen if the electron is supplied with an amount of energy at least equal to  $\Delta E$ . Insulators, which do not carry electric current, have a high band gap energy value,  $\Delta E > 10$  eV. Undoped conducting polymers have a  $\Delta E \approx 2$  eV, for which thermal energy is sufficient to promote the electrons into the CB, forming a semiconductor. Metallic conduction is observed when the VB and CB overlap to form a single diffuse band described as an electron cloud ( $\Delta E = 0$ ).

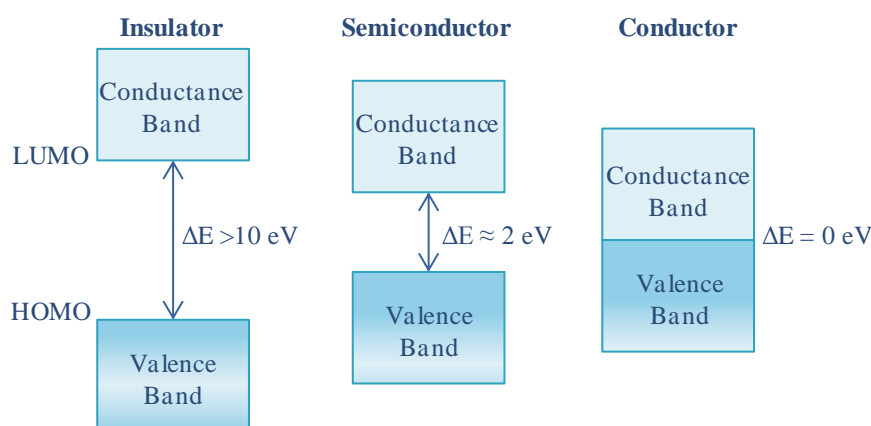
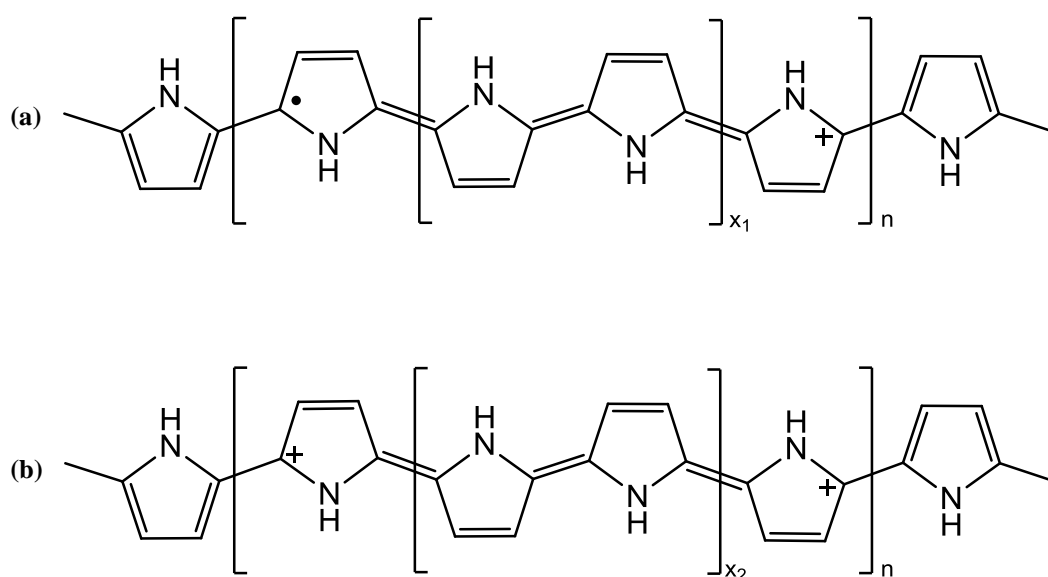


Figure 1.4: The differences in band gap,  $\Delta E$ , for insulators, semiconductors and conductors.

The band gap energy of Ppy in its reduced, or de-doped state, has been reported as 3.16 eV.<sup>29</sup> Doping of the polymer with dopant counterions, during oxidation, facilitate the formation of charge carrier entities known as polarons and bipolarons.<sup>29</sup> Upon oxidation (removal of an electron), these charges become localised on the polymer chain, which causes a local distortion and relaxation of the polymer geometry. This distortion, due to the presence of a polaron (Figure 1.5 a), results in an increase in the energy of the HOMO and a decrease in the energy of the LUMO. Further oxidation may result in the removal of a second electron. It is thermodynamically favourable for this electron to be removed from the polaron and this results in the formation of a bipolaron (Figure 1.5 b).<sup>32</sup>



**Figure 1.5:** Ppy chain showing (a) polaron and (b) bipolaron species ( $X_2 < X_1$ ).

The amount of dopant incorporated into the polymer plays a crucial role in polaron and bipolaron formation, as well as stabilising these charges.<sup>32, 63</sup> The removal of one electron from the Ppy chain results in the formation of two band states: one above and one below the band gap edges. At low doping levels, these states are polaronic and appear approximately 0.5 eV from the CB and VB edges (Figure 1.6 a). At moderate doping levels, bipolaron formation begins as these two states move further away from the band edges upon removal of another electron from the Ppy chain (Figure 1.6 b). At high doping levels bipolaron bands are formed in the band gap (now 3.6 eV) due to the superposition of several bipolaronic states (Figure 1.6 c) These two bands are responsible for the high conductivity observed in the polymer, as the spinless bipolarons can become mobile under the application of an electrical field.

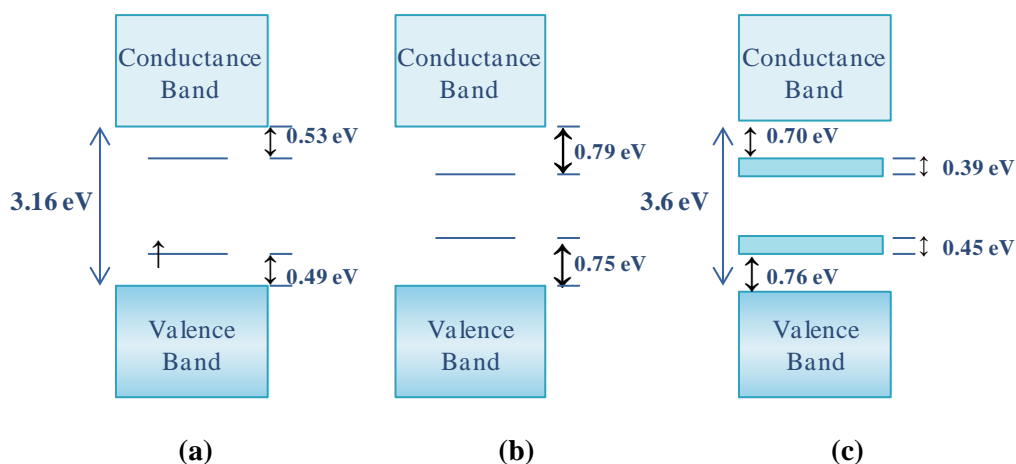


**Figure 1.6:** Effect of doping structure on the band structure of Ppy. a) Polaronic band states generated at low doping levels, b) bipolaronic band states formed at medium doping levels and c) at high doping levels, several bipolaronic states overlap to form two bands within the band gap.<sup>63</sup>

### 1.3.3 Redox Properties of Polypyrrole

The positive charges generated on the Ppy backbone during the oxidation process are stabilised by the incorporation of dopant counterions, which are opposite in charge.<sup>32, 63</sup> As this is a reversible process, the reduction of the Ppy to its neutral state will result in the expulsion of the dopant anions. In this way, conducting polymers can be doped or de-doped by changing their oxidation state, with the dopant moving in and out of the polymer as required, to maintain electroneutrality. This process is illustrated in Figure 1.7.

The ion-exchange properties of Ppy films have been extensively researched.<sup>41-44</sup> Shimidzu *et al.* correlated the size of the anionic dopant with the ion-exchange properties of Ppy.<sup>64</sup> They found, through the incorporation of 1-alkyl sulfonate dopants of varying size, that when the dopant anion was small, it could move in and out of the Ppy matrix during redox switching. Large sulfonate dopants were trapped within the polymer, imparting an overall negative charge on the polymer backbone. Thus, cations were uptaken from the electrolyte to balance this negative charge. This is seen for when large dopant anions such as polystyrene sulfonate (PSS) and polyvinyl sulfonate (PVS) are employed.<sup>41, 65, 66</sup> Intermediate size dopant anions such as dodecylbenzenesulfonate (DBS) or tosylate can result in mixed anion and cation exchange, but cation exchange is more favoured.<sup>67-69</sup>

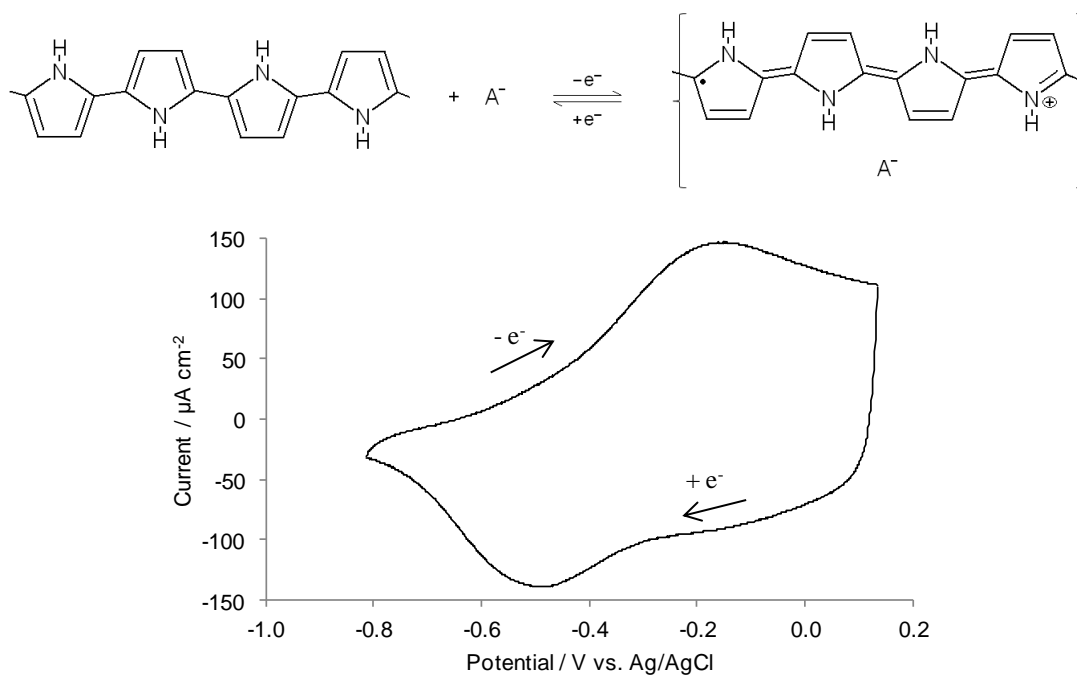


**Figure 1.7: Doping and redox switching of polypyrrole during an electrochemical oxidation/reduction process, for which a typical cyclic voltammogram is illustrated.**

As will be discussed further in Chapter 4, dopant mobility is not the only governing factor in the ion-exchange mechanism of Ppy. Scan rate and the properties of the electrolyte ions also play a role in determining the predominance of anion or cation exchange. Research conducted by Weidlich *et al.* found that both dopant ions and the ions present in the electrolyte solution influenced the ion-exchange behaviour of Ppy.<sup>49</sup> It was found that for Ppy doped with small monovalent or divalent dopant ions, anion exchange was dominant when the electrolyte solution contained monovalent or divalent anions. Also, cation exchange predominated for Ppy doped with immobile polyanionic dopants, regardless of the electrolyte composition. Mixed anion and cation exchange was observed when Ppy films doped with divalent dopant ions were electrochemically switched in a solution containing divalent anions and monovalent cations. More recently, Akieh *et al.* found that cation exchange was the prevalent charge compensation mechanism for Ppy doped with a large immobile dopant, when electrochemically switched in an electrolyte containing monovalent or divalent metal ions.<sup>48</sup> However a more complex mechanism was observed when the same polymer was cycled in an electrolyte containing trivalent metal ions. They proposed that the movement of cations and neutral species into and out of the polymer may be occurring simultaneously. It has also been reported that hydronium cations ( $\text{H}_3\text{O}^+$ ) in solution may compete with the

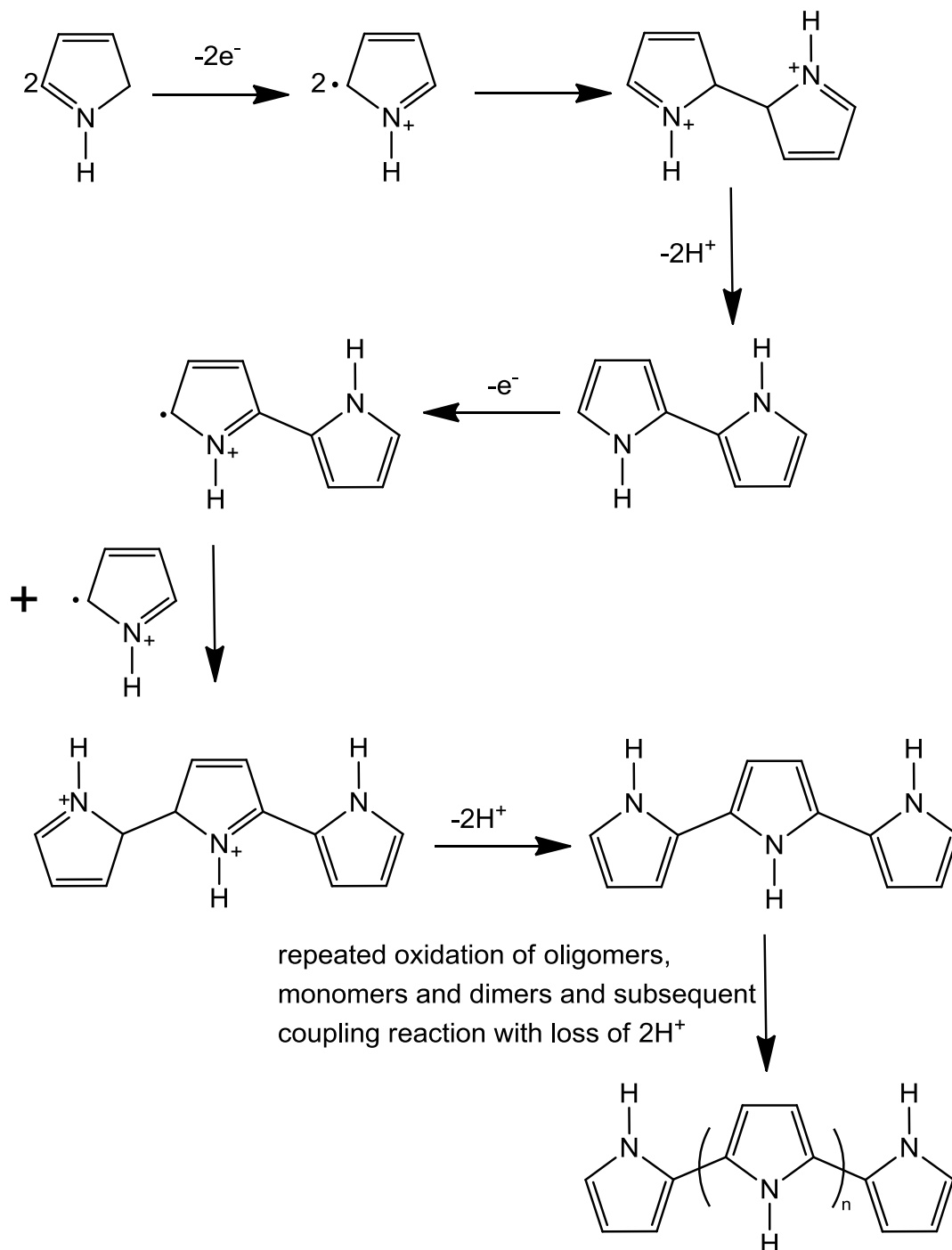
metal cation in the cation exchange process.<sup>70</sup> Akieh *et al.* noted that the scan rate, at which the electrochemical switching was carried out, influenced the ion-exchange properties of Ppy doped with polyanionic dopants.<sup>41, 48</sup>

### 1.3.4 Polymerisation of Polypyrrole

Polypyrrole is produced by polymerisation of the pyrrole monomer unit. This can occur through either chemical or electrochemical methods.<sup>71, 72</sup> Ppy is chemically synthesised through oxidation of the monomer by a strong oxidising agent such as ammonium persulfate<sup>73</sup> or iron(III) chloride.<sup>74</sup> During the polymerisation process, the charge on the oxidised pyrrole species is balanced by the anionic counterions ( $A^-$ ) of the oxidant, and the resulting Ppy $A^-$  precipitates as an insoluble solid. Chemical polymerisation of Ppy at a solid support will be discussed in Section 1.5.

Electrochemical polymerisation of pyrrole, in comparison to chemical polymerisation, is simple and easily controlled<sup>3</sup> using various electrochemical techniques such as potentiostatic amperometry and cyclic voltammetry. The mechanism reported by Diaz *et al.* and later by Baker and Reynolds is the most commonly accepted for the polymerisation of pyrrole (Scheme 1.1).<sup>75, 76</sup> The electrochemical polymerisation consists of a number of steps<sup>29</sup> as shown in Scheme 1.1. Oxidation of the pyrrole monomer is initiated by the application of an anodic potential to the electrode. This results in the formation of a radical cation, which can have a number of resonance states. The radical cations then combine through the formation of a  $\sigma$  bond between the two  $\alpha$ -positions, to form a radical dication. This coupling reaction is favoured due to the higher concentration of radical cations compared to neutral monomers at the electrode surface. A neutral dimer is formed through the loss of two protons from the radical dication. The neutral dimer is further oxidised to form a radical dimer which combines with a radical monomer to form a trimer. Electro-oxidation of the trimer produces a radical cation trimer, which reacts with a radical cation monomer. The process of oxidation, coupling and deprotonation continues until a polymer is formed and chain growth terminates by a reaction with water or other nucleophilic species. Coupling at the  $\alpha$ -position is predominant up until the dimerisation of the radical cation trimer. At this point however,  $\beta$ -coupling may also occur which can result in chain defects<sup>60</sup> and a decrease in the conductivity of the polymer.<sup>61</sup> With increasing numbers of monomer units in the polymer chain, the stability of the radical cation increase. This allows for

greater delocalization of the charges, which results in an oxidation potential for the Ppy chain which is less than that of the pyrrole monomer. This leads to an overall positive charge on the Ppy backbone after polymerisation, which is balanced by the incorporation of dopant anions.<sup>29</sup>



Scheme 1.1: Steps involved in the oxidation of pyrrole resulting in radical cations, radical dication and neutral species which ultimately lead to the formation of polypyrrole.<sup>76</sup>

## 1.4 Polypyrrole Nanostructures

The development of Ppy nanowires and nanostructures has been researched in recent years,<sup>77</sup> due to the attractive properties they exhibit compared to conducting polymers in the bulk morphology. These include improved electrical conductivity,<sup>38</sup> the increase in specific surface area, and shorter path lengths for ion transport.<sup>6, 7</sup> Ppy nanowires have also been observed to deal better than bulk polymer films, with the mechanical strain caused by volume changes during the electrochemical switching process.<sup>78</sup> Ppy nanostructures can be synthesised using three different methods; the hard template approach, the soft template approach or the template-less approach.<sup>7, 77, 79</sup> There are advantages and disadvantages to each method. The hard template approach results in nanowires arrays of controlled length and diameter, but a post processing step to remove the template may damage the nanowires.<sup>80</sup> The soft template method is less expensive as it requires no post processing to remove the template, but it is difficult to control the size and morphology of the nanowires.<sup>77</sup> Electrochemical template-less polymerisation of Ppy can produce nanowire of controllable length and diameter,<sup>81</sup> though increasing polymerisation duration can result in nanowires that are not oriented.<sup>3</sup>

### 1.4.1 Hard Template Approach

Polypyrrole nanotubes/nanowires were first prepared by Penner and Martin by polymerisation of pyrrole in the pores of polycarbonate membranes.<sup>82</sup> This method can be used for the chemical or electrochemical polymerisation of conducting polymers. The conducting polymer is usually deposited in the channels or pores of the template material (Figure 1.8 a). The morphology of the nanowires is controlled by the size of the membrane pores, while their length can be adjusted by changing the duration of the polymerisation. Once polymerisation is complete, the template is removed to reveal the nanowire structures. Chemical polymerisation usually takes place by immersion of the template membrane in a solution containing the monomer, oxidant and dopant. Polymerisation then takes place within the channels of the membrane.<sup>83</sup> Hard-template guided electrochemical polymerisation requires that one side of the template be coated with a conductive metal film. This then acts as the working electrode and polymerisation of the polymer occurs at the metal film surface within the membrane pores. Although porous membranes are the most common template used in this

technique, pre-existing nanostructures have also been employed as seeds or templates for the polymerisation of conducting polymers in the nanomorphology (Figure 1.8 b). These include carbon nanotubes,<sup>84</sup> electrospun degradable polymer nanofibres<sup>85</sup> and vanadium(V) oxide nanofibres.<sup>86</sup> In this last case, the template also acts as the oxidant, removing the need for post-polymerisation removal of the template.

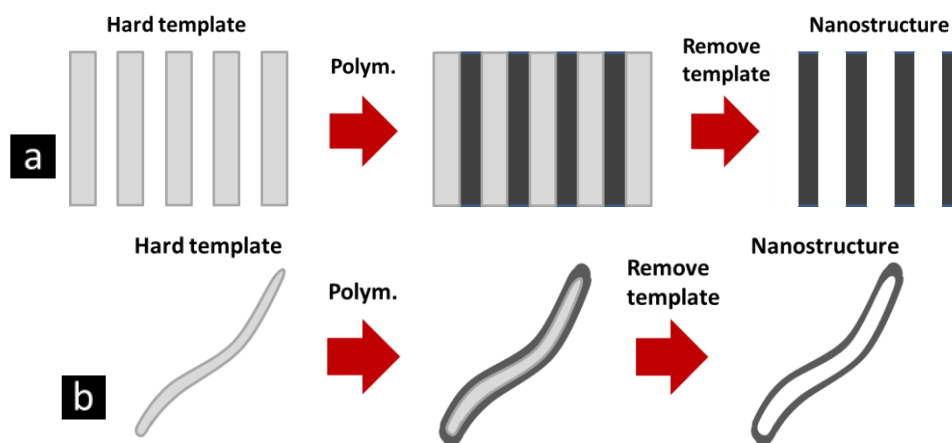


**Figure 1.8: Conducting polymer nanostructures: (a) nanowires and (b) nanotubes polymerised using the hard-template method.<sup>7</sup>**

### 1.4.2 Soft Template Approach

The self assembly of nanostructured conducting polymers, guided by structure-directing species in solution, is known as the soft template or self-assembly process. Control of non-covalent interactions, such as hydrogen bonding, Van der Waals forces and  $\pi$ - $\pi$  stacking interactions, is the main method by which the formation is guided.<sup>7, 77</sup> Fibrillar complexes of methyl orange and iron(III) chloride,<sup>45, 87, 88</sup> surfactants such as cetyltrimethylammonium bromide,<sup>89, 90</sup> “soap bubbles”<sup>91</sup> and molecular templates such as sodium alginate<sup>92, 93</sup> are some of the templates employed for the formation of nanostructured conducting polymers. Surfactants act as soft templates by assembling into micelles (Figure 1.9) that can be spherical, cylindrical or oblate in shape. This micellar formation occurs above a critical concentration (called the critical micelle concentration or CMC) due to the amphiphilic nature of the surfactants in aqueous environments.<sup>79</sup> The micelles act to separate and organise the hydrophobic pyrrole monomers within the micelle cavity. Diffusion of the oxidising agent into the micelle results in polymerisation of the pyrrole which is restricted and guided by the micelle template.<sup>79</sup> The formation of surfactant micelles in a non-polar solvent results in the polymerisation of the monomer on the external surface of the micelle, which forms a

nanotube.<sup>94</sup> Fibrillar methyl orange-iron(III) chloride complexes act to direct the growth of the Ppy nanostructure, but are degraded in the process as they are also the oxidant.<sup>95</sup> Sanju Gupta reported that electrochemically generated hydrogen bubbles, stabilised by anionic surfactant molecules, acted as “soap bubble” templates for the formation of Ppy nanobowls/nanocups at an electrode surface.<sup>91</sup> In this thesis, the formation of Ppy nanowires on a membrane surface, guided by methyl orange-iron(III)chloride complexes will be reported. The polymerisation of Ppy particles in the presence of the molecular template biopolymer sodium alginate will be discussed in Chapter 5.

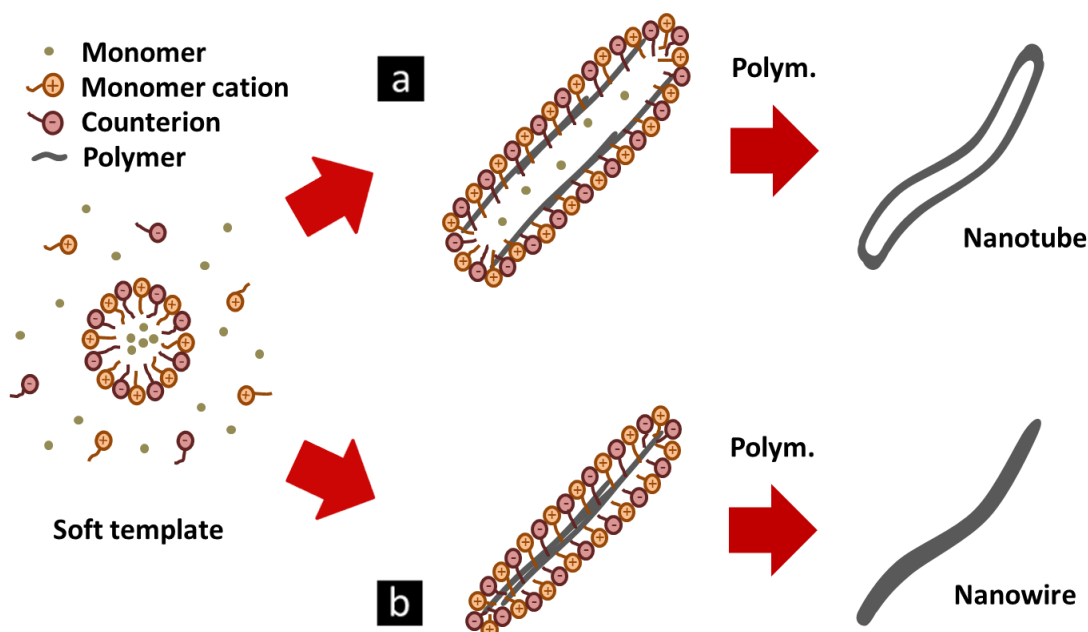


Figure 1.9: Conducting polymer nanostructures synthesised using the soft template method a) nanotubes formation on the external surface of the micelle and b) nanowire formation through polymerisation inside the micelle cavity.<sup>7</sup>

### 1.4.3 Template-Less Approach

An electrochemical template-less polymerisation approach was used for the formation of Ppy nanowires in the current research. This technique has been developed by a number of research groups over the last number of years for the formation of ordered polymer nanostructures. Changing the electrochemical conditions such as the charge density, applied potential and polymerisation duration, as well as the electrolyte solution can effect the morphology of the polymer nanostructures.<sup>96</sup> The successful formation of nanowires through this electrochemical template-less approach is dependant on two

processes. The first is the fast nucleation process, which deposits the polymer at nucleation points across the electrode surface. This must then be followed by a slow growth process, with a controlled propagation of the polymer, to yield orientated polymer nanowires.

Liu *et al.* developed a stepwise electrochemical process for the deposition of uniform and orientated PANI nanowire arrays.<sup>97, 98</sup> This consisted of the application of a high current density to the substrate for 30 minutes, to induce a rapid nucleation. This was followed by two sequential steps at increasingly lower current densities to promote a slow rate of polymer propagation. Although this resulted in uniform thin PANI nanowires, the total polymerisation duration was over 6 hours.

Wei *et al.* first developed a biphasic electropolymerisation technique, in which polymerisation was controlled by limiting the monomer concentration near the electrode surface. This was achieved by the formation of an aqueous-organic interface between the aqueous dopant solution and a pyrrole/chloroform solution. The slow diffusion of the monomer into the aqueous phase, where electropolymerisation occurred at the electrode surface, resulted in oriented Ppy nanowires of controllable length.<sup>99</sup> They went on to develop an alternative method, in which an organic sulfonic acid dopant and a phosphate buffer system were used to produce well defined arrays of Ppy nanowires, that exhibited a superior capacitance when compared to bulk Ppy.<sup>100</sup> Concurrently, Zang *et al.* reported the deposition of a Ppy nanowire network from a solution of phosphate and the dopant perchlorate, with both a controllable length and diameter.<sup>101</sup> They suggested that hydrogen bonding between the pyrrole oligomers and the phosphate resulted in alignment of the oligomers to form oligomer bundles, which promoted the formation of nanowires. They also demonstrated that the concentration of the monomer, the concentration of the perchlorate, and the electrolyte pH are all important parameters in the formation of nanowires.

Debiecme-Chouvy *et al.* used a phosphate/perchlorate electrolyte system for the controlled deposition of Ppy nanowires.<sup>81, 102</sup> They observed that the phosphate acted to slow down the polymerisation process, which resulted in the controlled formation of a nanowire morphology. Most recently, McCarthy *et al.* observed that *N*-substituted Ppy nanowire formation was only supported in the presence of both the phosphate and perchlorate anions. They suggested that the role of the phosphate anion was the

prevention of a build up  $H^+$  ions close to the polymer surface during the polymerisation process.<sup>103</sup> This would help to control the rate of polymerisation as acidic conditions are known to increase the polymerisation rate of pyrrole.<sup>104</sup>

Borm *et al.* classified nanomaterials as materials whose components have at least one dimension in the range of 1 to 100 nm. They further defined nanofibres as having two dimensions less than 100 nm but with a much larger third dimension.<sup>105</sup> This size limitation is based on the knowledge that as nanomaterials approach this size threshold, their physical properties resemble those exhibited by the bulk material. More recently, the argument was put forward that this is dependent on material type, and so the size threshold of 100 nm is arbitrary.<sup>106</sup> Thus, Buzea *et al.* proposed the size range be extended to between 1 nm and 1  $\mu\text{m}$ , with nanomaterials being classed as 1-dimensional, 2-dimensional or 3-dimensional nanomaterials depending on how many of their dimensions fall within this range.<sup>106</sup> In literature reports of Ppy nanowire structures, the designation “nanowire” is usually applied to Ppy wires of diameter 40 nm – 220 nm.<sup>81, 99, 101, 107, 108</sup> The Ppy wires developed in this thesis have a diameter of  $122 \pm 5$  nm, with a maximum diameter of  $154 \pm 5$  nm diameter observed for wires seeded with  $\text{LiBF}_4$ . Thus, although these nanowires do not conform to the range defined by Borm *et al.*,<sup>105</sup> for the purposes of adhering to the precedent set in the literature, the Ppy wires in this thesis will be referred to as nanowires.

## 1.5 Polypyrrole on Porous Membrane Supports

The use of Ppy coated solid supports for the removal of heavy metals from wastewater has been described in the literature. In particular, Ppy coated on sawdust, cellulose and porous carbon substrates has been investigated.<sup>22, 109-111</sup> Of particular interest to the current work was the use of porous membranes as a support for Ppy. Textiles coated with conducting polymers have potential applications in electromagnetic shielding,<sup>112</sup> chemical sensors<sup>113</sup> and heating fabrics.<sup>114</sup> A range of fabrics have been coated with Ppy; wool,<sup>115</sup> cotton,<sup>116</sup> paper,<sup>117</sup> polyester<sup>118</sup> and poly(ethylene terephthalate),<sup>74</sup> but polyamide appears to offer a higher affinity for pyrrole monomers and coated polyamide fabrics have shown higher conductivity and superior adhesion.<sup>119</sup>

The use of porous membranes is particularly attractive for use in separation technologies for a number of reasons. Not only can membranes be applied in a variety of system types involving liquids, gases and volatile species, but scale up and combinations with other separation techniques are possible.<sup>120</sup> The membranes used in separation technology are typically non-conductive. The application of a conducting polymer coating can dramatically increase the conductivity of the membrane, resulting in an electrochemically switchable membrane<sup>121</sup> which may also suppress membrane fouling during the application of an electric field.<sup>122</sup>

Conducting polymer coated porous membranes can be formed in a number of different ways such as contact polymerisation, vapour phase polymerisation and electrochemical polymerisation of the monomer at the membrane surface. To carry out chemical contact polymerisation the membrane substrate is immersed in a solution of the monomer, oxidant and dopant. While polymerisation will occur in the solution, spontaneous deposition of oligomers from the polymerisation solution will lead to the formation of a coating of polymer on the membrane surface.<sup>2</sup> Vapour phase polymerisation usually takes place when the substrate is coated with oxidant and exposed to monomer vapour. Unfortunately, this often results in a non-uniform coating of the substrate surface.<sup>123</sup> Electrochemical polymerisation is carried out as described in Section 1.3.4., where electro-oxidation of the monomer results in the formation of a conducting polymer coating. Typically, electropolymerisation of conducting polymers is restricted, as only conducting substrates can be coated by this method.<sup>2</sup>

Weidlich *et al.* initially investigated the ion-exchange properties of Ppy films doped with polystyrene sulfonate (PSS) on conventional electrodes. They found that the PpyPSS films could be used in the removal of  $\text{Na}^+$ ,  $\text{Ca}^{2+}$  and  $\text{Mg}^{2+}$  from water which could lead to the use of PpyPSS films in water softening.<sup>49, 124, 125</sup> They further developed this by depositing the PpyPSS on porous carbon substrates through a chemical contact polymerisation method.<sup>5, 42</sup> The most recent work by Weidlich *et al.* found that control of the polymer thickness and the size and type of the incorporated anions could provide the porous membrane substrate with certain attributes such as permeability and surface wettability.<sup>121</sup> In addition to this, due to the Ppy coating, the membrane could be electrochemically polarised, which reduced the formation of biofilms on the surface.<sup>126</sup>

Wallace, Ralph and colleagues have also developed conducting polymer membranes for the separation and transport of metal ions in solution.<sup>127</sup> Initial studies into the effect of membrane configuration, electrode materials and electrical stimuli were investigated on standalone Ppy films.<sup>120, 128, 129</sup> Typically these polymer membranes were formed on a flat electrode, and then peeled off for use as standalone switchable membranes. It was found that the standalone membranes were neither sufficiently strong nor porous, and so composite membranes of Ppy electropolymerised on platinum sputter-coated polyvinylidene difluoride substrates (PVDF) were formed.<sup>130, 131</sup> When doped with metal complexing ligands such as bathocuproinedisulfonic acid and sulfated  $\alpha$ - and  $\beta$ -cyclodextrins (CD), it was found that these Ppy composite membranes were permeable to a range of metal ions such as  $\text{K}^+$ ,  $\text{Mg}^{2+}$ ,  $\text{Ca}^{2+}$ ,  $\text{Co}^{2+}$ ,  $\text{Ni}^{2+}$  and  $\text{Cu}^{2+}$  ions.<sup>40, 132</sup>

Recent publications by Akieh *et al.* have further investigated the ion-exchange properties of Ppy doped with sulfated  $\beta$ -cyclodextrin and *p*-sulfonatocalix[6]arene (C6S).<sup>41, 127</sup> They reported that the PpyC6S coated PVDF membrane composite showed significant permeability towards  $\text{K}^+$ ,  $\text{Mn}^{2+}$  and  $\text{Ca}^{2+}$  ions.<sup>127</sup> The use of an electrochemical quartz crystal microbalance (EQCM) revealed that the ion exchange process involved the movement of anions, cations and neutral solvent species, and that the PpyCD and PpyC6S films were non-permselective ion exchange materials when cycled in  $\text{KNO}_3$ ,  $\text{Ca}(\text{NO}_3)_2$  and  $\text{Mn}(\text{NO}_3)_2$  solutions.<sup>41</sup>

## 1.6 Sulfonated Calixarenes

Sulfonated calixarenes (*p*-sulfonatocalix[n]arenes) are a class of water soluble calixarenes. Calixarenes are macromolecules consisting of a number of phenol units in a cyclic arrangement, linked by methylene bridges. This endows the calixarene with a flexible, 3-dimensional cavity, rich in  $\pi$ -electrons<sup>133</sup> which has led to the application of calixarenes in the fields of molecular recognition and supramolecular chemistry. For example, water soluble calixarenes have been used in fields such as biomimetic catalysis, biomimetic receptors, enzyme inhibitors and ion channel blockers.<sup>134</sup> Calix[4]arenes, calix[6]arenes and calix[8]arenes are known as the major calixarenes (Figure 1.10), while minor calixarenes such as calix[5]arene and calix[7]arene may be obtained in lesser yields.<sup>135</sup> Substitution of the calixarene rim with carboxyl groups, amino groups, nitro groups and phosphate groups has been attempted in order to improve the water solubility of these macrocycles.<sup>134</sup> The greatest water solubility is observed for sulfonated calixarenes, first prepared by Shinkai *et al.*,<sup>136, 137</sup> which display water solubilities greater than  $0.10 \text{ mol dm}^{-3}$ .<sup>134</sup> In this thesis, *p*-sulfonatocalix[4]arene (C4S) was employed as a large immobile dopant, incorporated into a polypyrrole matrix. The application of the prepared *p*-sulfonatocalix[4]arene-polypyrrole film (PpyC4S) is discussed in Chapter 4.

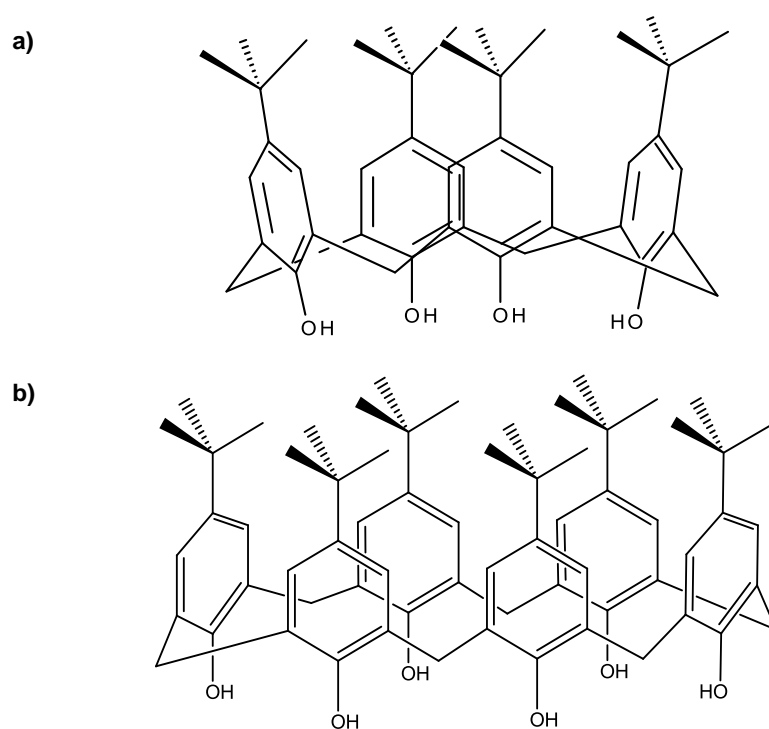


Figure 1.10: The structures of a) calix[4]arene and b) calix[6]arene.

### 1.6.1 Structural Properties of Sulfonated Calixarenes

The most significant structural property of calixarenes is their flexibility. Each is composed of a number of phenol units, which can rotate around the axis passing through the carbon atoms bonded to the bridging methylene groups. This results in a number of possible conformations of each calixarenes.<sup>134, 138</sup> For C4S, there are four possible conformers which are referred to as; cone, partial cone, 1,3-alternate and 1,2-alternate (Figure 1.11).<sup>134, 138</sup>

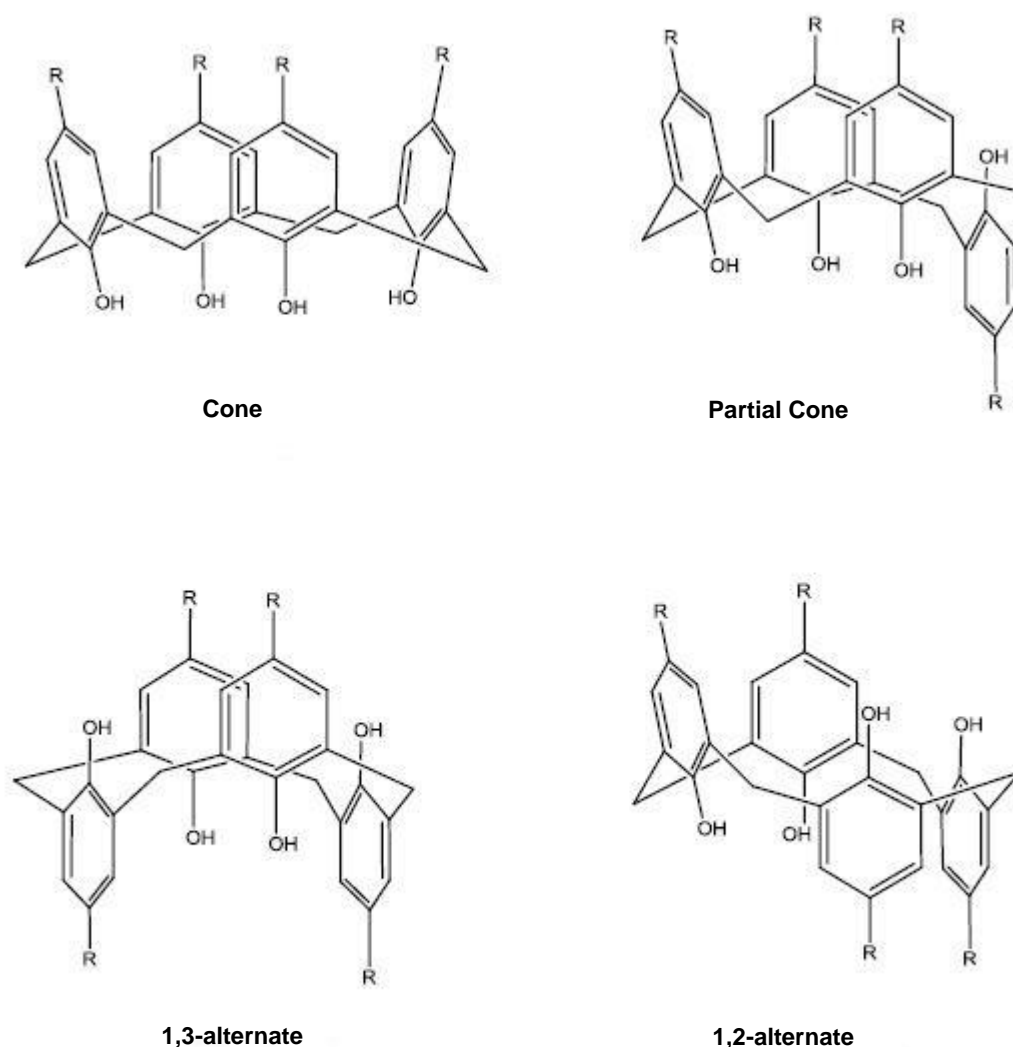


Figure 1.11: The four possible structural conformations of calix[4]arenes.

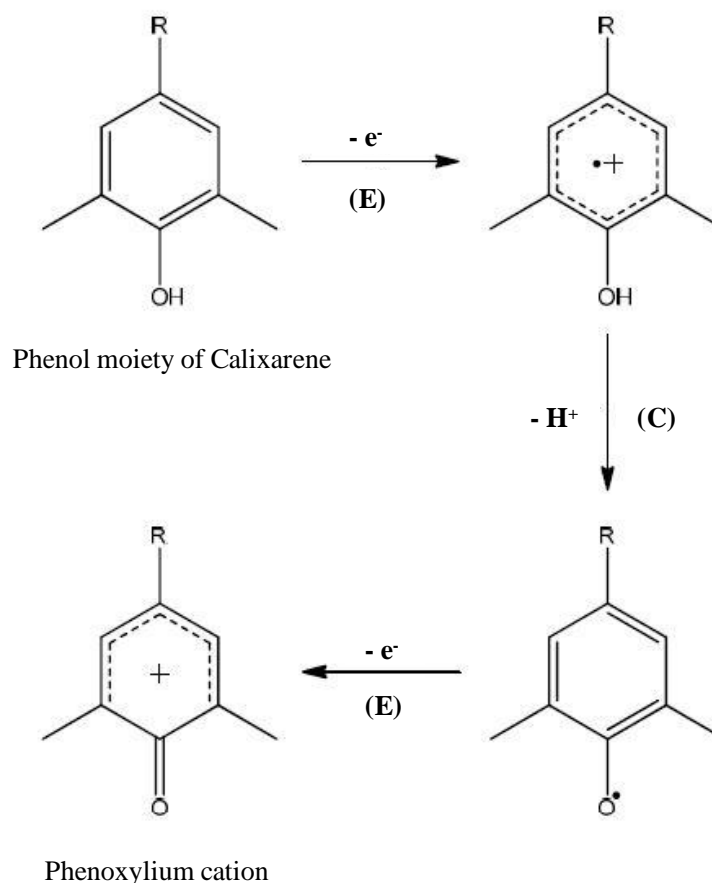
The cone conformation is generally the most stable in the solid state, however, in solution, the calixarene is conformationally mobile, which can result in a temperature dependent inversion of the calixarene ring. The process of this conformational inversion

is not known however, computational studies suggest it involves a cone  $\rightarrow$  partial cone  $\rightarrow$  1,2-alternate/1,3-alternate  $\rightarrow$  inverted partial cone  $\rightarrow$  inverted cone sequence.<sup>134</sup>

Intramolecular hydrogen bonding interactions between the hydroxyl groups of calixarenes have been credited with the stabilisation of the cone conformation.<sup>134</sup> This is particularly applicable to C4S. Its lower rim hydroxyl groups are dissociated, with  $pK_a$  values of 3.26 for the first group and 12.30 for the second.<sup>139</sup> Shinkai *et al.*, using variable temperature  $^1\text{H}$  NMR spectroscopy, concluded that in acidic media the oxide anion acted as a stronger acceptor for intramolecular hydrogen bonding than the hydroxyl groups, increasing the stabilisation of the cone conformation of C4S.<sup>138</sup>

### 1.6.2 Electrochemical Activity of Sulfonated Calixarenes

The electrochemical activity of sulfonated calixarenes has been studied over the last number of years, with particular interest shown by Diao *et al.*<sup>140, 141</sup> and Pailleret *et al.*<sup>142, 143</sup> The research showed that sulfonated calixarenes can be irreversibly oxidised at applied potentials greater than 0.70 V vs. SCE. Most relevant to the work presented herein is the determination by Diao *et al.* that the oxidation of C4S was an irreversible two-electron reaction.<sup>140</sup> It has been suggested that this oxidation results in the formation of a phenoxylium cation, via the mechanism described in Scheme 1.2.<sup>144</sup> This mechanism, which is known as an ECE mechanism, was first proposed by Ronlan *et al.* for the oxidation of sterically hindered phenols.<sup>145</sup> It was later employed by Louati and Vataj for the oxidation of the phenol moiety of a number of *para* substituted calix[4]arenes.<sup>146-148</sup> Spectroelectrochemical experiments carried out by their research group showed an increase in the characteristic phenoxylium band with increasing oxidation duration. The ECE mechanism consists of an electrochemical step (E), during which one electron is transferred. This is followed by a chemical step (C) in which a proton is lost. Lastly, another electrochemical step occurs in which a second electron is transferred. As this oxidation has been shown to occur at applied potentials greater than 0.70 V vs. SCE, the potentials applied to PpyC4S films in this thesis were maintained below this value. Otherwise, the electrochemical activity of the C4S may have impacted on the electrochemical behaviour and stability of the PpyC4S films.



Scheme 1.2: Mechanism for the irreversible electrochemical oxidation of a calixarene phenol moiety and the formation of a phenoxylum cation.<sup>145-148</sup>

### 1.6.3 Inclusion Complexes of Sulfonated Calixarenes

Calixarenes are macrocycles with 3-dimensional, flexible,  $\pi$ -electron rich cavities.<sup>133</sup> Exhibiting similar selectivity to cyclodextrins,<sup>149</sup> these cavities allow calixarenes to act as host molecules. The formation of an inclusion complex between a host and a guest can involve one or more of the following interactions; hydrogen bonding, electrostatic attraction, van der Waals attraction, hydrophobic effects,  $\pi$ - $\pi$  stacking, cation- $\pi$  or CH- $\pi$  interactions or charge-transfer interactions.<sup>134</sup> In water, the soluble *p*-sulfonatocalix[4]arene is able to complex a variety of metal and organic cations.<sup>150</sup> The sulfonate functional groups on C4S can participate in electrostatic interactions with cations, while the lower rim of C4S has the potential for hydrogen bonding. The hydrophobic cavity of C4S allows for the inclusion of non-polar molecules. Interactions such as  $\pi$ - $\pi$  stacking, cation- $\pi$  or CH- $\pi$  interactions are facilitated by the  $\pi$ -system of C4S.

Using microcalorimetry, Bonal *et al.*<sup>150</sup> and Morel *et al.*<sup>151</sup> investigated the binding affinities and thermodynamics of the complexation of C4S with a range of metals and ammonium cations. It was observed that C4S exhibited weak binding abilities for monovalent cations such as Na<sup>+</sup> and Cs<sup>+</sup>, in contrast with the moderately strong binding abilities seen for divalent cations (Ca<sup>2+</sup> and Mg<sup>2+</sup>) and trivalent lanthanide cations. Data obtained for the enthalpy and entropy changes were used to indicate the interactions involved in the complex formation. Complexation of C4S with monovalent cations was enthalpically favoured, indicating that these cations were included in the C4S cavity through cation- $\pi$  interactions. Conversely, complexation of C4S with divalent and trivalent cations was entropically favoured. This indicated that the driving force behind complexation was electrostatic interactions of the cations with the sulfonate groups. As the divalent and trivalent cations were more hydrated than the monovalent cations, they were not included in the C4S cavity.<sup>150, 151</sup> It has also been observed that *p*-sulfonatocalix[6]arene retains its inclusion properties when immobilised in a polymer film.<sup>152, 153</sup> Thus, in this thesis, the incorporation of C4S into a polypyrrole matrix was investigated for the purpose of metal remediation.

#### 1.6.4 Immobilisation of Sulfonated Calixarenes in Polypyrrole

In this thesis, C4S was employed as a large immobile dopant, incorporated into a polypyrrole matrix. The doping of polypyrrole with sulfonated calixarenes has been investigated by a number of research groups.<sup>41, 70, 127, 152-154</sup> Although *p*-sulfonatocalix[6]arene is most widely studied, Bidan *et al.*<sup>152</sup> and Mousavi *et al.*<sup>153</sup> successfully doped polypyrrole with C4S. Bidan *et al.* noted that the C4S was irreversibly immobilised within the polypyrrole film,<sup>152</sup> however more recent work by Latonen *et al.* suggested that over an extended experimental period, C6S may leach from the polypyrrole film.<sup>41</sup> They continued the work begun by Akieh *et al.*, investigating the ion exchange abilities of the PpyC6S film, and the assumption was made that the C6S was immobile within the film for the beginning of the redox cycling process. An EQCM study showed that although the PpyC6S displayed an affinity for K<sup>+</sup>, Mn<sup>2+</sup> and Ca<sup>2+</sup> ions, the ion exchange process could not simply be described in terms of cation exchange.<sup>41, 127</sup> It was hoped that the PpyC4S in this study would exhibit similar affinities for metal cations.

## 1.7 Remediation of Heavy Metals

The Millennium Development Goal (Target 7.C) which aimed to halve, by 2015, the proportion of the population without sustainable access to safe drinking water, was met in 2010. However in 2011, 768 million people still remained without access to an improved source of drinking water.<sup>155</sup> This included 185 million people who relied on surface water for their every day drinking water requirements.<sup>156</sup> Water pollution by heavy metal ions is thus a huge concern, as heavy metals can enter the water supply from a variety of anthropogenic sources. Chromium, for example, is discharged in the untreated effluents from industries such as leather tanning, electroplating and pigment manufacturing.<sup>157</sup> The Irish EPA 2020 Vision strategy document set key goals to protect the quality of water resources and to sustainably use resources such as water, in Ireland.<sup>158</sup> This is in keeping with the EU Joint Programming Initiative “Water challenges for a changing world”, which aims to pool the national resources of European member states in the areas of water quality and the environment.<sup>159</sup>

Although chromium was used as a model environmental pollutant in the course of this research, the ion-exchange and adsorption properties of the developed Ppy nanomaterials may make them suitable materials for the remediation of a range of heavy metals in the future.

### 1.7.1 Common Heavy Metal Pollutants – Toxicity and Sources

The use of heavy metals is heavily regulated across the European Union. Their use in electrical equipment and in packaging is restricted under EU Directive 2011/65/EU and Directive 94/62/EC.<sup>160, 161</sup> These regulatory directives set mandatory limits for the following heavy metals; nickel ( $20 \mu\text{g L}^{-1}$ ), copper ( $2 \text{ mg L}^{-1}$ ), arsenic ( $10 \mu\text{g L}^{-1}$ ), cadmium ( $5 \mu\text{g L}^{-1}$ ), mercury ( $1 \mu\text{g L}^{-1}$ ) and lead ( $10 \mu\text{g L}^{-1}$ ) whose limits are indicated in parentheses.<sup>162</sup> The most threatening of these, in relation to human health, are thought to be arsenic, cadmium, lead and mercury.<sup>163</sup> Heavy metals are of major concern due to their persistence in the environment and their effect on human health. Heavy metals cannot be destroyed biologically, and are usually remediated by changing oxidation state or from one organic complex to another.<sup>164, 165</sup>

Exposure to arsenic via drinking water has been found to cause cancer of the lungs, kidneys, bladder and skin.<sup>166</sup> Ingestion of inorganic arsenic leads to gastrointestinal symptoms, cardiovascular and nervous system disturbances and is eventually fatal.<sup>163</sup> Smelting activities and the burning of fossil fuels are the two main industrial processes associated with arsenic pollution. Other sources include the production of wood preservatives, semi-conductors, animal feed additives, pesticides and herbicides.<sup>163, 167</sup> While a reduction in the amount of arsenic released into the air has been observed since the 1980s,<sup>163</sup> in 2005 the EPA reported that elevated levels of arsenic were detected in marine sediments at Dublin Port, Dun Laoghaire harbour, the Boyne and Avoca estuaries and Bantry harbour.<sup>168</sup>

Cadmium can be lethal if inhaled or ingested, and is associated with kidney damage and chronic renal failure. Skeletal damage associated with long term cadmium exposure was first reported in Japan in the 1950s. Rice field workers were exposed to cadmium polluted irrigation water over long periods of time, which resulted in a combination of osteomalacia and osteoporosis. Cadmium is also classed as a human carcinogen and has been linked to lung, prostate and kidney cancers.<sup>163</sup> It is found in rechargeable batteries, metal alloys, colour pigments and cigarettes. However, the application of fertilizers and sewage sludge to farm land, leading to the uptake of cadmium by crops and vegetables, is the main route through which human exposure occurs.<sup>163</sup>

Lead was classified as a possible human carcinogen in 1987, and this classification was extended to include inorganic lead compounds in 2006.<sup>163, 169</sup> The main symptoms associated with lead poisoning are headaches, abdominal pain and irritability. In severe cases confusion and unconsciousness are also experienced. Long term exposure can result in anaemia and kidney damage.<sup>163</sup> Ireland is the tenth largest producer of lead in the world, and its anthropogenic sources include mining and electroplating waste, smelting and glass production as well as batteries and leaded petrol and paints.<sup>167, 168</sup>

Humans are primarily exposed to mercury in the form of methyl mercury, which is ingested, as fish are a major source of methyl mercury. The main symptoms of methyl mercury exposure are related to the central nervous system. Numbness of the extremities, coordination problems and visual and auditory difficulties are experienced, with high doses leading to death.<sup>163</sup> Anthropogenic sources of mercury are mainly related to the industrial burning of peat, coal and wood, the production of gold and the

improper disposal of mercury containing waste products such as batteries, thermometers and car components.<sup>167</sup>

The use of PpyC4S films for the remediation of nickel from solution was investigated in the course of this thesis. Although it has been suggested that nickel is required in lipid metabolism and iron absorption,<sup>170, 171</sup> in high doses it can adversely affect the kidneys, skin, cardiovascular and respiratory systems. It has also been found to be teratogenic and carcinogenic if ingested in high amounts.<sup>171</sup> Nickel compounds and alloys are used in electroplating and in the production of batteries, electronic components, tools, machinery and jewellery. The processing, recycling and disposal of these items are sources of nickel pollution. Combustion of fossil fuels can release a large amount of nickel into the atmosphere. Natural leaching from rock and sediments can also contribute to high nickel levels in water sources.<sup>171</sup>

### **1.7.2 Current Remediation Techniques for Heavy Metal Pollutants**

The most common methods for the remediation of heavy metal pollutants from ground water include; chemical reduction and precipitation, ion exchange, reverse osmosis and phytoremediation.<sup>172, 173</sup> Chemical precipitation can be achieved through a simple pH change, and often involves the addition of sodium hydroxide, calcium carbonate or granulated lime. However, each metal hydroxide has its own maximum precipitation point, and thus a number of pH changes could be required in a system polluted with a number of heavy metals.<sup>172</sup> Heavy metals can be reduced to a less toxic oxidation state by reducing agents such as sulfur dioxide, dithionite and colloidal iron.<sup>173</sup> Ion exchange resins are preferable to other adsorbents as the most common ion exchange resins can be regenerated up to 100% efficiency.<sup>173</sup> Reverse osmosis and microfiltration techniques are effective in heavy metal remediation but the membranes utilised are expensive to produce and operate.<sup>172</sup> Phytoremediation is the use of plants to remediate pollutants in soils, sludge, groundwater, surface water and wastewater. This remediation category includes phytoextraction, in which the pollutants are absorbed and stored by the plants; phytodegradation, in which pollutants are broken down by the metabolic processes in the plant; and rhizofiltration, in which the plants roots absorb pollutants from the water source they are immersed in.<sup>172</sup> As these biological processes can be slow, they are most suitable for use in long term remediation, in conjunction with a more intense remediation process.<sup>173</sup>

### 1.7.3 Chromium – Toxicity, Sources and Regulatory Directives

The toxicity of chromium is dependent on its oxidation state. In fact Cr(III) is considered an essential trace element, which has been reported to be responsible for the control of lipid metabolism in mammals.<sup>174</sup> On the other hand, Cr(VI) is one hundred times more toxic and one thousand times more mutagenic than Cr(III).<sup>175</sup> This is mainly due to its high water solubility and mobility and it is classified as a known carcinogen.<sup>176</sup> Common dissolved Cr(VI) species are  $\text{HCrO}_4^-$ ,  $\text{CrO}_4^{2-}$  and  $\text{Cr}_2\text{O}_7^{2-}$ , the dominance of which is contingent on the pH, total chromium concentration and the chemical makeup of the aqueous environment.<sup>157, 177</sup> Occupational exposure to Cr(VI) compounds has been linked to contact dermatitis, nasal septum perforation, asthma, bronchitis and inflammation of the larynx and liver.<sup>178</sup> Carcinogenic effects of Cr(VI) species are thought to be due to its strong oxidising nature, which can result in its reduction to Cr(V). Pentavalent chromium may lodge in body tissues, forming cancerous growths and it has been linked to premature senility.<sup>157</sup> The highly soluble Cr(VI) can freely diffuse through cell membranes. Whether absorbed by the skin or ingested, blood and stomach acid can reduce Cr(VI) to Cr(III).<sup>176</sup> However, if this reduction occurs within the cells, the build-up of insoluble Cr(III) may have adverse effects as Cr(III) is known to co-ordinate various organic molecules, which could inhibit some enzyme systems in the body.<sup>178</sup>

Chromium is used in a variety of industrial areas, but most commonly in metallurgy, leather tanning, wood preservation and pigment manufacture. Chrome electroplating of an item requires a chromic acid bath of which the hexavalent chromium acid bath is most widely used.<sup>157</sup> During this process, the chromic acid bath can become contaminated with chlorine, which requires drainage. The discharge associated with this industry can contain  $0.60 \text{ g L}^{-1}$  chromium at acidic pH, and the sludge produced can contain 9-11 percent chromium as hexavalent and trivalent chromium, Cr(VI) and Cr(III).<sup>179</sup> Chromium is used in leather tanning to stabilise and confer water-repellent properties on the leather. This occurs through cross-linking of the chromium with the collagen or protein in the hide. Leather tanning also requires large baths of chromium, and the effluent discharged can contain 40 percent chromium as Cr(VI) and Cr(III).<sup>157</sup> The preservation of wood entails a range of chromium compounds too. Chromic acid and sodium dichromate are both registered as insecticides, and are used to prevent

termite damage and to treat the lumber used in construction pilings.<sup>176</sup> In 2004, the United States EPA banned the use of a common, green coloured wood treatment, known as chromate copper arsenate, which was used in pressure treated lumber commonly used in decking, picnic tables and swings. It was found that, when exposed to a low pH solution, such as rain, Cr could be leached from the wood surface.<sup>176</sup> Chromium compounds are also commonly used in pigments for textiles and paints.<sup>157</sup> Compounds such as Cr(III) oxide, barium chromate, calcium chromate and basic lead chromate are brightly coloured green, yellow and red compounds.

The use of chromium in electrical equipment and in packaging is restricted under EU Directive 2011/65/EU and Directive 94/62/EC.<sup>160, 161</sup> Mandatory limits for the amount of chromium present in drinking water and in sludge waste are also set out in the EC Drinking Water Regulations (2007/2) and in Directive 86/278/EEC.<sup>180, 181</sup> The mandatory limit for chromium is  $50 \mu\text{g L}^{-1}$  of total chromium.

#### 1.7.4 Current Remediation Techniques for Chromium

The most common treatment methods for removing Cr(VI) from industrial wastewaters include chemical and electrochemical reduction to Cr(III), ion exchange, membrane separation and adsorption.<sup>182-186</sup> These techniques rely on three main processes, namely the reduction of Cr(VI) to Cr(III), adsorption of chromium species and precipitation of chromium species.<sup>176</sup> The reduction of Cr(VI) to Cr(III) can be carried out electrochemically, or chemically through the addition of strong reducing agents such as sulfur dioxide and ferrous sulfate. The enzymatic redox activity of microorganisms may also be employed for the reduction of Cr(VI). The adsorption process is usually most successful at removing Cr(III) species and can be carried out by adsorption on clays and soils containing iron and manganese oxides. Ion exchange materials may also act in an adsorption capacity for the removal of chromium. The loaded ion exchange materials are typically regenerated with a sodium hydroxide wash.<sup>179</sup> Chemical, electrochemical and biological reduction treatment is usually followed by the precipitation of Cr(III) as  $\text{Cr}(\text{OH})_3$ . This can then be separated from the system. While these methods of remediation are often very effective many produce Cr(VI) or Cr(III) impregnated secondary waste products which are difficult to dispose of or recycle.<sup>187, 188</sup> This problem of post removal processing, in addition to the high costs associated with many

of these methods gives rise to the need for an efficient, environmentally friendly removal method for Cr(VI).

### 1.7.5 Remediation by Conducting Polymers

The application of conducting polymers in the removal of heavy metal ions, such as gold, silver, mercury, lead, and copper, has been extensively studied.<sup>22, 109, 111, 189</sup> Hepel *et al.* exploited the cation exchange properties of Ppy doped with melanin or polystyrene sulfonate for the electrochemically assisted uptake of lead, cadmium and nickel ions from solution. They found that the amount of ions removed depends on the potential applied, polymer thickness and doping levels. More recently, Weidlich *et al.* employed PpyPSS films for removal of calcium ions in order to soften water.<sup>49, 124, 125</sup> They reported that the PpyPSS films were selective towards calcium ions when a potential was applied in binary calcium/sodium or calcium/ magnesium solutions. Increased polymer surface area was achieved by Ding and Wang *et al.*, who coated vitreous carbon and polyvinylidene difluoride (PVDF) nanofibre membranes for the recovery of gold from solution.<sup>189-191</sup> They noted that membrane thickness, initial gold concentration and rate of solution flow through the polymer coated membrane influenced the removal efficiency. Choi and Jang explored the use of Ppy coated porous carbon as a heavy metal adsorbent.<sup>22</sup> The polymer-impregnated porous carbon showed an improved complexation affinity for mercury, lead and silver ion which was attributed to the amine group on polypyrrole.

The ability of Ppy to reduce Cr(VI) to the less toxic Cr(III) was first reported by Rajeshwar and co-workers in 1993.<sup>192</sup> Rajeshwar *et al.* employed a Ppy coated platinum mesh to reduce Cr(VI) in acidic solutions. The Ppy was reduced in a conducting solution prior to being placed in an acidic solution containing Cr(VI). It was found to reduce 100 percent of the Cr(VI) in solution over a 1 hour duration.<sup>192</sup> This work was followed by the development of Ppy coated on glassy carbon and Ppy-carbon black composites for use in the reduction of Cr(VI) to Cr(III).<sup>193, 194</sup> These reports provided insights into the effect of the Ppy amount and Cr(VI) concentration on the reduction of Cr(VI) by Ppy.

Breslin *et al.* have also investigated the reduction of Cr(VI) by polyaniline (PANI) electrochemically deposited on platinum and Ppy deposited on aluminium or titanium

electrodes.<sup>13, 195, 196</sup> They reported on the effect of film thickness, oxidation state and solution agitation on the reduction of Cr(VI) by the conducting polymers. They found that the maximum level of Cr(VI) reduction was achieved through a combination of parameters: thick Ppy coatings, pre-reduction step at a low applied potential and vigorous solution agitation.<sup>13</sup>

The reduction of Cr(VI) to Cr(III) by Ppy is a chemical reduction process which is the result of two phenomena; a) the spontaneous electron transfer from the Ppy to Cr(VI) present in solution and b) anion exchange which occurs to maintain the electroneutrality of the Ppy film as it is oxidised by the Cr(VI).<sup>197, 198</sup> The application of a reduction potential prior to immersion of the Ppy material in acidic aqueous Cr(VI) solutions ensures the polymer is in its reduced state.<sup>196</sup> This enhances the adsorption of negatively charged species through electrostatic interactions with the Ppy backbone, which is positively charged due to deprotonation in the acidic solution.<sup>199, 200</sup> The main advantage of using conducting polymers is the potential for regeneration. During the reduction of Cr(VI) to Cr(III), the polymer is oxidised. However, it can be electrochemically recycled back to its reduced state, through the application of a reduction potential, for further use.<sup>13, 194</sup> Ppy nanowires can have advantages over bulk Ppy, such as a larger surface area with increased access to surface access sites. Bhaumik *et al.* have reported on the use of Ppy-PANI nanofibres and Ppy-Fe<sub>3</sub>O<sub>4</sub> magnetic nanocomposites for the adsorption of Cr(VI) from solution.<sup>17, 18, 201</sup> They investigated the effect of solution pH, Cr(VI) concentration and adsorbent mass on the adsorption of Cr(VI) and noted the presence of Cr(III) at the adsorbent surface, which suggested the reduction of Cr(VI) to Cr(III) by the Ppy nanocomposites. Regeneration of the nanomaterials necessitated the use of NaOH washes for the desorption of Cr(VI), however only ~ 30 percent desorption was observed. The research reported in this work aims to incorporate the benefits of nanostructured Ppy with the potential for electrochemical regeneration through the development of Ppy coated on electroactive porous membranes.

## 1.8 References

1. U. Lange, N. V. Roznyatovskaya and V. M. Mirsky, *Analytica Chimica Acta*, 2008, **614**, 1-26.
2. A. Malinauskas, *Polymer*, 2001, **42**, 3957-3972.
3. Y. Chen, Z. Zhao and C. Wang, *Nanoscience and Nanotechnology Letters*, 2013, **5**, 186-190.
4. W. S. Choi, T. An and G. Lim, *Fabrication of Conducting Polymer Nanowires - Implementations and Applications*, InTech, 2011.
5. M. M. Saleh, C. Weidlich, K. M. Mangold and K. Juettner, *Journal of Applied Electrochemistry*, 2006, **36**, 179-186.
6. J. Yang, J. Wang, Y. Tang, D. Wang, B. Xiao, X. Li, R. Li, G. Liang, T.-K. Sham and X. Sun, *Journal of Materials Chemistry A*, 2013, **1**, 7306-7311.
7. L. Xia, Z. Wei and M. Wan, *Journal of Colloid and Interface Science*, 2010, **341**, 1-11.
8. C. Janaky and C. Visy, *Analytical and Bioanalytical Chemistry*, 2013, **405**, 3489-3511.
9. X. Guo, G. T. Fei, H. Su and L. D. Zhang, *Journal of Physical Chemistry C*, 2011, **115**, 1608-1613.
10. D.-H. Nam, S.-J. Lim, M.-J. Kim and H.-S. Kwon, *RSC Advances*, 2013, **3**, 16102-16108.
11. K. Wang, H. Wu, Y. Meng and Z. Wei, *Small*, 2013, Ahead of Print.
12. A. S. Lee, S. F. Peteu, J. V. Ly, A. A. G. Requicha, M. E. Thompson and C. Zhou, *Nanotechnology*, 2008, **19**, 165501.
13. S. T. Earley, B. E. Alcock, J. P. Lowry and C. B. Breslin, *Journal of Applied Electrochemistry*, 2009, **39**, 1251-1257.
14. F. J. Rodriguez, L. A. de la Rosa-Garcia, A. Alatorre, J. Ibanez, L. Godinez, S. Gutierrez and P. Herrasti, *Progress in Organic Coatings*, 2007, **60**, 297-302.
15. K. Roy, P. Mondal, S. P. Bayen and P. Chowdhury, *Journal of Macromolecular Science, Part A: Pure and Applied Chemistry*, 2012, **49**, 931-935.
16. S. Li, X. Lu, X. Li, Y. Xue, C. Zhang, J. Lei and C. Wang, *Journal of Colloid and Interface Science*, 2012, **378**, 30-35.

17. M. Bhaumik, K. Setshedi, A. Maity and M. S. Onyango, *Separation and Purification Technology*, 2013, **110**, 11-19.
18. M. Bhaumik, A. Maity, V. V. Srinivasu and M. S. Onyango, *Chemical Engineering Journal*, 2012, **181-182**, 323-333.
19. J. Wang, K. Pan, Q. He and B. Cao, *Journal of Hazardous Materials*, 2013, **244-245**, 121-129.
20. T. Yao, T. Cui, J. Wu, Q. Chen, S. Lu and K. Sun, *Polymer Chemistry*, 2011, **2**, 2893-2899.
21. K. G. Neoh, K. K. Tan, P. L. Goh, S. W. Huang, E. T. Kang and K. L. Tan, *Polymer*, 1999, **40**, 887-893.
22. M. Choi and J. Jang, *Journal of Colloid and Interface Science*, 2008, **325**, 287-289.
23. Y. Tian, Z. Li, K. Shi and F. Yang, *Separation Science and Technology*, 2008, **43**, 3891-3901.
24. E. Tamburri, S. Orlanducci, F. Toschi, M. L. Terranova and D. Passeri, *Synthetic Metals*, 2009, **159**, 406-414.
25. H. Shirakawa, *Reviews of Modern Physics*, 2001, **73**, 713-718.
26. A. G. MacDiarmid, *Reviews of Modern Physics*, 2001, **73**, 701-712.
27. A. J. Heeger, *Reviews of Modern Physics*, 2001, **73**, 681-700.
28. H. S. Nalwa, *Handbook of Organic Conductive Molecules and Polymers*, Wiley, 1997.
29. P. Chandrasekhar, *Conducting Polymers, Fundamentals and Applications: A Practical Approach*, Springer, 1999.
30. T. A. Skotheim and J. R. Reynolds, *Handbook of Conducting Polymers*, CRC Press, 2007.
31. G. Inzelt, *Conducting Polymers: A New Era in Electrochemistry*, Springer, 2008.
32. J. L. Bredas and G. B. Street, *Accounts of Chemical Research*, 1985, **18**, 309-315.
33. D. Li, J. Huang and R. B. Kaner, *Accounts of Chemical Research*, 2009, **42**, 135-145.

34. H. D. Tran, J. M. D'Arcy, Y. Wang, P. J. Beltramo, V. A. Strong and R. B. Kaner, *Journal of Materials Chemistry*, 2011, **21**, 3534-3550.
35. J. Wang, X. Mo, D. Ge, Y. Tian, Z. Wang and S. Wang, *Synthetic Metals*, 2006, **156**, 514-518.
36. N. Anwar, M. Vagin, F. Laffir, G. Armstrong, C. Dickinson and T. McCormac, *Analyst*, 2012, **137**, 624-630.
37. K. Gurunathan, A. V. Murugan, R. Marimuthu, U. P. Mulik and D. P. Amalnerkar, *Materials Chemistry and Physics*, 1999, **61**, 173-191.
38. S. I. Cho and S. B. Lee, *Accounts of Chemical Research*, 2008, **41**, 699-707.
39. P. M. George, D. A. LaVan, J. A. Burdick, C. Y. Chen, E. Liang and R. Langer, *Advanced Materials*, 2006, **18**, 577-581.
40. D. A. Reece, S. F. Ralph and G. G. Wallace, *Journal of Membrane Science*, 2005, **249**, 9-20.
41. R.-M. Latonen, M. N. Akieħ, K. Vavra, J. Bobacka and A. Ivaska, *Electroanalysis*, 2013, **25**, 991-1004.
42. C. Weidlich, K. M. Mangold and K. Jüttner, *Electrochimica Acta*, 2005, **50**, 5247-5254.
43. S. Skaarup, L. Bay, K. Vidanapathirana, S. Thybo, P. Tofte and K. West, *Solid State Ionics*, 2003, **159**, 143-147.
44. V. Syrĭtski, A. Opik and O. Forsen, *Electrochimica Acta*, 2003, **48**, 1409-1417.
45. X. Yang, T. Dai, Z. Zhu and Y. Lu, *Polymer*, 2007, **48**, 4021-4027.
46. U. Johanson, M. Marandi, T. Tamm and J. Tamm, *Electrochimica Acta*, 2005, **50**, 1523-1528.
47. J. Tamm, A. Alumaa, A. Hallik and V. Sammelselg, *Journal of Electroanalytical Chemistry*, 1998, **448**, 25-31.
48. M. N. Akieħ, W. E. Price, J. Bobacka, A. Ivaska and S. F. Ralph, *Synthetic Metals*, 2009, **159**, 2590-2598.
49. C. Weidlich, K. M. Mangold and K. Jüttner, *Electrochimica Acta*, 2005, **50**, 1547-1552.
50. S. Bruckenstein, K. Brzezinska and A. R. Hillman, *Physical Chemistry Chemical Physics*, 2000, **2**, 1221-1229.

51. J. Y. Lim, W.-K. Paik and I.-H. Yeo, *Synthetic Metals*, 1995, **69**, 451-454.
52. S. Geetha, C. R. K. Rao, M. Vijayan and D. C. Trivedi, *Analytica Chimica Acta*, 2006, **568**, 119-125.
53. R. G. Davidson and T. G. Turner, *Synthetic Metals*, 1995, **72**, 121-128.
54. A. O. Patil, A. J. Heeger and F. Wudl, *Chemical Reviews*, 1988, **88**, 183-200.
55. P. Burgmayer and R. W. Murray, *Journal of the American Chemical Society*, 1982, **104**, 6139-6140.
56. A. Dall'Olio, G. Dascola, V. Varacca and V. Bocchi, *Comptes Rendus des Seances de l'Academie des Sciences, Serie C: Sciences Chimiques*, 1968, **267**, 433-435.
57. K. K. Kanazawa, A. F. Diaz, W. D. Gill, P. M. Grant, G. B. Street, G. P. Gardini and J. F. Kwak, *Synthetic Metals*, 1980, **1**, 329-336.
58. K. K. Kanazawa, A. F. Diaz, R. H. Geiss, W. D. Gill, J. F. Kwak, J. A. Logan, J. F. Rabolt and G. B. Street, *Journal of the Chemical Society, Chemical Communications*, 1979, 854-855.
59. P. Pfluger and G. B. Street, *Journal of Chemical Physics*, 1984, **80**, 544-553.
60. R. J. Waltman, A. F. Diaz and J. Bargon, *Journal of Physical Chemistry*, 1984, **88**, 4343-4346.
61. J. Jang, J. H. Oh and X. L. Li, *Journal of Materials Chemistry*, 2004, **14**, 2872-2880.
62. T. F. Otero, R. Tejada and A. S. Elola, *Polymer*, 1987, **28**, 651-658.
63. J. L. Bredas, J. C. Scott, K. Yakushi and G. B. Street, *Physical Review B: Condensed Matter and Materials Physics*, 1984, **30**, 1023-1025.
64. T. Shimidzu, A. Otani and K. Honda, *Bulletin of the Chemical Society of Japan*, 1988, **61**, 2885-2890.
65. S. Bruckenstein, J. H. Chen, I. Jureviciute and A. R. Hillman, *Electrochimica Acta*, 2009, **54**, 3516-3525.
66. Y. Velmurugu and S. Skaarup, *Ionics*, 2005, **11**, 370-374.
67. P. M. Dziejowski and M. Grzeszczuk, *Journal of Physical Chemistry B*, 2010, **114**, 7158-7171.

68. K. Naoi, M. Lien and W. H. Smyrl, *Journal of The Electrochemical Society*, 1991, **138**, 440-445.
69. R. Ansari, *E-Journal of Chemistry*, 2006, **3**, 186-201.
70. L. T. T. Kim, C. Gabrielli, A. Pailleret and H. Perrot, *Electrochimica Acta*, 2011, **56**, 3516-3525.
71. N. Toshima and S. Hara, *Progress in Polymer Science*, 1995, **20**, 155-183.
72. W. J. Feast, J. Tsibouklis, K. L. Pouwer, L. Groenendaal and E. W. Meijer, *Polymer*, 1996, **37**, 5017-5047.
73. S. Sahoo, S. Dhibar and C. K. Das, *eXPRESS Polymer Letters*, 2012, **6**, 965-974.
74. A. Kaynak and R. Beltran, *Polymer International*, 2003, **52**, 1021-1026.
75. A. F. Diaz and J. I. Castillo, *Journal of the Chemical Society, Chemical Communications*, 1980, 397-398.
76. C. K. Baker and J. R. Reynolds, *Journal of Electroanalytical Chemistry and Interfacial Electrochemistry*, 1988, **251**, 307-322.
77. Y.-Z. Long, M.-M. Li, C.-Z. Gu, M.-X. Wan, J.-L. Duvail, Z.-W. Liu and Z.-Y. Fan, *Progress in Polymer Science*, 2011, **36**, 1415-1442.
78. Y. Zhang, Z. Bakenov, Y. Zhao, A. Konarov, T. N. L. Doan, M. Malik, T. Paron and P. Chen, *Journal of Power Sources*, 2012, **208**, 1-8.
79. X. Zhang, J. Zhang, W. Song and Z. Liu, *Journal of Physical Chemistry B*, 2006, **110**, 1158-1165.
80. J. Duchet, R. Legras and S. Demoustier-Champagne, *Synthetic Metals*, 1998, **98**, 113-122.
81. C. Debiemme-Chouvy, *Electrochemistry Communications*, 2009, **11**, 298-301.
82. R. M. Penner and C. R. Martin, *Journal of the Electrochemical Society*, 1986, **133**, 2206-2207.
83. R. V. Parthasarathy and C. R. Martin, *Chemistry of Materials*, 1994, **6**, 1627-1632.
84. L. Cao, H.-Z. Chen, H.-B. Zhou, L. Zhu, J.-Z. Sun, X.-B. Zhang, J.-M. Xu and M. Wang, *Advanced Materials*, 2003, **15**, 909-913.
85. H. Dong, S. Prasad, V. Nyame and W. E. Jones, Jr., *Chemical Materials*, 2004, **16**, 371-373.

86. X. Zhang and S. K. Manohar, *Journal of the American Chemical Society*, 2004, **126**, 12714-12715.
87. X. Yang and L. Li, *Synthetic Metals*, 2010, **160**, 1365-1367.
88. T. Dai, X. Yang and Y. Lu, *Nanotechnology*, 2006, **17**, 3028-3034.
89. S. Xing and G. Zhao, *Materials Letters*, 2007, **61**, 2040-2044.
90. Q.-F. Wu, K.-X. He, H.-Y. Mi and X.-G. Zhang, *Materials Chemistry and Physics*, 2007, **101**, 367-371.
91. S. Gupta, *Journal of Raman Spectroscopy*, 2008, **39**, 1343-1355.
92. Y. Yu, Z. Si, S. Chen, C. Bian, W. Chen and G. Xue, *Langmuir*, 2006, **22**, 3899-3905.
93. B. Bhowmick, D. Mondal, D. Maity, M. M. M. Rahaman, B. M. Kanti, B. N. Kumar, D. Rana, S. Chattopadhyay and D. Chattopadhyay, *Journal of Applied Polymer Science*, 2013, **129**, 3551-3557.
94. J. Jang and H. Yoon, *Langmuir*, 2005, **21**, 11484-11489.
95. X. Yang, Z. Zhu, T. Dai and Y. Lu, *Macromolecular Rapid Communications*, 2005, **26**, 1736-1740.
96. L. Zhang and M. Wan, *Advanced Functional Materials*, 2003, **13**, 815-820.
97. J. Liu, Y. Lin, L. Liang, J. A. Voigt, D. L. Huber, Z. R. Tian, E. Coker, B. McKenzie and M. J. McDermott, *Chemistry - A European Journal*, 2003, **9**, 604-611.
98. L. Liang, J. Liu, C. F. Windisch, Jr., G. J. Exarhos and Y. Lin, *Angewandte Chemie International Edition*, 2002, **41**, 3665-3668.
99. M. Li, Z. Wei and L. Jiang, *Journal of Materials Chemistry*, 2008, **18**, 2276-2280.
100. J. Huang, K. Wang and Z. Wei, *Journal of Materials Chemistry*, 2010, **20**, 1117-1121.
101. J. Zang, C. M. Li, S. J. Bao, X. Cui, Q. Bao and C. Q. Sun, *Macromolecules*, 2008, **41**, 7053-7057.
102. L. Al-Mashat, C. Debiemme-Chouvy, S. Borensztajn and W. Wlodarski, *Journal of Physical Chemistry C*, 2012, **116**, 13388-13394.

103. C. P. McCarthy, N. B. McGuinness, P. B. Carolan, C. M. Fox, B. E. Alcock-Earley, C. B. Breslin and A. D. Rooney, *Macromolecules*, 2013, **46**, 1008-1016.
104. M. Zhou and J. Heinze, *Journal of Physical Chemistry B*, 1999, **103**, 8443-8450.
105. P. J. A. Borm, D. Robbins, S. Haubold, H. Fissan, K. Donaldson, R. Schins, V. Stone, W. Kreyling, J. Lademann, J. Krutmann and E. Oberdorster, *Particle and Fibre Toxicology*, 2006, **3**.
106. C. Buzea, I. I. Pacheco and K. Robbie, *Biointerphases*, 2007, **2**, MR17-MR71.
107. Y. Xiao, J. Che, C. M. Li, C. Q. Sun, Y. T. Chua, V. S. Lee and J. H. T. Luong, *Journal of Biomedical Materials Research Part A*, 2007, **80 A**, 925-931.
108. C. P. McCarthy, N. B. McGuinness, B. E. Alcock-Earley, C. B. Breslin and A. D. Rooney, *Electrochemistry Communications*, 2012, **20**, 79-82.
109. M. Ghorbani, H. Esfandian, N. Taghipour and R. Katal, *Desalination*, 2010, **263**, 279-284.
110. Y. Lei, X. Qian, J. Shen and X. An, *Industrial & Engineering Chemistry Research*, 2012, **51**, 10408-10415.
111. R. Ansari and N. Khoshbakht Fahim, *Reactive and Functional Polymers*, 2007, **67**, 367-374.
112. H. H. Kuhn, A. D. Child and W. C. Kimbrell, *Synthetic Metals*, 1995, **71**, 2139-2142.
113. D. Kincal, A. Kumar, A. D. Child and J. R. Reynolds, *Synthetic Metals*, 1998, **92**, 53-55.
114. J. P. Boutrois, R. Jolly and C. Petrescu, *Synthetic Metals*, 1997, **85**, 1405-1406.
115. A. Kaynak, L. Wang, C. Hurren and X. Wang, *Fibers and Polymers*, 2002, **3**, 24-30.
116. A. Kaynak, S. S. Najar and R. C. Foitzik, *Synthetic Metals*, 2008, **158**, 1-5.
117. R. B. Bjorklund and I. Lundstroem, *Journal of Electronic Materials*, 1984, **13**, 211-230.
118. T. Lin, L. Wang, X. Wang and A. Kaynak, *Thin Solid Films*, 2005, **479**, 77-82.
119. H. Seung Lee and J. Hong, *Synthetic Metals*, 2000, **113**, 115-119.
120. W. E. Price, C. O. Too, G. G. Wallace and D. Zhou, *Synthetic Metals*, 1999, **102**, 1338-1341.

121. C. Weidlich and K.-M. Mangold, *Electrochimica Acta*, 2011, **56**, 3481-3484.
122. L. Liu, F. Zhao, J. Liu and F. Yang, *Journal of Membrane Science*, 2013, **437**, 99-107.
123. B. Winther-Jensen, J. Chen, K. West and G. G. Wallace, *Macromolecules*, 2004, **37**, 5930-5935.
124. C. Weidlich, K. M. Mangold and K. Jüttner, *Electrochimica Acta*, 2001, **47**, 741-745.
125. K. M. Mangold, C. Weidlich, J. Schuster and K. Jüttner, *Journal of Applied Electrochemistry*, 2005, **35**, 1293-1301.
126. C. Weidlich, K.-M. Mangold, G. Schaule and A. K. Rumpf, *Vom Wasser*, 2009, **107**, 17-22.
127. M. N. Akieh, S. F. Ralph, J. Bobacka and A. Ivaska, *Journal of Membrane Science*, 2010, **354**, 162-170.
128. H. Zhao, W. E. Price, C. O. Too, G. G. Wallace and D. Zhou, *Journal of Membrane Science*, 1996, **119**, 199-212.
129. H. Zhao, W. E. Price and G. G. Wallace, *Journal of Membrane Science*, 1994, **87**, 47-56.
130. J. M. Davey, S. F. Ralph, C. O. Too, G. G. Wallace and A. C. Partridge, *Reactive and Functional Polymers*, 2001, **49**, 87-98.
131. J. M. Davey, S. F. Ralph, C. O. Too and G. G. Wallace, *Synthetic Metals*, 1999, **99**, 191-199.
132. V. Misoska, J. Ding, J. M. Davey, W. E. Price, S. F. Ralph and G. G. Wallace, *Polymer*, 2001, **42**, 8571-8579.
133. P. Kubat, J. Sebera, S. Zalis, J. Langmaier, M. Fuciman, T. Polivka and K. Lang, *Physical Chemistry Chemical Physics*, 2011, **13**, 6947-6954.
134. C. D. Gutsche, *Calixarenes: An Introduction*, Royal Society of Chemistry, 2008.
135. S. R. Izatt, R. T. Hawkins, J. J. Christensen and R. M. Izatt, *Journal of the American Chemical Society*, 1985, **107**, 63-66.
136. S. Shinkai, K. Araki, T. Tsubaki, T. Arimura and O. Manabe, *Journal of the Chemical Society, Perkin Transactions 1: Organic and Bio-Organic Chemistry*, 1987, 2297-2299.

137. S. Shinkai, S. Mori, H. Koreishi, T. Tsubaki and O. Manabe, *Journal of the American Chemical Society*, 1986, **108**, 2409-2416.
138. S. Shinkai, K. Araki, M. Kubota, T. Arimura and T. Matsuda, *Journal of Organic Chemistry*, 1991, **56**, 295-300.
139. I. Yoshida, N. Yamamoto, F. Sagara, D. Ishii, K. Ueno and S. Shinkai, *Bulletin of the Chemical Society of Japan*, 1992, **65**, 1012-1015.
140. G. Diao and W. Zhou, *Journal of Electroanalytical Chemistry*, 2004, **567**, 325-330.
141. M. Chen, H.-L. Wang, J. Gu and G.-W. Diao, *Journal of Applied Electrochemistry*, 2007, **37**, 331-337.
142. A. Pailleret and D. W. M. Arrigan, *Langmuir*, 2002, **18**, 9447-9452.
143. A. Pailleret, N. Magan-Oliva, S. Ollivier and D. W. M. Arrigan, *Journal of Electroanalytical Chemistry*, 2001, **508**, 81-88.
144. R. Doyle, C. B. Breslin, O. Power and A. D. Rooney, *Electroanalysis*, 2012, **24**, 293-302.
145. A. Ronlan and V. D. Parker, *Journal of the Chemical Society*, 1971, 3214-3218.
146. R. Vataj, A. Louati, C. Jeunesse and D. Matt, *Journal of Electroanalytical Chemistry*, 2004, **565**, 295-299.
147. R. Vataj, A. Louati, C. Jeunesse and D. Matt, *Electrochemistry Communications*, 2000, **2**, 769-775.
148. A. Louati, J. Spraula, V. Gabelica, P. Kuhn and D. Matt, *Electrochemistry Communications*, 2006, **8**, 761-766.
149. J. Szejtli, *Cyclodextrins and Their Inclusion Complexes*, Akademiai Kiado, 1982.
150. C. Bonal, Y. Israeli, J.-P. Morel and N. Morel-Desrosiers, *Journal of the Chemical Society, Perkin Transactions 2*, 2001, 1075-1078.
151. J.-P. Morel and N. Morel-Desrosiers, *Organic and Biomolecular Chemistry*, 2006, **4**, 462-465.
152. G. Bidan and M.-A. Niel, *Synthetic Metals*, 1997, **85**, 1387-1388.
153. Z. Mousavi, J. Bobacka and A. Ivaska, *Electroanalysis*, 2005, **17**, 1609-1615.
154. K. Kaneto and G. Bidan, *Thin Solid Films*, 1998, **331**, 272-278.

155. U. N. Publications, Millennium Development Goals and Beyond 2015, <http://www.un.org/millenniumgoals/environ.shtml>.
156. W.H.O. and U.N.I.C.E.F., *Progress on Sanitation and Drinking Water, 2013 Update*, WHO/UNICEF Joint Monitoring Programme, 2013.
157. R. Saha, R. Nandi and B. Saha, *Journal of Coordination Chemistry*, 2011, **64**, 1782-1806.
158. E. P. Agency, *EPA · 2020 Vision Protecting and Improving Ireland's Environment*, E.P.A Ireland, 2000.
159. J. P. I. Water, Water Challenges for a Changing World, [http://www.waterjpi.eu/index.php?option=com\\_content&view=article&id=85&Itemid=478](http://www.waterjpi.eu/index.php?option=com_content&view=article&id=85&Itemid=478).
160. E. U. Directive, *Directive 2011/65/EU - The restriction of the use of certain hazardous substances in electrical and electronic equipment*, 2011.
161. E. U. Directive, *Directive 94/62/EC - Packaging and Packaging Waste*, 1994.
162. E. U. Directive, *Directive 98/83/EC - The Quality of Water Intended for Human Consumption*, 1998.
163. L. Järup, *British Medical Bulletin*, 2003, **68**, 167-182.
164. C. Garbisu and I. Alkorta, *Bioresource Technology*, 2001, **77**, 229-236.
165. C. Gisbert, R. Ros, A. De Haro, D. J. Walker, M. Pilar Bernal, R. Serrano and J. Navarro-Aviñó, *Biochemical and Biophysical Research Communications*, 2003, **303**, 440-445.
166. W.H.O., *Arsenic and Arsenic Compounds*, Environmental Health Criteria, Geneva, 2001.
167. M. I. Lone, Z. He, P. J. Stoffella and X. Yang, *Journal of Zhejiang University SCIENCE B*, 2008, **9**, 210-220.
168. C. Clenaghan, N. O'Neill and D. Page, *Dangerous Substances Regulations; National Implementation Report*, Environmental Protection Agency, 2005.
169. IARC, *Monographs on the Evaluation of Carcinogenic risks to Humans*, Lyon, France, 2014.
170. G. I. Stangl and M. Kirchgessner, *Journal of Nutrition*, 1996, **126**, 2466-2473.
171. E. Denkhaus and K. Salnikow, *Critical Reviews in Oncology/Hematology*, 2002, **42**, 35-56.

172. O. B. Akpor and M. Muchie, *International Journal of the Physical Sciences*, 2010, **5**, 1807-1817.
173. M. A. Hashim, S. Mukhopadhyay, J. N. Sahu and B. Sengupta, *Journal of Environmental Management*, 2011, **92**, 2355-2388.
174. R. A. Anderson, *Science of The Total Environment*, 1989, **86**, 75-81.
175. P. F. Nguema and Z. Luo, *Annals of Microbiology*, 2012, **62**, 41-47.
176. I. E. T. G. Group, *Chromium(VI) Handbook*, CRC Press, U.S.A., 2005.
177. R. K. Tandon, P. T. Crisp, J. Ellis and R. S. Baker, *Talanta*, 1984, **31**, 227-228.
178. J. Kotas and Z. Stasicka, *Environmental Pollution*, 2000, **107**, 263-283.
179. A. Agrawal, V. Kumar and B. D. Pandey, *Mineral Processing and Extractive Metallurgy Review*, 2006, **27**, 99-130.
180. D. Roche, *Department of the Environment, Heritage and Local Government - EC Drinking Water Regulations (2)*, Ireland, 2007.
181. E. U. Directive, *Directive 86/278/EEC - Protection of the Environment when Sewage Sludge is used in Agriculture*, 1986.
182. C. Fabiani, F. Ruscio, M. Spadoni and M. Pizzichini, *Desalination*, 1997, **108**, 183-191.
183. Y. Xie, X. Li and F. Li, *Zhongguo Huanjing Kexue*, 2009, **29**, 1260-1265.
184. G. Mahajan and D. Sud, *Applied Water Science*, 2012, **2**, 299-308.
185. Y. S. Dzyazko, A. Mahmoud, F. Lopicque and V. N. Belyakov, *Journal of Applied Electrochemistry*, 2007, **37**, 209-217.
186. Y.-X. Liu, D.-X. Yuan, J.-M. Yan, Q.-L. Li and T. Ouyang, *Journal of Hazardous Materials*, 2011, **186**, 473-480.
187. A. Olad and R. Nabavi, *Journal of Hazardous Materials*, 2007, **147**, 845-851.
188. F. Rodriguez-Valadez, C. Ortiz-Exiga, J. G. Ibanez, A. Alatorre-Ordaz and S. Gutierrez-Granados, *Environmental Science and Technology*, 2005, **39**, 1875-1879.
189. H. Wang, J. Ding, B. Lee, X. Wang and T. Lin, *Journal of Membrane Science*, 2007, **303**, 119-125.

190. J. Ding, W. E. Price, S. F. Ralph and G. G. Wallace, *Polymer International*, 2004, **53**, 681-687.
191. J. Ding, H. Wang, T. Lin and B. Lee, *Synthetic Metals*, 2008, **158**, 585-589.
192. C. Wei, S. German, S. Basak and K. Rajeshwar, *Journal of the Electrochemical Society*, 1993, **140**, L60-L62.
193. R. Senthurchelvan, Y. Wang, S. Basak and K. Rajeshwar, *Journal of the Electrochemical Society*, 1996, **143**, 44-51.
194. W. A. Wampler, S. Basak and K. Rajeshwar, *Carbon*, 1996, **34**, 747-755.
195. S. T. Farrell and C. B. Breslin, *Environmental Science & Technology*, 2004, **38**, 4671-4676.
196. K. G. Conroy and C. B. Breslin, *Journal of Applied Electrochemistry*, 2004, **34**, 191-195.
197. M. A. Alatorre, S. Gutierrez, U. Paramo and J. G. Ibanez, *Journal of Applied Electrochemistry*, 1998, **28**, 551-557.
198. F. J. Rodriguez, d. I. R. L. A. Garcia, A. Alatorre, J. Ibanez, L. Godinez, S. Gutierrez and P. Herrasti, *Progress in Organic Coatings*, 2007, **60**, 297-302.
199. X. Zhang and R. Bai, *Langmuir*, 2003, **19**, 10703-10709.
200. R. Bai and X. Zhang, *Journal of Colloid and Interface Science*, 2001, **243**, 52-60.
201. M. Bhaumik, A. Maity, V. V. Srinivasu and M. S. Onyango, *Journal of Hazardous Materials*, 2011, **190**, 381-390.

## Chapter 2

---

## Experimental

---

## 2.1 Introduction

The main aim of this research was concerned with the fabrication and characterisation of nanoscale polypyrrole films synthesised on electrode substrates and polyamide porous membranes. The application of these prepared materials for the remediation of heavy metals from water was also investigated.

The polymer materials investigated were polypyrrole nanowires doped predominantly with the  $\text{ClO}_4^-$  anion (PpyNW) and polypyrrole nanowires coated with polypyrrole films doped with *p*-sulfonatocalix[4]arene sodium salt (PpyC4S) or poly(sodium 4-styrenesulfonate) (PpyPSS). These films were formed through electrochemical oxidative polymerisation. Chemical oxidation was also employed, to form polypyrrole films with the functional dopants anthraquinone-2-sulfonic acid sodium salt and methyl orange. These films were coated on the polyamide porous membranes. Polypyrrole/sodium alginate composites were also formed by chemical oxidation. Surface characterisation of the polymer materials was performed using scanning electron microscopy (SEM). Raman, Fourier Transform Infra-red and Energy Dispersive X-ray (EDX) spectroscopy were utilised to elucidate the chemical structures of the films. Contact angle measurements revealed the surface wettability of the polypyrrole materials electropolymerised on electrode substrates.

The remediation of hexavalent chromium by the electropolymerised polypyrrole nanowires was investigated using UV-Visible (UV-Vis) spectroscopy and various electrochemical techniques. In order to establish the amount of Cr(VI) remediated, two colorimetric techniques were employed and will be described in this Chapter.

The ion exchange properties of the PpyC4S and PpyPSS coatings were investigated using an Electrochemical Quartz Crystal Microbalance (EQCM).

All details relating to synthesis, characterisation and application of the chemically and electrochemically formed polypyrrole films are given in the following sections together with a short description of each applied experimental technique. A brief description of the theoretical background for each of the different experimental techniques is also provided.

## 2.2 Experimental Procedures

### 2.2.1 Chemicals

Unless otherwise stated, all chemicals and solvents used in this work were purchased from Sigma-Aldrich. Pyrrole (98%) was distilled under vacuum before use and kept at -18 °C in the dark to prevent oxidation. All other chemicals were of analytical reagent grade and used as received. Solution pH was measured using a Jenway 430 pH meter, which was calibrated before use with buffer solutions of pH 4.0 and 7.0, respectively. These buffer solutions were also purchased from Sigma-Aldrich. All solutions were prepared with distilled or deionised water as appropriate. The molar concentrations of the poly(sodium 4-styrenesulfonate) solutions were calculated from the molecular weight of the corresponding monomer unit (183.21 g mol<sup>-1</sup>). The molar concentrations of the *p*-sulfonatocalix[4]arene sodium salt solutions used in this work were calculated from the molecular formula C<sub>28</sub>H<sub>19</sub>O<sub>16</sub>S<sub>4</sub>Na<sub>5</sub>·9H<sub>2</sub>O (1016.79 g mol<sup>-1</sup>). The number of water molecules was based on the average literature values.<sup>1-4</sup>

### 2.2.2 Chemical Polymerisation on a Polyamide Porous Membrane

#### 2.2.2.1 Using Anthraquinone-2-sulfonic Acid Sodium Salt (AQSA) as the Dopant

Polypyrrole was chemically polymerised on the surface of a porous polyamide membrane using an adaptation of the method proposed by Kaynak *et al.*<sup>5, 6</sup> Anthraquinone-2-sulfonic acid sodium salt (3.6 mM) was dissolved in distilled water (10 cm<sup>3</sup>) and pyrrole (6.0 mM) was added. To this, one polyamide membrane was added and the solution was stirred at 0 °C for 30 minutes. Iron(III) chloride (15.0 mM) was then added to the reaction mixture with vigorous swirling. This was allowed to react for 2 hours (0-4 °C), resulting in a fully coated membrane. The polymerisation duration, pyrrole concentration and reaction volume were altered to determine the optimum conditions for even polypyrrole coverage of the membranes with maintained membrane porosity.

#### 2.2.2.2 Using Methyl Orange as the Dopant

The formation of polypyrrole nanowires doped with methyl orange has been reported by Yang *et al.*, however they use an electrochemical approach with a template.<sup>7</sup> Thus,

initial attempts at polymerising polypyrrole nanowires using the functional dopant methyl orange adapted the experimental method described by Huang *et al.* in which they use a similar anion to methyl orange, (*p*-hydroxyl-azobenzene sulfonic acid), as the functional dopant.<sup>8</sup> In this method methyl orange (0.4 mM) and pyrrole (2.2 mM) were dissolved in distilled water (20 cm<sup>3</sup>) at room temperature. A polyamide membrane was added and the solution was cooled to a temperature of 0 °C over 30 minutes. Aqueous iron(III) chloride (3.6 cm<sup>3</sup>, 1 M) was added drop-wise with stirring and the solution was allowed to polymerise for 20 hours (0-4 °C). Unfortunately, the resulting polymer coating on the membrane did not display sufficient adherence and peeled off the membrane with washing. Thus it was decided to follow a similar method as that described in Section 2.2.2.1. Pyrrole (0.11 M) and methyl orange (0.02 M) were dissolved in distilled water (20 cm<sup>3</sup>). A polyamide membrane was added and the solution was stirred at 0 °C for 30 minutes. A pre-cooled solution of iron(III) chloride (3.6 cm<sup>3</sup>, 1 M) was then added to the reaction mixture with vigorous swirling. This was allowed to react with stirring for 2 hours (0-4 °C). The resulting polymer coating was uniform across the membrane surface. Polymers formed by the first and second approach were examined using SEM.

### 2.2.2.3 Combined Chemical Polymerisation Method

SEM analysis revealed that polypyrrole deposited on the membrane in the presence of AQSA formed a uniform thin layer of polypyrrole, in the bulk morphology, across the membrane surface. SEM analysis of adherent polypyrrole formed in the presence of methyl orange similarly showed a thin layer of polypyrrole in the bulk morphology. The polymerisation of polypyrrole doped with methyl orange resulted in the formation of polypyrrole in solution as well as on the membrane, and when SEM analysis was performed on the polymer formed in solution, nanofibrous morphology was apparent. Thus it was decided to combine the methods using AQSA and methyl orange as functional dopants. This allowed for the deposition of a uniform adherent layer of bulk polymer doped with AQSA to which methyl orange doped polypyrrole nanowires could become attached. The procedure described in Section 2.2.2.1 was followed and the resulting membranes were washed extensively with distilled water. The membrane was then placed in a new aqueous solution (20 cm<sup>3</sup>) containing a mixture of pyrrole (0.11 M) and methyl orange (0.02 M) which was cooled to 0 °C with stirring for 30 minutes. A pre-cooled solution of iron(III) chloride (3.6 cm<sup>3</sup>, 1 M) was then added to

the reaction mixture with vigorous swirling. This was allowed to react with stirring for 2 hours (0-4 °C). The membrane was removed from the reaction mixture and washed thoroughly with distilled water. Polymer formation on the membrane surface was indicated by the formation of a thin uniform black layer on the membrane. SEM analysis was performed to determine the morphology of the polypyrrole coating on the membrane.

### 2.2.3 Preparation of Polypyrrole-Sodium Alginate (PpySA) Particles

Polypyrrole-sodium alginate particles were prepared as described by Sahoo *et al.*<sup>9</sup> To an aqueous solution of sodium hydroxide (0.10 M, 300 cm<sup>3</sup>), alginic acid sodium salt (300 mg) was added and stirred at 60 °C for 16 hours. Pyrrole (0.05 M) was added and stirring was continued at 60 °C for a further hour. The mixture was then cooled to 0-4 °C over ice and the pH was adjusted to pH 7 by the drop-wise addition of sulfuric acid (1.0 M). Ammonium persulfate (0.015 M) was added with stirring for 5 minutes and the solution was allowed to polymerise for 24 hours (0-4 °C). The resulting black precipitate was collected by vacuum filtration and washed extensively with distilled water. Lastly, the polymer composite was dried at 50 °C for one week before being investigated as an adsorbent for hexavalent chromium (Chapter 5, Section 5.7).

### 2.2.4 The Electrochemical Set-up

The majority of the materials developed and characterised in this study were prepared electrochemically. Electrochemical experiments such as open circuit potential measurements (OCP), potentiostatic amperometry and cyclic voltammetry (CV) were performed using a Solartron Potentiostat Model 1285/1287. Electrochemical quartz crystal microbalance (EQCM) measurements were carried out using Chi440 Potentiostat Model EA160. Each system was controlled using a computer and the relevant software package, which were Corrware for Windows™ Version 2.0 (Scribner Associates) and Chi440 software Version 1.0.0.1. The resulting data were analysed using Corrview Version 3.0 (Scribner Associates) and Microsoft Excel 2007/2010.

Electrochemical experiments employed a standard three-electrode cell set-up, which is shown in Figure 2.1. This set-up consisted of a working electrode (WE), an auxiliary or counter electrode (CE) and a reference electrode (RE). The electrochemical cell was a

glass cylinder of 20 or 50 cm<sup>3</sup> volume and had a Teflon lid with openings for each of the electrodes. The three electrodes were connected to the potentiostat and immersed in the electrolyte solution. A standard saturated calomel electrode (SCE) was utilised as the reference electrode for all experiments carried out on Solartron potentiostats. A silver/silver chloride (Ag/AgCl) electrode (3.0 mol dm<sup>-3</sup> KCl filling solution) was used as a reference electrode for EQCM experiments. The working electrode was either a gold, platinum or glassy carbon substrate, embedded in a Teflon holder using epoxy resin, with a surface area of 0.1257 cm<sup>2</sup>; a gold wire, or a polyamide membrane (0.8 μm pore diameter) sputter coated with gold plasma. The counter electrode was a platinum wire of high surface area. The counter electrodes were brushed regularly with silicon carbide based abrasive paper (Buheler P2500), rinsed with distilled water and then sonicated consecutively in acetone; a 50:50 mixture of ethanol and distilled water; and in distilled water. When not in use, the reference electrode was stored in a saturated solution of potassium chloride (KCl), to prevent the porous frit at the tip of the electrode from drying out. This electrode was rinsed with distilled water between experiments to avoid contamination of electrolyte solutions with KCl.

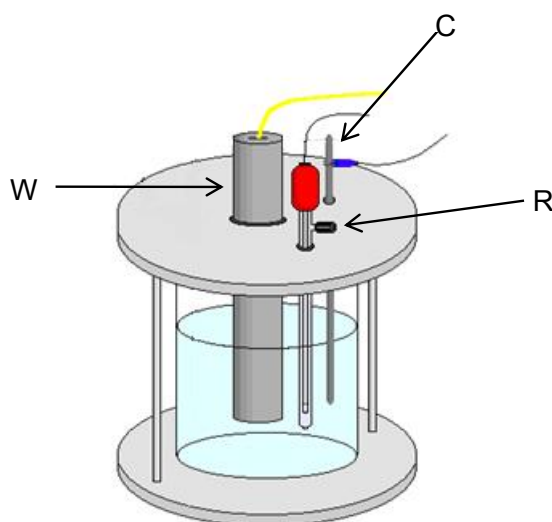


**Figure 2.1:** Schematic of the cell set-up used for the majority of the electrochemical measurements. The working, counter and reference electrodes are denoted by the symbols W, C and R respectively.<sup>10</sup>

### 2.2.4.1 Electrode Materials and Preparation

Gold electrodes for EQCM experiments were purchased from IJ Cambria Scientific, used as received and disposed of after use. All other electrode materials were purchased from Goodfellow Metals, of a high purity grade (99.9 %). Working electrodes were made by forming an electrical contact between the metal substrate of choice and copper wire using conducting silver epoxy resin. The quality of the connection was tested with an Avometer 2001 multimeter to ensure that the resistance between the electrode surface and the wire connection to the potentiostat was less than 1  $\Omega$ . The wire was threaded through a Teflon holder, leaving the metal substrate exposed at one end. The electrode was then sealed into the Teflon holder using non-conducting epoxy resin. Figure 2.2 shows an image of the two main electrode assemblies used in the present work.

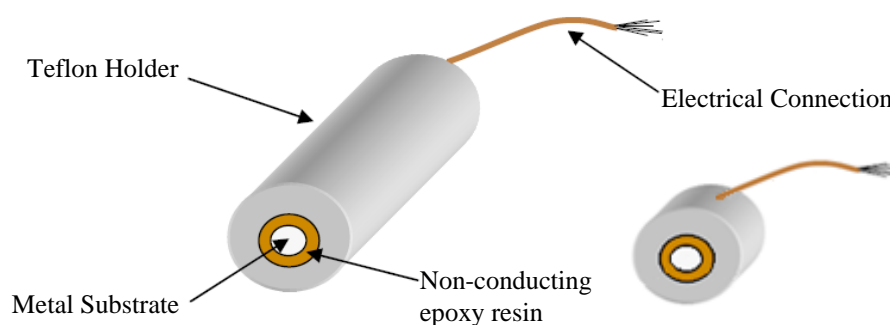


**Figure 2.2: Image of a rod (left) and a disk (right) shaped electrode, with identification of the working electrode surface, the epoxy resin glue, the Teflon holder and the electrical connection.<sup>11</sup>**

Prior to each experiment, the exposed electrode surface was polished with successively finer grades of Buehler MetaDi Monocrystalline Diamond suspension (30  $\mu\text{m}$  to 1  $\mu\text{m}$ ), and ultra-fine aluminium oxide powder (0.05  $\mu\text{m}$ ) on a Buehler polishing microcloth to ensure a smooth finish. The electrodes were then rinsed with distilled water and sonicated consecutively in acetone; a 50:50 mixture of ethanol and distilled water; and distilled water. This ensured the removal of any diamond or aluminium oxide pastes which had adhered to the electrode surface during polishing. In the case of particularly adhesive polymers a Buehler METASERV grinder-polisher with silicon carbide based abrasive paper (Buehler P2500) was used and then the polishing steps were repeated. The gold wire electrodes were brushed with silicon carbide based abrasive paper (Buehler P2500), rinsed with distilled water and then sonicated consecutively in acetone; a 50:50 mixture of ethanol and distilled water; and distilled water.

Polyamide membranes (25 mm diameter, pore size 0.8  $\mu\text{m}$ ) were purchased from Merck Millipore Ireland. Each membrane was washed in acetone, blotted and dried prior to use. In order to make the polyamide membranes conducting, such that they could be utilised as a working electrode, a thin layer of gold was sputter deposited onto one face of the polyamide membrane using an AGAR Automatic Sputter Coater controlled by an AGAR Terminating Film Thickness Monitor. The thickness of the gold coating was varied in order to find a coating thickness that conferred sufficient conductivity to the polyamide film, without hindering the flow rate of water through the membrane. Attempts were made to affix a conducting copper wire using bees wax, silver solder and conducting silver epoxy resin, but it was established that the best connection was made by direct connection to the potentiostat using a stainless steel crocodile clip. The gold coated membranes were disposed of after each use.

### 2.2.5 Electrochemical Polymerisation of Pyrrole

#### 2.2.5.1 Electropolymerisation of Bulk Polypyrrole and Nanowires on a Conventional Electrode

Bulk polypyrrole films doped with chloride ions (PpyCl) were obtained using 0.15 M pyrrole monomer in 0.10 M NaCl aqueous solution, at an applied potential of 0.70 V vs. SCE until a charge density of 400  $\text{mC cm}^{-2}$  was achieved. Bulk polypyrrole films doped with sodium dodecyl sulfate (PpySDS) were also formed potentiostatically by the application of a potential of 0.70 V vs. SCE, in an aqueous solution containing 0.15 M pyrrole and 0.10 M sodium dodecyl sulfate until a charge density of 400  $\text{mC cm}^{-2}$  was reached.

Bulk polypyrrole films doped with *p*-sulfonatocalix[4]arene sodium salt (PpyC4S) were formed from aqueous solutions of 0.20 M pyrrole and various concentrations of *p*-sulfonatocalix[4]arene sodium salt (0.002 M, 0.01 M and 0.10 M C4S). A constant potential of 0.55 V vs. Ag/AgCl was applied until a charge of 74  $\text{mC cm}^{-2}$  was achieved. Similarly, polypyrrole films doped with poly(sodium 4-styrenesulfonate) (PpyPSS), were electropolymerised from aqueous solutions of 0.20 M pyrrole and either 0.10 M PSS or 0.002 M PSS, at applied potentials of 0.55 V, 0.70 V and 0.80 V vs. Ag/AgCl until a charge density of 74  $\text{mC cm}^{-2}$  was attained.

Polypyrrole nanowires (PpyNW) were typically formed from an aqueous solution of 0.15 M pyrrole monomer, 0.20 M Na<sub>2</sub>HPO<sub>4</sub> and 0.001 M LiClO<sub>4</sub> at an applied potential of 0.80 V vs. SCE to a charge density of 400 mC cm<sup>-2</sup>. In experiments discussed in Chapter 3, the electrolyte salt solution was altered to investigate the use of alternative dopants on the nanowire morphology. In these studies, the LiClO<sub>4</sub> in solution was replaced by 0.001 M of the dopant of choice. The variations in the electrolyte solution are detailed in Section 3.3.1.2.

#### 2.2.5.2 Coating of Polypyrrole Nanowires with Ppy-Immobilised Dopant Films

PpyNW were electropolymerised from an aqueous solution of 0.15 M pyrrole monomer, 0.20 M Na<sub>2</sub>HPO<sub>4</sub> and 0.001 M LiClO<sub>4</sub> at an applied potential of 0.80 V vs. SCE to a charge density of 300 mC cm<sup>-2</sup>. The PpyNW films were thoroughly washed with deionised water before being placed in an aqueous solution of 0.20 M pyrrole monomer and 0.002 M *p*-sulfonatocalix[4]arene sodium salt. A potential of 0.55 V vs. SCE was applied until a charge density of either 74 mC cm<sup>-2</sup> or 150 mC cm<sup>-2</sup> was achieved. The PpyPSS coating was electropolymerised on pre-formed, rinsed polypyrrole nanowires, from an aqueous solution of 0.15 M pyrrole monomer and 0.05 M poly(sodium 4-styrenesulfonate), at an applied potential of 0.60 V vs. SCE until a charge density of 74 mC cm<sup>-2</sup> was reached.

#### 2.2.5.3 Electropolymerisation of Polypyrrole Nanowires on a Porous Membrane

First the polyamide membranes were washed in acetone, blotted and allowed to air dry. The membrane was then placed in the sputter coater and coated until the desired thickness of gold coating was achieved. Typically a thickness of 70 nm was sufficient to infer conductivity while maintaining membrane porosity. Experiments conducted using polyamide membranes coated with varying thicknesses of the gold coating are detailed in Chapter 3. The gold coated membranes were then attached to the potentiostat using a stainless steel crocodile clip and placed in a 50 cm<sup>3</sup> electrochemical cell. Polypyrrole nanowires were formed on the gold coated polyamide membrane, from a solution of 0.15 M pyrrole monomer, 0.20 M Na<sub>2</sub>HPO<sub>4</sub> and 0.001 M LiClO<sub>4</sub> at an applied potential of 0.80 V vs. SCE to a charge density of 300 mC cm<sup>-2</sup>.

### 2.2.6 Cyclic Voltammetry

Cyclic Voltammetry was carried out using the EQCM in order to investigate the ion-exchange mechanism of the polypyrrole films doped with *p*-sulfonatocalix[4]arene sodium salt or with poly(sodium 4-styrenesulfonate). A set of limitations must be adhered to when utilising the EQCM technique in which any film deposited upon the crystal oscillator must be rigid, homogeneous and acoustically thin.<sup>12</sup> Unfortunately, the condition of homogeneity of the film cannot be upheld using a polypyrrole nanowire film, and so for this section of the study, the PpyC4S and PpyPSS films were characterised as standalone polymers, grown directly onto the gold coated quartz crystal as opposed to being coated onto the polypyrrole nanowires. The PpyC4S and PpyPSS films were electropolymerised as described in Section 2.2.4.1 until a charge of 15.0 mC was achieved. This corresponds to a charge density of 74 mC cm<sup>-2</sup>. The films were washed thoroughly with deionised water and the salt solution of choice, before being cycled at scan rates of 10 mV s<sup>-1</sup>, 50 mV s<sup>-1</sup> or 100 mV s<sup>-1</sup>, for up to 20 cycles, in 0.10 M aqueous salt solutions. Typically the potential was cycled between set potentials of 0.10 V and -0.85 V vs. Ag/AgCl, with adjustments made to account for any drift observed in the measured potential by the reference electrode.

### 2.2.7 Polymer Characterisation

#### 2.2.7.1 Microscopy

The bulk of scanning electron microscopy (SEM) and energy dispersive X-ray (EDX) analysis carried out in this study were obtained using a Hitachi S-3200-N scanning electron microscope fitted with a tungsten filament electron source. This has a maximum magnification of 200,000X and a resolution of 3.5 nm. This microscope was equipped with an Oxford Instrument INCAx-act EDX system with a silicon drift detector. Some analysis was also carried out in the Tyndall National Institute at University College Cork, using a Hitachi S-4000 with a cold cathode field emission electron source (FE-SEM), a maximum magnification of 300,000X and a resolution of 1.5 nm. This microscope was equipped with a Princeton Gamma Technology Avalon 8000 EDX system with a liquid nitrogen cooled Li(Si) detector and was operated by Patrick Carolan and Vince Lodge as part of the National Access Programme.

SEM and EDX analysis was carried out on polypyrrole films which were deposited on flat disk electrodes. In preparation for SEM analysis, the polymer coated electrodes were dried gently under a nitrogen flow and then placed in the AGAR Automatic Sputter Coater under vacuum for up to 30 minutes, to remove any residual solvent. The chamber vacuum was allowed to reach 10 pa before sputter coating was performed under argon using a gold target. An AGAR Terminating Film Thickness Monitor was employed to obtain a coating of typically 5 nm of gold. In order to earth the electrode, electrically conducting copper tape was adhered to the working area of the electrode and connected to an earthed metal, usually the aluminium holder. This reduced the build-up of incident electrons gathering at the surface of the sample, a phenomenon which is known as charging. Depending on the thickness and conductivity of the sample, and the magnification required, the electrons were accelerated between 6 and 20 kV. For high resolution imaging the beam current was limited to below 20  $\mu\text{A}$ , and a working distance of 5 mm was employed. To reduce charging effects and increase the overall electron count at the detector the stage was usually tilted by a  $45^\circ$  angle. For cross section imaging the stage was tilted to an angle of  $90^\circ$ . To expose the base layers of polymer between the surface and the substrate a surgical blade was employed to make incisions along both the x and y axis of the polymer, perpendicular to the electrode surface. This was done before the sputter coating procedure was performed.

For EDX analysis the working distance was kept at 15 mm since the detector is poised at an incident angle compared to the secondary electron detector. The detector was moved from the stationary position and extended to its maximum distance. Typically the voltage was maintained at 20 kV with a beam current of up to 70  $\mu\text{A}$ . The stage was not tilted. Spectra were analysed using Inca software. The Infra-red camera was switched off while the spectra were being obtained, to limit any noise it would cause within the X-ray detector.

#### 2.2.7.2 Spectroscopy

Raman measurements were performed at the Focas Institute at the Dublin Institute of Technology, with a LabRAM high resolution Raman spectrometer using a solid state diode laser (100 mW), and employed a 660 nm laser line. The polymer materials and their associated starting materials were made into KBr disks and analysed, except for *p*-sulfonatocalix[4]arene sodium salt and  $\text{LiClO}_4$  which were analysed in powder form.

FTIR spectra were obtained using a Perkin Elmer 2000 FTIR spectrometer. Samples were prepared by grinding the polymers and starting materials into KBr and producing disks under a high pressure clamp.

UV-Visible (UV-Vis) spectroscopy was carried out using a Perkin Elmer Lambda 35 UV-Vis Spectrometer, with UV Winlab Version 6.0 software. The spectrometer comprised of a deuterium and a tungsten lamp with a combined wavelength range of 190-800 nm. Samples were placed in quartz cuvette, with a path length of 1 cm and volume of approximately 3 cm<sup>3</sup>. Analysis of the resulting spectra was carried out using Microsoft Excel 2007/2010.

### 2.2.7.3 Water Contact Angle

The static sessile drop technique was employed to determine the water contact angle for the polypyrrole films developed in this study. An FTA 1000 C Class Drop shape analyzer at the Institute of Technology, Tallaght was utilised and the data were interpreted with FTA 1000 software. The polymers were electropolymerised on an electrode surface, and this was mounted on the sample stage. A droplet of water of known volume was dropped onto the material surface and a contact angle goniometer was used to capture the profile of the liquid droplet on the solid material. The contact angle was measured after 30 seconds to ensure equilibration of the droplet on the polymer surface. An  $n = 2$  was obtained by drying the polymers between each experiment with a gentle nitrogen flow.

## 2.2.8 Analysis of Cr(VI) Remediation by Polypyrrole Nanowires

### 2.2.8.1 Concentration of Sodium Dichromate in Solution

Hexavalent chromium is a strongly coloured species with a characteristic absorption spectrum in the visible-ultraviolet region. The wavelength at which the maximum absorbance occurs is called the  $\lambda_{\text{max}}$ . A typical UV-Vis spectrum of Na<sub>2</sub>Cr<sub>2</sub>O<sub>7</sub> at pH 1.0 displays peaks at 350 nm and 260 nm (Figure 2.3). Using the Beer-Lambert Law (Equation 2.5), a calibration curve was constructed as shown in Figure 2.4 for various concentrations of Na<sub>2</sub>Cr<sub>2</sub>O<sub>7</sub>.2H<sub>2</sub>O in 0.10 M H<sub>2</sub>SO<sub>4</sub> using the absorbance measured at 350 nm. This allowed for the exact concentration of the Na<sub>2</sub>Cr<sub>2</sub>O<sub>7</sub>.2H<sub>2</sub>O in 0.10 M H<sub>2</sub>SO<sub>4</sub> to be obtained, from the absorbance observed at 350 nm.

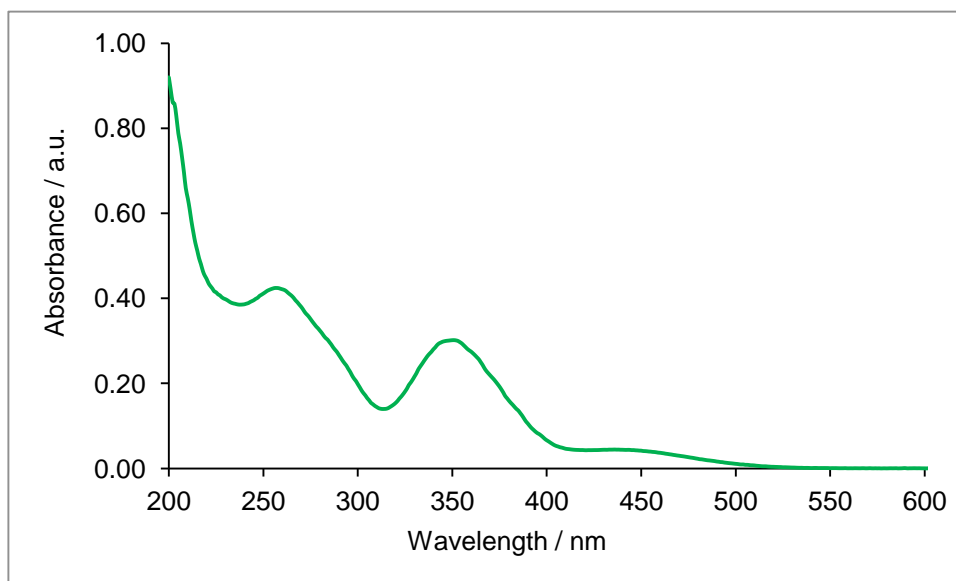


Figure 2.3: Typical UV-Vis spectrum of 0.10 mM  $\text{Na}_2\text{Cr}_2\text{O}_7 \cdot 2\text{H}_2\text{O}$  in 0.10 M  $\text{H}_2\text{SO}_4$ .

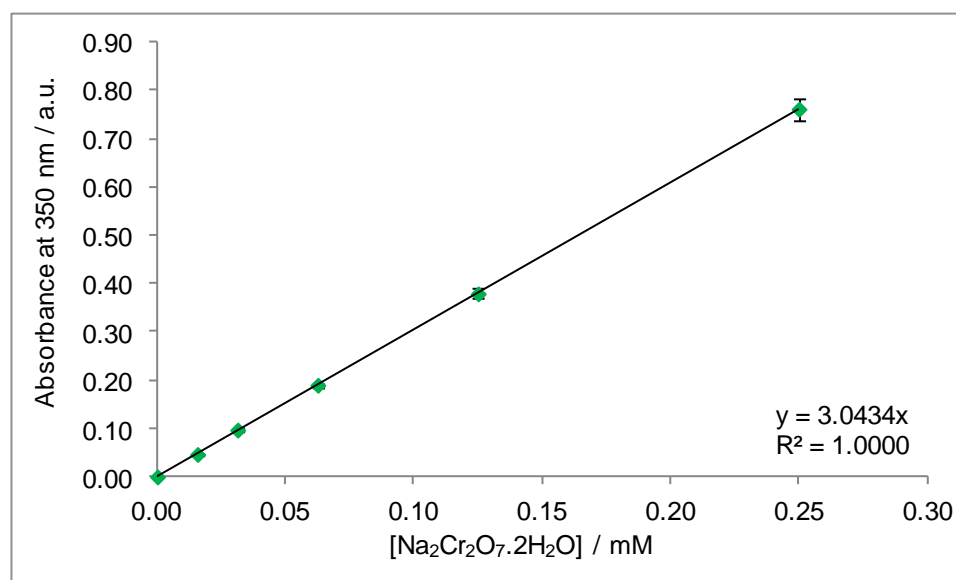


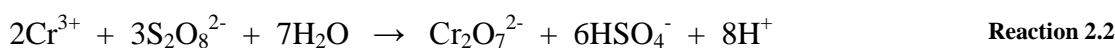
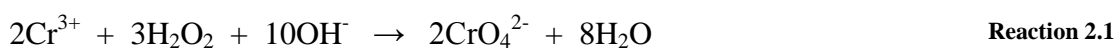
Figure 2.4: Calibration plot of absorbance at 350 nm against the concentration of  $\text{Na}_2\text{Cr}_2\text{O}_7 \cdot 2\text{H}_2\text{O}$  in 0.10 M  $\text{H}_2\text{SO}_4$ .

### 2.2.8.2 Colorimetric Tests

Immersion of the polypyrrole films in sodium dichromate for extended periods results in the complete discoloration of the solution. The studies outlined in Chapter 5 indicate that Cr(VI) in the form of  $\text{HCrO}_4^-$  is electrostatically adsorbed onto the polypyrrole surface, which is positively charged due to protonation of the nitrogen atoms of the polypyrrole backbone in the acidic solution.<sup>13</sup> The Cr(VI) is then reduced to Cr(III), oxidising the polypyrrole in the process. Having established that the Cr(VI) in solution was oxidising the polymer films, and being reduced to Cr(III), the location of this Cr(III) was investigated. A colorimetric test was necessary as UV-Vis spectroscopy is not sensitive enough to detect Cr(III) in the form of  $\text{Cr}_2(\text{SO}_4)_3$  in the small quantities present in this study.

#### 2.2.8.2(i) Colorimetric Test based on Hydrogen Peroxide / Potassium Peroxydisulfate Oxidation of Cr(III)

A preliminary colorimetric test was designed to oxidise any Cr(III) present in solution to Cr(VI) which could then be analysed using UV-Vis due to its strong yellow colour. In order to develop a calibration curve, a series of solutions of known concentration were prepared from a stock solution of 0.10 mM  $\text{Cr}_2(\text{SO}_4)_3$  in 0.10 M  $\text{H}_2\text{SO}_4$ . These solutions were then treated as follows. NaOH (0.10 cm<sup>3</sup>, 6 M) was added to bring the pH from 1.0 to 12.0. The solution was heated in a water bath held at 50 °C and hydrogen peroxide (0.05 cm<sup>3</sup>, 30 percent) was added, oxidising the Cr(III) in solution to Cr(VI) and causing the solution to become yellow in colour. The solution was then further heated before potassium peroxydisulfate was added, to oxidise any remaining Cr(III) to Cr(VI), and to reduce the pH to form dichromate, which caused the yellow colour to deepen. The reactions involved are shown in Reactions 2.1 and 2.2. The UV-Vis spectrum of each sample was obtained and the absorbance was recorded at a  $\lambda_{\text{max}}$  peak of 370 nm which is a characteristic peak of  $\text{CrO}_4^{2-}$  in a basic solution.<sup>14</sup> The calibration curve is shown in Figure 2.5. Due to the large error observed in this calibration curve, a second, more rigorous colorimetric test was carried out.



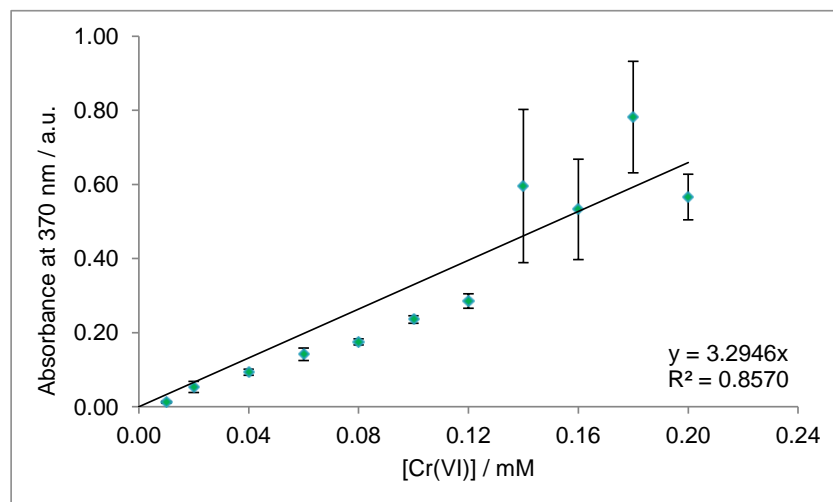


**Figure 2.5: Calibration Curve of known concentrations of  $\text{Cr}_2(\text{SO}_4)_3$  oxidised with hydrogen peroxide and potassium peroxydisulfate,  $n = 3$ .**

#### 2.2.8.2(ii) Formation of a Chromophore Complex of Cr(VI) and 1,5-diphenylcarbazide

An alternative colorimetric test is US EPA Method 7196A in which all chromium species in solution are oxidised to Cr(VI) which then forms a red-violet chromophore complex with 1,5-diphenylcarbazide, a colour chelating agent.<sup>15</sup> Two approaches employing 1,5-diphenylcarbazide were taken. The first involved immediate testing with 1,5-diphenylcarbazide to establish the amount of Cr(VI) remaining in solution. The second involved the oxidation of all chromium species in solution before addition of 1,5-diphenylcarbazide in order to determine the total amount of chromium remaining in solution. The compound 1,5-diphenylcarbazide will only form a coloured complex with Cr(VI) and this complex has a characteristic  $\lambda_{\text{max}}$  at 540 nm.<sup>16</sup>

The first calibration curve was made by treating a number of samples of known concentration which were prepared from a stock solution of 1.0 mM  $\text{Na}_2\text{Cr}_2\text{O}_7 \cdot 2\text{H}_2\text{O}$  in 0.10 M  $\text{H}_2\text{SO}_4$ . An aliquot ( $5 \text{ cm}^3$ ) of each sample was diluted to  $25 \text{ cm}^3$  with distilled  $\text{H}_2\text{O}$ . 1,5-diphenylcarbazide in acetone ( $0.5 \text{ cm}^3$ , 0.02 M) was added and the resulting red-violet colour was allowed to develop for 10 minutes before a UV-Vis spectrum was obtained. The calibration curve prepared from the resulting data is shown in Figure 2.6.

During the course of the study it was determined that the pre-steps, used to oxidise the Cr(III) in solution back to Cr(VI), resulted in an error in the concentration of Cr(VI) determined from the calibration curve prepared using the 1,5-diphenylcarbazide test. Therefore a separate calibration curve, which included these pre-steps, was prepared to

determine total chromium in solution (Figure 2.7). Solutions of known concentrations of Cr(VI) were prepared from a stock solution of 1.0 mM  $\text{Na}_2\text{Cr}_2\text{O}_7 \cdot 2\text{H}_2\text{O}$  in 0.10 M  $\text{H}_2\text{SO}_4$ . An aliquot ( $5 \text{ cm}^3$ ) of each sample was added to  $10 \text{ cm}^3$  distilled  $\text{H}_2\text{O}$  and potassium permanganate (0.25 M) was added drop wise, until a deep purple colour developed and persisted. The solution was boiled gently, with boiling chips, for approximately 2 minutes and sodium azide was added ( $1 \text{ cm}^3$ , 0.077 M). Boiling was continued for 2 minutes after the purple colour faded. The solution was then transferred, with washings to a  $25 \text{ cm}^3$  volumetric flask and cooled before diluting to the mark with distilled water. 1,5-diphenylcarbazide in acetone ( $0.5 \text{ cm}^3$ , 0.02 M) was added and the red-violet colour was allowed to develop for 10 minutes before a UV-Vis spectrum was obtained.

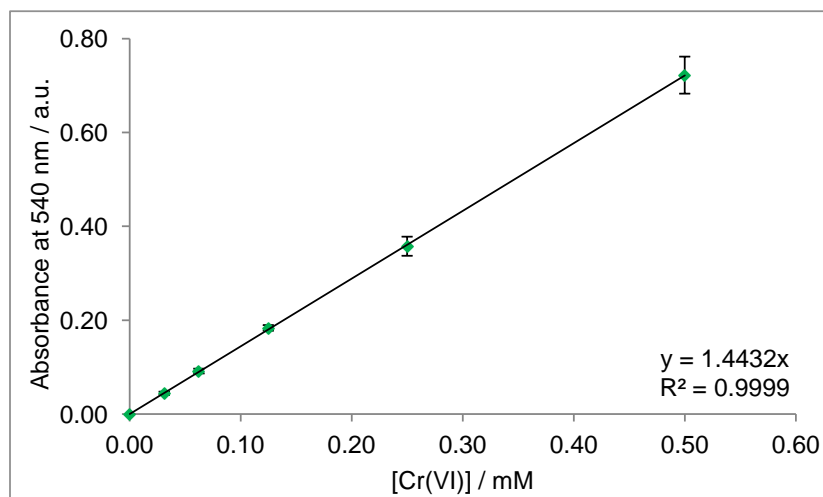


Figure 2.6: Calibration Curve of known concentrations of Cr(VI) treated with 1,5-diphenylcarbazide,  $n = 5$ .

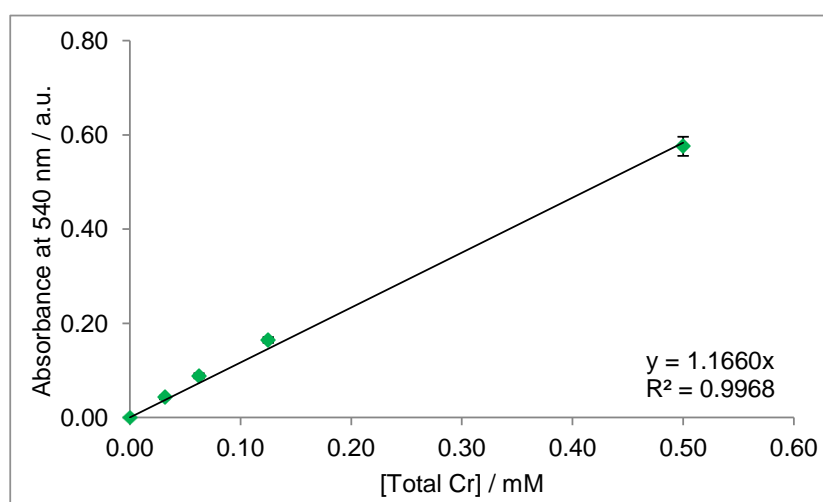


Figure 2.7: Calibration Curve of known concentrations of Cr(VI) with potassium permanganate and sodium azide added prior to treatment with 1,5-diphenylcarbazide to establish [Total Cr] in solution,  $n = 3$ .

## 2.3 Experimental Techniques

Polymerisation, characterisation and investigation of the applications of the developed polypyrrole films were carried out using various electrochemical, chemical and spectroscopic techniques. These techniques are described in the following sections, but the specific parameters employed will be detailed in the appropriate results chapters, as they vary throughout the current study.

### 2.3.1 Electrochemistry

#### 2.3.1.1 *Open Circuit Potential Measurements*

Open circuit potential is the potential of the working electrode relative to the reference electrode when no external potential or current is being applied to the system. This technique was used to monitor the open circuit potential of the polypyrrole films during the remediation of Cr(VI) and is detailed in Chapter 5.

#### 2.3.1.2 *Potentiostatic Amperometry*

This technique was employed to electrochemically deposit polypyrrole films doped with various dopants on the electrode surface. It involved applying a constant potential to the working electrode, for a fixed period of time or until a desired charge was achieved. The electrical potential at the working electrode was instantaneously stepped from a resting value where no electrolysis occurs to a value where conversion of the reactants begins.<sup>17, 18</sup> The resulting current was monitored as a function of time, which gave rise to characteristic current-time plots for the electropolymerisation of each polypyrrole film. In this study, all films were formed to a fixed charge at applied anodic potentials of between 0.55 V vs. SCE and 0.80 V vs. SCE. In order for electropolymerisation of the pyrrole monomer to occur, the applied potential must exceed 0.50 V vs. SCE. Applied potentials higher than 0.80 V vs. SCE were not employed as they are known to give rise to over-oxidation of the polymer film.<sup>19</sup>

Potentiostatic amperometry was also used in the studies discussed in Chapter 5, to reduce the polypyrrole film for the remediation of Cr(VI). A cathodic potential of -0.80 V vs. SCE was applied to the formed polypyrrole films in a solution of 0.10 M H<sub>2</sub>SO<sub>4</sub> for a fixed period of time.

### 2.3.1.3 Cyclic Voltammetry

Cyclic voltammetry is a widely used electroanalytical technique in electrochemistry which can reveal information about the nature of the electrode and the reactions taking place at it.<sup>20</sup> In this study it was primarily utilised in conjunction with EQCM, to investigate the interactions between the polypyrrole films and the ions in the electrolyte solution. It is a dynamic electrochemical technique in which the applied potential is swept between two chosen set potential limits, at a chosen scan rate ( $v$ ). The initial applied potential,  $E_i$ , is swept to a vertex potential,  $E_v$ , where the scan is reversed and swept back to the final potential,  $E_f$ . This process is cyclic and is typically repeated a number of times to observe the evolution of an electrochemical reaction occurring at the electrode surface. For a simple redox reaction (Equation 2.1), an anodic peak is produced as A is oxidised to B as the potential is swept to a higher potential. The reduction of B to A occurs as the potential scan is reversed, producing a cathodic peak. The resulting current-potential responses are useful for performing initial mechanistic investigations on a system.<sup>21</sup> The shape and dependence the responses have on scan rate are indicative of the reversibility of the redox process and whether the redox species are in solution or adsorbed on the electrode surface.

**Equation 2.1**



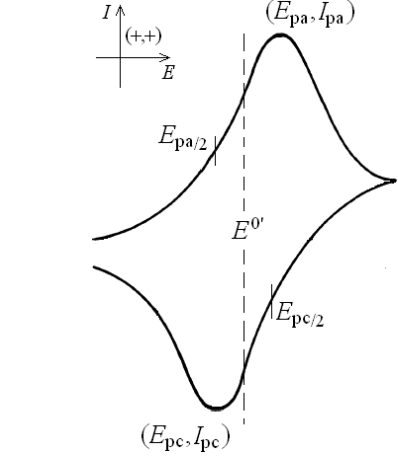
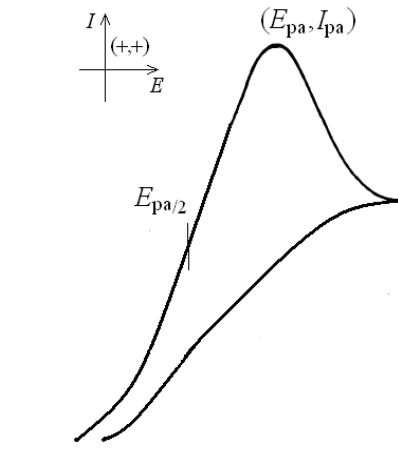
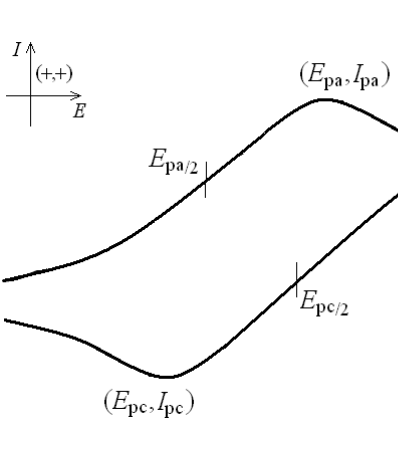
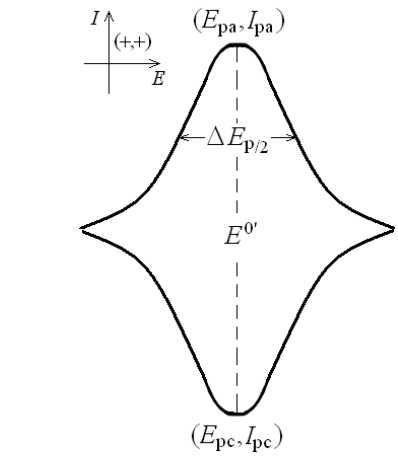
The electron transfer of the redox reaction takes place at the working electrode surface, creating an electrical current which is known as the faradic current. The counter electrode will balance this faradic process with an electron transfer of its own. For example, if oxidation occurs at the working electrode surface, a reduction process will take place at the counter electrode. For a simple redox couple, the CV exhibits an oxidation wave, with a peak current ( $I_p$ ), and a corresponding reduction wave, which are centred at a peak potential ( $E_p$ ). For a reversible redox couple, the ratio of the anodic-to-cathodic peak currents ( $I_{pa}/I_{pc}$ ) is unity, while the separation between the peak potentials ( $\Delta E_p$ ) is given by Equation 2.2. As the peak separation of a reversible redox response is independent of scan rate, it can be used to determine the number of electrons involved in the redox reaction and can also be used to establish Nernstian behaviour.<sup>20</sup>

Equation 2.2

$$\Delta E_p = E_{pa} - E_{pc} = \frac{59}{n} \text{ mV}$$

The four most typical current-potential curves observed for CV responses are displayed in Table 2.1. Each CV response is described by three key parameters, the peak current ( $I_p$ ), the peak potential ( $E_p$ ) and the potential width at half the height of the peak ( $|E_p - E_{p/2}|$ ), which is more commonly referred to as the half-wave potential. The dependence of each parameter on the potential scan rate ( $v$ ), allows for the full characterisation of the electrochemical system<sup>21</sup> and highlights the reversibility of the A/B redox reaction (Equation 2.1). The terms ‘reversible’ and ‘irreversible’ are commonly used in electrochemistry and refer to limiting cases according to whether the electrode kinetics are fast or slow. Intermediate behaviours are termed quasi-reversible.

**Table 2.1:** Cyclic voltammograms with their respective peak current ( $I_p$ ) and peak potential ( $E_p$ ) characteristics. The number of electrons involved in the redox process is denoted by  $n$  and  $\alpha$  is the corresponding transfer coefficient. All half-wave potentials are expressed at 298 K.<sup>22</sup>

Reversible	Irreversible
 <p style="text-align: center;"><math>I_p \propto v^{1/2}</math></p> <p style="text-align: center;"><math> E_p </math> independent of <math>v</math></p> <p style="text-align: center;"><math> E_p - E_{p/2}  = 59/n \text{ mV}</math></p>	 <p style="text-align: center;"><math>I_p \propto v^{1/2}</math></p> <p style="text-align: center;"><math> E_p </math> increases as <math>v</math> increases</p> <p style="text-align: center;"><math> E_p - E_{p/2}  = 48/\alpha n \text{ mV}^{20}</math></p>
Quasi-reversible	Reversible Adsorption
 <p style="text-align: center;"><math>I_p</math> not proportional to <math>v^{1/2}</math> as <math>v</math> increases</p> <p style="text-align: center;"><math> E_p </math> increases as <math>v</math> increases</p> <p style="text-align: center;"><math> E_p - E_{p/2}  = 26\Delta(\Lambda, \alpha) \text{ mV}</math></p>	 <p style="text-align: center;"><math>I_p \propto v</math></p> <p style="text-align: center;"><math>E_p</math> independent of <math>v</math></p> <p style="text-align: center;"><math>\Delta E_{p/2} = 90/n \text{ mV}</math></p>

### 2.3.1.4 Electrochemical Quartz Crystal Microbalance

The electrochemical quartz crystal microbalance (EQCM) was used to investigate the ion exchange properties of the PpyC4S and PpyPSS films. The experiments were conducted using a Chi440 Potentiostat Model EA160, which consists of a quartz crystal oscillator, a frequency counter, a fast digital function generator, high-resolution and high-speed data acquisition circuitry, a potentiostat and a computer (Figure 2.8). The EQCM monitors mass changes occurring at the electrode surface by recording the changes in the resonant frequency of the oscillating quartz crystal as the polymer is electrochemically cycled between its oxidised and reduced states. The change in frequency ( $\Delta f$  /Hz) of the oscillator is related to its change in mass ( $\Delta m$  /g) through the Sauerbrey equation (Equation 2.3).<sup>23</sup>

Equation 2.3

$$\Delta f = -\frac{2f_o^2}{A\sqrt{\mu_q\rho_q}}\Delta m$$

where  $\Delta f$  is the observed frequency change,  $\Delta m$  is the change in mass,  $A$  is piezoelectrically active area ( $0.203 \text{ cm}^2$ ),  $f_o$  is the resonant frequency of the unloaded crystal,  $\mu_q$  is the shear modulus of the quartz ( $2.947 \times 10^{11} \text{ g cm}^{-1} \text{ s}^{-2}$ ) and  $\rho_q$  is the density of the quartz ( $2.648 \text{ g cm}^{-3}$ ). It can be seen from Equation 2.3 that the change in frequency is equal to minus the change in mass per unit area multiplied by a constant. Thus, as the mass deposited on the oscillating quartz crystal increases, the frequency decreases.<sup>24</sup>

A set of limitations must be adhered to when using the EQCM to monitor the mass changes of a polymer film in order that the Sauerbrey equation holds true. Any film deposited upon the crystal oscillator must be rigid, homogeneous and acoustically thin, such that it moves synchronously with the crystal oscillator and can thus be treated as an extension of it.<sup>12</sup> Literature values as to the maximum permitted thickness of the film vary from  $400 \text{ nm} - 1 \text{ }\mu\text{m}$ .<sup>25-29</sup> Homogeneity of the film can be confirmed by the observation of a linear relationship between the change in mass and the charge passed during polymerisation of the polymer.<sup>24, 25, 30-33</sup> Unfortunately, the condition of homogeneity of the film cannot be upheld using a polypyrrole nanowire film, and so in this study the PpyC4S and PpyPSS films were characterised as standalone polymer

films, grown directly onto the gold coated quartz crystal as opposed to being coated onto the polypyrrole nanowires.

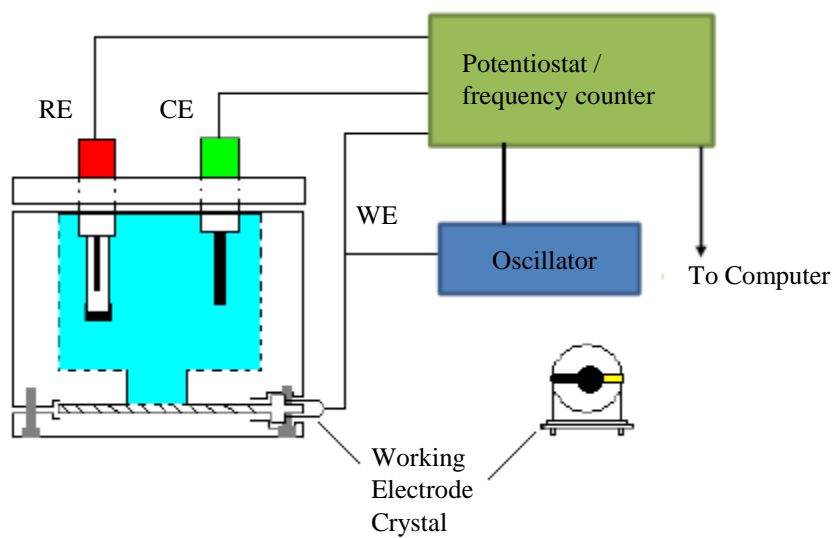


Figure 2.8: Schematic representation of the EQCM set-up.<sup>34</sup>

### 2.3.2 Surface Analysis

#### 2.3.2.1 Scanning Electron Microscopy

The advantage of electron microscopy is the ability to image objects in the nanoscale range. The fundamental principle of a microscope is the interaction between the material being examined and waves; visible electromagnetic waves in the case of an optical microscope, and high-energy electrons in the case of electron microscopy. The wavelength of visible light (~550 nm) limits the maximum resolution which can be achieved by an optical microscope. For electron microscopes a voltage (kV) is applied to an electron gun, which causes electrons to be ejected from a tungsten filament and accelerated down an optic column. A higher applied voltage generates electrons with higher energy and shorter wavelength, Equation 2.4. The observable resolution obtained by a microscope,  $d$ , between two small adjacent particles is proportional to the wavelength of the incident beam,  $\lambda$  ( $d \propto \lambda$ ). An electron beam accelerated at 80 kV has a wavelength of 0.004 nm.<sup>35</sup> Therefore, higher resolutions can be obtained using higher accelerating voltages (V).

Equation 2.4

$$\lambda = \left( \frac{1.5}{V} \right)^{1/2}$$

The scanning electron microscope (SEM) consists of an electron-optical column mounted in a vacuum chamber.<sup>36</sup> The electron gun is placed on top of the optical column and is typically a tungsten thermoionic cathode which emits electrons when heated. The electrons are driven down the column by an accelerating voltage ranging from 1 to 30 kV. The electron beam is focused on the sample and is scanned across its surface using magnetic lenses and scan coils. The sample is contained in a specimen chamber which has a pressure of  $10^{-3} - 10^{-5}$  Pa ( $\sim 10^{-7}$  mmHg). The specimen is placed on a stage that can be moved with great precision along the x, y, and z axes. The stage can also be rotated and tilted. The image generated is the result of the signals produced by the interactions of the high-energy electrons with the sample. These signals can be classified into two groups, depending on whether they result from elastic or inelastic interactions.<sup>37</sup> Elastic scattering produces backscattered electrons (BSE) with negligible energy loss and scattering angles larger than  $90^\circ$ . This elastic scattering occurs when the

incident electrons are deflected by atomic nuclei or shell electrons in the sample which have similar energy. Inelastic scattering generates signals such as secondary electrons (SE), Auger electrons, X-ray emission and cathodoluminescence, with a substantial energy loss experienced. Inelastic scattering occurs due to the deep interaction of the incident electrons with the nuclei and electrons of the sample.

The incident beam has a characteristic penetration volume in the sample and each signal originates from a different part of it (Figure 2.9 a). The BSE electrons have high energy ( $> 50$  eV) which is enough to allow them to emerge from underneath the sample surface. The SE electrons are of low energy ( $< 50$  eV) and consequently carry topographical information of the surface of the sample and are therefore the predominantly used electron source. The depth to which they can penetrate the sample is determined by the accelerating voltage and elemental composition of the sample (Figure 2.9 b). Auger electrons are emitted from atoms ionised by the incident electron beam and their energy is characteristic of the element. Auger electrons can therefore supply chemical information about the sample. Electron relaxation causes the emission of photons of infrared, visible and ultraviolet light, which results in cathodoluminescence. The emission of characteristic X-ray signals allows for chemical microanalysis of the sample surface to be carried out. This technique is known as energy dispersive X-ray (EDX) spectroscopy and is discussed separately.

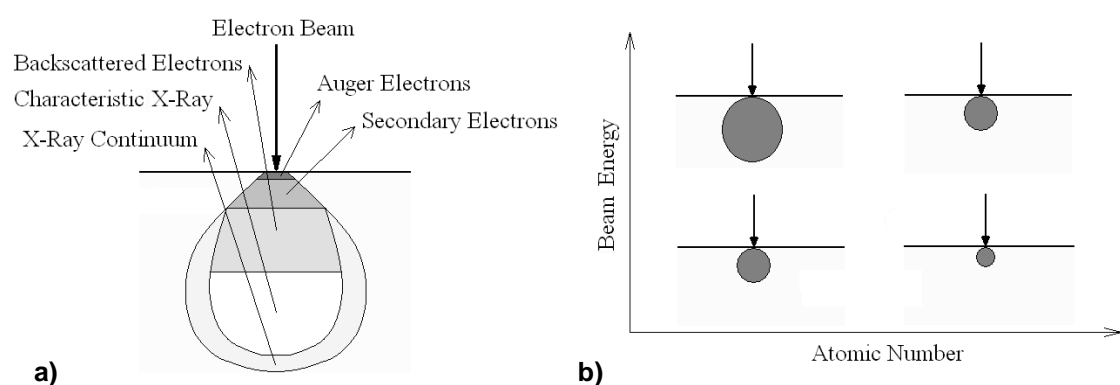


**Figure 2.9:** Schematic representation of the electron-material interactions in scanning electron microscopy (SEM). a) Cross section of the volume of interaction of the electron beam with the sample surface and corresponding areas from which different signals originate. b) Size of the electron interaction volume as a function of atomic number of the elements in the sample and the energy of the electron beam.<sup>22</sup>

When imaging non-conducting samples such as polymers, it is vital to limit surface charging phenomena. Surface charging occurs when electrons which have penetrated

the sample accumulate on the surface, which can cause a deflection of the incident electron beam (Figure 2.10 b). Non-conducting samples are often coated with a thin layer of a noble metal, for example Au, to increase the samples conductivity and decrease the build up of electrons on the sample surface. Completely drying the sample, tilting the stage, and reducing the beam current and accelerating voltage can also reduce these charging effects. Therefore, correct sample preparation and optimising the imaging conditions are vital for the production of high quality images with a tungsten filament electron gun.

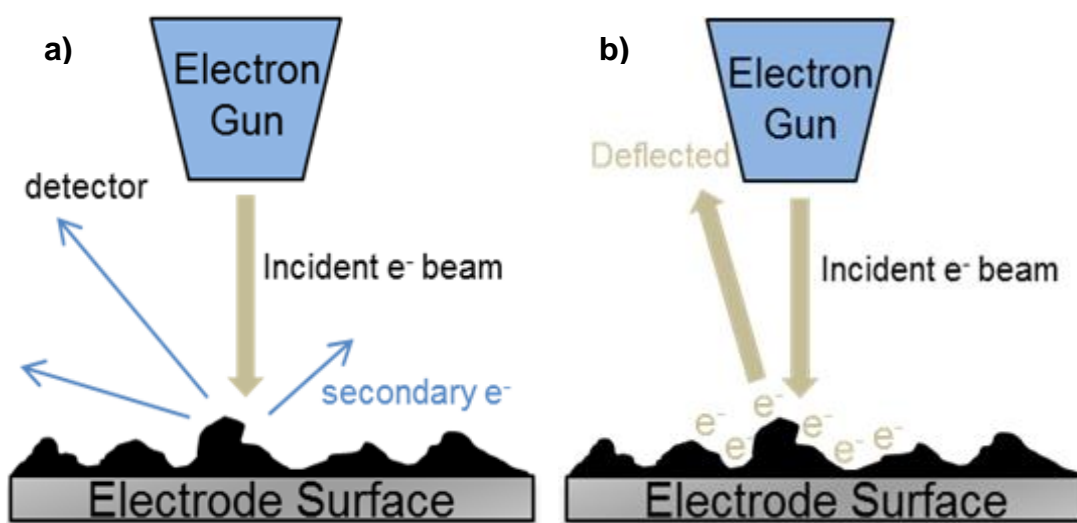


**Figure 2.10:** a) SEM analysis of a sufficiently conducting sample which produces secondary electrons in a high yield and b) a non-conducting sample which facilitates the build-up of electrons and deflection of the incident beam.<sup>38</sup>

### 2.3.2.2 Water Contact Angle

The surface wettability of a material can be determined from its water contact angle (WCA). The static sessile drop technique was employed in this study. A droplet of water of known volume is dropped onto the material surface and a contact angle goniometer is used to capture the profile of the liquid droplet on the solid material. The angle ( $\theta$ ) formed by the drop at a three phase boundary where the solid, liquid and vapour intersect is measured (Figure 2.11). A surface is deemed hydrophilic when the water contact angle is less than  $90^\circ$  and hydrophobic when greater than  $90^\circ$ . Surfaces with WCA values between  $150^\circ$  and  $180^\circ$  are called super-hydrophobic while WCA values below  $50^\circ$  are super-hydrophilic, Scheme 2.1.



### 2.3.3 Spectroscopy

#### 2.3.3.1 Energy Dispersive X-Ray Spectroscopy

Energy Dispersive X-ray spectroscopy (EDX) is used in conjunction with SEM analysis as X-rays are generated when the sample is bombarded with electrons. EDX allows for localised micro-elemental analysis of the top few micrometers of the sample. The X-ray signals are produced from the interaction of the beam electrons with the inner shell electrons of the sample. The beam electrons cause an inner electron to be ejected from the sample, and it is replaced by an outer shell electron. This transition results in the emission of X-rays with energies specific to the energy separation between the levels involved. The transition involved in this characteristic X-ray emission are labelled K, L, M and N, after the shell from which the electron is ejected, and  $\alpha$ ,  $\beta$  or  $\gamma$  depending on which outer shell electron transitions to fill the vacancy. Electron transitions from levels immediately after the emptied level are labelled  $\alpha$ , and subsequent transitions are labelled  $\beta$  and  $\gamma$ , in order of increasing energy. The X-rays emitted by the sample can reveal its chemical composition, as each element has characteristic orbital energies. Thus, an EDX spectrum consists of a series of peaks at specific energies, which correspond to the electronic transitions of the different elements present in the sample. These elemental peaks are proportional in intensity to the amount of a chemical element in the sample and to the energy carried by the associated X-ray signal. An X-ray continuum is also generated due to the deceleration of the incident electrons and this forms a continuous background signal which is present in all EDX spectra. This background signal, often referred to as Bremsstrahlung, has a much lower intensity than the elemental peaks and so does not hinder the identification of the main characteristic X-rays.

While it is therefore clear that EDX can provide both qualitative and quantitative information about the chemical makeup of a sample, the quality of this analysis may be affected by the surface roughness of the sample.<sup>40</sup> The BSE electrons generated by the incident electron beam can interact with zones surrounding the beam spot, causing the emission of additional X-rays which add to the X-ray signal generated at the point of analysis (Figure 2.12). This phenomenon poses a major limitation for the quantitative analysis of the elemental composition of a sample using EDX. Thus, quantitative EDX analysis is most suitable for high-quality flat-polished surfaces, and should be

performed against a known standard which has been prepared and analyzed in the same manner. In the study, EDX analysis was used only as a qualitative indicator of the elemental composition of the samples examined.

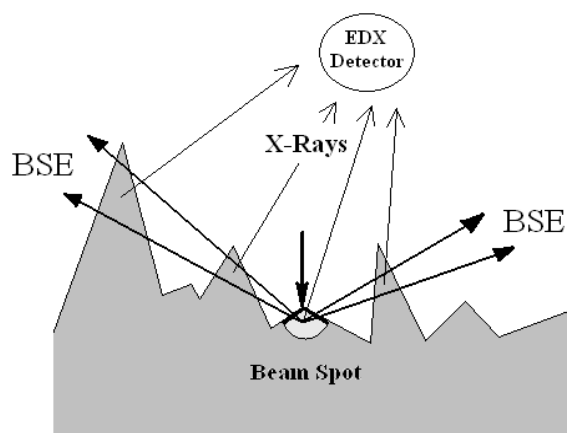


**Figure 2.12:** Schematic illustration of the effect of surface roughness on the detection of the X-ray signal. The interaction of the BSE with the surrounding surface causes the acquisition of a mixed signal by the EDX detector.<sup>22</sup>

### 2.3.3.2 Fourier Transform Infrared Spectroscopy

Infrared (IR) spectroscopy measures the vibrational motions of atoms, around their connecting bonds, when they are excited by electromagnetic radiation from the IR region of the electromagnetic spectrum. While infrared photons do not carry sufficient energy to cause electronic transitions, they do have sufficient energy to cause groups of atoms to vibrate with respect to the bonds that connect them. Since molecules will absorb IR radiation at specific wavelengths and frequencies, these vibrations are characteristic of certain energies and thus provide a means of identifying the groups and species present in a material. Every group has a characteristic frequency or band of absorption. The position of these characteristic IR bands is specified by their wavelength ( $\lambda$ ), or its reciprocal value which is called wavenumber, measured in  $\text{cm}^{-1}$ . The frequency of the vibrations between two atoms depends on two quantities; the masses of the atoms involved and the stiffness of the bond between them. Thus, heavier atoms will vibrate slower than lighter atoms, and as stronger bonds tend to be stiffer more energy will be required to stretch or compress them. This leads to an IR spectrum which can be used as a characteristic and unique fingerprint of a compound.<sup>41</sup>

In this research, IR spectra were obtained of samples prepared by grinding with potassium bromide (KBr) and pressed into a disk. The use of KBr limits the loss of

information, as KBr does not contain IR bands in the mid-IR region of the electromagnetic spectrum. FTIR spectra were obtained using a Perkin Elmer 2000 FTIR spectrometer.

### 2.3.3.3 Raman Spectroscopy

Raman spectroscopy is based on the inelastic scattering of monochromatic radiation. When a strong light source (usually a monochromatic laser beam) is focussed on a sample, most of its energy will be elastically scattered. The energy absorbed during a Raman experiment excites the molecules in the sample from a ground state to a virtual electronic state. The release of a photon allows the return to the electronic ground state. When the photon energy of this scattered light is equal to the energy of the incident light this elastic scattering process is known as Rayleigh scattering (Figure 2.13). Inelastic or Raman scattering occurs when the excited molecule returns to an energy level which is higher or lower than the original energy state. Radiation scattered with a frequency lower and higher than that of the incident beam is known as Stokes and anti-Stokes radiation respectively (Figure 2.13). The difference in energy between the incoming and scattered photon (Raman shift) corresponds to the energy difference between vibrational energy levels of the molecule. This energy difference is characteristic of the material and the different vibrational modes of the molecule can be identified by the Raman shifts (bands) observed in the inelastically scattered light spectrum.

The energy transitions for IR and Raman are depicted in Figure 2.13. The IR transition requires a smaller and exact amount of energy compared to the Raman transitions. The Rayleigh scattering is observed when the incident photon is elastically scattered. The Stokes and anti-Stokes lines correspond to the inelastic scattering. In the case of the Stokes line the starting vibrational level is the ground state, the ending is a vibrational level at higher energy which indicates that energy has been absorbed. In the case of the anti-Stokes line, the starting vibrational level is above the ground state, the ending is the ground level, and so energy is emitted in the form of a photon. The population of the vibrational levels above the ground level is low at ambient temperature (Boltzmann distribution).

The Raman measurements conducted for this thesis were performed at the Focas Institute at the Dublin Institute of Technology, with a LabRAM high resolution Raman

spectrometer using a solid state diode laser (100 mW), and employed a 660 nm laser line. The polymer materials and their associated starting materials were made into KBr disks and analysed, except for *p*-sulfonatocalix[4]arene sodium salt and LiClO<sub>4</sub> which were analysed in powder form.

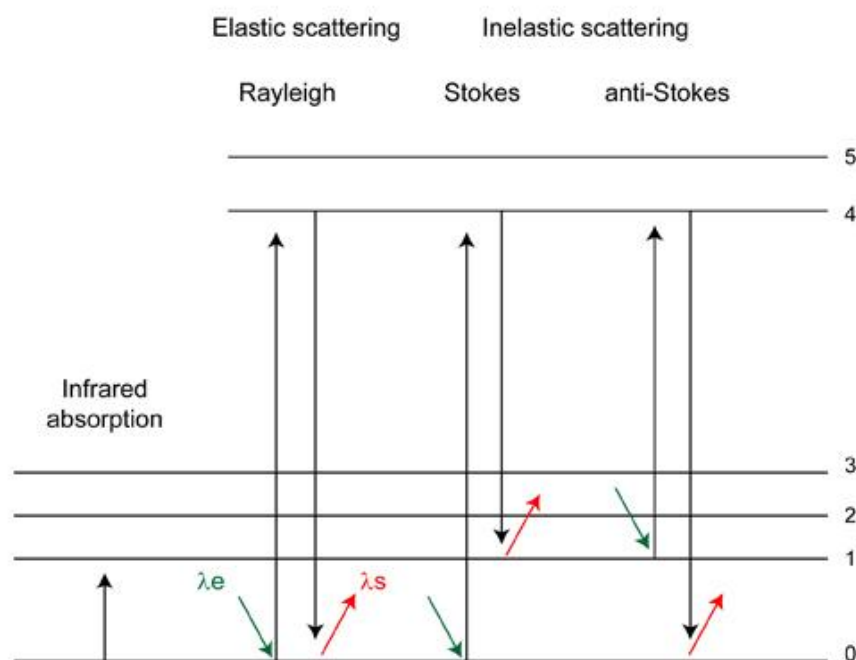


Figure 2.13: Simplified energy level diagram for the infrared and normal Raman energy transitions within the same molecular electronic level,  $E_0$ . The shift in wavelength between the incident light ( $\lambda_e$ ) and the scattered light ( $\lambda_s$ ) is related to Raman shift ( $\Delta\nu$  in  $\text{cm}^{-1}$ ) according to:  $\Delta\nu = (1/\lambda_e) + (1/\lambda_s)$ .<sup>42</sup>

#### 2.3.3.4 UV-Visible Spectroscopy

UV-Visible (UV-Vis) spectroscopy measures the amount of ultra-violet and visible light transmitted or absorbed by a sample placed in the spectrometer. The absorption of UV-Vis energy causes an electronic transition from an occupied energy level to an unoccupied energy level. UV-Vis spectrometers typically operate in the electromagnetic range of 190 nm to 800 nm. To obtain the UV-Vis spectrum of a sample, the sample is dissolved in a solvent which does not absorb above 190 nm. This is placed in a quartz cuvette and a sample of the solvent is placed in a reference cell. The UV-Vis spectrometer then compares the amount of light transmitted through the sample to the amount of light transmitted through the reference cell. This technique also compensates for any absorption of light by the solvent. The wavelength at which the maximum absorbance occurs is called the  $\lambda_{\text{max}}$ . The absorbance at a fixed wavelength is proportional to the concentration of the species in solution, according to the

Beer-Lambert Law, which means that as the concentration of the sample changes, it can be monitored by monitoring the absorbance of the sample at  $\lambda_{\text{max}}$ . The Beer-Lambert Law is shown in Equation 2.5.

Equation 2.5

$$A = \epsilon cl$$

where  $A$  is absorbance,  $\epsilon$  is the molar absorptivity coefficient ( $\text{cm}^2 \text{mol}^{-1}$ ),  $c$  is the concentration of the compound in solution ( $\text{mol cm}^{-3}$ ) and  $l$  is the path length (cm) through the cuvette.<sup>41</sup> In this research, UV-Vis spectroscopy was carried out using a Perkin Elmer Lambda 35 UV-Vis Spectrometer, with UV Winlab Version 6.0 software. The spectrometer comprised of a deuterium and tungsten lamp with a combined wavelength range of 190-800 nm. Samples were placed in quartz cuvettes, with a path length of 1 cm and a volume of approximately 3  $\text{cm}^3$ . Analysis was carried out using Microsoft Excel 2007/2010.

## 2.4 References

1. S. Shinkai, K. Araki, T. Tsubaki, T. Arimura and O. Manabe, *Journal of the Chemical Society, Perkin Transactions 1: Organic and Bio-Organic Chemistry*, 1987, 2297-2299.
2. G. Arena, R. Cali, G. G. Lombardo, E. Rizzarelli, D. Sciotto, R. Ungaro and A. Casnati, *Supramolecular Chemistry*, 1992, 1, 19-24.
3. I. Yoshida, N. Yamamoto, F. Sagara, D. Ishii, K. Ueno and S. Shinkai, *Bulletin of the Chemical Society of Japan*, 1992, 65, 1012-1015.
4. K. Suga, T. Ohzono, M. Negishi, K. Deuchi and Y. Morita, *Supramolecular Science*, 1998, 5, 9-14.
5. A. Kaynak and R. Beltran, *Polymer International*, 2003, 52, 1021-1026.
6. T. Lin, L. Wang, X. Wang and A. Kaynak, *Thin Solid Films*, 2005, 479, 77-82.
7. X. Yang, T. Dai, Z. Zhu and Y. Lu, *Polymer*, 2007, 48, 4021-4027.
8. K. Huang, M. Wan, Y. Long, Z. Chen and Y. Wei, *Synthetic Metals*, 2005, 155, 495-500.
9. S. Sahoo, S. Dhibar and C. K. Das, *eXPRESS Polymer Letters*, 2012, 6, 965-974.
10. C. Harley, Ph.D., NUI Maynooth, 2009.
11. G. M. Hendy, Ph.D., NUI Maynooth, 2009.
12. S. Bruckenstein and M. Shay, *Electrochimica Acta*, 1985, 30, 1295-1300.
13. R. Qian, Q. Pei and Y. Li, *Synthetic Metals*, 1993, 61, 275-278.
14. L. Xia, E. Akiyama, G. Frankel and R. McCreery, *Journal of the Electrochemical Society*, 2000, 147, 2556-2562.
15. E. P. Agency, *US EPA Method 7196A*, 1992.
16. R. T. Pflaum and L. C. Howick, *Journal of the American Chemical Society*, 1956, 78, 4862-4866.
17. A. C. Fisher, *Electrode Dynamics*, Oxford University Press, Oxford, 1996.
18. P. M. S. Monk, *Fundamentals of Electroanalytical Chemistry*, John Wiley and Sons, Inc., 2001.

19. F. Beck, P. Braun and M. Oberst, *Berichte der Bunsen-Gesellschaft Physical Chemistry*, 1987, 91, 967-974.
20. A. J. Bard and L. R. Faulkner, *Electrochemical Methods. Fundamentals and Applications*, John Wiley and Sons Inc., New York, 2001.
21. D. Pletcher, R. Greef, R. Peat, L. M. Peter and J. Robinson, *Instrumental Methods in Electrochemistry*, Ellis Horwood Ltd., 1985.
22. E. Andreoli, Ph.D., NUI Maynooth, 2010.
23. G. Sauerbrey, *Zeitschrift Fur Physik*, 1959, 155, 206-222.
24. K. Naoi, M. Lien and W. H. Smyrl, *Journal of The Electrochemical Society*, 1991, 138, 440-445.
25. M. N. Akieh, W. E. Price, J. Bobacka, A. Ivaska and S. F. Ralph, *Synthetic Metals*, 2009, 159, 2590-2598.
26. S. Bruckenstein, J. H. Chen, I. Jureviciute and A. R. Hillman, *Electrochimica Acta*, 2009, 54, 3516-3525.
27. C. Fruboese and K. Doblhofer, *Synthetic Metals*, 1993, 55, 1329-1334.
28. R. M. Torresi, S. I. Córdoba de Torresi, T. Matencio and M. A. De Paoli, *Synthetic Metals*, 1995, 72, 283-287.
29. K. M. Mangold, C. Weidlich, J. Schuster and K. Juettner, *Journal of Applied Electrochemistry*, 2005, 35, 1293-1301.
30. S. Bruckenstein, K. Brzezinska and A. R. Hillman, *Physical Chemistry Chemical Physics*, 2000, 2, 1221-1229.
31. V. Syritski, A. Opik and O. Forsen, *Electrochimica Acta*, 2003, 48, 1409-1417.
32. C. Debiemme-Chouvy, A. Rubin, H. Perrot, C. Deslouis and H. Cachet, *Electrochimica Acta*, 2008, 53, 3836-3843.
33. A. R. Hillman, *Journal of Solid State Electrochemistry*, 2011, 15, 1647-1660.
34. I. J. Cambria-Ltd., Time Resolved Electrochemical Quartz Crystal Microbalance - CHI400A Series, <http://ijcambria.com/TREQCM.htm>, 2013.
35. M. Paunovic and M. Schlesinger, *Fundamentals of Electrochemical Deposition*, John Wiley and Sons, Inc., New Jersey, 2006.
36. M. Szykowska, *Scanning Electron Microscopy*, Elsevier, 2005.

37. W. Zhou and Z. L. Wang, *Scanning Microscopy for Nanotechnology: Techniques and Applications*, Springer, 2006.
38. C. P. McCarthy, Ph.D., NUI Maynooth, 2013.
39. Y. C. Jung and B. Bhushan, *Nanotechnology*, 2006, 17, 4970-4980.
40. J. Goldstein, D. E. Newbury, D. C. Joy, C. E. Lyman, P. Echlin, E. Lifshin, L. Sawyer and J. R. Michael, *Scanning Electron Microscopy and X-ray Microanalysis*, Springer, 2003.
41. L. G. Wade, *Organic Chemistry*, Addison Wesley Longman, 1999.
42. M. Van Zuilen, N. McLoughlin and O. Tumyr, Raman Spectroscopy - Theory, <http://www.geo.uib.no/bgf/index.php/raman/ramanfac>.

## Chapter 3

---

# Growth and Characterisation of Polypyrrole Nanostructures

---

### 3.1 Introduction

The development of nanostructured conducting polymers and their deposition on solid supports have gained great interest in recent years.<sup>1, 2</sup> In particular, the applications of membrane based conducting polymers has become an area of significant research interest.<sup>3-5</sup> As discussed in the Introduction to this thesis, nanostructured conducting polymers can be polymerised in a number of ways, including the use of hard-template, soft-template and template-less methods.<sup>6, 7</sup> The use of a hard-template method for the formation of conducting polymer nanowires or nanotubes was first investigated by Martin *et al.*, who used nanoporous polycarbonate membranes to guide the growth of polyaniline nanotubules.<sup>8-10</sup> While this method results in well controlled and highly orientated nanostructures; its main disadvantage is the need for removal of the template post-formation. This process may destroy or disorder the nanostructures.<sup>11</sup> Soft-template and template-less polymerisation methods rely on the control of non-covalent interactions such as hydrogen bonding to promote the self assembly of conducting polymer nanostructures.<sup>11</sup> Thus, these methods are more facile and less destructive to the formed polymer nanostructures.

The polypyrrole nanostructures developed in this research were formed by either a soft-template or template-less method. Chemical polymerisation of pyrrole in the presence of functional dopants anthraquinone-2-sulfonic acid sodium salt (AQSA) and methyl orange was investigated for the deposition of polypyrrole nanowires on a polyamide membrane.<sup>12-14</sup> Chemical polymerisation of pyrrole in the presence of a soft-template was also employed for the formation of polypyrrole-sodium alginate nanofibres.<sup>15</sup> An electrochemical template-less polymerisation was employed for the formation of polypyrrole nanowires on conventional electrodes and on modified polyamide membranes. The coating of these nanowires was investigated in order to alter their ion-exchange properties.

In this chapter, the growth of polypyrrole nanostructures by each method will be examined and the effect of polymerisation conditions will be discussed. The characterisation of the resulting polymers, using scanning electron microscopy (SEM); Raman, Fourier Transform Infra-red (FTIR) and Energy Dispersive X-ray (EDX) spectroscopy; and contact angle measurements, is also detailed.

## 3.2 Chemical Approach

Two approaches employing the chemical oxidative polymerisation of polypyrrole are discussed in the following section. The first involved the polymerisation of polypyrrole at a polyamide membrane surface through the employment of functional or self-degraded template dopants. Polyamide membranes were chosen as the solid support as they exhibit a high affinity for pyrrole monomers and yield highly adherent and conductive polypyrrole coated membranes.<sup>16</sup> The second approach examined the formation of polypyrrole-sodium alginate particles for use in the adsorption of hexavalent chromium.

### 3.2.1 Functional Dopants

#### 3.2.1.1 Using Anthraquinone-2-sulfonic Acid Sodium Salt (AQSA) as the Dopant

The polymerisation of polypyrrole on textiles and fabrics, using AQSA as the dopant, is reported to result in a uniform, adherent and conductive Ppy coating of the fibres.<sup>12, 13</sup> Chemical oxidative polymerisation of polypyrrole in the presence of AQSA (Figure 3.1) was performed as described in Section 2.2.2.1.

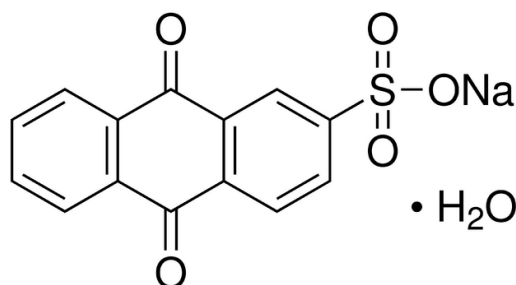


Figure 3.1: Structure of anthraquinone-2-sulfonic acid sodium salt.

Kaynak *et al.* report the formation of dendritic polypyrrole structures during the polymerisation of Ppy-AQSA<sup>12</sup> and so it was hoped that by varying polymerisation conditions, polypyrrole nanowires would form on the polyamide membrane surface. Thus the effect of polymerisation duration, pyrrole concentration and reaction volume were investigated. After each experiment, the resulting polymers were examined using SEM and weighed to examine the amount of polymer deposited. The flow rate of water through the membranes was also investigated to ensure porosity was maintained.

### 3.2.1.1(i) Influence of Polymerisation Duration

Polymerisation was carried out in a solution volume of 50 cm<sup>3</sup> for durations between 60 and 240 minutes. The amount of polymer on each membrane was determined by drying the membrane to a constant mass and measuring the weight gained by the membrane. It can be seen in Figure 3.2 that the amount of polypyrrole deposited on the membrane increases linearly with increasing polymerisation duration. Polymerisation of duration 120 minutes was chosen as membranes coated for longer than this exhibited pore occlusion which hinders porosity.

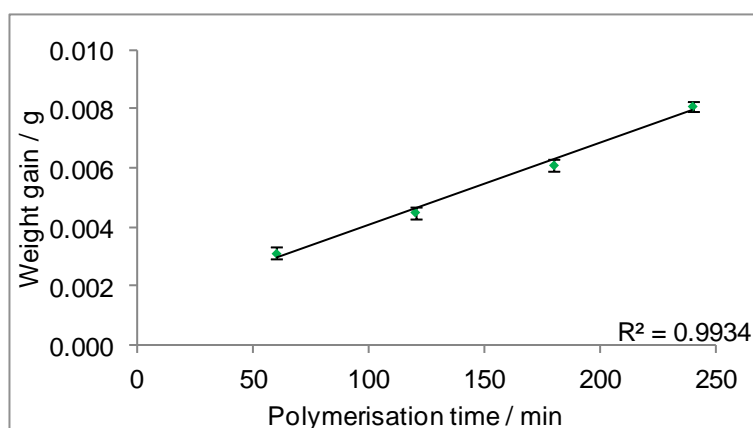


Figure 3.2: Weight gain of the polyamide membranes with increasing polymerisation time,  $n = 2$ .

### 3.2.1.1(ii) Influence of Monomer Concentration

As before, polymerisation was carried out in a solution volume of 50 cm<sup>3</sup> and the pyrrole monomer concentration was varied. It can be seen from Figure 3.3 that the weight of the membranes increases linearly with increasing monomer concentration. A pyrrole concentration of 6.0 mM was chosen as it resulted in porous, even Ppy coatings.

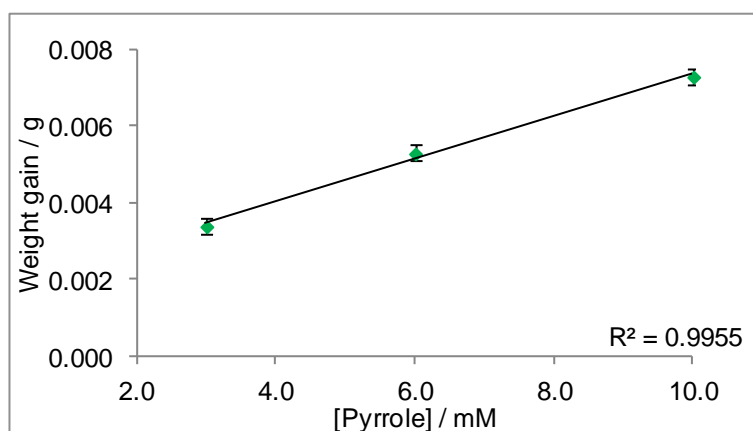


Figure 3.3: Weight gain of the polyamide membranes with increasing pyrrole concentration,  $n = 2$ .

### 3.2.1.1(iii) Influence of Reaction Volume

Previously, a reaction volume of 50 cm<sup>3</sup> was employed. It was decided to vary this solution volume to investigate the effect of changing the textile-to-liquid ratio on the weight gain of the polyamide membranes.<sup>13</sup> It can be observed in Figure 3.4 that reaction volume had no real effect on the amount of polypyrrole on the polyamide membrane. This coating was uniform and did not occlude the pores of the membrane (Figure 3.5). Unfortunately, no nanostructured polypyrrole was apparent on the membrane surfaces.

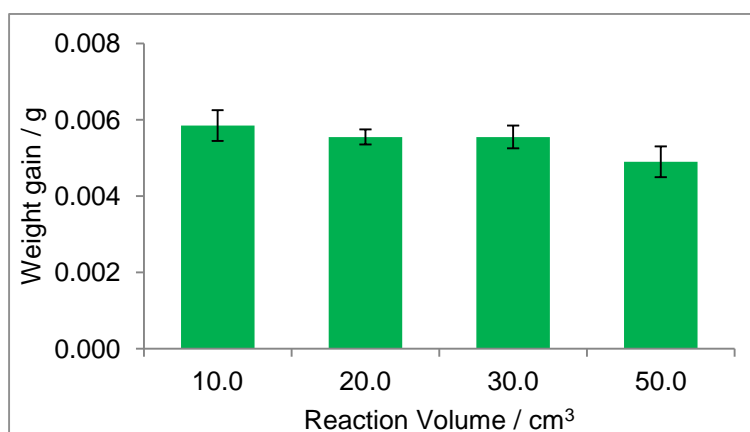


Figure 3.4: Weight gain of polyamide membranes as a function of reaction volume, n = 2.

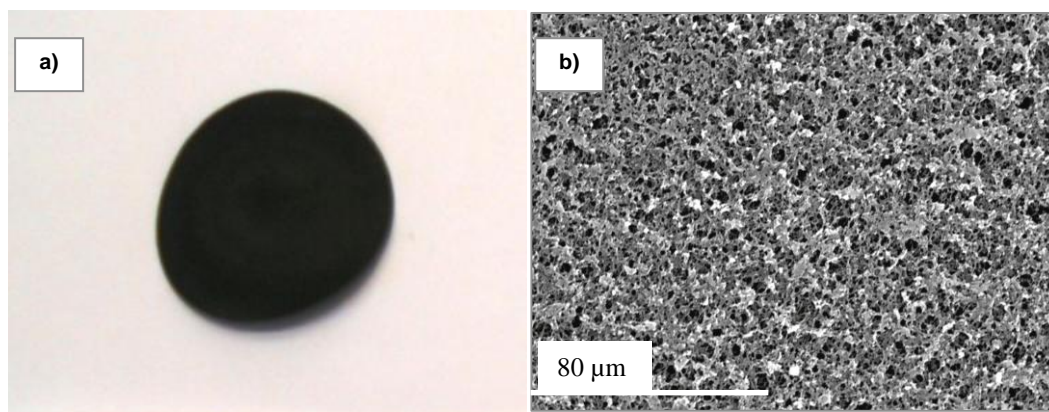


Figure 3.5: Photograph of a polyamide membrane coated evenly with polypyrrole, b) SEM micrograph of polypyrrole coated on a polyamide membrane, from a 10 cm<sup>3</sup> aqueous solution containing pyrrole:AQSA:oxidant in the ratio 1:0.6:2.5 polymerised for 120 minutes.

### 3.2.1.2 Using Methyl Orange as the Dopant

Methyl orange (Figure 3.6) and the oxidant iron(III) chloride form a fibrillar complex which has been widely used as a reactive self-degraded template for the formation of polypyrrole nanowires and nanotubules.<sup>17-19</sup> As discussed in Section 2.2.2.2, two processes were attempted for the coating of polypyrrole on polyamide membranes using the methyl orange-iron(III) chloride complex as a reactive template. The first method, which adapted the experimental method described by Huang *et al.*, in which a similar anion to methyl orange was used as the functional dopant,<sup>14</sup> did not result in an adherent polypyrrole coating on the polyamide membranes. A second method was attempted using a similar method to that described by Kaynak *et al.* was employed, which increased the reactants in solution.<sup>12, 13</sup> This resulted in a polymer uniform coating across the membrane, but no nanostructures were evident. Polymerisation in solution also occurred however, and when this polypyrrole precipitate was analysed using SEM, nanofibrous morphology was apparent (Figure 3.7).

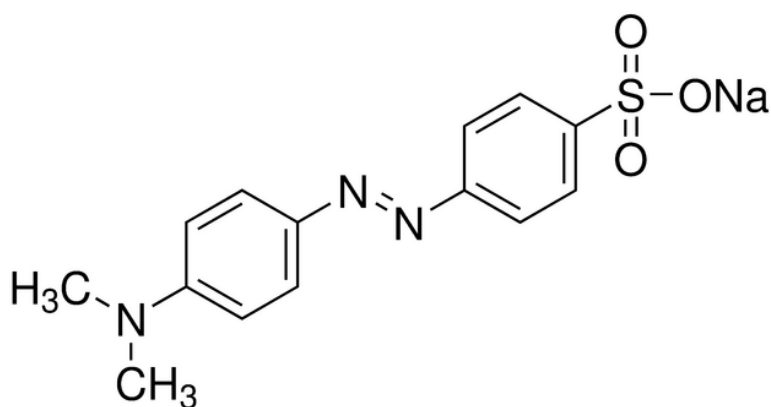


Figure 3.6: Structure of methyl orange.

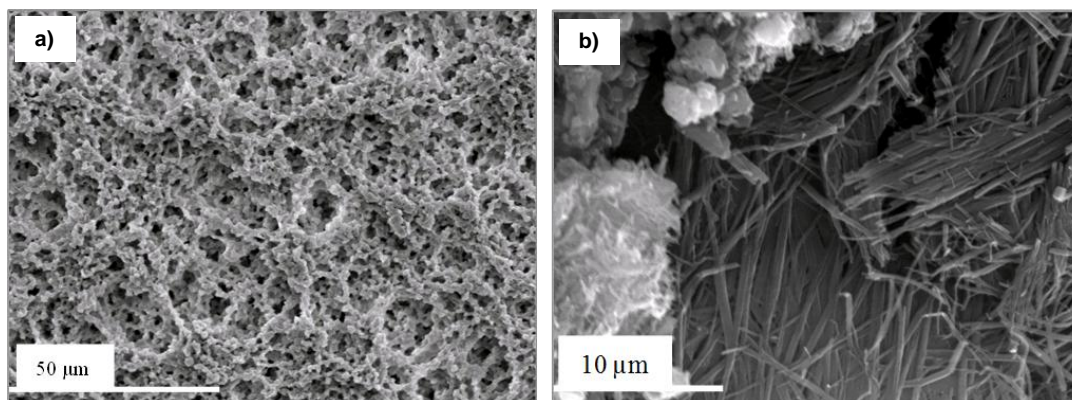
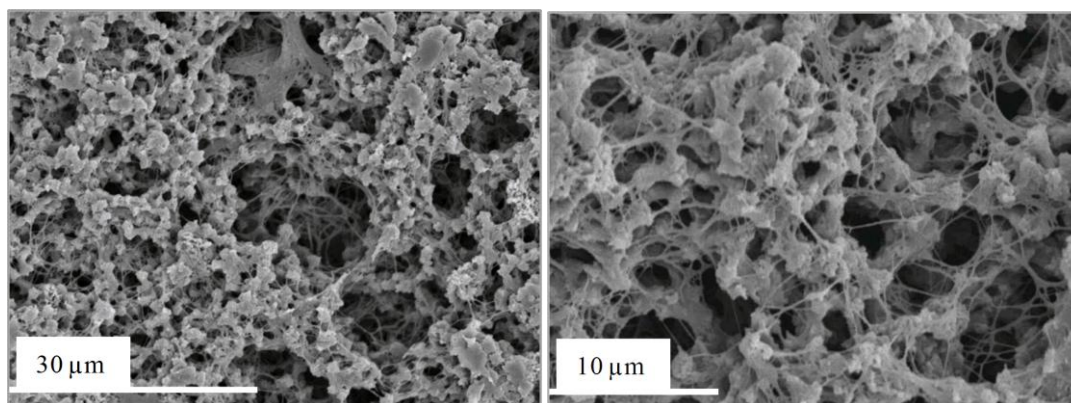


Figure 3.7: SEM micrograph of a) a pristine polyamide membrane and b) polypyrrole formed in solution using methyl orange as a reactive self-degraded template.

### 3.2.1.3 Combined Chemical Polymerisation Methods

In order to provide a base layer to which the methyl orange doped nanowires might adhere, it was decided to combine the methods discussed in Section 2.2.2.1 and 2.2.2.2. Thus, an initial layer of polypyrrole doped with AQSA was deposited on the polyamide membranes. These membranes were washed thoroughly and a second polymerisation was carried out, using the methyl orange-iron (III) chloride complex as a reactive template. Polymer formation was indicated by the presence of a black uniform coating on the membrane. SEM analysis was carried out to confirm the presence of polypyrrole nanowires (Figure 3.8). The average diameter of the nanowires was 180 nm; however the range of diameters extended from 100 nm to 400 nm. Nanowire length was estimated to be approximately 5  $\mu\text{m}$ , as they form a mesh across the membrane surface and the ends are not easily distinguishable.

The resulting membranes were washed extensively with water and ethanol. It was apparent after extensive washings that the methyl orange template was continuously leached from the nanowires coated membranes, indicating that it was not effectively immobilised within the polypyrrole matrix. Thus, the membranes developed in this manner were not employed in this study for the remediation of heavy metals from water. Optimisation of the polymerisation conditions may result in greater immobilisation of the methyl orange, but further studies would be required to investigate this.



**Figure 3.8: SEM micrographs of polyamide membranes coated with polypyrrole nanowires, at low and high magnification.**

### 3.2.2 Using Sodium Alginate as a Soft Template

#### 3.2.2.1 Preparation of Polypyrrole-Sodium Alginate Particles

Sodium alginate has been described as a molecular soft-template in the formation of conducting polymer nanostructures.<sup>11</sup> When used in the formation of polyaniline-sodium alginate nanowires, Yu *et al.* suggested that the biopolymer forms a complex with the monomer and that polymerisation to form a conducting polymer-biopolymer composite occurs upon addition of an oxidant.<sup>20</sup> A similar pyrrole-sodium alginate complex is proposed by Sahoo *et al.* and is shown in Figure 3.9.<sup>15</sup> Polypyrrole-sodium alginate particles were prepared as described in Section 2.2.3. The resulting particles were characterised by SEM, Raman and FTIR spectroscopy. The application of these particles as adsorbents for the remediation of hexavalent chromium will be detailed in Chapter 5.

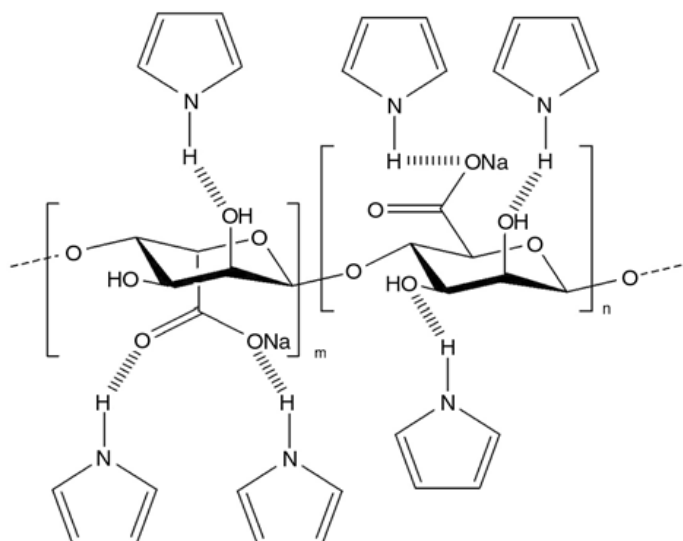


Figure 3.9: Proposed structure of the pyrrole-sodium alginate complex.<sup>15</sup>

### 3.2.2.2 Characterisation of the PpySA Particles

SEM analysis was carried out on the PpySA particles. It can be observed that the dried particles agglomerate and form clusters (Figure 3.10 a). Thus, in order to determine the diameter and shape of the individual particles, a sample was dispersed with sonication in ethanol, drop cast onto an SEM holder and allowed to dry before SEM analysis was carried out. It was determined that the particles are spherical in morphology, and exhibit a diameter of  $225 \pm 15$  nm.

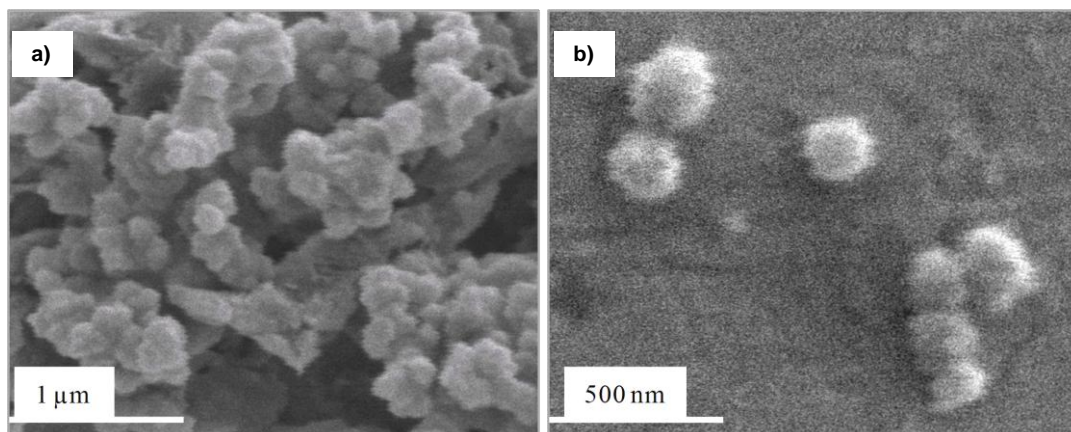


Figure 3.10: SEM micrographs of a) agglomerated PpySA particles and b) dispersed PpySA particles.

FTIR analysis produced spectra similar to that seen in the literature, with characteristic polypyrrole bands seen at  $1559\text{ cm}^{-1}$ ,  $1470\text{ cm}^{-1}$ ,  $1199\text{ cm}^{-1}$  and  $1043\text{ cm}^{-1}$  which are attributed to the stretching vibrations of the polypyrrole.<sup>15</sup> When comparing the spectra of bulk polypyrrole and PpySA particles, a new peak at  $1716\text{ cm}^{-1}$  was immediately apparent. Yu *et al.* attributed this peak to the asymmetric  $\text{-COO}$  stretch in alginate, which is shifted to a higher wavenumber than usual due to the changed environment around the alginate carbonyl group upon complexation with a conducting polymer.<sup>20</sup> This peak was both stronger in intensity and present at a higher wavenumber than the carbonyl band observed in over-oxidised polypyrrole and so it indicates that the sodium alginate was successfully incorporated into the PpySA particles. Raman spectroscopy also offered confirmation of the incorporation of PpySA. In addition to the characteristic bands of polypyrrole, two new bands at  $665\text{ cm}^{-1}$  and  $881\text{ cm}^{-1}$  were seen. These bands can be attributed to symmetric C-O-C glycosidic linkage and to symmetric C-O-C 1,4-glycosidic linkage in the alginate biopolymer.<sup>21</sup> Similar to the FTIR spectra, a band was also observed at  $1720\text{ cm}^{-1}$ .

### 3.3 Electrochemical Approach

There is current interest shown in the deposition of conducting polymers in nanowire/tube morphology, through a template-free electropolymerisation process.<sup>22-24</sup> The particular appeal of this method is its facile nature and that it does not require removal of a hard template after the deposition process. In this section studies were carried out in which the deposition of polypyrrole nanowires was examined and the effect of polymerisation conditions was investigated. The resulting polymer films were characterised using SEM; and Raman, FTIR and EDX spectroscopy. Contact angle measurements were also used to reveal the surface wettability of the electropolymerised polypyrrole materials.

#### 3.3.1 Electropolymerisation of Ppy Nanowires on a Conventional Electrode

The electropolymerisation of polypyrrole nanowires on a conventional electrode was typically carried out as described in Section 2.2.5.1. It has been shown that the electropolymerisation of conducting polymers is influenced by applied potential, polymerisation duration and the electrolyte system used.<sup>7, 25</sup> In this section, the influence of these three parameters on the formation of Ppy nanowires is investigated.

The deposition of a conducting polymer on a substrate can be monitored by recording the change in current density,  $j$ , of the system as a function of time. The shape of the resulting current density-time ( $j-t$ ) plot can reveal the steps involved in the deposition process. Thus, the influence of applied potential, polymerisation time and electrolyte solution on the electropolymerisation of polypyrrole nanowires was monitored using the  $j-t$  plots. The resulting polymer films were then investigated using SEM.

A typical  $j-t$  profile for the formation of PpyNW is shown in Figure 3.11. It may be described in terms of three regions, called transients. The first transient (I) occurs after the electric double layer is charged and the current drops to a minimum ( $t_0, j_0$ ). This drop in current is due to diffusion of the monomer units to the electrode surface and is often called the induction period,  $\tau$ . Once oxidised, the monomer units return to the solution and oligomerisation takes place, forming an oligomer high-density region (ODHR) in close proximity to the electrode surface. When the ODHR is saturated and the oligomer chains are of a sufficient length to be rendered insoluble, they precipitate onto the

electrode, generating the first polymer nuclei. Thus, up to the point  $t_0, j_0$ , polymer nucleation occurs. The second transient (II) observed in Figure 3.11, sees an increase in  $j$ , corresponding to the propagation of the polymer chains and successive growth of polymer nuclei on the electrode surface. This continues until the discrete diffusion zones of each growing nuclei begin to overlap at approximately  $t_{max}, j_{max}$ . The third transient (III) sees the development of either a plateau or a slow decrease in  $j$ , as polymerisation occurs over the whole surface of the electrode.<sup>26-28</sup>

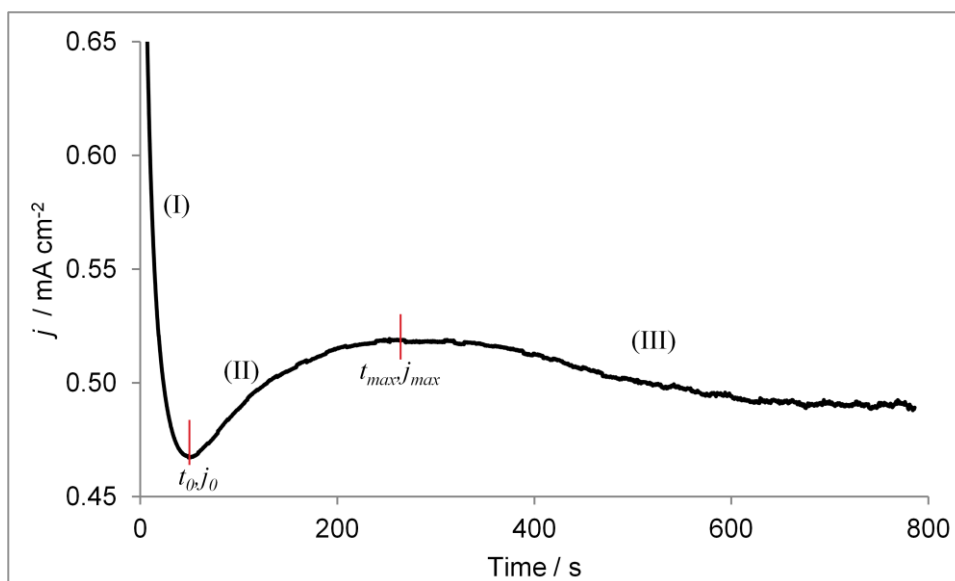
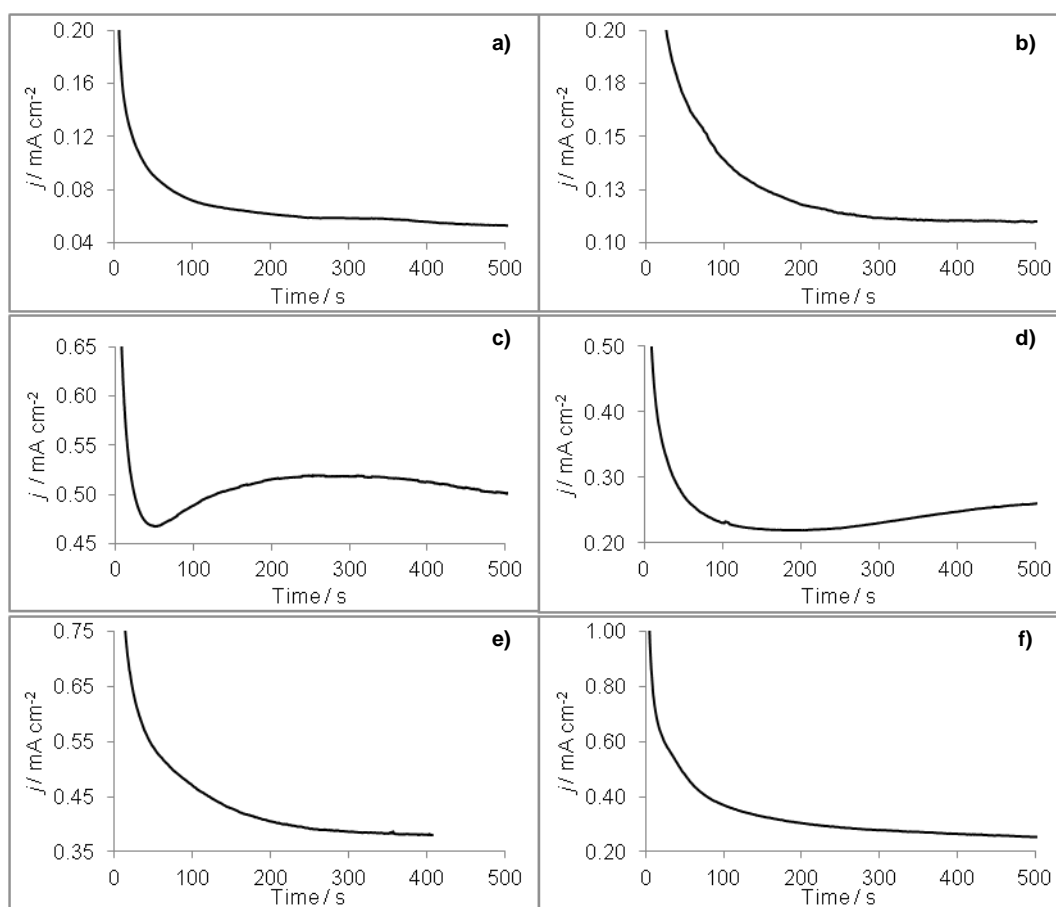


Figure 3.11: Current density - time plots of a polypyrrole film polymerised on Au at an applied potential of 0.80 V vs. SCE to a charge density of  $400 \text{ mC cm}^{-2}$ , from an aqueous solution of 0.15 M pyrrole, 0.20 M  $\text{Na}_2\text{HPO}_4$  and 0.001 M  $\text{LiClO}_4$ .

## 3.3.1.1 Influence of Applied Potential

In order to determine the optimum applied potential for the electropolymerisation of PpyNW, a range of potentials was applied to a gold electrode in an aqueous solution of 0.15 M pyrrole monomer, 0.20 M  $\text{Na}_2\text{HPO}_4$  and 0.001 M  $\text{LiClO}_4$ . Figure 3.12 shows the  $j$ - $t$  plots recorded for polymer formation at applied potentials of 0.70 V to 1.0 V vs. SCE. It was found that nanowire formation will only occur within a specific potential range (0.75 V – 0.80 V vs. SCE). Application of potentials outside of this window result in the deposition of bulk polypyrrole, exhibiting the typical “cauliflower” morphology associated with bulk polypyrrole deposition (Figure 3.13 a).<sup>29</sup> The  $j$ - $t$  plots for applied potentials of 0.70 V, 0.75 V, 0.90 V and 1.0 V vs. SCE do not appear to exhibit an induction period. Instead, the current density decreases steadily from an initial high value. It can be observed in Figure 3.12 (c) that the  $j$ - $t$  plot recorded at an applied potential of 0.80 V vs. SCE exhibits a clear induction time with well defined  $t_0, j_0$  and  $t_{max}, j_{max}$  points.



**Figure 3.12:** Current density - time plots of polypyrrole films polymerised on Au from an aqueous solution of 0.15 M pyrrole, 0.20 M  $\text{Na}_2\text{HPO}_4$  and 0.001 M  $\text{LiClO}_4$  at applied potentials (vs. SCE) of a) 0.70 V, b) 0.75 V, c) 0.80 V, d) 0.85 V, e) 0.90 V and f) 1.0 V.

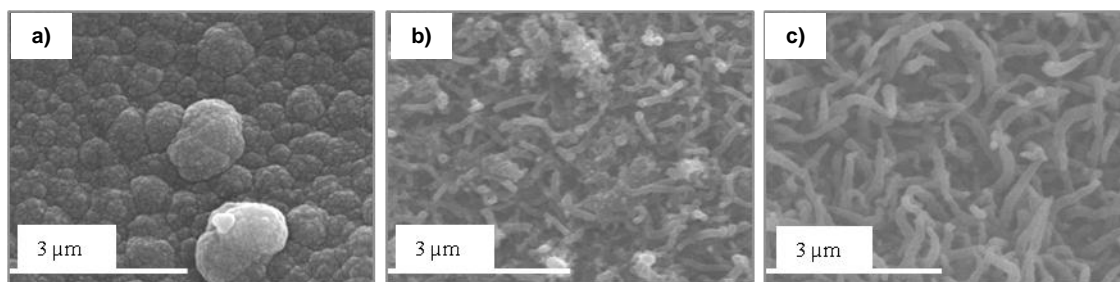


Figure 3.13: SEM micrographs (plan-view) of a) polypyrrole in the cauliflower morphology, b) PpyNW formed at an applied potential of 0.75 V vs. SCE and c) PpyNW formed at an applied potential of 0.80 V vs. SCE, from an aqueous solution of 0.15 M pyrrole, 0.20 M  $\text{Na}_2\text{HPO}_4$  and 0.001 M  $\text{LiClO}_4$ .

In Figure 3.13 (b), it can be seen that polypyrrole nanowires formed at an applied potential of 0.75 V vs. SCE are not as clearly defined and uniform in length and diameter as those formed at an applied potential of 0.80 V vs. SCE (Figure 3.13 c). Thus, an applied potential of 0.80 V vs. SCE was utilised for the electropolymerisation of PpyNW throughout the remainder of this study.

### 3.3.1.2 Polymerisation Charge Density

In order to examine the effect of polymerisation duration on the PpyNW morphology, a number of experiments were carried out where PpyNW were grown to different charge densities. As charge and film thickness are connected, increasing the charge to which the polymer is grown results in greater deposition of Ppy.<sup>30</sup> Figure 3.14 shows the growth profiles obtained for PpyNW films grown to different charge densities (Q).

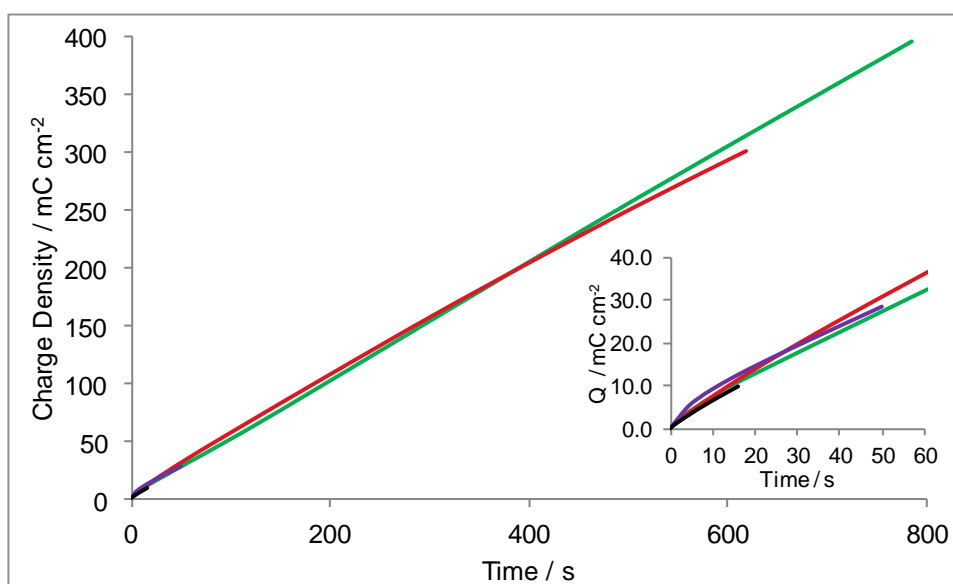


Figure 3.14: Growth profile of PpyNW grown at 0.80 V vs. SCE to a charge density of 10  $\text{mC cm}^{-2}$  (—), 30  $\text{mC cm}^{-2}$  (—), 300  $\text{mC cm}^{-2}$  (—) and 400  $\text{mC cm}^{-2}$  (—). Inset shows the first minute of the profile.

It can be observed that the growth profiles are very reproducible, and thus the method of growing to a set charge density was employed to ensure consistency in the formation of the PpyNW films. Comparing the SEM micrographs obtained for each PpyNW film, to the corresponding points on the  $j-t$  plot allow for the progression of the polymer morphology to be examined. It appears that the growth stages of the PpyNW are similar to those observed by Kemp *et al.* for the formation of polyaniline nanowires (Figure 3.15).<sup>31</sup> They found that initially, polyaniline deposits as nucleation sites on the electrode surface. The polymer then grows in a horizontal and vertical manner until the nucleation points coalesce to form a compact base layer of polymer. Once this base layer is formed, vertical growth occurs preferentially at the tips of the small polymer nodules. These nodules continue to grow vertically, until nanowires are formed.

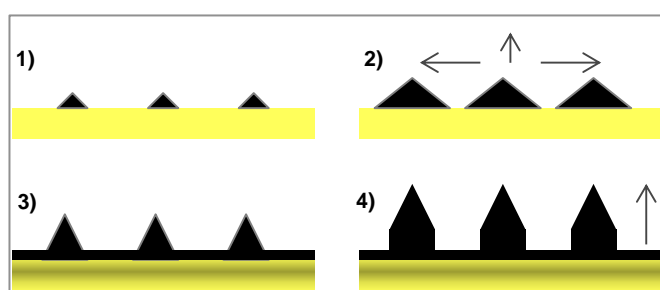


Figure 3.15: Growth stages of polypyrrole nanowire formation, 1) nucleation, 2) horizontal and vertical growth, 3) formation of a base layer with nanowire nodules and 4) vertical growth of nanowires.

The  $j-t$  plot recorded in this study, indicating the points at which the various charge densities were achieved is shown in Figure 3.16. The SEM micrographs obtained for each film are displayed in Figure 3.17. The nucleation of the PpyNW formed in this study can be observed in Figure 3.17 (a) and are clearly much larger than the nodules observed in Figure 3.17 (b). This supports the theory that these original nucleation points grow in both a horizontal and vertical manner until they overlap, forming a compact base layer upon which the polypyrrole nanowires will form.<sup>7, 32</sup> The nanowires increase in length as polymerisation continues (Figure 3.17 c), and it can be observed in Figure 3.17 (d) that nodules may form along the polypyrrole nanowires with prolonged polymerisation durations. It has been suggested that the propagation of the polymer nanowires occurs due to polymerisation at the end of the nanowire closest to the electrode, with the newly formed polymer pushing the previously formed polymer away from the electrode.<sup>33</sup> The appearance of nodules along the length of some nanowires

suggests that the PpyNW remain conducting throughout, and nucleation can take place along their length.

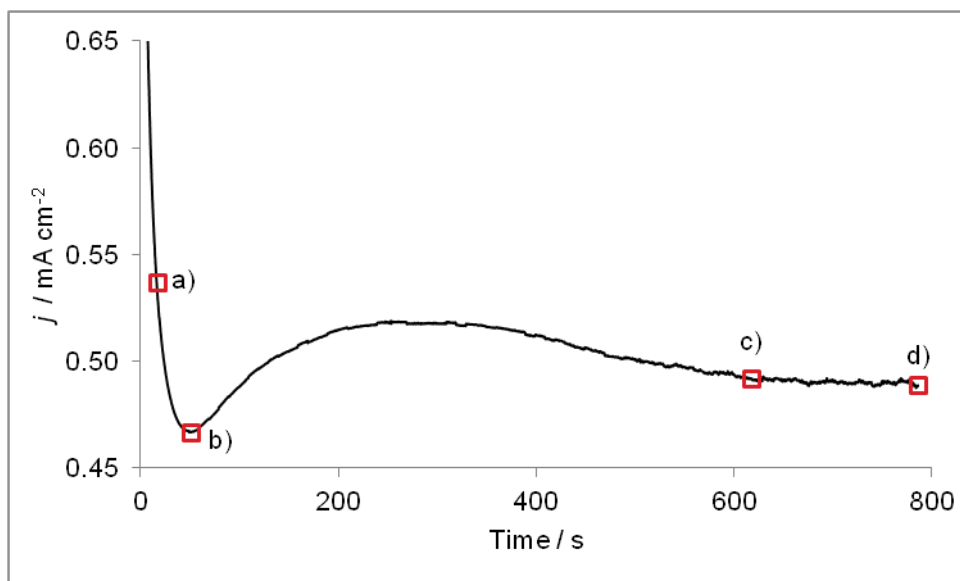


Figure 3.16: Current density - time plot for polypyrrole films polymerised on Au at an applied potential of 0.80 V vs. SCE to a charge density of a) 10  $\text{mC cm}^{-2}$ , b) 30  $\text{mC cm}^{-2}$ , c) 300  $\text{mC cm}^{-2}$  and d) 400  $\text{mC cm}^{-2}$ .

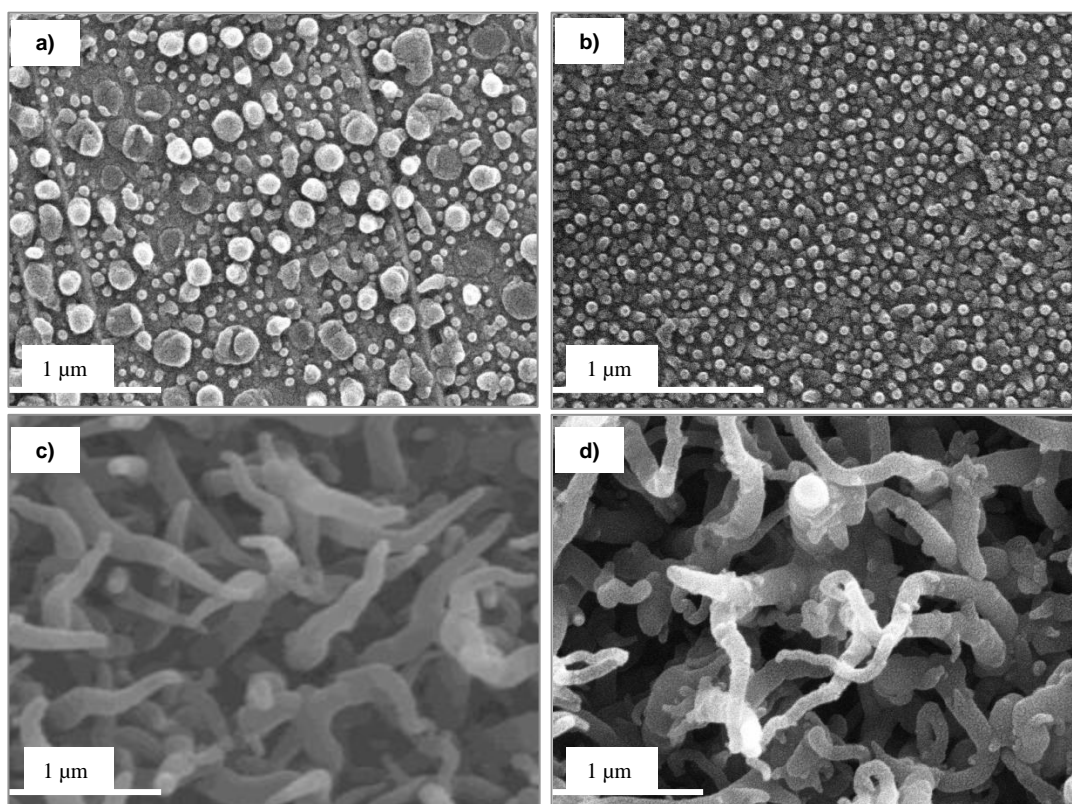
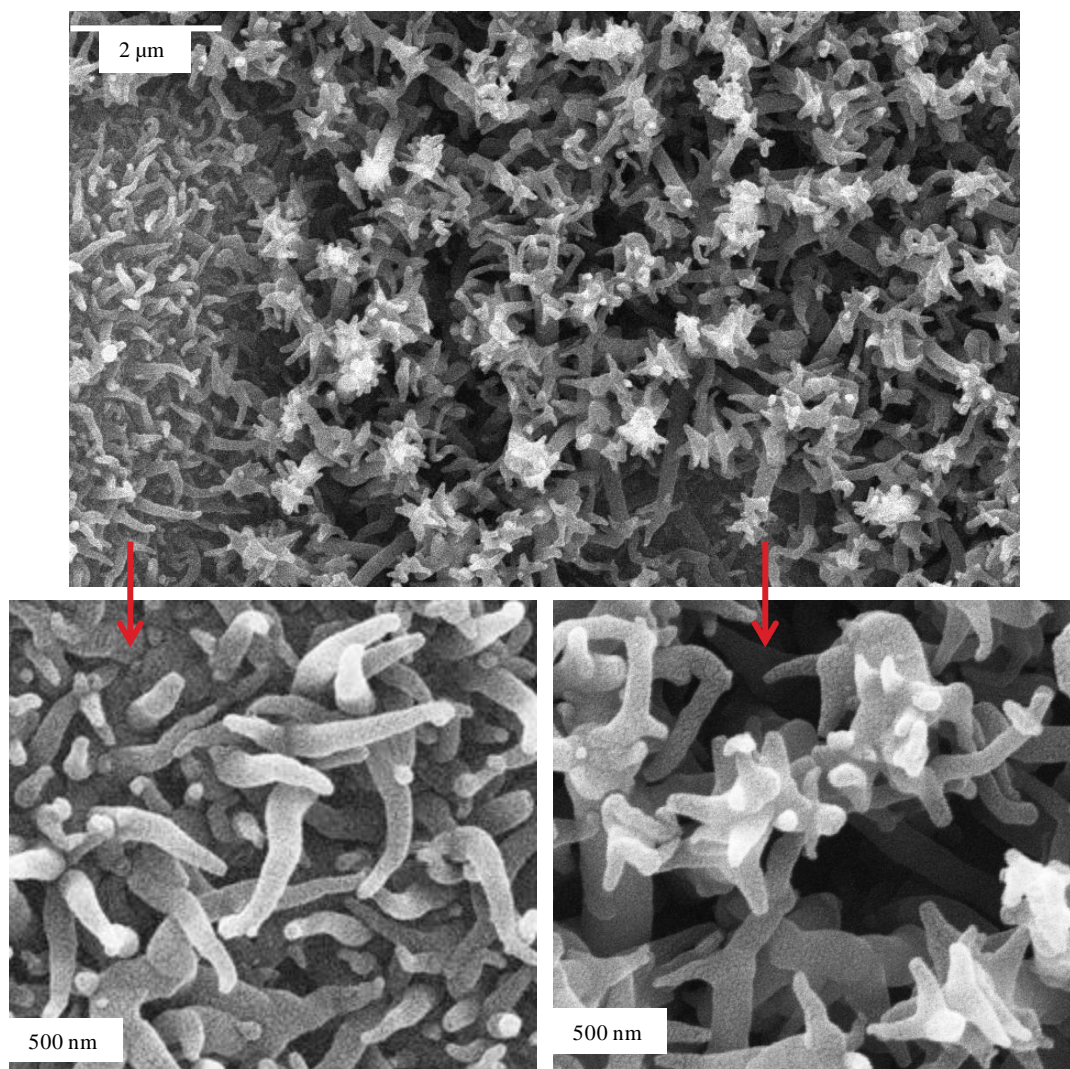


Figure 3.17: SEM micrographs of polypyrrole films polymerised on Au at an applied potential of 0.80 V vs. SCE to a charge density of a) 10  $\text{mC cm}^{-2}$ , b) 30  $\text{mC cm}^{-2}$ , c) 300  $\text{mC cm}^{-2}$  and d) 400  $\text{mC cm}^{-2}$ .

The SEM micrographs in Figure 3.18 show that branching of the PpyNW sometimes occurs as the nucleation points along the nanowires develop into polymer nodules with increasing polymerisation times.<sup>34</sup> These hierarchical polypyrrole structures do not form homogeneously across the surface of the polymer. Previous studies have shown that the formation of dendritic or hierarchical polypyrrole structures can occur at current densities greater than  $5 \text{ mA cm}^{-2}$ , and are thought to be due to a diffusion limited polymerisation process.<sup>35</sup> These PpyNW structures warrant further investigation as they offer a high specific surface area which may result in higher conductivity,<sup>36</sup> and hierarchical polymer structures are known to better accommodate mechanical stress induced by volume changes during charging processes, than bulk polymers. This may make them attractive for use in batteries.<sup>37</sup>



**Figure 3.18:** SEM micrograph of a polypyrrole films polymerised on Au at an applied potential of 0.80 V vs. SCE to a charge density of  $400 \text{ mC cm}^{-2}$ . Branching of the polypyrrole nanowires can be clearly seen (Right), occurring in close proximity to unbranched polypyrrole nanowires (Left).

### 3.3.1.3 Influence of Dopant Concentration

The electrolyte mixture of  $\text{LiClO}_4$  and  $\text{Na}_2\text{HPO}_4$  which is used in this study was chosen as previous studies suggest that this electrolyte system promotes the formation of nanofibrous polypyrrole in a unidirectional manner.<sup>7, 22</sup> The electrolyte systems reported usually consist of a mixture of phosphate salts (bulk electrolyte) and a smaller concentration of a perchlorate salt (seed electrolyte).<sup>7, 22, 23, 38</sup> Zang *et al.* proposed that the  $\text{HPO}_4^{2-}$  anions promote self-alignment of the Ppy oligomers through hydrogen bonding.<sup>22</sup> These ordered oligomer bundles could then act as scaffolding agents for the vertical growth of the Ppy nanowires. Alternatively, Debiemme-Chouvy *et al.* found that the  $\text{ClO}_4^-$  anion is preferentially incorporated into the polymer to balance out the positive charges on the polymer backbone which are generated during oxidative electropolymerisation.<sup>23</sup> They suggest that this is due to the formation of uncharged phosphoric acid which does not act as a dopant. This phosphoric acid is formed in close proximity to the polymer surface when the amphoteric  $\text{HPO}_4^{2-}$  anions in the electrolyte are protonated by the  $\text{H}^+$  cations expelled during polymer formation. For *N*-substituted polypyrrole films, it has been proposed that the monomer forms nanodroplets, and that some of the seed electrolyte is present in these droplets. It is thought that these droplets may then act as a soft template for the formation of *N*-substituted polypyrrole nanowires.<sup>39</sup> Another factor which may influence nanowire formation is the size attained by the oligomers before they precipitate out of solution and it is expected that this may also be anion dependent.

The following sections will examine whether a correlation can be drawn between the properties of the seed dopant and the morphology of the obtained nanowires. Thus, the effect of the concentration of the perchlorate anions on the *j-t* profiles and morphologies of the polypyrrole films will be examined. In addition, the  $\text{LiClO}_4$  in solution was exchanged for other supporting electrolytes, selected due to their different solubilities, ion mobilities and ionic size. These electrolytic salts are displayed in Table 3.1, accompanied by their respective physical property data, as determined from the literature. The solubility of each salt in ethanol is listed as an example of the solubility of the salt in an organic solvent. This may indicate the solubility of the salt in the proposed pyrrole nanodroplets. The influence of these different electrolyte salts on the recorded *j-t* profiles and polypyrrole morphologies will be discussed in Sections 3.3.1.4 and 3.3.1.5.

**Table 3.1: Ionic properties of salts employed for the deposition of PpyNW.** <sup>a</sup>Ionic size in picometres (pm). <sup>b</sup>Ionic mobility relative to K<sup>+</sup> in H<sub>2</sub>O. <sup>c</sup>Solubility in g/100 cm<sup>3</sup> EtOH.

<u>Cationic Data Values</u>			
Dopant	Ionic size (pm) <sup>a</sup>	Relative ion mobility <sup>b</sup>	Solubility (g/100 cm <sup>3</sup> ) <sup>c</sup>
LiClO <sub>4</sub>	~ 68	0.5260	151.800
NaClO <sub>4</sub>	~ 97	0.6820	14.700
KClO <sub>4</sub>	~ 133	1.0000	0.012
<u>Anionic Data Values</u>			
Dopant	Ionic size (pm) <sup>a</sup>	Relative ion mobility <sup>b</sup>	Solubility (g/100 cm <sup>3</sup> ) <sup>c</sup>
LiCl	~ 181	1.0382	2.500
LiTFSI	~ 325	-	Soluble
LiBF <sub>4</sub>	~ 218	-	Soluble
Li <sub>2</sub> SO <sub>4</sub>	~ 230	0.5440	0.000
LiClO <sub>4</sub>	~ 288	0.9160	151.800

Figure 3.19 displays the polymer growth  $j-t$  plot in an aqueous solution of 0.20 M Na<sub>2</sub>HPO<sub>4</sub> containing no LiClO<sub>4</sub>. At the beginning a high anodic current is seen, (45 mA cm<sup>-2</sup>) but this decreases rapidly. After ~200 minutes, the current density is relatively stable, and while very low the current density does not reach zero over the experimental timescale (~16 μA cm<sup>-2</sup>). Studies have shown that this may indicate the deposition of a very thin passive polypyrrole film (10 nm)<sup>40</sup> and the low current density observed is thought to be due to water oxidation which over oxidises the initial thin layer of polypyrrole formed.<sup>41</sup> The presence of a thin layer of Ppy was not discernible in the current study, as the SEM used was not powerful enough to determine if a film was deposited in this case. Thus, similar to the conclusions of McCarthy *et al.*, it can be seen that HPO<sub>4</sub><sup>2-</sup> does not efficiently support the electropolymerisation of polypyrrole.<sup>38</sup>

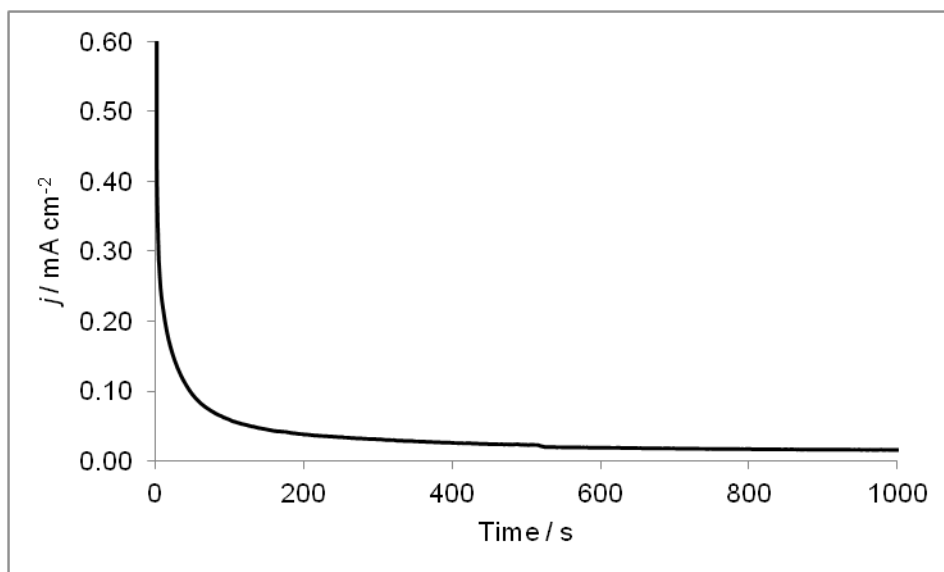


**Figure 3.19:** Current density - time plot for a gold electrode in 0.20 M  $\text{Na}_2\text{HPO}_4$  / 0.15 M pyrrole at an applied potential of 0.80 V vs. SCE. No polymer formation was discernible by SEM.

The effect of changing the concentration of the  $\text{LiClO}_4$  on the  $j-t$  plot recorded during application of an oxidising potential is shown in Figure 3.20. Figure 3.20 (a) displays the  $j-t$  profile obtained for in an aqueous solution containing exclusively  $\text{LiClO}_4$  (0.10 M). It can be seen that there is a very short induction period (0.64 seconds) followed by a sharp rise in the current density to a  $t_{max}, j_{max}$  point. Interestingly, a second  $t_{max}, j_{max}$  point occurs at a higher current-density which indicates a second process. This has been observed by del Valle *et al.* during the electropolymerisation of poly(thiophene) and was attributed to the deposition of a second layer of polymer.<sup>25</sup> Figure 3.21 (a-c) shows the SEM micrographs of the polypyrrole films formed from an aqueous solution of 0.10 M  $\text{LiClO}_4$  and Table 3.2 lists the average diameter and length of nanowire structures and the thickness of the base layer. It can be observed that the films formed from an aqueous solution of 0.10 M  $\text{LiClO}_4$  have a very thick base layer which has a morphology reminiscent of the typical cauliflower morphology exhibited by bulk polypyrrole. SEM micrographs taken at higher magnifications show the presence of nodules or microwires on top of this base layer. It is possible that the initial increase in current density corresponds to the deposition of the initial base layer of polymer. The following drop in current density may occur due to depletion of the oligomer high-density region at the electrode surface. The second increase in current density and achievement of  $t_{max}, j_{max}$  point could then occur as further oligomers diffuse

to the electrode surface and are deposited as micro wires on the bulk polypyrrole base layer.

Figure 3.20 (b) and (c) show the  $j-t$  plots of films formed in aqueous solutions containing 0.20 M  $\text{Na}_2\text{HPO}_4$  and either 0.01 M or 0.001 M  $\text{LiClO}_4$ . It can be observed that both exhibit similar induction periods and both approach a  $t_{max}j_{max}$  point after approximately 200 seconds of polymerisation. The main difference in the  $j-t$  plots is that the polymer formed in 0.01 M  $\text{LiClO}_4/0.20$  M  $\text{Na}_2\text{HPO}_4$  (Figure 3.20 b) exhibits a greater current density than that seen for the polymer formed in 0.001 M  $\text{LiClO}_4/0.20$  M  $\text{Na}_2\text{HPO}_4$ . This greater current density also accounts for the shorter time required to reach the desired charge density of  $400 \text{ mC cm}^{-2}$ .

Figure 3.21 displays the SEM micrographs obtained of the above polypyrrole films and Table 3.2 lists the average diameter and length of nanowire structures and the thickness of the base layer. It can be seen that polypyrrole nanowires are formed in both cases and exhibit similar diameters and base layer thicknesses. From the SEM micrographs it can be observed that polypyrrole films formed at a higher concentration of  $\text{LiClO}_4$  (0.01 M) are deposited in a “hills and valleys” morphology<sup>34</sup> and the nanowires formed are much longer than those formed at low concentrations of  $\text{LiClO}_4$ . The formation of a “hills and valleys” morphology can be associated with the polymer film losing adhesion to the electrode surface, and this may occur due to the faster rate of polymerisation. This loss of adherence can be seen in greater detail in the cross-sectional SEM micrographs in Section 3.3.1.6. Thus, it appears that a slow rate of polymerisation results in the more clearly defined and adherent polypyrrole nanowire films.

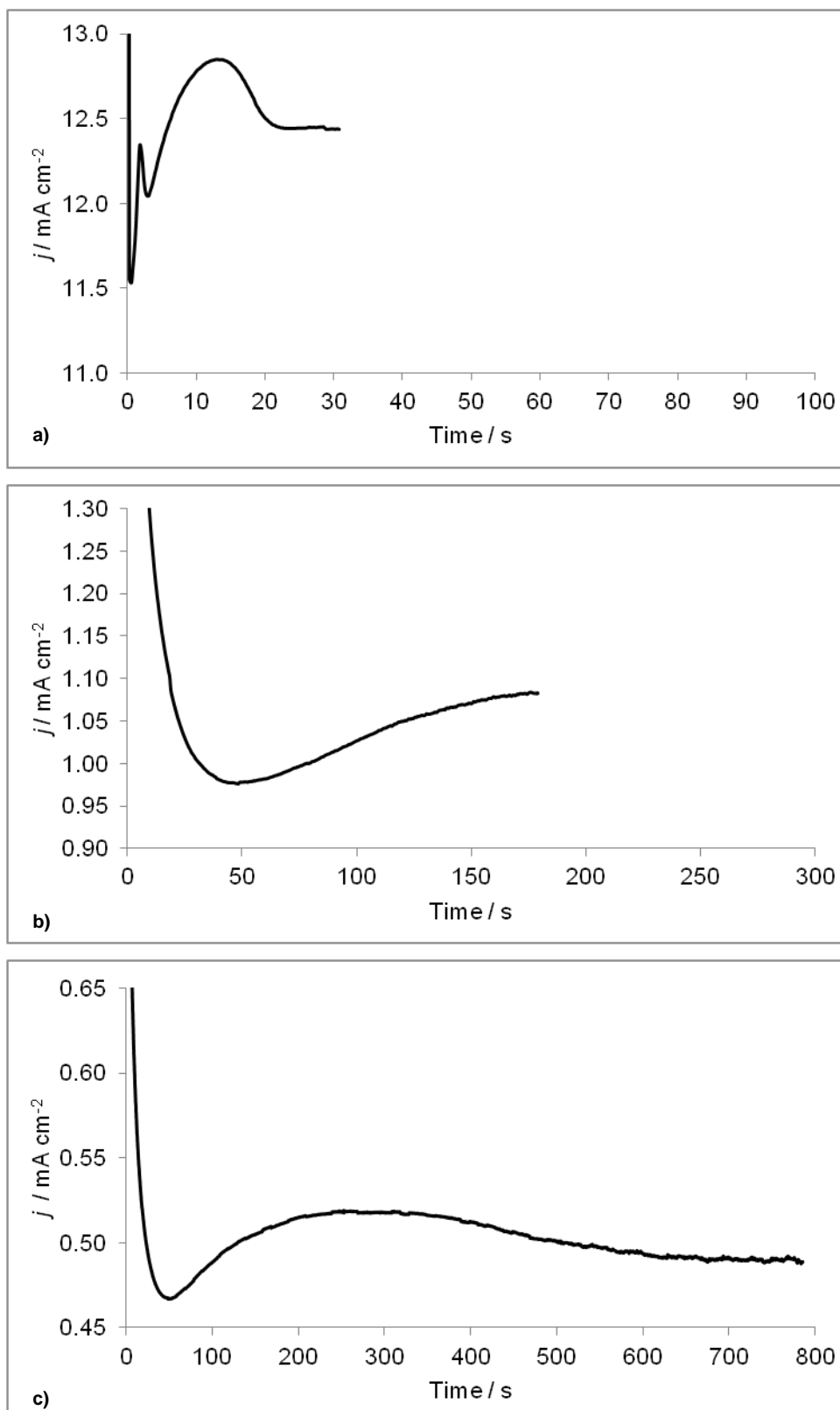


Figure 3.20: Current density - time plots of polypyrrole films polymerised on Au at an applied potential of 0.80 V vs. SCE to a charge density of  $400 \text{ mC cm}^{-2}$ , from an aqueous solution of 0.15 M pyrrole and; a) 0.10 M  $\text{LiClO}_4$ , b) 0.01 M  $\text{LiClO}_4$  / 0.20 M  $\text{Na}_2\text{HPO}_4$  and c) 0.001 M  $\text{LiClO}_4$  / 0.20 M  $\text{Na}_2\text{HPO}_4$ .

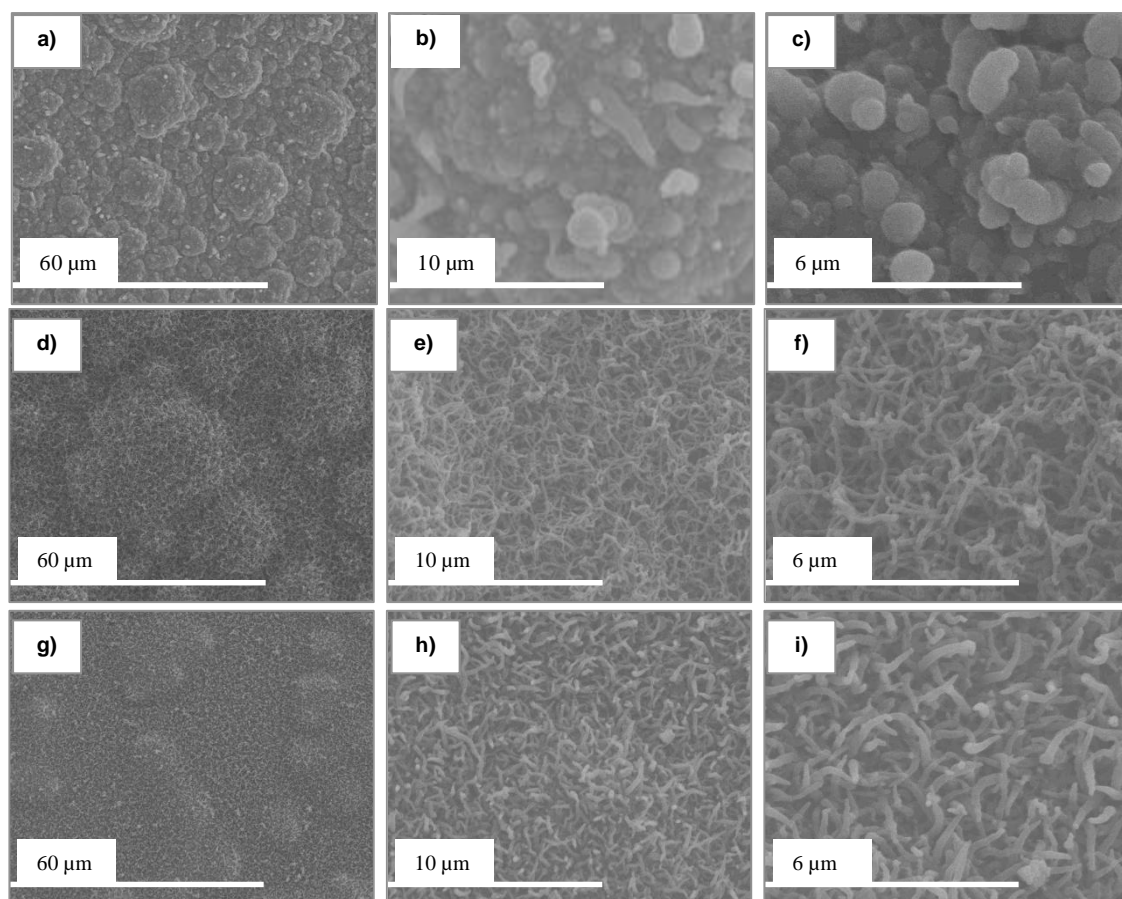


Figure 3.21: SEM micrographs (plan-view) of polypyrrole films polymerised at an applied potential of 0.80 V vs. SCE to a charge density of  $400 \text{ mC cm}^{-2}$ , from an aqueous solution of 0.15 M pyrrole and; (a-c) 0.100 M  $\text{LiClO}_4$ , (d-f) 0.010 M  $\text{LiClO}_4$  / 0.20 M  $\text{Na}_2\text{HPO}_4$  and (g-i) 0.001 M  $\text{LiClO}_4$  / 0.20 M  $\text{Na}_2\text{HPO}_4$ .

Table 3.2: Average diameter, length and base layer thickness for polypyrrole films polymerised at an applied potential of 0.80 V vs. SCE to a charge density of  $400 \text{ mC cm}^{-2}$ , from an aqueous solution of 0.15 M pyrrole and 0.100 M  $\text{LiClO}_4$ ; 0.010 M  $\text{LiClO}_4$  / 0.20 M  $\text{Na}_2\text{HPO}_4$  or 0.001 M  $\text{LiClO}_4$  / 0.20 M  $\text{Na}_2\text{HPO}_4$ ,  $n = 20$  (diameter), 10 (length and thickness).

Electrolyte	Diameter / nm	Length / nm	Base Layer Thickness / nm
0.100 M $\text{LiClO}_4$	$1241 \pm 37$	$4223 \pm 594$	$1244 \pm 56$
0.010 M $\text{LiClO}_4$ / 0.20 M $\text{Na}_2\text{HPO}_4$	$110 \pm 5.5$	$2024 \pm 193$	$510 \pm 19$
0.001 M $\text{LiClO}_4$ / 0.20 M $\text{Na}_2\text{HPO}_4$	$122 \pm 5.1$	$941 \pm 56$	$406 \pm 22$

## 3.3.1.4 Effect of Seed Dopant Anion

In order to investigate the influence of the seed electrolyte on the morphology of the polypyrrole nanowires, it was decided to first conduct a study in which the  $\text{LiClO}_4$  was replaced with different lithium salts (0.001 M). The salts chosen were lithium chloride, lithium sulfate, lithium tetrafluoroborate and lithium bis(trifluoromethane)sulfonimide (LiTFSI). Table 3.1 lists the physical properties of these electrolyte salts. The  $j$ - $t$  plots recorded during the electropolymerisation of pyrrole from aqueous solutions of 0.20 M  $\text{Na}_2\text{HPO}_4$  and 0.001 M of each lithium salt are shown in Figure 3.22.

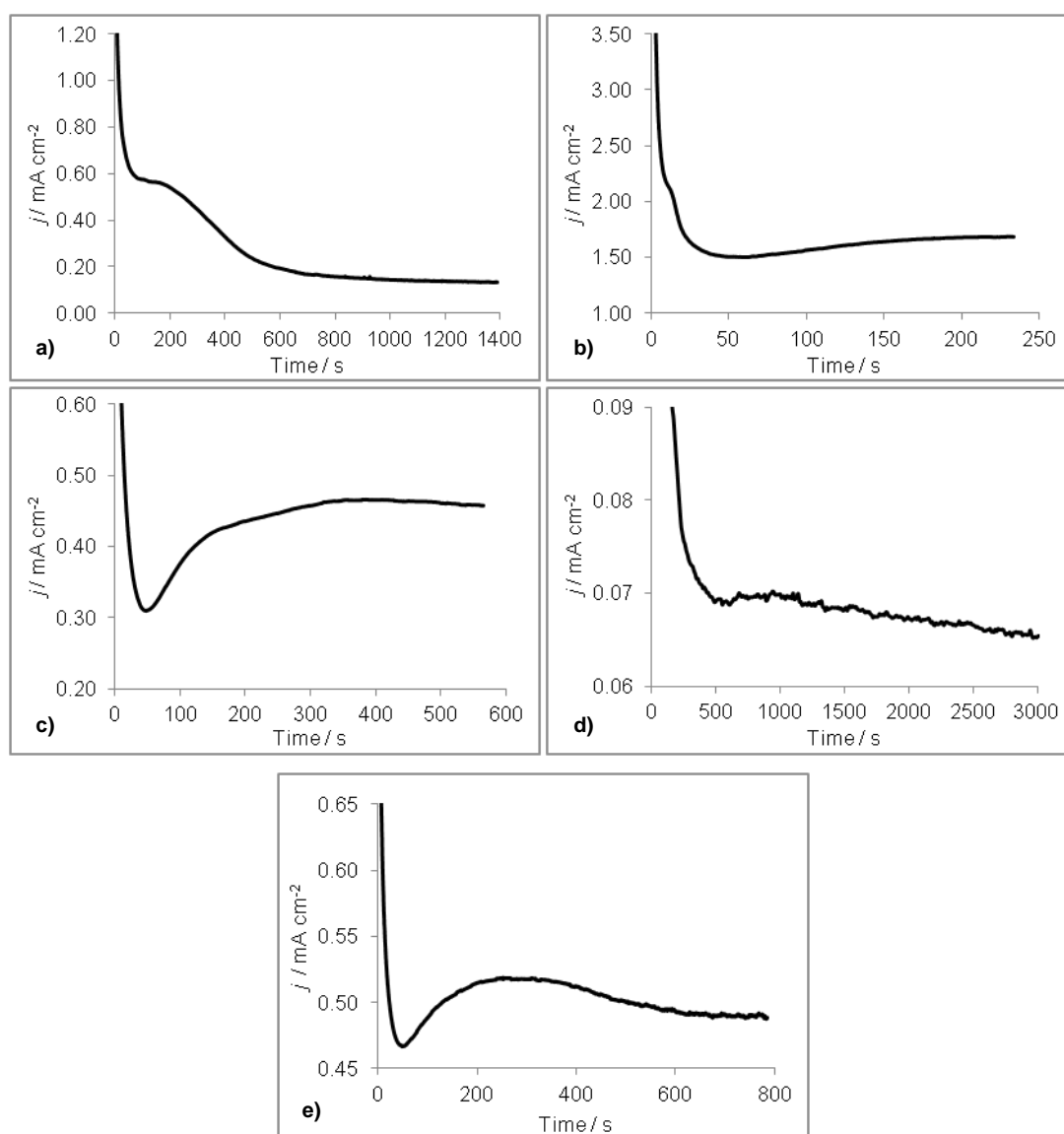
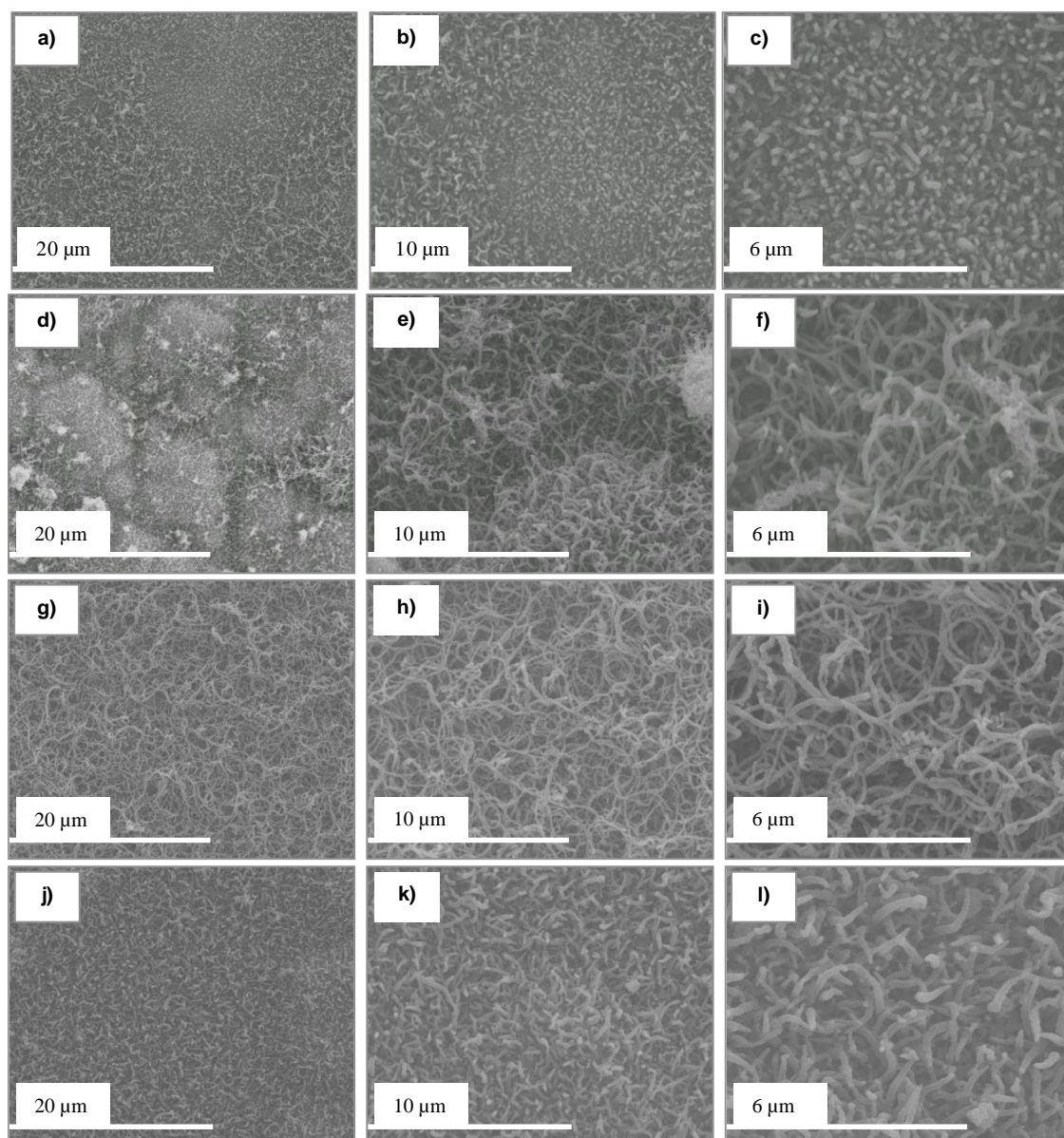


Figure 3.22: Current density - time plots of polypyrrole films polymerised on Au at an applied potential of 0.80 V vs. SCE to a charge density of  $400 \text{ mC cm}^{-2}$ , from an aqueous solution of 0.15 M pyrrole/ 0.20 M  $\text{Na}_2\text{HPO}_4$  and; a) 0.001 M LiCl, b) 0.001 M  $\text{LiBF}_4$ , c) 0.001 M LiTFSI, d) 0.001 M  $\text{Li}_2\text{SO}_4$ , and e) 0.001 M  $\text{LiClO}_4$ .

It can be seen in Figure 3.22 that the  $j-t$  traces are quite different; indicating that although it is present in very low concentrations, the seed dopant has a consistently different effect on the polymerisation. No polymer deposition was observed when polymerisation was attempted in solutions containing  $\text{Li}_2\text{SO}_4$ . The  $j-t$  plot recorded shows a very low current density that decreases gradually over the course of the experiment (Figure 3.22 d). The  $j-t$  plots recorded during the formation of polypyrrole films from aqueous solution containing  $\text{LiCl}$  does not have clearly defined induction periods (Figure 3.22 a). The current density decreases gradually, achieves a plateau for a short duration before another decrease is observed to occur followed by another plateau. Figure 3.23 shows the SEM micrographs of the films polymerised in this section. It can be seen that the films formed in the presence of  $\text{LiCl}$  exhibit patches of long and short nanowires (Figure 3.23 a-c). This may be due to the processes that are seen in the  $j-t$  plot. The nanowires have similar diameters regardless of length (Table 3.3) and the base layer thickness is similar to that seen for PpyNW films formed in the presence of  $\text{LiClO}_4$ . The  $j-t$  plot recorded for polymerisation in solutions containing  $\text{LiBF}_4$  exhibit a short induction period similar in duration to that seen for PpyNW films formed in the presence of  $\text{LiClO}_4$ . This is followed by an increase in current density to a  $t_{max}, j_{max}$  after approximately 200 seconds polymerisation duration. Interestingly, during the initial drop in current density of the induction period, the current density plateaus briefly after 15 seconds of polymerisation before continuing to decrease (Figure 3.22 b). The SEM micrographs of the resulting polypyrrole films are seen in Figure 3.23 (d-f) and a “hills and valleys” morphology covered in long nanowires can be observed. This film also exhibits the thickest base layer, which may account for the brief plateau observed during the induction period. The  $j-t$  plot recorded for the polymerisation of PpyNW in the presence of  $\text{LiTFSI}$  is shown in Figure 3.22 (c) and it displays some similarities to that seen for PpyNW films formed in the presence of  $\text{LiClO}_4$  (Figure 3.22 e). The induction period reaches  $t_0, j_0$ , after approximately 50 seconds, and the current density increases, exhibiting two  $t_{max}, j_{max}$  points. The SEM micrograph of PpyNW formed in the presence of  $\text{LiTFSI}$  (Figure 3.23 g-i) show that long, narrow PpyNW form a nanowire network over the surface of the electrode. It will also be seen in Section 3.3.1.6 that the PpyNW formed in the presence of  $\text{LiTFSI}$  have the thinnest base-layer deposition.



**Figure 3.23:** SEM micrographs (plan-view) of polypyrrole films polymerised at an applied potential of 0.80 V vs. SCE to a charge density of  $400 \text{ mC cm}^{-2}$ , from an aqueous solution of 0.15 M pyrrole/ 0.20 M  $\text{Na}_2\text{HPO}_4$  and; (a-c) 0.001 M LiCl, (d-f) 0.001 M  $\text{LiBF}_4$ , (g-i) 0.001 M LiTFSI and (j-l) 0.001 M  $\text{LiClO}_4$ .

**Table 3.3:** Average diameter, length and base layer thickness of polypyrrole films polymerised at an applied potential of 0.80 V vs. SCE to a charge density of  $400 \text{ mC cm}^{-2}$ , from an aqueous solution of 0.15 M pyrrole/ 0.20 M  $\text{Na}_2\text{HPO}_4$ , and the listed dopants,  $n = 20$  (diameter), 10 (length and thickness).

Dopant	Diameter / nm	Length / nm	Base Layer Thickness / nm
0.001 M $\text{LiClO}_4$	$122 \pm 5$	$941 \pm 56$	$406 \pm 22$
0.001 M LiCl	$127 \pm 5$	$960 \pm 59 / 456 \pm 27$	$392 \pm 18$
0.001 M $\text{LiBF}_4$	$154 \pm 5$	$1326 \pm 80$	$480 \pm 38$
0.001 M LiTFSI	$150 \pm 6$	$1672 \pm 143$	$342 \pm 33$

## 3.3.1.5 Effect of Seed Dopant Cation

In order to investigate the influence of the electrolytic cation on the morphology of the PpyNW film, studies were performed substituting  $\text{LiClO}_4$  for either sodium perchlorate or potassium perchlorate. Polymerisation of polypyrrole nanowires using these three salts resulted in quite different  $j$ - $t$  plots, shown in Figure 3.24.

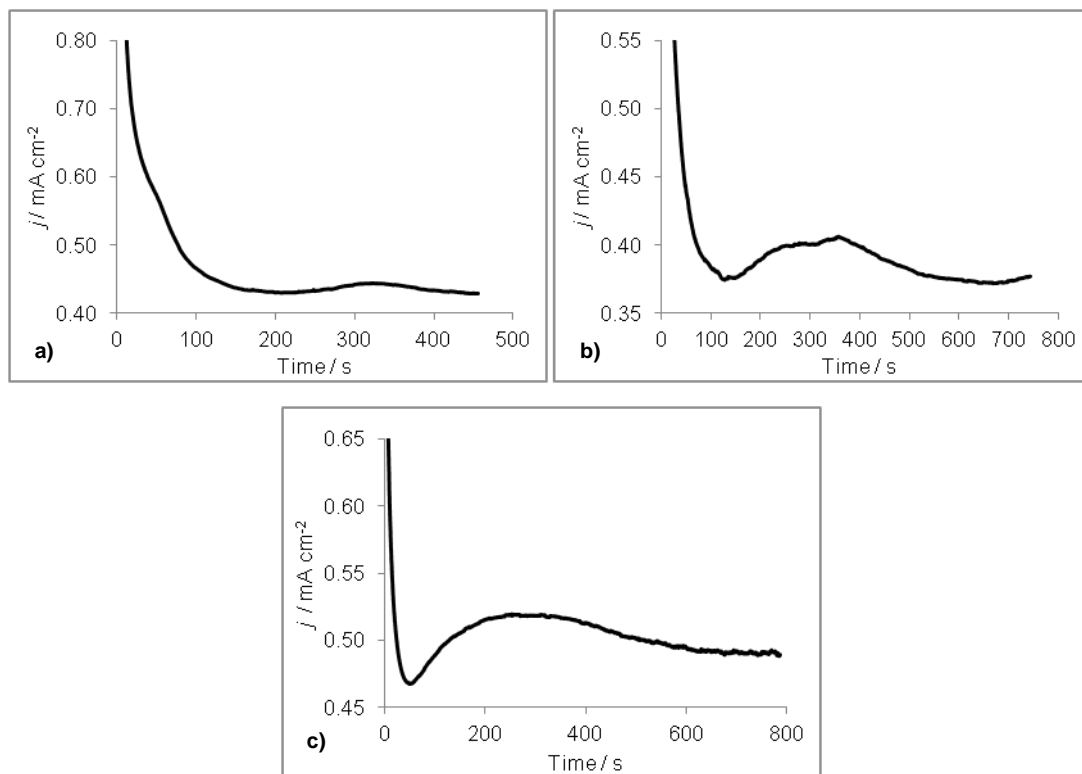


**Figure 3.24:** Current density - time plots of polypyrrole films polymerised on Au at an applied potential of 0.80 V vs. SCE to a charge density of  $400 \text{ mC cm}^{-2}$ , from an aqueous solution of 0.15 M pyrrole/ 0.20 M  $\text{Na}_2\text{HPO}_4$  and; a) 0.001 M  $\text{NaClO}_4$ , b) 0.001 M  $\text{KClO}_4$  and c) 0.001 M  $\text{LiClO}_4$ .

The  $j$ - $t$  profile for  $\text{NaClO}_4$  reaches a  $t_{0,j_0}$  point after 200 seconds, compared to 125 seconds for  $\text{KClO}_4$  and 50 seconds for  $\text{LiClO}_4$ . It is clear that the solution containing  $\text{LiClO}_4$  promotes the fastest nucleation. Similar to the  $j$ - $t$  profile observed for  $\text{LiBF}_4$ , the  $j$ - $t$  plot recorded for polymerisation in solutions containing  $\text{NaClO}_4$  exhibit a brief plateau after 30 seconds of polymerisation before continuing to decrease (Figure 3.24 a). A  $t_{max,j_{max}}$  point is not reached until approximately 320 seconds of polymerisation and only experiences a small increase in the current density. The SEM micrographs obtained of the PpyNW films show a “hills and valleys” morphology of narrow nanowires, of dramatically varying lengths (Figure 3.25 a-c). Long tapered nanowires are present in the “valleys” while much shorter nanowires of similar diameter are deposited on the “hills”. This may occur due to loss of adherence of the films, as the

hill morphology appears to occur as the film peels away from the substrate. This would reduce the conductivity of the film at these points, causing the propagation of the nanowires to cease. The  $j-t$  plot for films polymerised in the presence of  $\text{KClO}_4$  is shown in Figure 3.25 (b). It can be observed that there are two  $t_{max}, j_{max}$  points and the current density decreases rapidly after, before rising slightly during the last moments of the polymerisation. The films formed show long twisted nanowires (Figure 3.25 d-f), and the base layer deposited is similar in thickness to that of the PpyNW formed from aqueous solutions containing  $\text{LiClO}_4$  (Table 3.4).

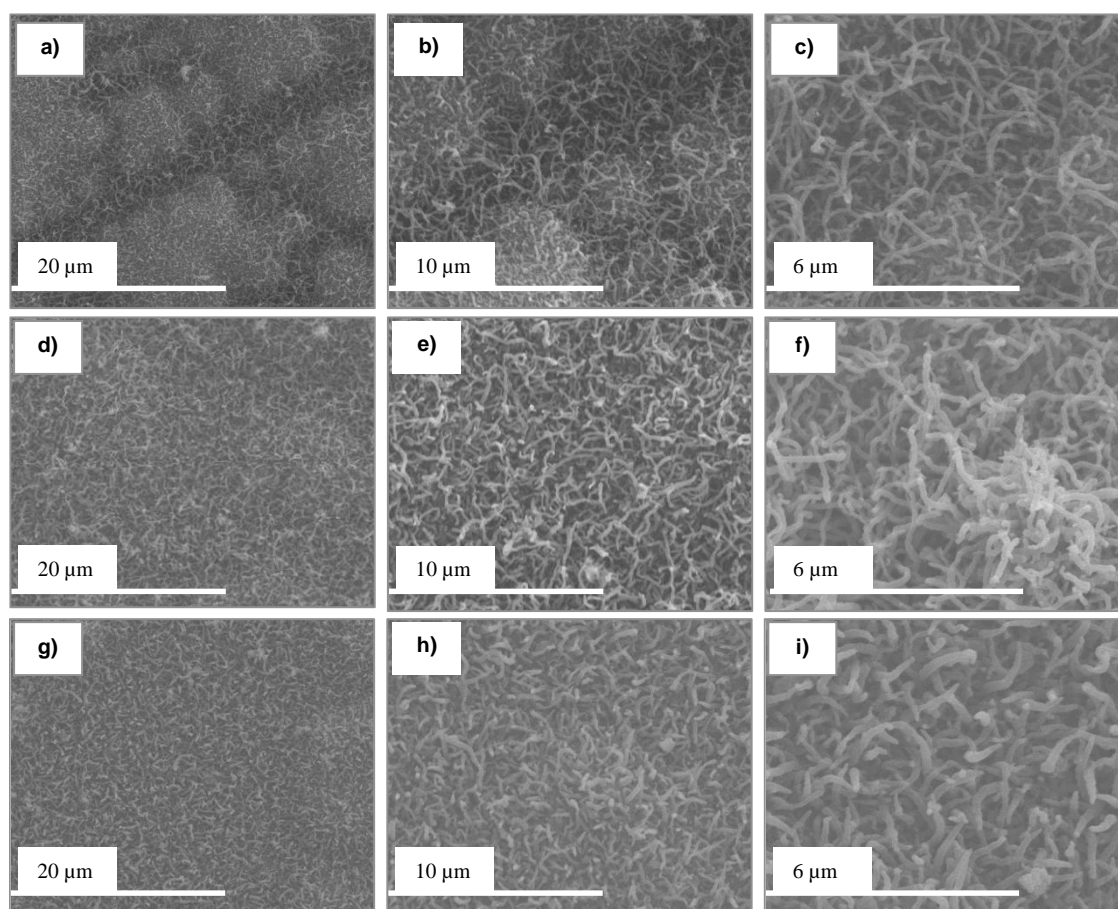


**Figure 3.25:** SEM micrographs (plan-view) of polypyrrole films polymerised at an applied potential of 0.80 V vs. SCE to a charge density of  $400 \text{ mC cm}^{-2}$ , from an aqueous solution of 0.15 M pyrrole/ 0.20 M  $\text{Na}_2\text{HPO}_4$  and; (a-c) 0.001 M  $\text{NaClO}_4$ , (d-f) 0.001 M  $\text{KClO}_4$  and (g-i) 0.001 M  $\text{LiClO}_4$ .

**Table 3.4: Average diameter, length and base layer thickness of polypyrrole films polymerised at an applied potential of 0.80 V vs. SCE to a charge density of 400 mC cm<sup>-2</sup>, from an aqueous solution of 0.15 M pyrrole/0.20 M Na<sub>2</sub>HPO<sub>4</sub> and the listed dopants, n = 20 (diameter), 10 (length and thickness).**

Electrolyte	Diameter / nm	Length / nm	Base Layer Thickness / nm
0.001 M LiClO <sub>4</sub>	122 ± 5	941 ± 56	406 ± 22
0.001 M NaClO <sub>4</sub>	111 ± 3	1520 ± 77 / 518 ± 28	323 ± 12
0.001 M KClO <sub>4</sub>	133 ± 7	1332 ± 137	405 ± 28

It can be observed that the seed electrolyte is crucial to the formation of polypyrrole films in the nanowire morphology, however, a number of salts with quite different physical characteristics have been demonstrated to act as a seed dopant. No correlation was found between the properties of the anion dopants and the morphology of the formed nanowires, which is contrary to the results observed for *N*-substituted polypyrrole nanowires.<sup>39</sup> However, the present study uses different polymerisation conditions. The difference in the *j-t* plots indicates that although the seed dopant is present in small amounts, it plays a significant role in the polymerisation process. Under the present conditions, it would appear that both LiTFSI and NaClO<sub>4</sub> result in the longest nanowires, with the thinnest base layer.

### 3.3.1.6 Investigation of the Polymer Base Layer

In order to examine the base layer of polymer which was deposited on the electrode surface, SEM micrographs were obtained of the cross section of each film. In addition to this, preliminary peel tests were carried out to examine the adhesion of the films to the electrode substrate. The adhesion was graded depending on how much of the polymer film remained on the electrode after a peel – off test was employed; 0 = no polymer remaining, 5 = completely adherent polymer. Figure 3.26 shows the cross-sectional SEM micrographs of PpyNW films formed in solutions of varying concentrations of LiClO<sub>4</sub>. It can be clearly seen in Figure 3.26 and in Table 3.5 that increasing the concentration of LiClO<sub>4</sub> results in the deposition of a thicker base layer of polypyrrole. It can also be seen in Figure 3.26 (a) that the “hills and valleys” morphology observed is a result of the polypyrrole film losing adherence with the surface. None of the polypyrrole nanowire films formed in the presence of LiClO<sub>4</sub> showed adherence when subjected to a peel off test.

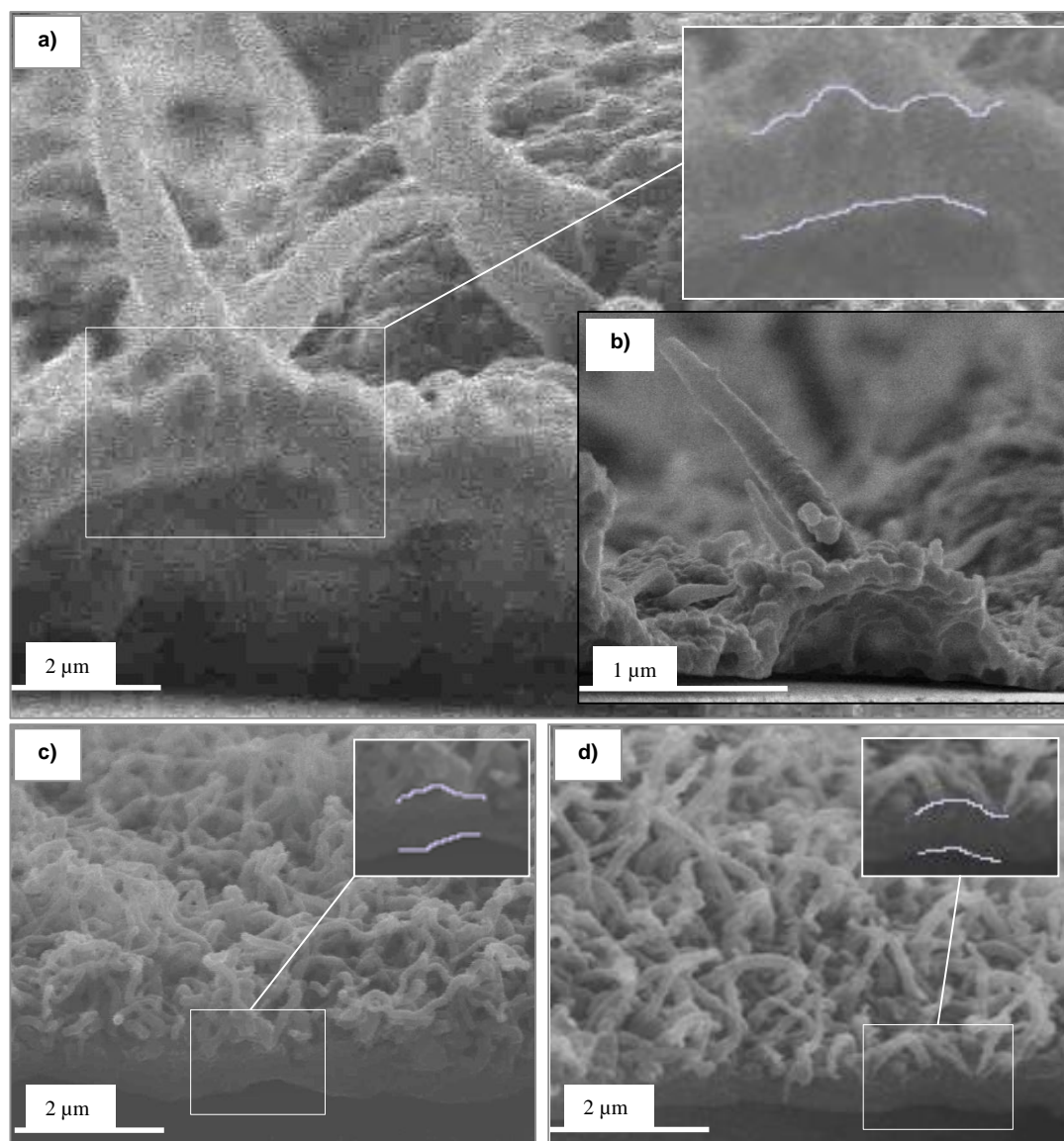


Figure 3.26: SEM micrographs (cross section) of polypyrrole films polymerised at an applied potential of 0.80 V vs. SCE to a charge density of  $400 \text{ mC cm}^{-2}$ , from an aqueous solution of 0.15 M pyrrole and; (a / b) 0.100 M  $\text{LiClO}_4$ , (c) 0.010 M  $\text{LiClO}_4$  / 0.20 M  $\text{Na}_2\text{HPO}_4$  and (d) 0.001 M  $\text{LiClO}_4$  / 0.20 M  $\text{Na}_2\text{HPO}_4$ . The inset in each image illustrates the thickness of the bulk base layer.

Table 3.5: Average base layer thickness of polypyrrole films polymerised at an applied potential of 0.80 V vs. SCE to a charge density of  $400 \text{ mC cm}^{-2}$ , from an aqueous solution of 0.15 M pyrrole and the listed concentration of  $\text{Na}_2\text{HPO}_4$  and  $\text{LiClO}_4$ ,  $n = 10$ . Also listed are the adhesion levels observed for each film.

Electrolyte	Base Layer Thickness / nm	Adhesion
0.10 M $\text{LiClO}_4$	$1244 \pm 56$	0
0.01 M $\text{LiClO}_4$ / 0.20 M $\text{Na}_2\text{HPO}_4$	$510 \pm 19$	0
0.001 M $\text{LiClO}_4$ / 0.20 M $\text{Na}_2\text{HPO}_4$	$406 \pm 22$	0

Table 3.6 lists the average base layer thickness and adhesion test scores of the polypyrrole nanowires polymerised from solutions containing different lithium and perchlorate salts. It can be clearly seen from the adhesion scores that films with the thinnest base layers display the greatest adherence. This is bolstered by SEM micrographs in Figure 3.27 in which it can be seen that films formed in solutions containing LiTFSI and NaClO<sub>4</sub> exhibit less of a gap between the base layer and the electrode substrate. This suggests that the thinner polymer base layers are less likely to lose adherence, forming the “hills and valley” morphology. Thus it would appear that NaClO<sub>4</sub> and LiTFSI are the best choice of seed electrolytes for the formation of polypyrrole nanowires. It would be expected that the increased adherence that they exhibit would lead to greater conductivity in the nanowire films, due to the increased contact of the base layer with the electrode surface.

**Table 3.6: Average base layer thickness of polypyrrole films polymerised at an applied potential of 0.80 V vs. SCE to a charge density of 400 mC cm<sup>-2</sup>, from an aqueous solution of 0.15 M pyrrole/ 0.20 M Na<sub>2</sub>HPO<sub>4</sub> and the dopant, n = 10. Also listed are the adhesion levels observed for each film.**

Dopant (0.001 M)	Base Layer Thickness / nm	Adhesion
LiClO <sub>4</sub>	406 ± 22	0
LiCl	392 ± 18	0
LiBF <sub>4</sub>	480 ± 38	0
LiTFSI	342 ± 33	3
NaClO <sub>4</sub>	323 ± 12	2
KClO <sub>4</sub>	405 ± 28	0

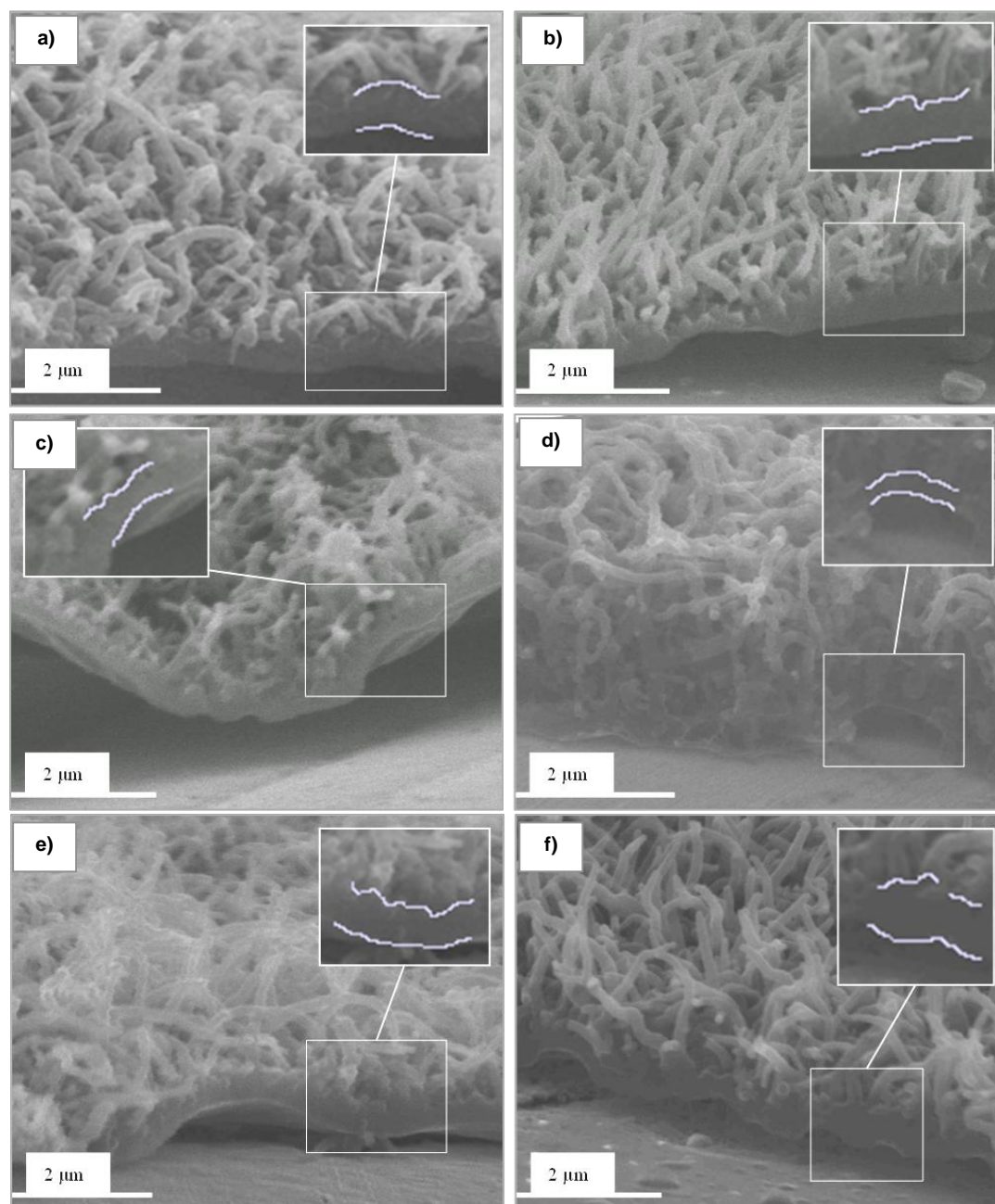


**Figure 3.27:** SEM micrographs (cross section) of polypyrrole films polymerised at an applied potential of 0.80 V vs. SCE to a charge density of 400 mC cm<sup>-2</sup>, from an aqueous solution of 0.15 M pyrrole/ 0.20 M Na<sub>2</sub>HPO<sub>4</sub> and; (a) 0.001 M LiClO<sub>4</sub>, b) 0.001 M LiCl, c) 0.001 M LiBF<sub>4</sub>, d) 0.001 M LiTFSI e) 0.001 M NaClO<sub>4</sub> and f) 0.001 M KClO<sub>4</sub>. The inset in each image illustrates the thickness of the bulk base layer.

### 3.3.2 Formation of Polypyrrole Nanowires Doped with an Immobile Dopant

The polypyrrole nanowires discussed in Section 3.3.1 are doped with relatively small and mobile dopant anions. These dopant anions are incorporated into the polymer film during oxidative polymerisation, to maintain the overall electroneutrality of the polymer. If a reduction potential is applied to the polypyrrole nanowires, the small and mobile dopant anions will be expelled from the polymer. When the polypyrrole is re-oxidised, mobile anions in the surrounding electrolyte solution will be uptaken to ensure polymer neutrality. In this way, polypyrrole films can be employed as ion exchange materials.<sup>42-45</sup> If however, the dopant anions are large and bulky, such as polystyrene sulfonate (PSS) or polyvinyl sulfonate (PVS), polymer entanglement and electrostatic interactions hinder the expulsion of the dopants from the polymer during the application of a reduction potential.<sup>46-48</sup> Therefore, electrochemical reduction of these films results in the incorporation of mobile cations from the surrounding electrolyte solution to balance out the positive charge on the polypyrrole backbone. As a result, polypyrrole films can be utilised as electrochemically controlled anion or cation exchange materials, depending on the size of dopant anion incorporated during polymerisation.<sup>49-51</sup>

The polymerisation of polypyrrole nanowires doped with a large immobile dopant was therefore attempted. The chosen dopant was *p*-sulfonatocalix[4]arene sodium salt (C4S), which displays high binding affinities for di- and trivalent metal cations and weak binding affinities for monovalent cations.<sup>52</sup> Impedance Spectroscopy (EIS) studies carried out by our group have shown that *p*-sulfonatocalix[4]arene acts as an immobile anionic dopant within the polypyrrole matrix.<sup>53</sup> A conventional gold electrode was placed in a solution of 0.15 M pyrrole, 0.20 M Na<sub>2</sub>HPO<sub>4</sub> and 0.001 M C4S, and a potential of 0.80 V vs. SCE was applied until a charge density of 400 mC cm<sup>-2</sup> was achieved. Figure 3.28 displays the *j-t* plot recorded during the experiment; however no polymer formation was discernible on the electrode surface. An alternative approach was therefore attempted in which the polypyrrole nanowires were polymerised from a solution of 0.15 M pyrrole, 0.20 M Na<sub>2</sub>HPO<sub>4</sub> and 0.001 M LiClO<sub>4</sub> and then a layer of polypyrrole doped with C4S (PpyC4S) was polymerised as a coating on the nanowires. Polypyrrole nanowires coated with a layer of polypyrrole–polystyrene sulfonate were also examined as a comparison. The ion exchange properties of the PpyC4S and

PpyPSS films are discussed in Chapter 4. To the best of our knowledge, this is the first example of the template-less electrochemical deposition of nanowires containing an immobile dopant.

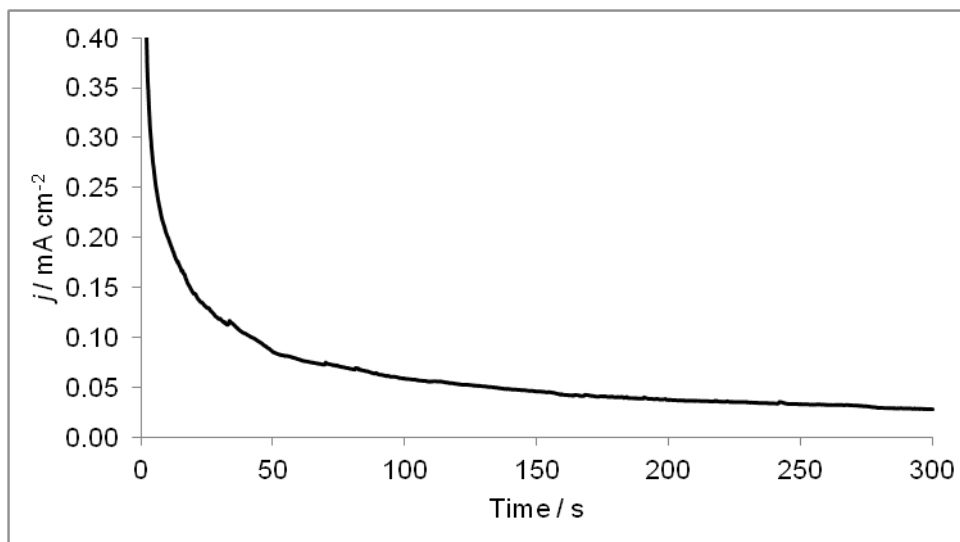


**Figure 3.28:** Current density - time plot of polypyrrole films polymerised on Au at an applied potential of 0.80 V vs. SCE to a charge density of 400 mC cm<sup>-2</sup>, from an aqueous solution of 0.15 M pyrrole, 0.20 M Na<sub>2</sub>HPO<sub>4</sub> and 0.001 M *p*-sulfonatocalix[4]arene sodium salt. An identical current-time plot is seen in Figure 3.19, in which polymerisation was attempted from a solution of 0.15 M and 0.20 M Na<sub>2</sub>HPO<sub>4</sub>.

### 3.3.2.1 Coating Polypyrrole Nanowires with PpyC4S and PpyPSS films

Polypyrrole nanowires were polymerised on a conventional gold electrode from a solution of 0.15 M pyrrole, 0.20 M Na<sub>2</sub>HPO<sub>4</sub> and 0.001 M LiClO<sub>4</sub>, at an applied potential of 0.80 V vs. SCE until a charge density of 300 mC cm<sup>-2</sup> was achieved. The films were thoroughly washed with deionised water before placing in a solution of 0.20 M pyrrole and 0.002 M *p*-sulfonatocalix[4]arene sodium salt. A potential of 0.55 V vs. SCE was applied until a charge density of either 74 mC cm<sup>-2</sup> or 150 mC cm<sup>-2</sup> was achieved. A typical *j-t* plot observed for the polymerisation of PpyC4S on the polypyrrole nanowires is shown in Figure 3.29. A short induction period is observed,<sup>54</sup> followed by an increase in the current density until it reaches a  $t_{max}, j_{max}$  point. The current density then decreases slightly before levelling out. The observed levelling out of the current density indicates that polymerisation is continuing in a unidirectional manner.<sup>55</sup>

In order to confirm that the C4S was incorporated into the polypyrrole film, energy-dispersive X-ray spectroscopy (EDX) was carried out as the sulfur in

*p*-sulfonatocalix[4]arene should be apparent. The PpyC4S film was polymerised at a platinum electrode surface and sputter coated with gold. The characteristic X-ray peak for sulfur is  $K_{\alpha} = 2.307$  keV. Unfortunately, one of the characteristic X-ray peaks for gold occurs at 2.120 keV. The X-ray peak for Pt which occurs at 2.048 keV should not overlap with the sulfur peak. Figure 3.30 displays the EDX spectrum obtained from the PpyNW film coated with PpyC4S. The gold and platinum peaks come from the gold sputter coating and the platinum electrode, respectively. The characteristic X-ray peak corresponding to sulfur is visible at 2.3 keV, which confirms that C4S is present.

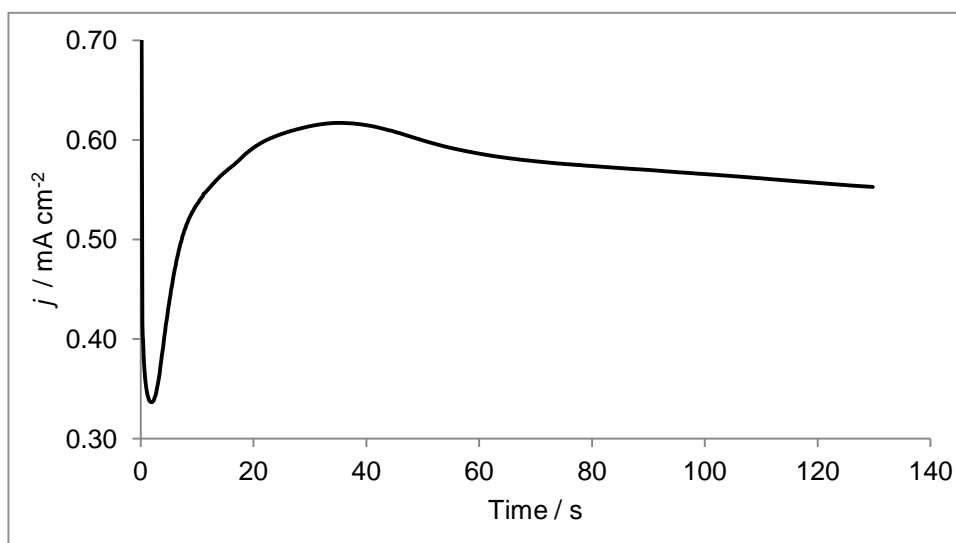


Figure 3.29: Current density - time plot of a PpyC4S film polymerised from an aqueous solution of 0.20 M pyrrole and 0.002 M C4S at an applied potential of 0.55 V vs. SCE to a charge density of  $74 \text{ mC cm}^{-2}$ , onto polypyrrole nanowires which were polymerised from an aqueous solution of 0.15 M pyrrole, 0.20 M  $\text{Na}_2\text{HPO}_4$  and 0.001 M  $\text{LiClO}_4$  at an applied potential of 0.80 V vs. SCE to a charge density of  $300 \text{ mC cm}^{-2}$ .

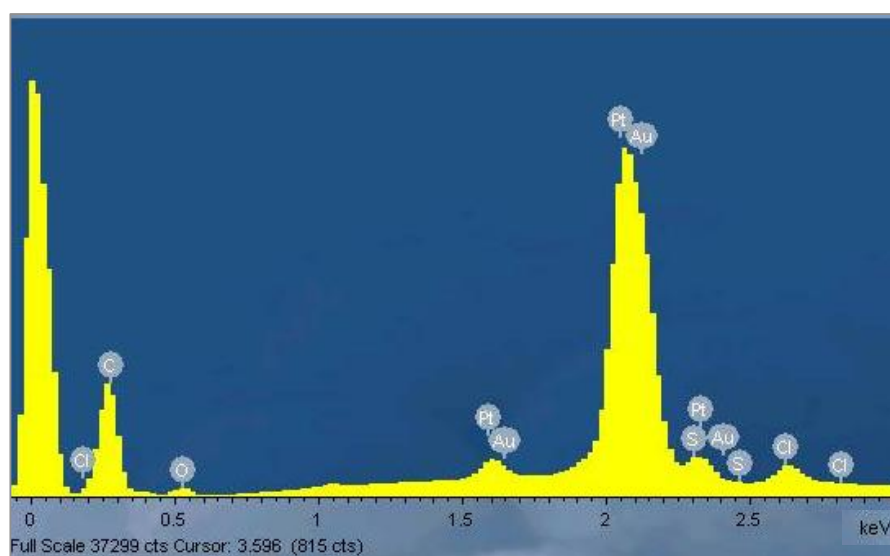
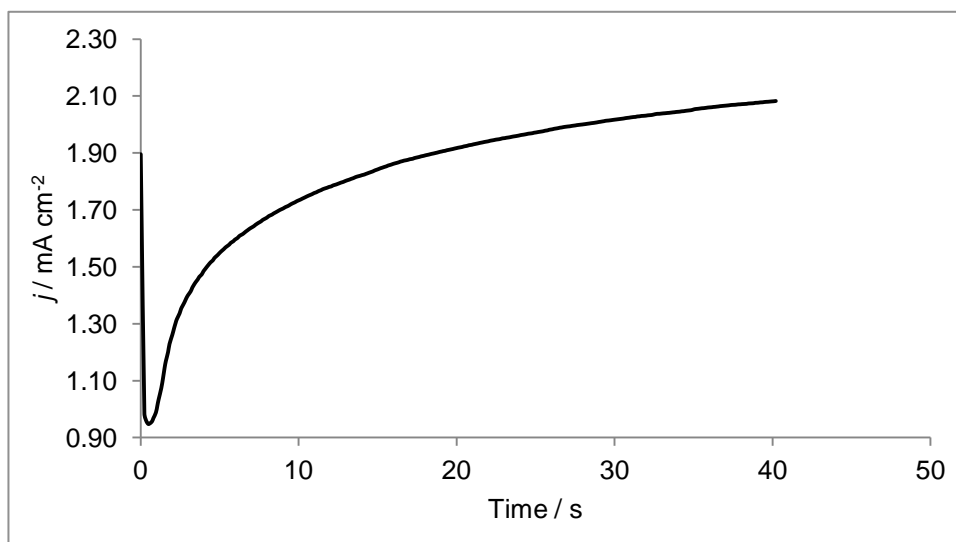


Figure 3.30: EDX spectrum of PpyC4S coated on a PpyNW film, polymerised on a platinum electrode.

The coating of the polypyrrole nanowires with a PpyPSS film was carried out in a similar manner to coating the PpyNW with a PpyC4S film. Polypyrrole nanowires were polymerised on a conventional gold electrode from a solution of 0.15 M pyrrole, 0.20 M  $\text{Na}_2\text{HPO}_4$  and 0.001 M  $\text{LiClO}_4$ , at an applied potential of 0.80 V vs. SCE until a charge density of  $300 \text{ mC cm}^{-2}$  was achieved. The films were thoroughly rinsed with water before placing in a solution of 0.20 M pyrrole and 0.05 M poly(sodium 4-styrenesulfonate). A potential of 0.60 V vs. SCE was applied until a charge density of  $74 \text{ mC cm}^{-2}$  was achieved. A typical  $j-t$  plot observed for the polymerisation of PpyPSS on the polypyrrole nanowires is shown in Figure 3.31. A short induction period is observed,<sup>54</sup> followed by an increase in the current density. The polymerisation time scale is much shorter than that observed for the polymerisation of PpyC4S film on polypyrrole nanowires and so a levelling out of the current density is not seen.

As with the PpyC4S coated polypyrrole nanowires, an experiment was also carried out using a platinum electrode so that EDX spectroscopy could be used to confirm the presence of sulfur from the PSS dopant incorporated into the polypyrrole film. The characteristic peak of  $K_\alpha = 2.307 \text{ keV}$  for sulfur was observed and the EDX spectrum obtained very closely resembles that seen in Figure 3.30.



**Figure 3.31:** Current density - time plot of a PpyPSS film polymerised from an aqueous solution of 0.20 M pyrrole and 0.05 M PSS at an applied potential of 0.60 V vs. SCE to a charge density of  $74 \text{ mC cm}^{-2}$ , onto polypyrrole nanowires which were polymerised from an aqueous solution of 0.15 M pyrrole, 0.20 M  $\text{Na}_2\text{HPO}_4$  and 0.001 M  $\text{LiClO}_4$  at an applied potential of 0.80 V vs. SCE to a charge density of  $300 \text{ mC cm}^{-2}$ .

### 3.3.2.2 SEM Characterisation of the PpyNW Coated with PpyC4S and PpyPSS Films

The PpyC4S coated polypyrrole nanowires and the PpyPSS coated polypyrrole nanowires were characterised using Scanning Electron Microscopy, Infra-red spectroscopy and Raman spectroscopy. Figure 3.32 depicts the SEM micrographs obtained of PpyNW coated with PpyC4S films to a charge density of  $150 \text{ mC cm}^{-2}$  or  $74 \text{ mC cm}^{-2}$ . It was determined that the average diameter of the PpyNW increases from approximately  $122 \pm 5 \text{ nm}$  to a diameter of  $224 \pm 8 \text{ nm}$  when coated with PpyC4S to a charge density of  $150 \text{ mC cm}^{-2}$ , and to a diameter of  $172 \pm 5 \text{ nm}$  when coated with PpyC4S to a charge density of  $74 \text{ mC cm}^{-2}$ . This difference in nanowire diameter can be clearly seen in Figure 3.32 (b/d/f), in which clearly defined and individual nanowires are apparent for PpyNW coated with PpyC4S to a charge density of  $74 \text{ mC cm}^{-2}$ . The PpyNW coated with PpyC4S to a charge of  $150 \text{ mC cm}^{-2}$  increase in diameter to the extent that the individual nanowires begin to overlap, with polymer forming in the spaces between them (Figure 3.32 a/c/e). This causes the nanowires to lose definition. It can also be observed that the surface of the coated PpyNW has a much rougher texture than the uncoated PpyNW (Figure 3.21 g-i). This surface roughness is comparable to the cauliflower morphology which is characteristic of bulk polypyrrole, and will only serve to further increase the surface area of the polypyrrole nanowires. SEM micrographs of PpyNW coated with a PpyPSS film to a charge density of  $74 \text{ mC cm}^{-2}$  were also obtained and are presented in Figure 3.33. Similar to the PpyNW coated with a thin film of PpyC4S ( $74 \text{ mC cm}^{-2}$ ), the PpyPSS coated nanowires retain their definition and merging of the individual nanowires is not visible. The surface of the Ppy-PSS coated nanowires is also rougher and more textured than the uncoated polypyrrole nanowires.

The characterisation of the PpyC4S and PpyPSS coated PpyNW will be further discussed in Section 3.3.3.

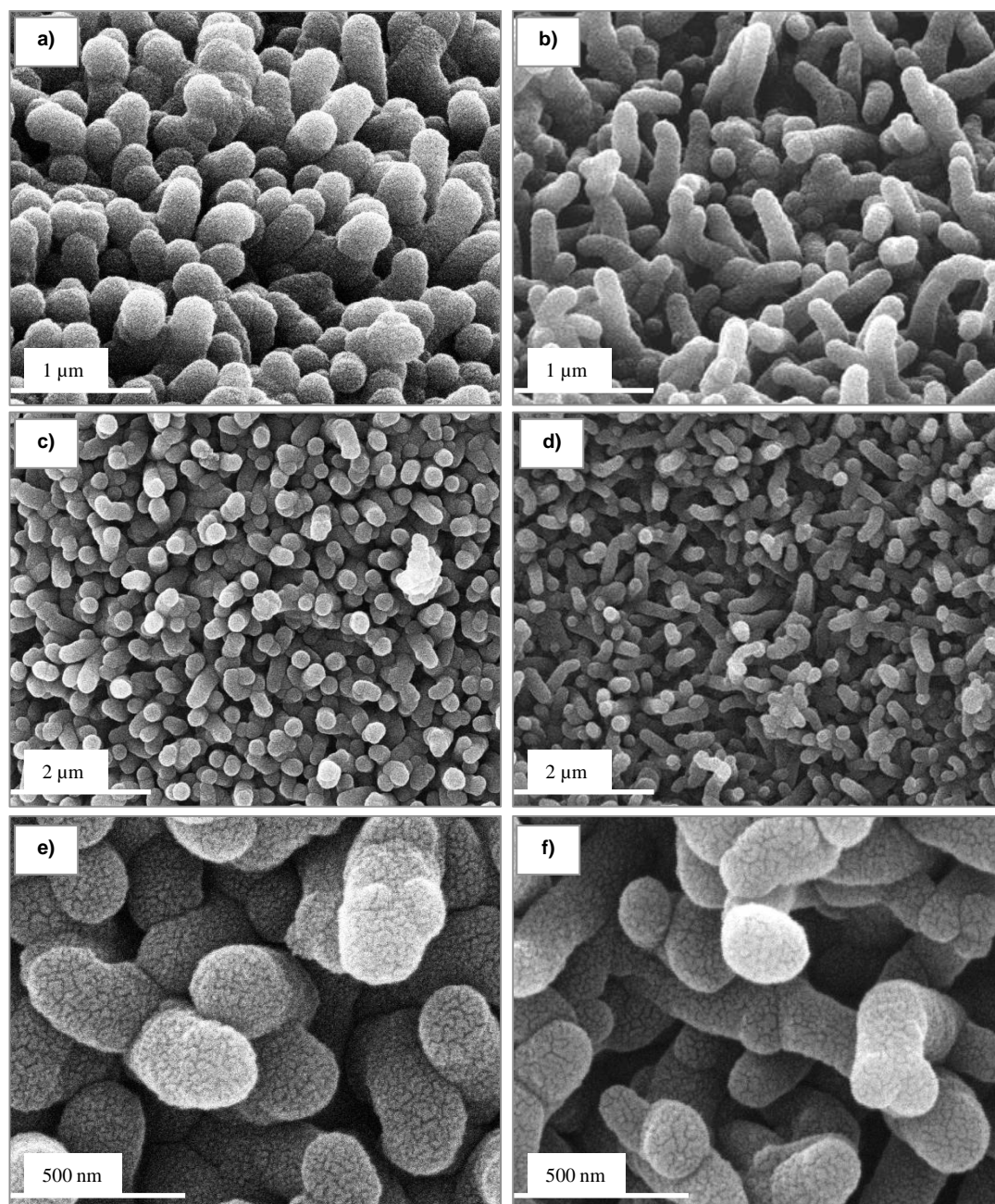


**Figure 3.32:** SEM micrographs of PpyNW coated with Ppy-C4S films to a charge density of  $150 \text{ mC cm}^{-2}$  (a/c/e) or  $74 \text{ mC cm}^{-2}$  (b/d/f). Micrographs a and b show an oblique-angle view of the films, while micrographs c-f show a plan-view at increasing magnifications.

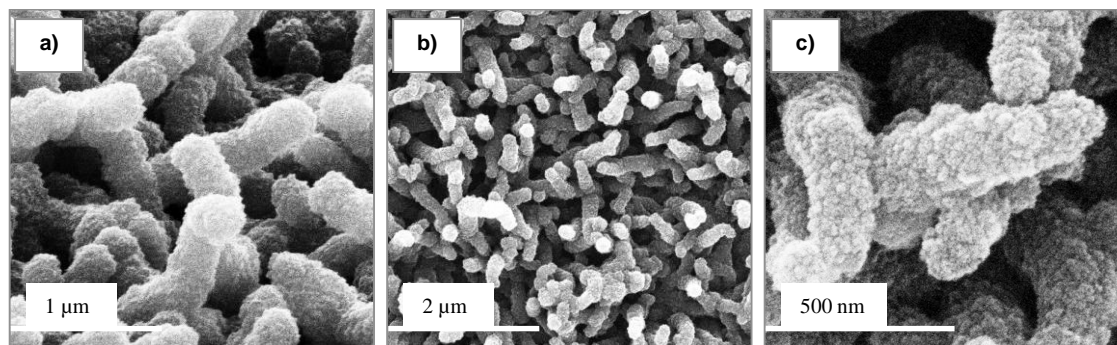


Figure 3.33: SEM micrographs of PpyNW coated with Ppy-PSS films to a charge density of  $74 \text{ mC cm}^{-2}$ . Micrograph a shows an oblique-angle view of the films, while micrographs b and c show a plan-view at increasing magnifications.

### 3.3.3 Characterisation of Polypyrrole Nanowires

Two spectroscopic techniques were employed to characterise the polypyrrole nanowire films, the applications of which are described in Chapters 4 and 5. This section details the results of FTIR and Raman spectroscopy which were used to characterise the PpyNW in both their non-reduced and reduced form; PpyC4S coated PpyNW and PpyPSS coated PpyNW. As comparison, PpyCl films in the bulk morphology were also characterised. Water contact angle measurements were also carried out to examine the surface wetting of the polypyrrole materials.

#### 3.3.3.1 Infrared Spectroscopy

The samples for FTIR spectroscopic analysis were polymerised on a conventional gold electrode, removed, ground into KBr and pressed into disks in a high pressure clamp. The main bands observed for PpyCl, PpyNW non-reduced and PpyNW reduced are tabulated and assigned in Table 3.7. The corresponding spectra can be seen in Figure 3.34. The bands at  $1526\text{ cm}^{-1}$  and  $1463\text{ cm}^{-1}$  in the FTIR spectrum of PpyCl are characteristic of the pyrrole ring fundamental stretches. It can be observed that the band at  $1526\text{ cm}^{-1}$  shifts to higher frequencies in the spectra of PpyNW. Tian and Zerbi noted that a shift in wavenumber and band intensity can indicate the extent of  $\pi$ -electron delocalisation in the polypyrrole chains.<sup>56, 57</sup> This may indicate that nanowires have a shorter conjugated chain length.<sup>58</sup> The ratios of the integrated areas of the peaks centred at  $1526\text{ cm}^{-1}$  and  $1463\text{ cm}^{-1}$  have also been used in the literature to determine the  $\pi$ -conjugation length of polypyrrole nanotubes.<sup>10, 59</sup> This technique was not employed in this study as the intensity of the bands at  $1465\text{ cm}^{-1}$  is not sufficient for analysis. However, it can be observed that the intensity of the peak centred at  $1465\text{ cm}^{-1}$  is greater in the spectra of the reduced PpyNW. This is in keeping with the spectra observed by Kim *et al.*, who attributed this increase to the shortening of the effective-conjugation length of the PpyNW after the nanowires were reduced.<sup>59</sup> The reduction step causes the film to become de-doped, so this ratio could also be used to indicate the degree of doping of the polypyrrole films.<sup>60</sup>

It can also be noted that a band occurs at  $1695\text{ cm}^{-1}$  in the spectra of the PpyNW films, which is absent in the spectrum of PpyCl. This can be attributed to a carbonyl stretching vibration, which is due to the incorporation of carbonyl groups at the  $\beta$ -position of the pyrrole ring when the polymer is over-oxidised. This band is often observed in the FTIR

spectra of overoxidised polypyrrole films.<sup>60-62</sup> The incorporation of carbonyl groups may cause disruption in the conjugation of the polymer chains, which results in the PpyNW exhibiting a lower conductivity.<sup>63</sup>

**Table 3.7: Position and assignment of adsorption bands for PpyNW reduced and non-reduced, compared to PpyCl. Assignments made based on literature values.**<sup>61, 62, 64-68</sup>

PpyCl	Band Positions / $\text{cm}^{-1}$		Assignments
	PpyNW non-reduced	PpyNW reduced	
1526	1538	1545	C=C/C-C stretch of Ppy ring
1463	1465	1465	C-N stretch of Ppy ring
1280	1276	1276	=C-H in plane deformation
1163	1121	1190	C-N stretching vibration
1030	1038	1039	C-H/N-H in plane stretch
889/771	914/781	928/779	C-H out of plane ring deformation
-	1695	1693	Carbonyl stretching vibration

The FTIR spectra obtained for PpyNW films coated with PpyC4S and PpyPSS are shown in Figures 3.35 and 3.36. For comparison purposes the FTIR of C4S and PSS, as well as uncoated PpyNW, are displayed. The FTIR spectrum of C4S is in keeping with that seen in the literature,<sup>69</sup> but to ensure that the dopant was successfully incorporated by the polypyrrole coating on the PpyNW, the bands at  $1170 \text{ cm}^{-1}$  and  $1034 \text{ cm}^{-1}$  were investigated. These bands are attributed to the asymmetric and symmetric stretching vibrations of the  $\text{SO}_3^-$  moiety. The FTIR spectrum of PpyC4S coated nanowires clearly indicates the presence of these bands, and in comparison to the spectrum of the uncoated nanowires, it can be seen that the band at  $1038 \text{ cm}^{-1}$  has shifted and increased greatly in intensity, which shows that it is due to the S=O stretch rather than the C-H/N-H in plane stretch of the polypyrrole.

It can also be seen that the FTIR spectrum of PSS is in keeping with that observed in the literature.<sup>70</sup> Its characteristic bands at  $1184 \text{ cm}^{-1}$  and  $1038 \text{ cm}^{-1}$  are assigned to the asymmetric and symmetric stretching vibrations of the  $\text{SO}_3^-$  group, while the band at  $1128 \text{ cm}^{-1}$  can be attributed to the in-plane skeleton vibration of the benzene ring.<sup>70, 71</sup>

This band is not visible in the spectrum of the PpyPSS coated PpyNW, but the two bands attributed to the  $\text{SO}_3^-$  group are clearly visible at  $1174\text{ cm}^{-1}$  and  $1032\text{ cm}^{-1}$ , and as with the PpyC4S coated PpyNW, the intensity of the band at  $1032\text{ cm}^{-1}$  confirms that it arises from the presence of PSS in the polymer coating. A peak at  $\sim 1695\text{ cm}^{-1}$  is visible in both the spectrum of PpyC4S coated PpyNW and the spectrum of PpyPSS coated nanowires, which is attributed to the presence of carbonyl groups due to over oxidation of the polypyrrole.

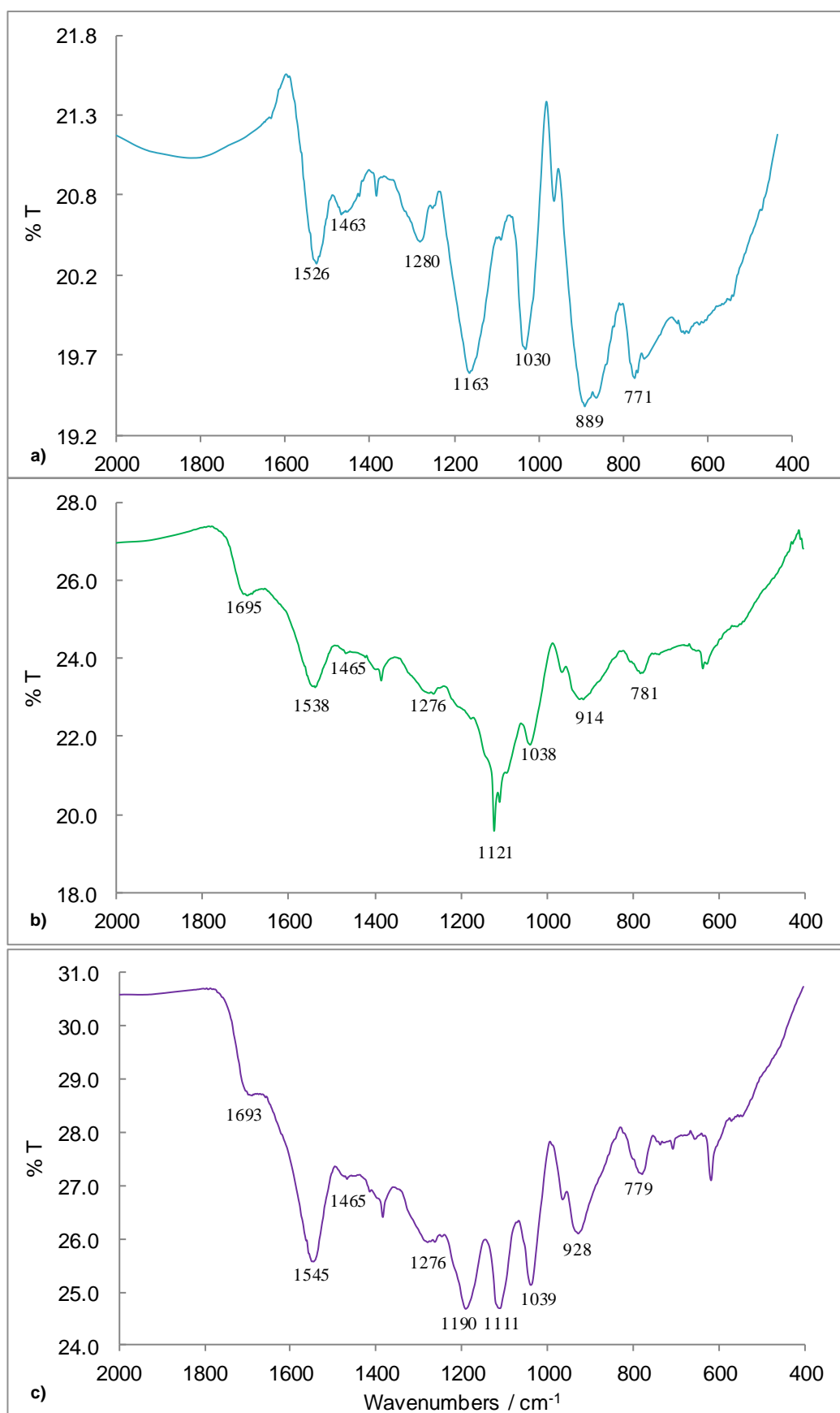


**Figure 3.34: FTIR Spectrum of a) PpyCl (—), b) PpyNW non-reduced (—) and c) Reduced PpyNW (—) in KBr and polymerised as described in Section 2.2.5.1.**

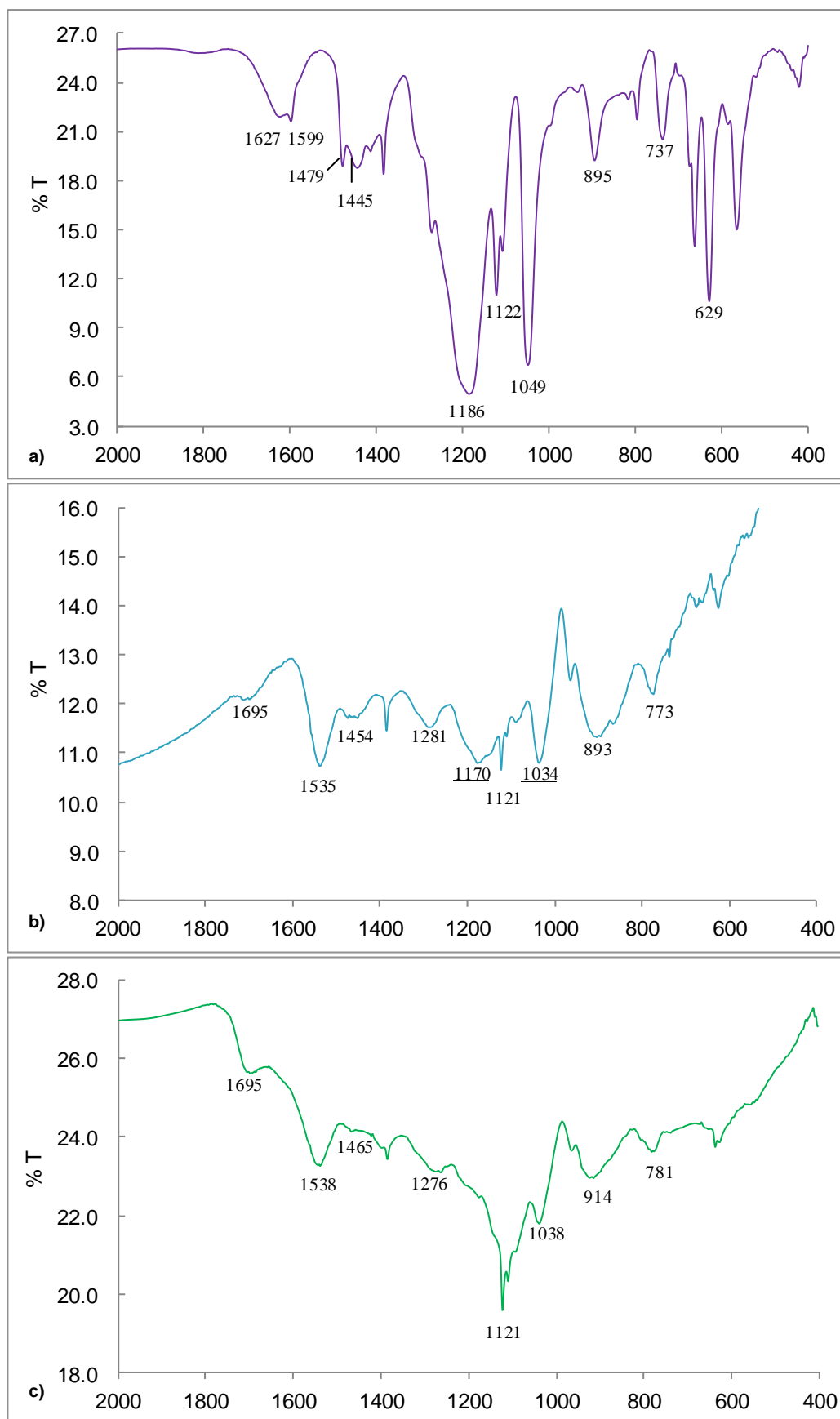


Figure 3.35: FTIR Spectrum of a) *p*-sulfonatocalix[4]arene sodium salt(—), b) PpyNW coated with PpyC4S (—) and c) PpyNW (—) in KBr and polymerised as described in Section 2.2.5.1.

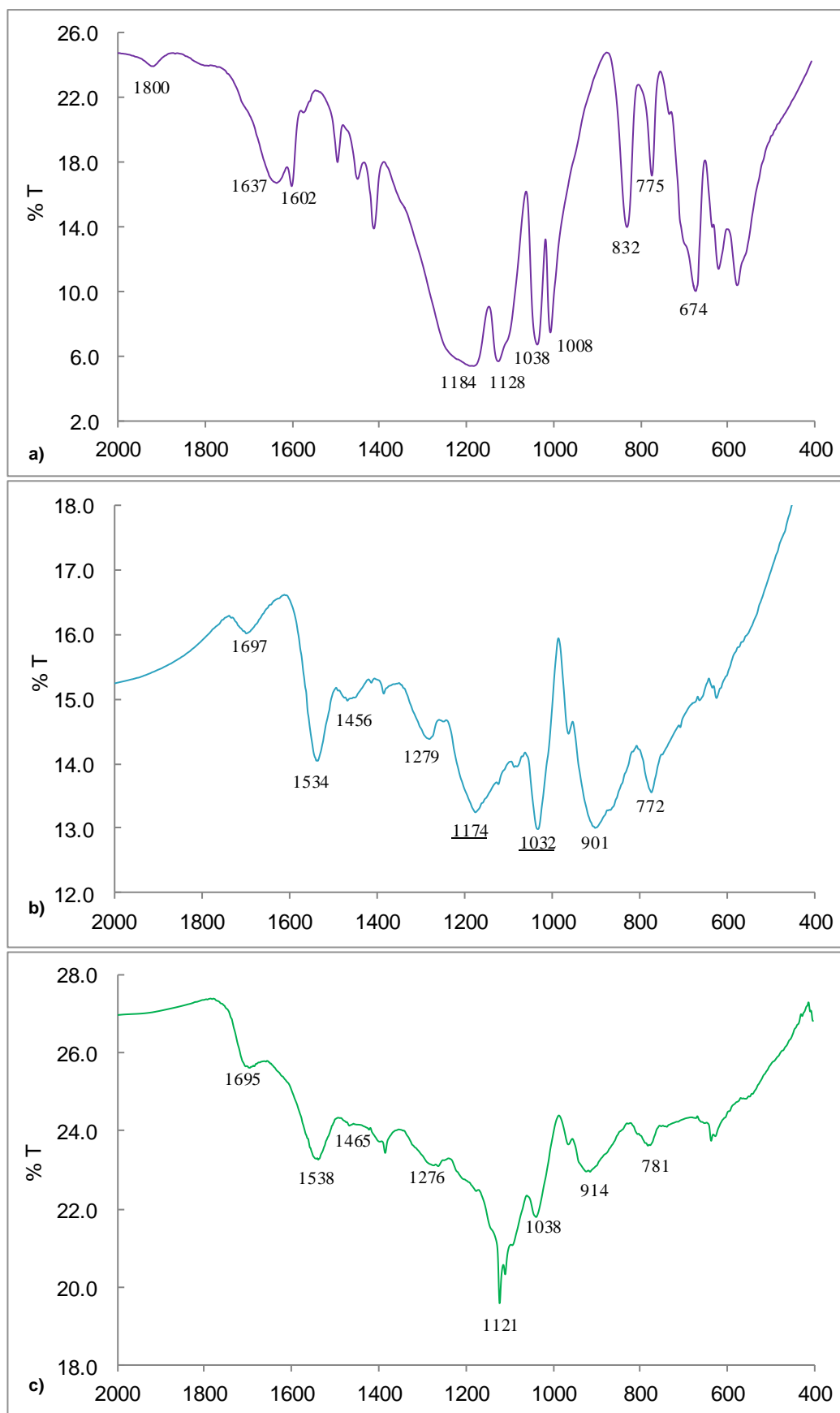


Figure 3.36: FTIR Spectrum of a) poly(sodium 4-styrenesulfonate) (—), b) PpyNW coated with PpyPSS (—) and c) PpyNW (—) in KBr and polymerised as described in Section 2.2.5.1.

### 3.3.3.2 Raman Spectroscopy

The polymer materials and their associated starting materials were made into KBr disks for analysis with Raman spectroscopy, except for p-sulfonatocalix[4]arene sodium salt and LiClO<sub>4</sub> which were analysed in powder form. Raman spectroscopy is an important technique for gaining structural information on the polypyrrole and there are extensive reports on applying it to this polymer.<sup>66, 72, 73</sup> However, the relative intensity of the Raman signals is dependent on a number of factors, one of which is the laser wavelength, due to resonance effects. The UV-Vis spectrum of polypyrrole is well known to depend on its oxidation state and this forms the basis of its much studied electrochromic properties.<sup>74, 75</sup> In the present study a laser wavelength of 660 nm was the only laser wavelength employed. It would be expected that this line would lie to the low energy side of the absorption band associated with the polaron and the high energy side of the band associated with the bipolaron.<sup>74</sup> Therefore the band arising from the C=C stretch of polaron species might be expected to be resonantly enhanced and this band would decrease in intensity relative to that of the bipolaron if a longer laser wavelength was employed. Cassidy *et al.* found that bands associated with radical cation species dominate Raman spectra recorded of polypyrrole doped with dodecylbenzenesulfonate obtained at 632 nm laser line, as they are fully resonant at this wavelength.<sup>76</sup> In addition to the complications associated with the intensity of the Raman bands the positions of individual Raman bands can depend on factors such as the oxidation state,<sup>76</sup> the thickness of the polymer and the identity of the dopant.<sup>77</sup> Therefore, it can be difficult to make definitive assignments and conclusions about the structure of the polymers on the basis of a single experiment carried out at one laser wavelength. However, tentative assignments were made and the main bands observed for PpyCl, PpyNW non-reduced and PpyNW reduced are tabulated and assigned in Table 3.8. The corresponding spectra are shown in Figure 3.37. The bands seen for each polymer are comparable to those commonly reported in the literature for polypyrrole.<sup>66, 72, 73</sup> The bands observed can give information on the oxidation state, doping levels and conjugation length within the polymer. The ratio of the C=C band (at *ca.* 1580 cm<sup>-1</sup>) and the skeletal band at (*ca.* 1500 cm<sup>-1</sup>) can be used to determine the relative conjugation length of the polymer chains.<sup>78</sup> This analysis was not carried out in this study as in most cases the skeletal band was not clearly resolved.

The band which appears at *ca.* 1580  $\text{cm}^{-1}$  is assigned as arising from the C=C stretch of both the polaron (*ca.* 1570 - 1590  $\text{cm}^{-1}$ ) and bipolaron species (*ca.* 1610 – 1620  $\text{cm}^{-1}$ ).<sup>76</sup> <sup>79</sup> This band appeared at 1570, 1585 and 1580  $\text{cm}^{-1}$  in the spectra recorded of bulk PPyCl, PpyNW non-reduced and PpyNW reduced respectively. In addition this band was significantly broader in the spectrum recorded of the bulk polymer compared to those of the nanowire analogues. This shift in band position and sharpening of the band (*ca.* 1580 – 1585  $\text{cm}^{-1}$ ) for the polypyrrole in the nanowire morphology is probably indicative of disorder in this polymer.<sup>80</sup> Moreover, the shift of the C=C band to higher wavenumbers has also been observed for oxidised polypyrrole films, indicating structural changes.<sup>78</sup> Thus it would be incorrect to definitively state that the reduced PpyNW are more conductive than the non-reduced PpyNW as the difference seen between them may also be due to the oxidation state of the polypyrrole film. Although the C=C stretching band appeared at the lowest wavenumber for the bulk polymer it is likely that this polymer actually contains the most bipolaron content. Evidence for this comes from the position of the band which is assigned to the ring deformation. This band appears at 920  $\text{cm}^{-1}$  for the bulk polymer and at 940  $\text{cm}^{-1}$  for both PpyNW. Spectroelectrochemical studies show that this band clearly shifts to lower wavenumbers as the polymer becomes more oxidised.<sup>79</sup>

The bands at 984  $\text{cm}^{-1}$  and 1043  $\text{cm}^{-1}$  arise due to C-H bending and ring deformations due to the radical cation (polaron) and the bands at 940  $\text{cm}^{-1}$  and 1081  $\text{cm}^{-1}$  are due to the dication (bipolaron). Thus, these bands are often used to provide information on the levels of polaron and bipolaron species in the polymer. When bipolarons are the main charge carriers, high levels of conductivity are observed.<sup>81</sup> It can be observed in Figure 3.37 (b and c), that the 984  $\text{cm}^{-1}$  and 1043  $\text{cm}^{-1}$  bands due to the radical cation are more intense than the 940  $\text{cm}^{-1}$  and 1081  $\text{cm}^{-1}$  dication bands for the PpyNW films. This suggests that the polaron is the primary charge carrier in the PpyNW films. The presence of polarons as the main charge carriers would explain the lower conductivity indicated for polypyrrole nanowires by impedance measurements carried out by another member of the research group. The bands observed in the spectrum of the reduced PpyNW are sharper due to the de-doping of the film that occurs during its reduction in sulfuric acid.<sup>59</sup> The signal-to-noise ratio in the spectrum of the PpyCl film may preclude the identification of these bands as the signals are poorly resolved. The bands visible at 920  $\text{cm}^{-1}$  and 1100  $\text{cm}^{-1}$  may be due to dication C-H bending and ring deformation and,

as discussed above, may indicate a greater amount of bipolaron content in the bulk polymer compare to the nanowires.

**Table 3.8: Position and assignment of Raman bands for PpyNW reduced and non-reduced, compared to PpyCl. Assignments made based on literature values.**<sup>72, 78</sup>

PpyCl	Band Positions / $\text{cm}^{-1}$		Assignments
	PpyNW non-reduced	PpyNW reduced	
650	645	647	C-C ring torsional
735	728	725	C-H wagging
810	810	845	C-H wagging
	907	886	C-C ring deformation
920	940	940	Ring deformation Dication
990	984	981	Ring deformation Cation
	1043	1040	C-H in plane bending Cation
1100	1081	1083	C-H in plane bending Dication
	1246	1254	C-H in plane bending
1320	1310	1310	Ring stretching
1380	1385	1393	Ring stretching
	1500	1495	Skeletal band
1570	1585	1575	C=C in ring stretch
	1712	1714	C=C stretch

Figure 3.38 shows the Raman spectra obtained for PpyNW coated with PpyC4S and PpyPSS, compared to the spectra for non-reduced PpyNW. It can be observed that the main spectral bands for polypyrrole are present. The C=C band at  $1585 \text{ cm}^{-1}$  has shifted to slightly lower wavenumbers when the PpyNW are coated, which suggests a greater conjugation length in the coated PpyNW films. A band at  $1717 \text{ cm}^{-1}/ 1712 \text{ cm}^{-1}$  is also visible, due to over-oxidation of the polymer. These observations are in keeping with the conclusions drawn from the FTIR spectra obtained for the same films.

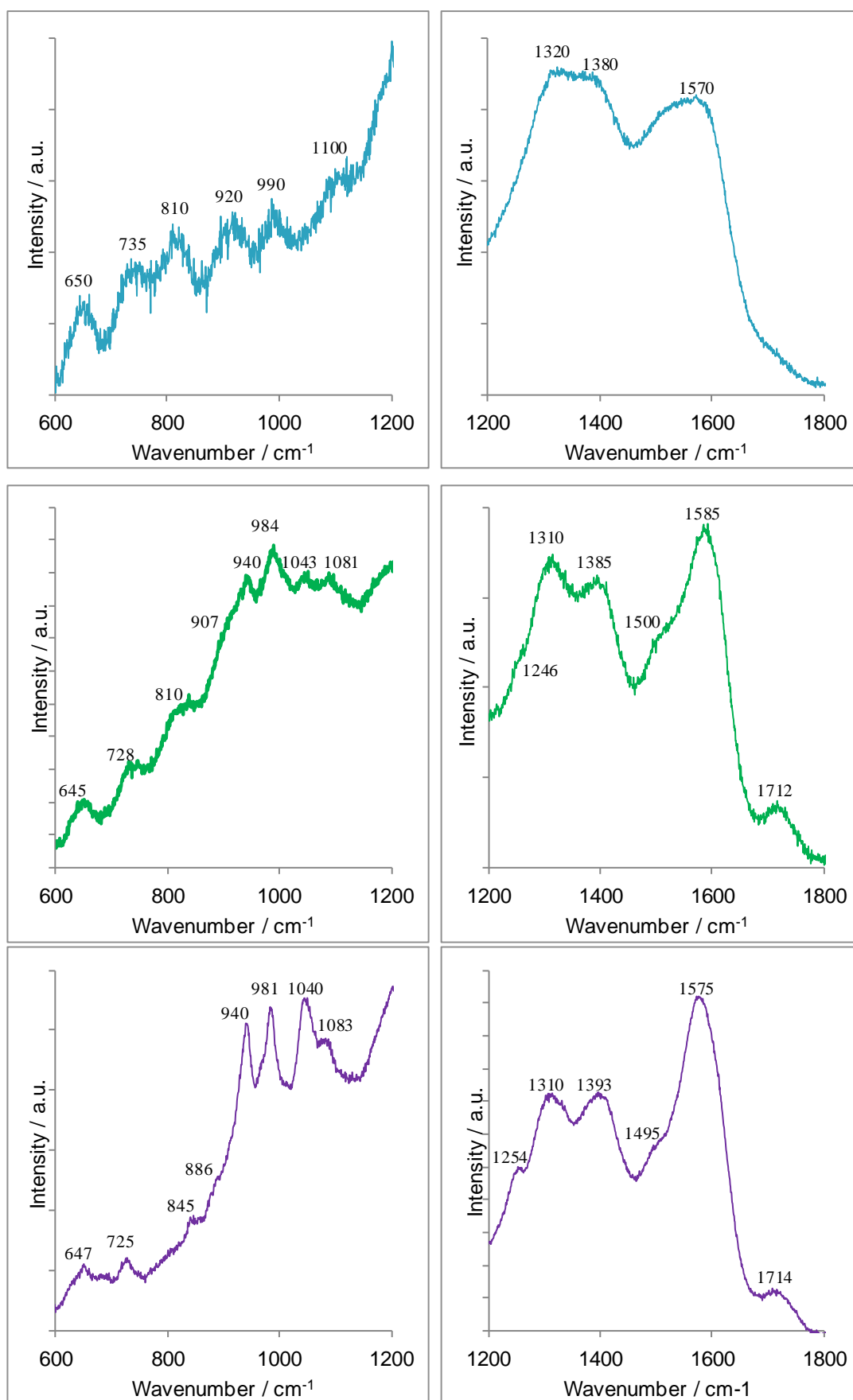


Figure 3.37: Raman Spectra in the low (left) and high (right) wavenumber regions at 660 nm of a) PpyCl (—), b) PpyNW non-reduced (—) and c) Reduced PpyNW (—) in KBr.

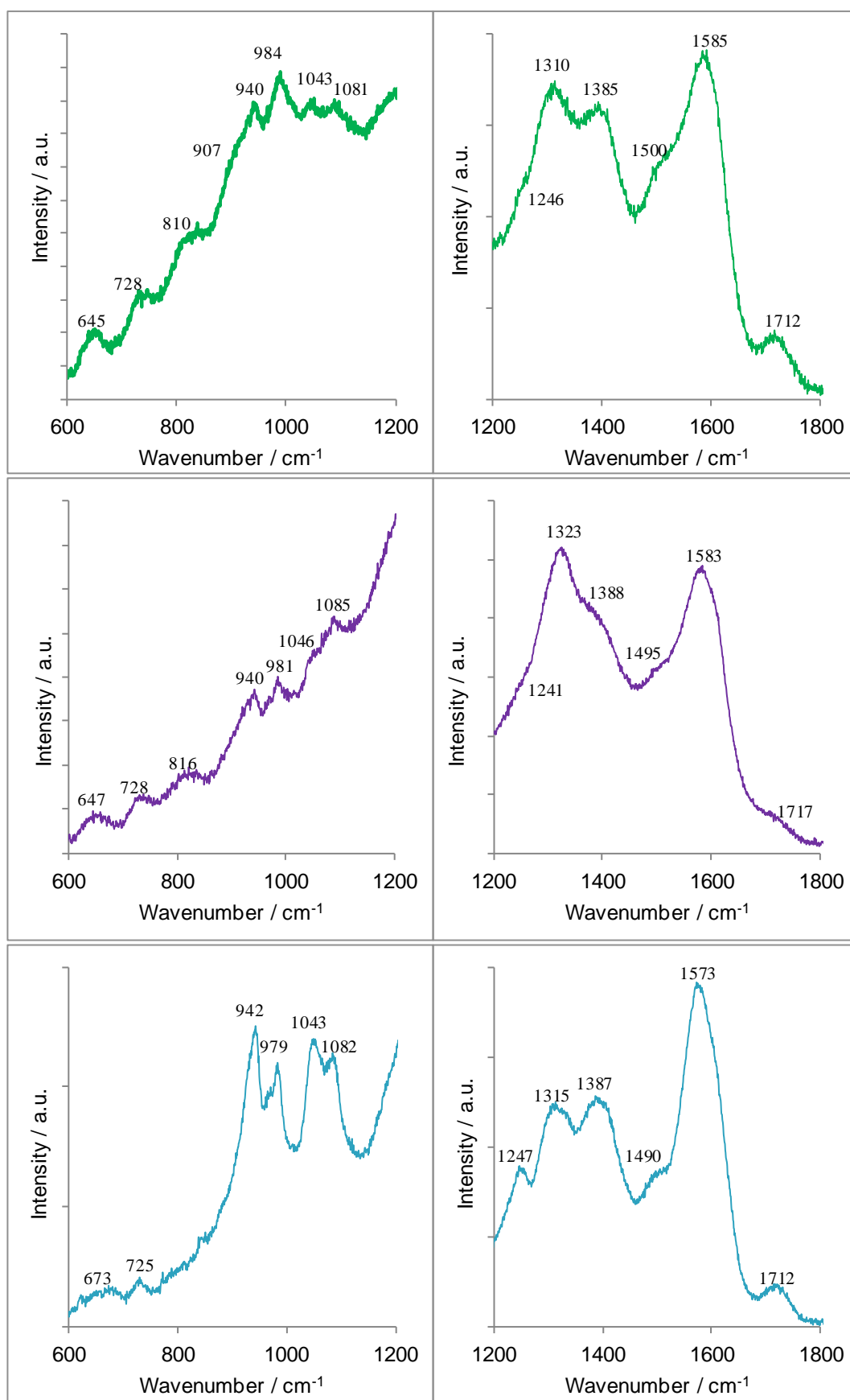


Figure 3.38: Raman Spectra in the low (left) and high (right) wavenumber regions at 660 nm of a) PpyNW non-reduced (—), b) PpyNW coated with PpyC4S (—) and c) PpyNW coated with PpyPSS (—) in KBr.

### 3.3.3.3 Water Contact Angle

The static sessile drop technique was employed to determine the water contact angle of PpyNW, PpyNW coated with PpyC4S or PpyPSS and PpyCl films. A surface is deemed hydrophilic when the water contact angle is less than  $90^\circ$  and hydrophobic when it is greater than  $90^\circ$ . Materials with water contact angles between  $150^\circ$  and  $180^\circ$  are called superhydrophobic, while materials with water contact angles below  $50^\circ$  are deemed superhydrophilic.

It can be seen in Figures 3.39 and 3.40 that the PpyPSS coated PpyNW films are superhydrophilic with a contact angle of  $46.2 \pm 2.5^\circ$ . This is due to the free charges from the exposed PSS chains.<sup>82</sup> The PpyNW films display similar contact angle measurements, which are lower than those exhibited by the PpyCl films. This was unexpected as it is thought that increasing surface roughness and the formation of hierarchical structures can increase the water contact angle.<sup>83</sup> This may indicate that the surface of the nanowires tested was smoother than the cauliflower morphology of the PpyCl films. The water contact angle exhibited by the PpyCl is in keeping with values observed in the literature.<sup>84</sup> The PpyC4S coated PpyNW are less hydrophilic than the PpyNW and PpyCl films. This can be attributed to the rougher surface of the PpyC4S coated PpyNW as seen in Figure 3.32.

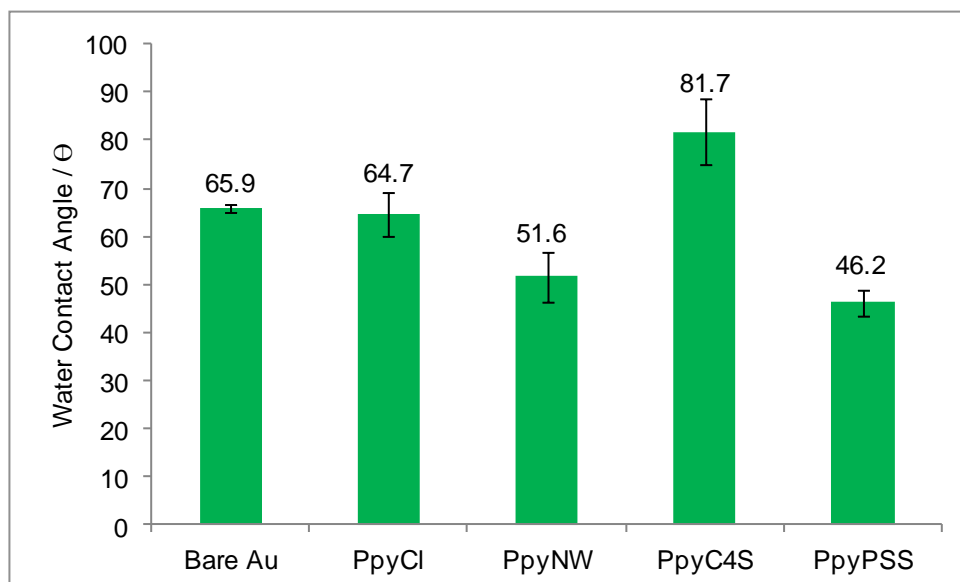


Figure 3.39: Water contact angles for polymers formed on conventional gold electrodes as described in Section 2.2.5.1.

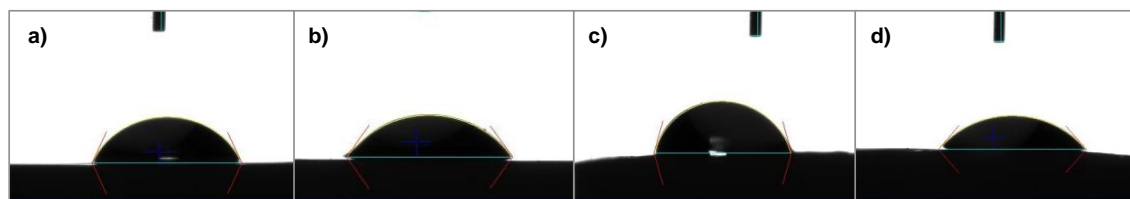


Figure 3.40: Water droplets on a) PpyCl, b) PpyNW, c) PpyC4S coated PpyNW and d) PpyPSS coated PpyNW.

### 3.3.4 Polymerisation of PpyNW on a Porous Membrane

In the previous sections it was established that polypyrrole nanowires could be electrochemically formed on conventional electrodes and that a coating of polypyrrole doped with an immobile dopant could be applied to the pre-formed polypyrrole nanowires. The applications of both the PpyNW and the coated PpyNW for the removal of heavy metals from solution will be discussed in Chapters 4 and 5. In order to maximise the potential of the nanowires for use in water treatment, it was decided to coat them on micro-porous polyamide membranes (pore size  $\sim 0.8 \mu\text{m}$ ), through which water could then be filtered. In order to make the polyamide membranes conducting, such that they could be utilised as the working electrode in a conventional three electrode electrochemical set-up, a thin layer of gold was deposited onto one face of the polyamide membrane using an AGAR Automatic Sputter Coater controlled by an AGAR Terminating Film Thickness Monitor. The thickness of the gold coating was varied in order to find a coating thickness that conferred sufficient conductivity to the polyamide film, without hindering the flow rate of water through the membrane.

#### 3.3.4.1 Resistance Across the Gold Sputter Coated Membranes

Literature reports of polyamide membranes sputter coated with gold, for use as working electrodes, see them being primarily employed as biosensors.<sup>85-87</sup> Each of these studies sputter coat the polyamide membrane with a gold layer up to a thickness of  $600 \text{ \AA}$  (60 nm). However, as the pore size of the membranes used in the literature studies were only  $0.2 - 0.4 \mu\text{m}$ , a range of thicknesses of the gold coating were examined in order to find the optimum thickness of gold coating for the polyamide membranes used in this investigation. First the polyamide membranes were washed in acetone, blotted and allowed to air dry. This was in order to remove any grease or residue from the membrane.<sup>13</sup> The membrane was then placed in the sputter coater and coated until the desired thickness of gold coating was achieved. The resistance across the gold coated membrane was measured with an Avometer 2001 multimeter. Figure 3.41 shows a bar chart depicting the resistance across a number of membranes, coated with thicknesses of gold of 50 - 100 nm. It can be clearly observed that the measured resistance across the gold coated polyamide membranes decreases with an increase in the thickness of the gold coating. It is necessary to keep the resistance as low as possible in order to use the sputter coated membrane as the working electrode in a conventional three electrode cell.

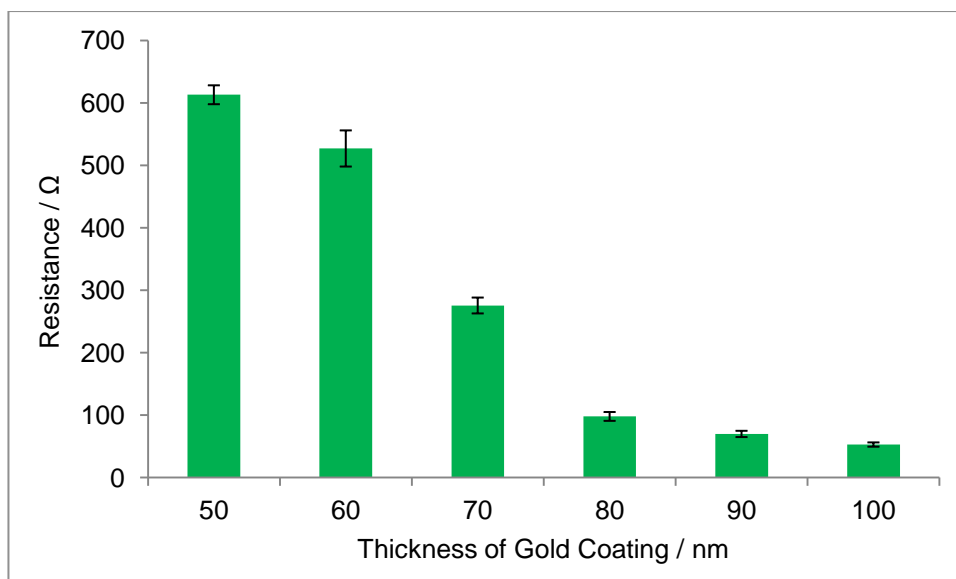
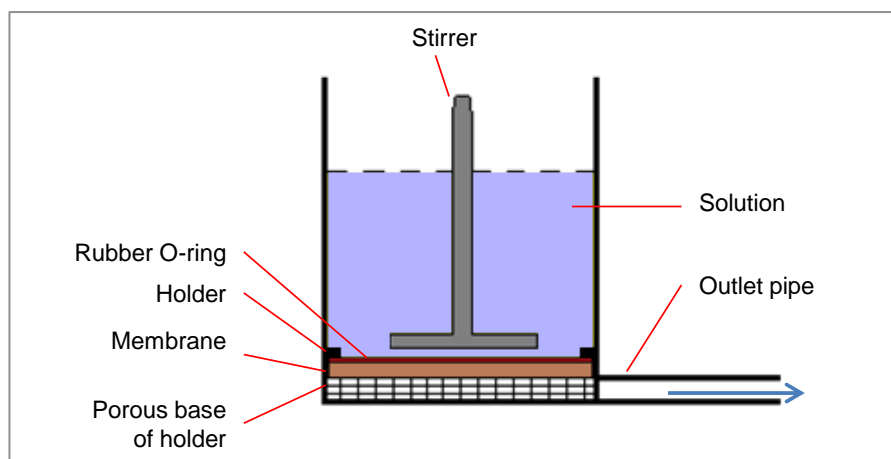


Figure 3.41: The measured resistance across gold sputter coated polyamide membranes, which can be observed to decrease as the thickness of the gold coating increases. Number of membranes tested for each thickness of gold = 5.

#### 3.3.4.2 Flow Rate Through the Gold Sputter Coated Membranes

As it was envisaged that the polypyrrole nanowire modified polyamide membranes would be used as filtration membranes, it was important to prevent occlusion of the membrane pores, such that a sufficient flow rate could be maintained. Thus membranes coated with different thicknesses of gold were loaded into a stirred filtration cell and 10 cm<sup>3</sup> of water was allowed to filter through the membrane under gravity (Figure 3.42). This was also repeated with unmodified polyamide membranes. The flow rate was calculated in cm<sup>3</sup>/min and the rate calculated for the flow of water through each membrane is depicted in Figure 3.43. It can be clearly seen that there is little difference in the rate at which water flows through the gold coated membranes, regardless of the thickness of the gold coating. Thus it can be concluded that coating the polyamide membranes with gold up to a thickness of 100 nm will not hinder the passage of water under the influence of gravity.



**Figure 3.42:** The gold coated membrane is loaded into a stirred filtration cell and held in place with a rubber O-ring. 10 cm<sup>3</sup> of water is then placed into the vessel and allowed to flow through the membrane under gravity. The flow through is timed and collected at the outlet pipe to determine the rate of flow through the membrane.

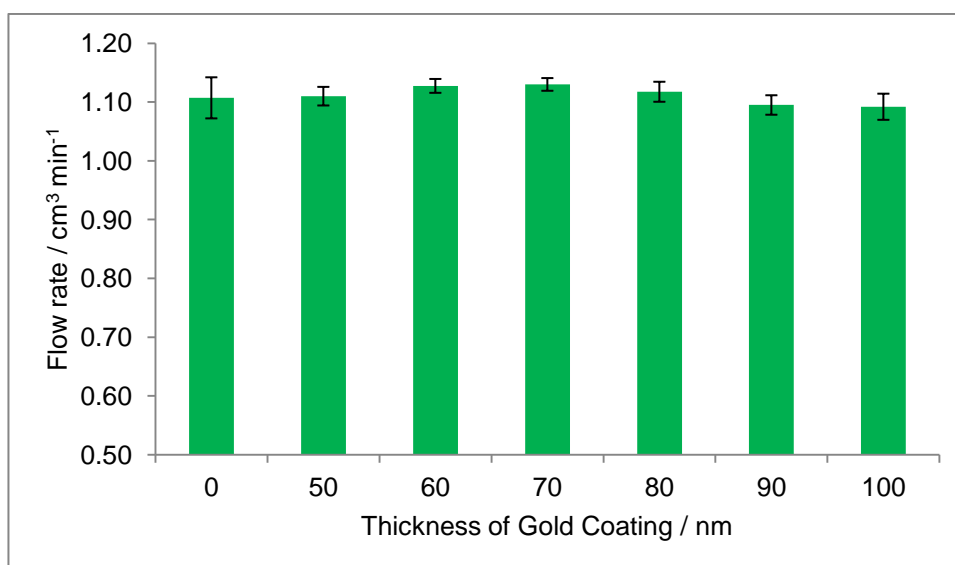


**Figure 3.93:** Flow rate (cm<sup>3</sup>/min) of water through polyamide membranes coated with different thicknesses of gold as indicated on the chart. The flow rate through an uncoated membrane is shown as comparison, n = 4.

SEM micrographs were obtained of the polyamide films coated with 60 nm-100 nm of gold, although the resistance across the polyamide films coated with 60 nm is too high for them to be employed as a working electrode. This was in order to establish if occlusion of the pores was occurring, even though the flow rate of water through the gold coated membranes was not hindered. Figure 3.44 presents the SEM micrographs of the polyamide membranes coated with 60 nm – 100 nm of gold. An uncoated polyamide membrane is also displayed for comparison purposes. It can be observed that the roughness and porosity of the polyamide membranes is maintained when coated with

either 60 nm or 70 nm of gold. When the gold coating thickness is increased to 80 nm of gold, patches of the membrane can be observed to lose their porosity. This is also seen for polyamide membranes coated with 90 nm and 100 nm of sputtered gold. As the aim of this investigation was to coat the films with the minimum amount of gold needed to confer sufficient conductivity for polypyrrole nanowire growth, while maintaining membrane porosity, it was decided to investigate the growth of polypyrrole nanowires on membranes, beginning with those coated with 60 nm of gold.

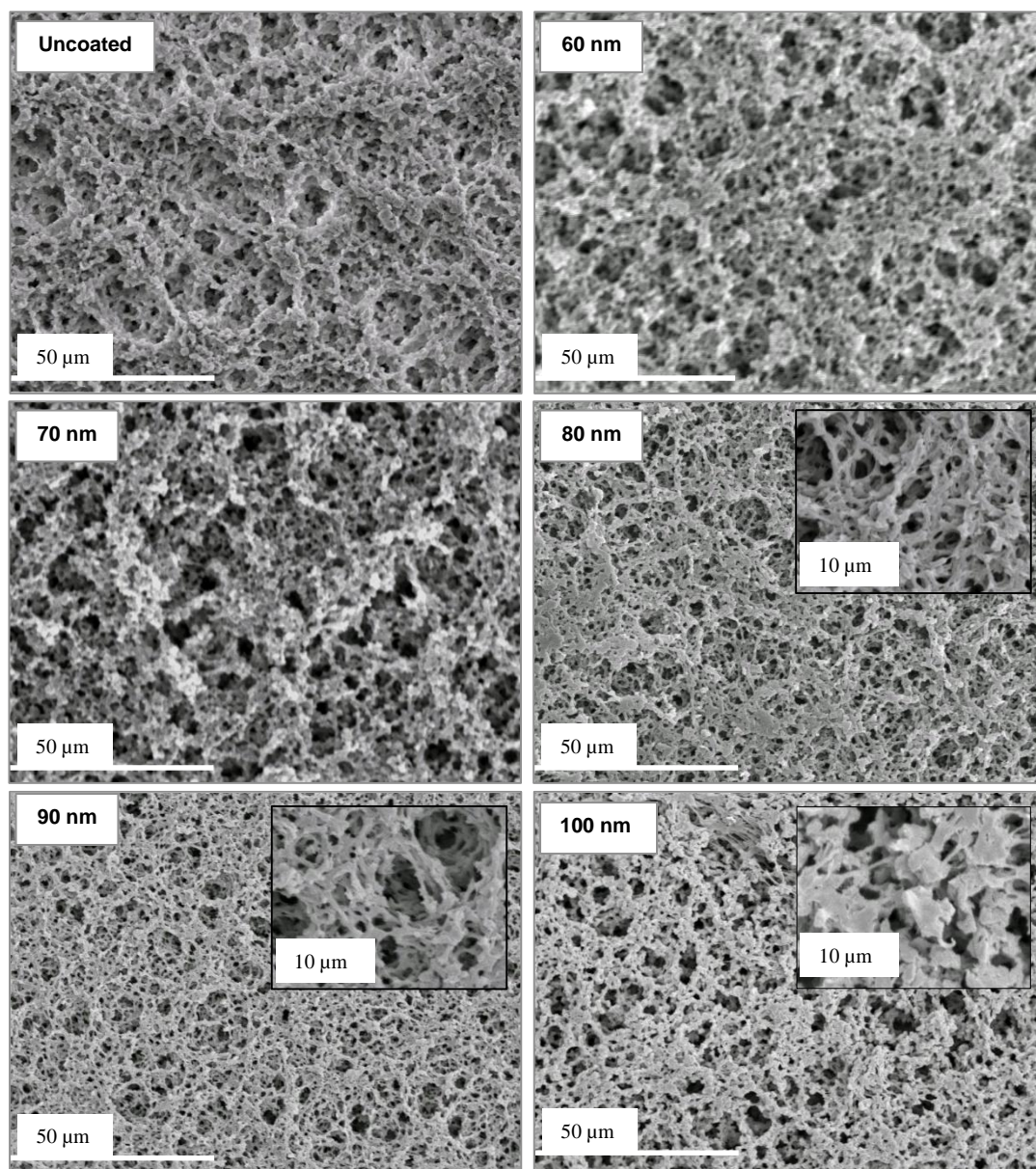


**Figure 3.44:** SEM micrographs (plan-view) of polyamide membranes (of pore diameter  $0.8\ \mu\text{m}$ ) sputter coated with gold to the thickness indicated in the top left corner of each image. The inset images depict a higher magnification of the membranes coated with 80 nm, 90 nm and 100 nm of gold, to illustrate the increasing occlusion of the pores by the gold coating.

#### 3.3.4.3 Polymerisation of PpyNW on the Gold Sputter Coated Membranes

While the use of gold coated membranes in the field of biosensors has been investigated,<sup>86</sup> the electropolymerisation of polypyrrole on metal sputter coated porous membranes is also reported in the literature for the development of actuators.<sup>88, 89</sup> In the knowledge that polypyrrole could be successfully polymerised on a metal sputter coated membrane, the formation of polypyrrole nanowires was investigated and optimised at the gold coated membrane surface.

It was established in Section 3.3.1.1 that the polypyrrole nanowires form most effectively on a standard gold electrode at an applied potential of 0.80 V vs. SCE. This section examines the formation of polypyrrole nanowires on polyamide membranes coated with a thickness of 60 nm of gold and thicker. Once the minimum thickness of gold coating was determined, studies were carried out to establish the optimum applied potential and charge density to which the polypyrrole nanowires were grown. SEM micrographs were taken of each membrane after polymerisation to determine whether the polypyrrole formed was in the nanowire morphology. Polyamide membranes coated with 60 nm of gold, were placed in an aqueous solution of 0.15 M pyrrole, 0.20 M Na<sub>2</sub>HPO<sub>4</sub> and 0.001 M LiClO<sub>4</sub>, and a potential of 0.80 V vs. SCE was applied to a charge density of 300 mC cm<sup>-2</sup>. Polymer formation was not observed and so it was concluded that 60 nm coating of gold was not sufficiently conducting to act as a working electrode. Figure 3.45 depicts the SEM micrographs obtained when a potential of 0.80 V vs. SCE was applied to polyamide membranes coated with 70 nm of gold, in an aqueous solution of 0.15 M pyrrole, 0.20 M Na<sub>2</sub>HPO<sub>4</sub> and 0.001 M LiClO<sub>4</sub>, to a charge density of 300 mC cm<sup>-2</sup>. Polypyrrole with nanofibrous morphology is clearly apparent and so a gold coating of 70 nm on the polyamide membrane was concluded to be the minimum thickness of gold required to confer sufficient conductivity for the formation of polypyrrole nanowires. Therefore, with 70 nm of gold established as being the minimum coating required to ensure the polyamide membranes conductivity, the potential applied and the charge density to which the polypyrrole was grown were investigated.

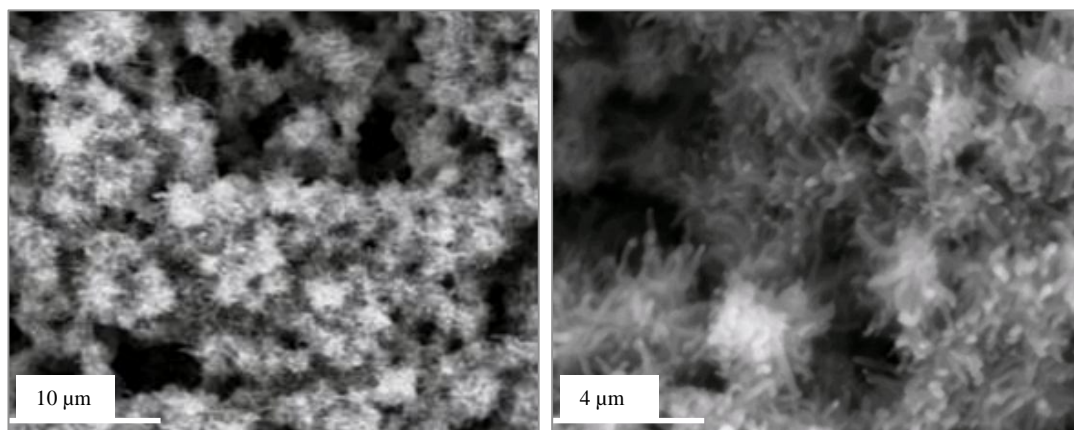


**Figure 3.45:** SEM micrographs of polypyrrole films polymerised at an applied potential of 0.80 V vs. SCE, to a charge density of  $300 \text{ mC cm}^{-2}$ , from an aqueous solution of 0.15 M pyrrole/ 0.20 M  $\text{Na}_2\text{HPO}_4$ /0.001 M  $\text{LiClO}_4$  on polyamide membranes coated with gold to a thickness of 70 nm.

Polypyrrole films were formed on polyamide membranes coated with 70 nm of gold, at applied potentials of 0.60 V, 0.70 V and 0.80 V vs. SCE, until a charge density of  $300 \text{ mC cm}^{-2}$  or  $400 \text{ mC cm}^{-2}$  was achieved. The polypyrrole films were electropolymerised from an aqueous solution of 0.15 M pyrrole, 0.20 M  $\text{Na}_2\text{HPO}_4$  and 0.001 M  $\text{LiClO}_4$ . It can be observed in Figure 3.46 that polypyrrole films formed at an applied potential of 0.60 V vs. SCE adopt a bulk morphology, which coats the polyamide film with an agglomeration of polypyrrole with no visible nanowires (Figure 3.46 a and b). The polypyrrole films formed at an applied potential of 0.70 V vs. SCE to a charge density of  $300 \text{ mC cm}^{-2}$  exhibit nanofibrous morphologies but the coverage of nanowires is patchy and bulk polypyrrole is also observed (Figure 3.46 c). It can also be seen in the inset in Figure 3.46 (c) that the length and diameter of the nanowires formed at an applied potential of 0.70 V vs. SCE to a charge density of  $300 \text{ mC cm}^{-2}$  varies. When a potential of 0.70 V vs. SCE is applied to a charge density of  $400 \text{ mC cm}^{-2}$  (Figure 3.46 d), the nanowires become less defined. This may be due to secondary growth of polypyrrole as the polymerisation takes place over a longer period of time than films formed to a charge density of  $300 \text{ mC cm}^{-2}$ . The most reproducible polypyrrole nanowires are formed at an applied potential of 0.80 V vs. SCE to a charge density of  $300 \text{ mC cm}^{-2}$  (Figure 3.46 e). The polypyrrole nanowires polymerised at an applied potential of 0.80 V vs. SCE on a standard gold electrode are successfully formed to a charge density of  $400 \text{ mC cm}^{-2}$ . However, when using the same conditions to polymerise polypyrrole nanowires on a gold coated membrane, the nanowires formed are less defined. As with the films formed at an applied potential of 0.70 V vs. SCE to a

charge density of  $400 \text{ mC cm}^{-2}$ , this is most likely due to secondary polymer growth which occurs over the longer experimental time period. This may thicken the base layer of polypyrrole, obscuring the polypyrrole nanowires from the base upwards. Thus it was decided that polypyrrole nanowires formed on the gold coated polyamide membranes would be polymerised at an applied potential of  $0.80 \text{ V}$  vs. SCE to a charge density of  $300 \text{ mC cm}^{-2}$ . The applications of these polypyrrole nanowires modified membranes are investigated in Section 5.5.

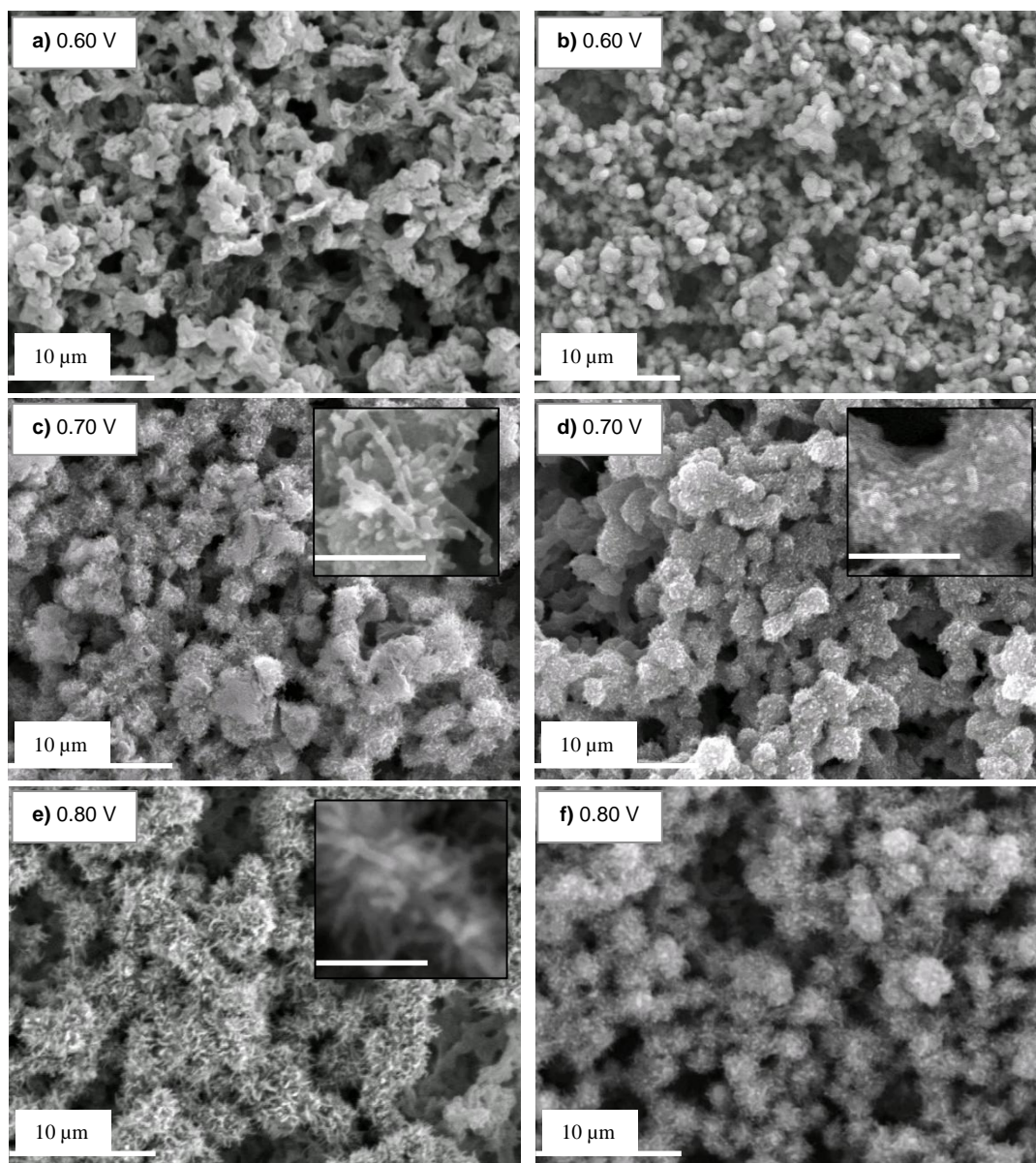


**Figure 3.46:** SEM micrographs of polypyrrole films polymerised from an aqueous solution of  $0.15 \text{ M}$  pyrrole/ $0.20 \text{ M}$   $\text{Na}_2\text{HPO}_4$ / $0.001 \text{ M}$   $\text{LiClO}_4$ , on polyamide membranes coated with gold to a thickness of  $70 \text{ nm}$ . The polypyrrole films were polymerised at applied potentials of  $0.60 \text{ V}$  (a/b),  $0.70 \text{ V}$  (c/d) and  $0.80 \text{ V}$  (e/f) vs. SCE to a charge density of  $300 \text{ mC cm}^{-2}$  (a/c/e) or  $400 \text{ mC cm}^{-2}$  (b/d/f). The scale bars in the inset images represent  $2 \mu\text{m}$ .

The flow rate of water through polyamide membranes, upon which polypyrrole nanowires were formed at an applied potential of 0.80 V vs. SCE to a charge density of  $300 \text{ mC cm}^{-2}$ , was measured by loading the modified membranes into a stirred filtration cell as in Section 3.3.4.2. It can be seen in Figure 3.47 that the flow rate of water through the polypyrrole nanowire coated membranes is greater than 20 percent less than the flow rate through the unmodified membranes. It appears therefore, that coating the membranes with polypyrrole nanowires does hinder the flow of water to an extent.

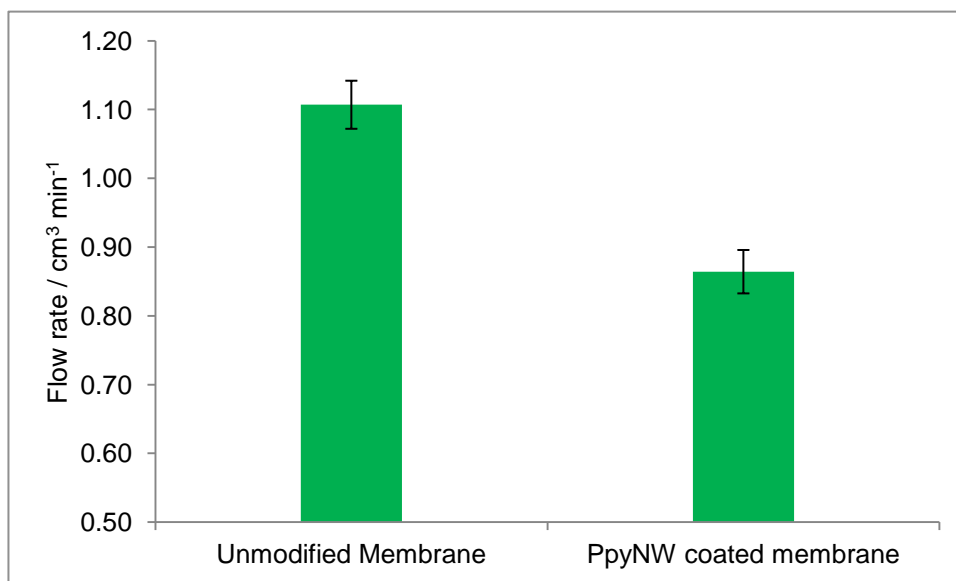


**Figure 3.47:** Flow rate ( $\text{cm}^3 \text{ min}^{-1}$ ) of water through unmodified polyamide membranes and through polyamide membranes coated with 70 nm gold upon which polypyrrole nanowires were formed at an applied potential of 0.80 V vs. SCE to a charge density of  $300 \text{ mC cm}^{-2}$ ,  $n = 4$ .

### 3.4 Summary and Conclusions

Chemical oxidation and electrochemical methods were successfully employed for the polymerisation of polypyrrole nanowires on a porous membrane support. The polypyrrole nanowires were also successfully coated with polypyrrole/immobile dopant films which could influence the ion-exchange properties of the polypyrrole nanowires.

The chemically oxidised nanowire films did not sufficiently immobilise the methyl orange dopant, which leached from the coated membrane and so the applications of these nanowire coated membranes were not investigated further. The electropolymerised polypyrrole nanowires were characterised using SEM, Raman and FTIR spectroscopy and water contact angle measurements. It was found that the polypyrrole nanowires may be less conducting than bulk PpyCl films due to the shorter conjugation lengths in the Ppy chains. Coating the PpyNW with PpyC4S and PpyPSS films appeared to improve the conjugation in the polymer film. Water contact angle measurements indicated that the PpyNW films were more hydrophilic than bulk polypyrrole. Applying a coating of PpyC4S to the nanowires causes the material to become less hydrophilic, while coating the nanowires with a PpyPSS film causes the PpyNW film to become superhydrophilic. To the best of our knowledge, this is the first example of the template-less electrochemical deposition of nanowires containing an immobile dopant. As this was a simple and straightforward process, it could be very easily applied in a range of systems.

The effect of changing the seed dopant in the electropolymerisation of polypyrrole nanowires was found to affect the length, diameter and base layer thickness of the polypyrrole nanowires. Although no connection could be made between the physical properties of the seed dopant salts and the morphology of the nanowires, it was apparent that both the anion and cation of the salt affected the  $j-t$  plot and nanowire morphology. The only possible trend which was observed was the lack of nanowire formation in the presence of the multivalent anions,  $\text{Li}_2\text{SO}_4$  and *p*-sulfonatocalix[4]arene sodium salt. Polypyrrole nanowires formed from electrolyte solutions containing  $\text{NaClO}_4$  or LiTFSI exhibited a thin base layer of polypyrrole and were found to adhere better to the electrode surface, which may improve the conductivity of the polypyrrole nanowires.

Finally, polypyrrole-sodium alginate particles, which have previously been reported in the literature,<sup>15</sup> were successfully formed and characterised using SEM microscopy, FTIR and Raman spectroscopy. It was determined that the particles were spherical in morphology, and exhibited a diameter of  $225 \pm 15$  nm. The presence of sodium alginate in the particles was confirmed with FTIR and Raman spectroscopy, with characteristic bands of alginate carbonyl groups and glycosidic linkages occurring in addition to the characteristic polypyrrole bands.

### 3.5 References

1. A. Malinauskas, *Polymer*, 2001, **42**, 3957-3972.
2. U. Lange, N. V. Roznyatovskaya and V. M. Mirsky, *Analytica Chimica Acta*, 2008, **614**, 1-26.
3. M. N. Akieh, S. F. Ralph, J. Bobacka and A. Ivaska, *Journal of Membrane Science*, 2010, **354**, 162-170.
4. D. A. Reece, S. F. Ralph and G. G. Wallace, *Journal of Membrane Science*, 2005, **249**, 9-20.
5. G. Jeon, S. Y. Yang, J. Byun and J. K. Kim, *Nano Letters*, 2011, **11**, 1284-1288.
6. W. S. Choi, T. An and G. Lim, *Fabrication of Conducting Polymer Nanowires - Implementations and Applications*, InTech, 2011.
7. C. Debiemme-Chouvy, *Electrochemistry Communications*, 2009, **11**, 298-301.
8. C. R. Martin, R. Parthasarathy and V. Menon, *Synthetic Metals*, 1993, **55**, 1165-1170.
9. R. V. Parthasarathy and C. R. Martin, *Chemistry of Materials*, 1994, **6**, 1627-1632.
10. C. R. Martin, *Accounts of Chemical Research*, 1995, **28**, 61-68.
11. L. Xia, Z. Wei and M. Wan, *Journal of Colloid and Interface Science*, 2010, **341**, 1-11.
12. A. Kaynak and R. Beltran, *Polymer International*, 2003, **52**, 1021-1026.
13. T. Lin, L. Wang, X. Wang and A. Kaynak, *Thin Solid Films*, 2005, **479**, 77-82.
14. K. Huang, M. Wan, Y. Long, Z. Chen and Y. Wei, *Synthetic Metals*, 2005, **155**, 495-500.
15. S. Sahoo, S. Dhibar and C. K. Das, *eXPRESS Polymer Letters*, 2012, **6**, 965-974.
16. H. Seung Lee and J. Hong, *Synthetic Metals*, 2000, **113**, 115-119.
17. T. Dai, X. Yang and Y. Lu, *Nanotechnology*, 2006, **17**, 3028-3034.
18. X. Yang, Z. Zhu, T. Dai and Y. Lu, *Macromolecular Rapid Communications*, 2005, **26**, 1736-1740.

19. X. Yang and L. Li, *Synthetic Metals*, 2010, **160**, 1365-1367.
20. Y. Yu, Z. Si, S. Chen, C. Bian, W. Chen and G. Xue, *Langmuir*, 2006, **22**, 3899-3905.
21. M. M. Campos-Vallette, N. P. Chandia, E. Clavijo, D. Leal, B. Matsuhiro, I. O. Osorio-Roman and S. Torres, *Journal of Raman Spectroscopy*, 2010, **41**, 758-763.
22. J. Zang, C. M. Li, S.-J. Bao, X. Cui, Q. Bao and C. Q. Sun, *Macromolecules*, 2008, **41**, 7053-7057.
23. L. Al-Mashat, C. Debiemme-Chouvy, S. Borensztajn and W. Wlodarski, *The Journal of Physical Chemistry C*, 2012, **116**, 13388-13394.
24. J. Liu, Y. Lin, L. Liang, J. A. Voigt, D. L. Huber, Z. R. Tian, E. Coker, B. McKenzie and M. J. McDermott, *Chemistry - A European Journal*, 2003, **9**, 604-611.
25. M. A. del Valle, P. Cury and R. Schrebler, *Electrochim. Acta*, 2002, **48**, 397-405.
26. E. Tamburri, S. Orlanducci, F. Toschi, M. L. Terranova and D. Passeri, *Synthetic Metals*, 2009, **159**, 406-414.
27. J. P. Soto, F. R. Diaz, V. M. A. del, J. H. Velez and G. A. East, *Applied Surface Science*, 2008, **254**, 3489-3496.
28. G. C. Arteaga, V. M. A. del, M. Antilen, M. Romero, A. Ramos, L. Hernandez, M. C. Arevalo, E. Pastor and G. Louarn, *International Journal of Electrochemical Science*, 2013, **8**, 4120-4130.
29. P. R. Teasdale, L. A. P. Kane-Maguire, G. G. Wallace and G. M. Spinks, *Conductive Electroactive Polymers: Intelligent Materials Systems*, CRC Press, 2002.
30. A. A. A. Almario and R. L. T. Caceres, *Journal of the Chilean Chemical Society*, 2009, **54**, 14-19.
31. N. T. Kemp, J. W. Cochrane and R. Newbury, *Synthetic Metals*, 2009, **159**, 435-444.
32. B. J. Hwang, R. Santhanam and Y.-L. Lin, *Journal of the Electrochemical Society*, 2000, **147**, 2252-2257.
33. J. Wang, X. Mo, D. Ge, Y. Tian, Z. Wang and S. Wang, *Synthetic Metals*, 2006, **156**, 514-518.

34. D. T. Ge, S. Q. Huang, R. C. Qi, J. Mu, Y. Q. Shen and W. Shi, *ChemPhysChem*, 2009, **10**, 1916-1921.
35. M. A. De Paoli, R. C. D. Peres and J. M. Pernaut, *Journal of the Brazilian Chemical Society*, 1990, **1**, 50-52.
36. K. Xue, Y. Xu and W. Song, *Electrochimica Acta*, 2012, **60**, 71-77.
37. Y. Zhang, Z. Bakenov, Y. Zhao, A. Konarov, T. N. L. Doan, M. Malik, T. Paron and P. Chen, *Journal of Power Sources*, 2012, **208**, 1-8.
38. C. P. McCarthy, N. B. McGuinness, P. B. Carolan, C. M. Fox, B. E. Alcock-Earley, C. B. Breslin and A. D. Rooney, *Macromolecules*, 2013, **46**, 1008-1016.
39. N. B. McGuinness, Ph.D., NUI Maynooth, 2013.
40. C. Debiemme-Chouvy, *Electrochemical and Solid-State Letters*, 2007, **10**, E24-E26.
41. C. Debiemme-Chouvy, *Biosensors and Bioelectronics*, 2010, **25**, 2454-2457.
42. M. N. Akieh, W. E. Price, J. Bobacka, A. Ivaska and S. F. Ralph, *Synthetic Metals*, 2009, **159**, 2590-2598.
43. C. Weidlich, K. M. Mangold and K. Jüttner, *Electrochimica Acta*, 2005, **50**, 1547-1552.
44. S. Bruckenstein, K. Brzezinska and A. R. Hillman, *Physical Chemistry Chemical Physics*, 2000, **2**, 1221-1229.
45. J. Y. Lim, W.-k. Paik and I.-H. Yeo, *Synthetic Metals*, 1995, **69**, 451-454.
46. S. Bruckenstein, J. H. Chen, I. Jureviciute and A. R. Hillman, *Electrochimica Acta*, 2009, **54**, 3516-3525.
47. Y. Velmurugu and S. Skaarup, *Ionics*, 2005, **11**, 370-374.
48. R.-M. Latonen, M. N. Akieh, K. Vavra, J. Bobacka and A. Ivaska, *Electroanalysis*, 2013, **25**, 991-1004.
49. C. Weidlich, K. M. Mangold and K. Jüttner, *Electrochimica Acta*, 2005, **50**, 5247-5254.
50. S. Skaarup, L. Bay, K. Vidanapathirana, S. Thybo, P. Tofte and K. West, *Solid State Ionics*, 2003, **159**, 143-147.
51. V. Syritski, A. Opik and O. Forsen, *Electrochimica Acta*, 2003, **48**, 1409-1417.

52. D.-S. Guo, K. Wang and Y. Liu, *Journal of Inclusion Phenomena and Macrocyclic Chemistry*, 2008, **62**, 1-21.
53. R. Doyle, C. B. Breslin, O. Power and A. D. Rooney, *Electroanalysis*, 2012, **24**, 293-302.
54. R. Schrebler, P. Grez, P. Cury, C. Veas, M. Merino, H. Gómez, R. Córdova and M. A. del Valle, *Journal of Electroanalytical Chemistry*, 1997, **430**, 77-90.
55. R. Rajagopalan and J. O. Iroh, *Electrochimica Acta*, 2002, **47**, 1847-1855.
56. B. Tian and G. Zerbi, *Journal of Chemical Physics*, 1990, **92**, 3886-3891.
57. B. Tian and G. Zerbi, *Journal of Chemical Physics*, 1990, **92**, 3892-3898.
58. R. Turcu, L. V. Giurgiu, R. Ordean, R. Grecu and M. Brie, *Synthetic Metals*, 2001, **119**, 287-288.
59. H. S. Kim, D. H. Park, Y. B. Lee, D.-C. Kim, H.-J. Kim, J. Kim and J. Joo, *Synthetic Metals*, 2007, **157**, 910-913.
60. I. Carrillo, E. S. De La Blanca, J. L. G. Fierro, M. A. Raso, F. Accion, E. Enciso and M. I. Redondo, *Thin Solid Films*, 2013, **539**, 154-160.
61. G. Gustafsson, I. Lundstroem, B. Liedberg, C. R. Wu, O. Inganaes and O. Wennerstroem, *Synthetic Metals*, 1989, **31**, 163-179.
62. G. Lu, C. Li and G. Shi, *Polymer*, 2006, **47**, 1778-1784.
63. C. P. McCarthy, Ph.D., NUI Maynooth, 2013.
64. M. Liu, Y. Zhang, M. Wang, C. Deng, Q. Xie and S. Yao, *Polymer*, 2006, **47**, 3372-3381.
65. P. Xu, X. Han, C. Wang, D. Zhou, Z. Lu, A. Wen, X. Wang and B. Zhang, *Journal of Physical Chemistry B*, 2008, **112**, 10443-10448.
66. Y. Chen, Z. Zhao and C. Wang, *Nanoscience and Nanotechnology Letters*, 2013, **5**, 186-190.
67. I. Carrillo, d. I. B. E. Sanchez, J. L. G. Fierro, M. A. Raso, F. Accion, E. Enciso and M. I. Redondo, *Thin Solid Films*, 2013, **539**, 154-160.
68. J. V. Thombare, M. C. Rath, S. H. Han and V. J. Fulari, *Materials Physics and Mechanics*, 2013, **16**, 118-125.
69. P. Sreedevi, K. Chennakesavulu, G. Bhaskar-Raju and S. Prabhakar, *Journal of Dispersion Science and Technology*, 2011, **32**, 1531-1536.

70. J. Xu, X. Cui, H. Wang, J. Li and S. Dong, *Bulletin of Materials Science*, 2011, **34**, 531-533.
71. J. C. Yang, M. J. Jablonsky and J. W. Mays, *Polymer*, 2002, **43**, 5125-5132.
72. L. Dauginet-De Pra and S. Demoustier-Champagne, *Polymer*, 2005, **46**, 1583-1594.
73. I. Das, N. Goel, S. K. Gupta and N. R. Agrawal, *Journal of Electroanalytical Chemistry*, 2012, **670**, 1-10.
74. M. Grzeszczuk, A. Kepas, C. Kvarnstrom and A. Ivaska, *Synthetic Metals*, 2010, **160**, 636-642.
75. A. O. Patil, A. J. Heeger and F. Wudl, *Chemical Reviews*, 1988, **88**, 183-200.
76. K. Crowley and J. Cassidy, *Journal of Electroanalytical Chemistry*, 2003, **547**, 75-82.
77. F. Chen, G. Shi, M. Fu, L. Qu and X. Hong, *Synthetic Metals*, 2003, **132**, 125-132.
78. S. Gupta, *Journal of Raman Spectroscopy*, 2008, **39**, 1343-1355.
79. M. J. L. Santos, A. G. Brolo and E. M. Girotto, *Electrochimica Acta*, 2007, **52**, 6141-6145.
80. V. Varade, G. V. Honnavar, P. Anjaneyulu, K. P. Ramesh and R. Menon, *Journal of Physics D: Applied Physics*, 2013, **46**, 365306, 365308 pp.
81. P. Chandrasekhar, *Conducting Polymers, Fundamentals and Applications: A Practical Approach*, Springer, 1999.
82. J. M. Fonner, L. Forciniti, H. Nguyen, J. D. Byrne, Y.-F. Kou, J. Syeda-Nawaz and C. E. Schmidt, *Biomedical Materials*, 2008, **3**, 034124.
83. K. S. Teh, Y. Takahashi, Z. Yao and Y.-W. Lu, *Sensors and Actuators A: Physical*, 2009, **155**, 113-119.
84. X. Du, X. Hao, Z. Wang, X. Ma, G. Guan, A. Abuliti, G. Ma and S. Liu, *Synthetic Metals*, 2013, **175**, 138-145.
85. C. M. Duan and M. E. Meyerhoff, *Analytical Chemistry*, 1994, **66**, 1369-1377.
86. A. M. Smith, M. W. Ducey, Jr. and M. E. Meyerhoff, *Biosensors and Bioelectronics*, 2000, **15**, 183-192.

87. F. Zhang, S. S. Cho, S. H. Yang, S. S. Seo, G. S. Cha and H. Nam, *Electroanalysis*, 2006, **18**, 217-222.
88. A. D. Price, T. Gillen, C. C. Liu, C. A. O'Shaughnessy and H. E. Naguib, *Journal of Cellular Plastics*, 2012, **48**, 25-42.
89. J. Wang, Masters of Applied Science, University of Toronto, 2012.

## Chapter 4

---

Investigation of the Ion-Exchange Properties of  
*p*-Sulfonatocalix[4]arene-Polypyrrole and  
Polypyrrole-Polystyrene Sulfonate Films using  
EQCM

---

## 4.1 Introduction

Polypyrrole is an electrochemically switchable conducting polymer whose redox activities are accompanied by ion exchange. Sequential oxidation and reduction of polypyrrole films is also accompanied by changes in conductivity, morphology and polymer volume.<sup>1</sup> The ion exchange properties of polypyrrole have been widely studied.<sup>2-5</sup> As detailed in Chapter 1, during oxidative polymerisation of the pyrrole monomer, dopant anions are incorporated into the polymer film to balance positive charges on the polymer backbone. This results in a polymer with an overall neutral charge. If the dopant anion is small and mobile (such as  $\text{Cl}^-$ ,  $\text{ClO}_4^-$  or  $\text{BF}_4^-$ ), reduction of the polypyrrole will result in the anions expulsion from the film (Figure 4.1). When the polypyrrole is re-oxidised, mobile anions in the surrounding electrolyte solution will be uptaken to ensure polymer neutrality.

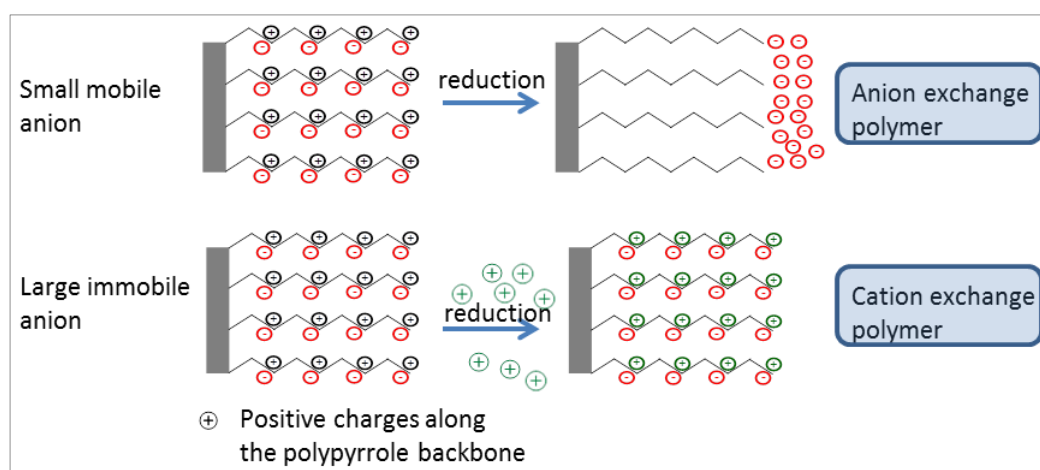
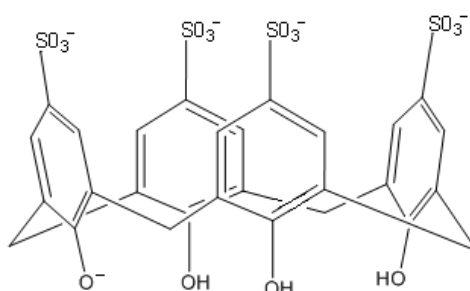


Figure 4.1: Idealised ion exchange properties of polypyrrole doped with mobile/immobile dopant anions which are denoted by the red circles.<sup>6</sup>

However, large dopant anions such as polystyrene sulfonate (PSS) and polyvinyl sulfonate (PVS) are immobilised in the polymer film due to polymer entanglement and electrostatic interactions and cannot be expelled.<sup>7-9</sup> In addition, if the polymerisation proceeds slowly, the polymer will be densely packed and the mobility of large dopant anions will be hindered.<sup>10</sup> Thus, electrochemical reduction of these films results in the incorporation of mobile cations from the surrounding electrolyte solution to maintain polymer electroneutrality (Figure 4.1). During re-oxidation, the incorporated cations will be expelled, or anions in the solution will enter. Medium sized dopant anions, such as dodecylbenzenesulfonate (DBS) or tosylate result in mixed anion and cation

exchange, but cation exchange is more favoured.<sup>11, 12</sup> In this way, polypyrrole can be utilised as an electrochemically switchable anion or cation exchange polymer, depending on the size of dopant anion incorporated during polymerisation.<sup>13-15</sup>

Sulfonated calixarenes are water soluble macrocycles with 3-dimensional, flexible,  $\pi$ -electron rich cavities.<sup>16</sup> Exhibiting similar selectivity to cyclodextrins,<sup>17</sup> these cavities, along with their sulfonate groups impart the ability to bind with a range of organic and inorganic cations and neutral organic molecules.<sup>18</sup> It has been reported that *p*-sulfonatocalix[4]arene has an inner cavity size of 5.2 Å.<sup>19</sup> As represented in Figure 4.2, its upper rim is completely ionised and has four negatively charged sites at almost all pH values. Its lower rim hydroxyl groups are dissociated, with  $pK_a$  values of 3.26 for the first group and 12.30 for the second,<sup>20</sup> which infers that *p*-sulfonatocalix[4]arene is penta-anionic over a large pH range.



**Figure 4.2:** Structure of the anionic dopant *p*-sulfonatocalix[4]arene (C4S).

Impedance Spectroscopy (EIS) studies carried out by our group have shown that *p*-sulfonatocalix[4]arene acts as an immobile anionic dopant within the polypyrrole matrix.<sup>21</sup> It has also been observed that *p*-sulfonatocalix[6]arene retains its inclusion properties when immobilised in a polymer film.<sup>22, 23</sup> The complex stability constants, for the intermolecular complexation of *p*-sulfonatocalix[4]arene with some of the cations investigated in this study, are shown in Table 4.1. It can be observed that *p*-sulfonatocalix[4]arene exhibits weak binding abilities for monovalent cations and moderately strong binding abilities for divalent cations.<sup>18</sup> Recent work by Latonen *et al.* has revealed that some molecules of *p*-sulfonatocalix[6]arene (C6S) leach from the polymer matrix with prolonged redox cycling of 100 cycles, however it was assumed that the *p*-sulfonatocalix[6]arene was immobile within the film for the beginning of the redox cycling process.<sup>9</sup> Consequently, *p*-sulfonatocalix[4]arene will be regarded as a

practically immobile dopant for the development of a polypyrrole cation exchange film but the possibility of leaching with prolonged cycling will be taken into consideration.

**Table 4.1: Complex stability constants ( $K_s$ ) for the intermolecular complexation of inorganic cations with *p*-sulfonatocalix[4]arene, in pH = 2 acidic aqueous solution at 298.15 K assembled from the results of Morel *et al.*<sup>18, 24, 25</sup>**

Cations	log $K_s$	$K_s(M^{-1})$
Na <sup>+</sup>	–	–
Cs <sup>+</sup>	1.16	14.6
Mg <sup>2+</sup>	3.30	1995.3
Ca <sup>2+</sup>	3.32	2089.3

Chapter 3 details the successful application of a *p*-sulfonatocalix[4]arene-polypyrrole film (PpyC4S) as a functional coating on the already polymerised polypyrrole nanowires. To fully characterise the ion exchange abilities of the *p*-sulfonatocalix[4]arene-polypyrrole film (PpyC4S), a study was carried out using an electrogravimetric technique, the results of which are presented and discussed in this chapter. The electrochemical quartz crystal microbalance (EQCM) monitors mass changes occurring at the electrode surface by recording the changes in the resonant frequency of the oscillating quartz crystal as the polymer is electrochemically cycled between its oxidised and reduced states. The change in frequency ( $\Delta f$  /Hz) of the oscillator is related to its change in mass ( $\Delta m$  /g) through the Sauerbrey equation (Equation 4.1).<sup>26</sup>

Equation 4. 1

$$\Delta f = - \frac{2f_o^2}{A\sqrt{\mu_q\rho_q}} \Delta m$$

where  $\Delta f$  is the observed frequency change,  $\Delta m$  is the change in mass,  $A$  is piezoelectrically active area (0.203 cm<sup>2</sup>),  $f_o$  is the resonant frequency of the unloaded crystal,  $\mu_q$  is the shear modulus of the quartz ( $2.947 \times 10^{11}$  g cm<sup>-1</sup> s<sup>-2</sup>) and  $\rho_q$  is the density of the quartz (2.648 g cm<sup>-3</sup>).

The Sauerbrey equation was originally developed for gas phase deposition measurements and it was long thought that this relationship would not hold true in the presence of a contacting liquid. However, since the 1980s a set of limitations have been established, within which the Sauerbrey equation can be utilised. That is, any film deposited upon the crystal oscillator must be rigid, homogeneous and acoustically thin, such that it moves synchronously with the crystal oscillator and can thus be treated as an extension of it.<sup>27</sup> Literature values as to the maximum permitted thickness of the polypyrrole film vary from 400 nm – 1  $\mu\text{m}$ .<sup>2, 7, 28-30</sup> Homogeneity of the film can be confirmed by the observation of a linear relationship between the change in mass and the charge passed during polymerisation of the polymer.<sup>2, 4, 12, 15, 31, 32</sup> Unfortunately, the condition of homogeneity of the film cannot be upheld using a polypyrrole nanowire film, and so for this section of the study the PpyC4S film was characterised as a standalone polymer, grown directly onto the gold coated quartz crystal as opposed to being coated onto the polypyrrole nanowires.

In addition to investigating the PpyC4S films, data for polypyrrole-polystyrene sulfonate (PpyPSS) films will be presented as a reference. PSS (Figure 4.3) is a well known immobile dopant.<sup>33, 34</sup> This will allow data from the PpyC4S films to be placed in context with the wide range of published studies on the ion exchange properties of polypyrrole doped with large anionic dopants.<sup>2, 7, 14, 15, 35</sup>

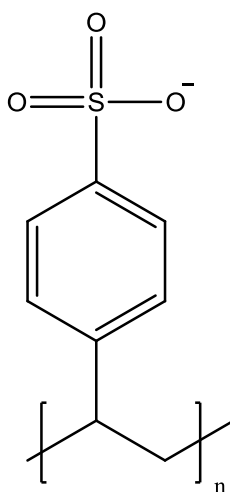


Figure 4.3: Structure of the anionic dopant polystyrene sulfonate (PSS).

## 4.2 Results and Discussion

### 4.2.1 Electropolymerisation of Polymer Films

Chronoamperometry was employed to polymerise the PpyC4S and PpyPSS films at the gold electrode surface ( $0.203 \text{ cm}^2$ ) from an aqueous solution of 0.20 M pyrrole and various concentrations of *p*-sulfonatocalix[4]arene sodium salt or poly(sodium 4-styrenesulfonate). Polymerisation in the absence of a supporting electrolyte ensures that the polypyrrole is doped with the anionic dopant of choice (C4S or PSS). Films were formed to a charge of 15.0 mC as controlling the amount of charge passed through the system controls the thickness to which the polymer forms, and so films of uniform thickness are expected.<sup>36, 37</sup> In order to confirm the validity of Equation 4.1, the growth of each polymer had to be closely monitored before the polymer could be employed as an ion exchange film.

#### 4.2.1.1 Electropolymerisation of *p*-Sulfonatocalix[4]arene-Polypyrrole Film

A constant potential of 0.55 V vs. Ag/AgCl was applied until a charge of 15.0 mC was achieved for the PpyC4S films. This applied potential was chosen as the C4S in the film can be irreversibly oxidised at higher applied potentials.<sup>21, 38</sup> PpyC4S films were formed from aqueous solutions of 0.20 M pyrrole and various concentrations of *p*-sulfonatocalix[4]arene sodium salt (0.002 M, 0.01 M and 0.10 M C4S). Although a concentration of 0.002 M may result in an electrolyte with a low ionic strength, it is in keeping with the concentrations used by Latonen *et al.* and Kim *et al.* in investigations of the ion exchange properties of polypyrrole films doped with C6S.<sup>9, 39</sup> In these studies, 0.0017 M C6S is used, and no additional salt is added; this ensures that C6S is the only dopant molecule. The growth profiles of the three PpyC4S films formed in this study are illustrated in Figure 4.4. The oxidation current, which indicates the rate of polymer growth, is plotted as a function of time. A similar profile is observed for PpyC4S films polymerised from aqueous solutions of 0.20 M Ppy and either 0.002 M C4S or 0.01 M C4S. A short induction period is observed,<sup>40</sup> which increases in duration for the PpyC4S film grown with a higher concentration of C4S (see inset, Figure 4.4). This is followed by an increase in the current until it reaches a current plateau. The observed levelling out of the current indicates that polymerisation is continuing in a unidirectional manner.<sup>41</sup> A similar current-time trend is observed for the film polymerised in 0.10 M

C4S/0.20 M Ppy, however a greater increase in the current is observed. This can indicate a faster rate of electropolymerisation. For example, the maximum current observed for a film grown in 0.002 M C4S/0.20 M Ppy is 81  $\mu\text{A}$ , whereas a maximum current of 295  $\mu\text{A}$  is recorded for the film polymerised in 0.10 M C4S/0.20 M Ppy.

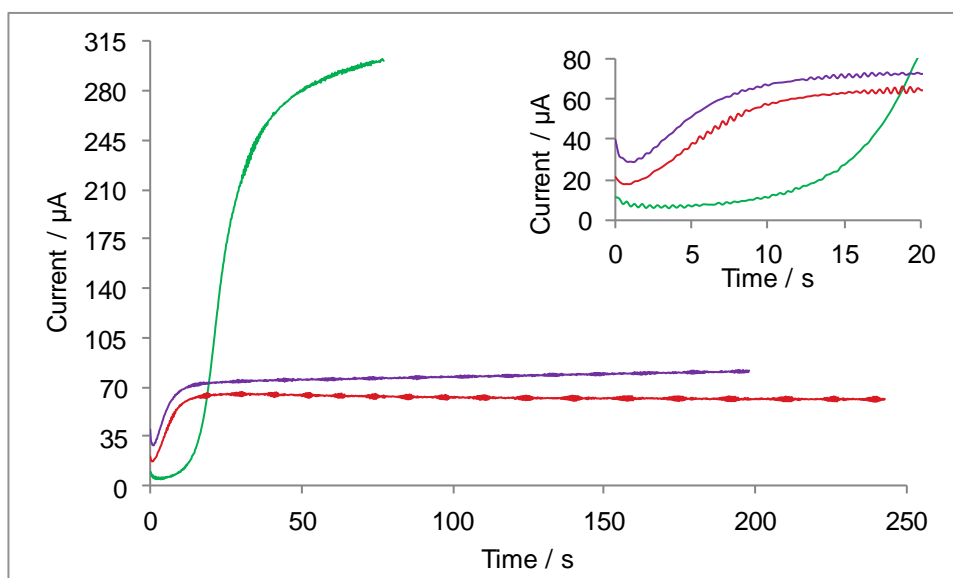


**Figure 4.4:** Current–time plot for the electropolymerisation of PpyC4S films on an Au electrode ( $0.203 \text{ cm}^3$ ), at an applied potential of 0.55 V vs. Ag/AgCl until a charge of 15.0 mC was consumed. 0.20 M Ppy and 0.002 M C4S (—), 0.01 M C4S (—) or 0.10 M C4S (—). Inset: Initial seconds of current –time plot.

The initial induction phase of the polymerisation, for the film polymerised in 0.10 M C4S/0.20 M Ppy, is slower and continues for  $\sim 10$  s, which is most likely due to the higher concentration of dopant anions in the electrolyte. A high local concentration of the dopant at the electrode interface may initially impede the diffusion of pyrrole monomer to the surface.<sup>40</sup> After  $\sim 10$  s, the highly conducting electrolyte solution allows the polymerisation to progress rapidly with a sharp rise in current. The high concentration of C4S in solution, with its ionised sulfonate groups, causes the solution to be highly conducting. This fast rate of polymerisation is also seen for Ppy-sulfonated- $\beta$ -cyclodextrin films and is attributed to the high conductivity of the electrolyte solution.<sup>42</sup>

As the literature values for the maximum film thickness (for which Equation 4.1 holds true) vary from 400 nm – 1  $\mu\text{m}$ , it was decided to keep the films formed in this study less than 300 nm thick. Growing to a charge of 15.0 mC corresponds to a charge density of 74  $\text{mC cm}^{-2}$ . Tencor profilometry measurements on PpyC4S films grown to a charge

density of  $80 \text{ mC cm}^{-2}$  showed that the thickness of these films was approximately  $250 \text{ nm}$ .<sup>21</sup> Thus it is reasonable to assume that the films formed in this study are in this acoustically thin range. Figure 4.5 shows the mass change plotted as a function of the charge passed during the synthesis of the PpyC4S polymer films with three dopant concentrations. The linear relationship between the mass variation ( $\Delta m$ ) and the charge passed ( $Q$ ) during polymerisation, suggests homogeneous film deposition. This also confirms that the films formed are rigid.<sup>2, 4, 12</sup>

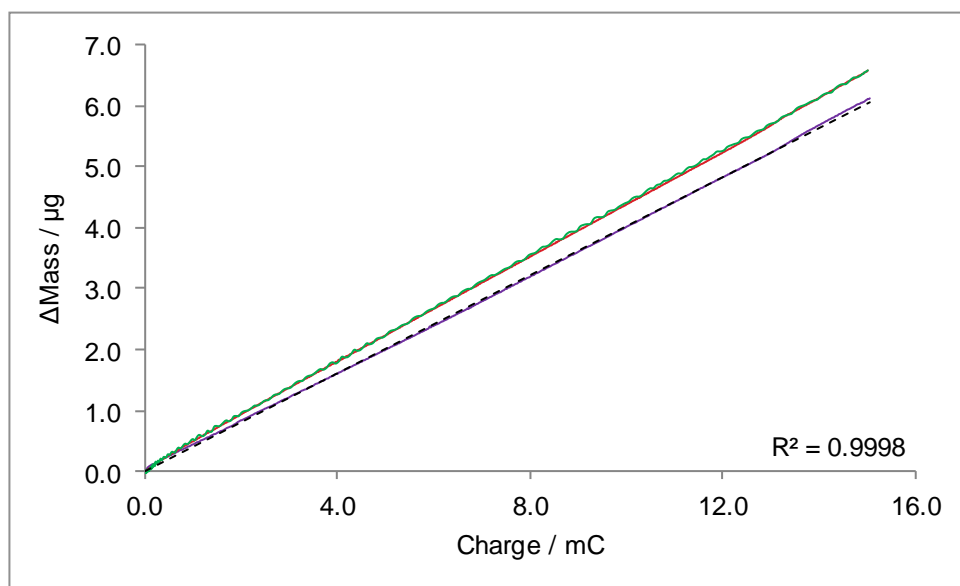


**Figure 4.5:** Mass Change as a function of charge passed during the electropolymerisation of PpyC4S films formed from aqueous solutions of 0.20 M Ppy and 0.002 M C4S (—), 0.01 M C4S (—) or 0.10 M C4S (—). 0.55 V vs. Ag/AgCl was applied until a charge of 15.0 mC was achieved. The dashed line is an example of a linear regression line applied.

#### 4.2.1.2 Electropolymerisation of Polypyrrole-Polystyrene Sulfonate Film

As there are less constraints as to what polymerisation potential could be applied, PpyPSS films were formed at applied potentials of 0.55 V, 0.70 V and 0.80 V vs. Ag/AgCl in aqueous solutions of 0.20 M pyrrole and either 0.10 M PSS or 0.002 M PSS. There is no initial drop in current measured for any of the current-time plots (Figure 4.6) which indicates no distinguishable induction time, in comparison to the short induction period observed for PpyC4S films. It has been proposed that the large PSS polyanions adsorb to the electrode providing favourable adsorption sites for pyrrole monomers.<sup>43</sup> As expected, a fast rate of electropolymerisation characterised by high currents transpires for PpyPSS films formed in solutions with high concentrations of anionic dopant, at high applied potentials (Figure 4.6 a). However, although the dopant

concentration is high (and the electrolyte highly conducting), films formed at an applied potential of 0.55 V vs. Ag/AgCl have a much slower rate of polymerisation, as polypyrrole oxidises more readily at higher applied potentials.<sup>44</sup> The lower concentration of dopant results in slower rates of electropolymerisation (Figure 4.6 b), due to the lower conductivity of the solution. For example, the maximum current observed for PpyPSS films grown at an applied potential of 0.80 V vs. Ag/AgCl was 870  $\mu\text{A}$  at a dopant concentration of 0.10 M PSS in comparison to a maximum current of 115  $\mu\text{A}$  for PpyPSS films grown with a lower dopant concentration of 0.002 M PSS.

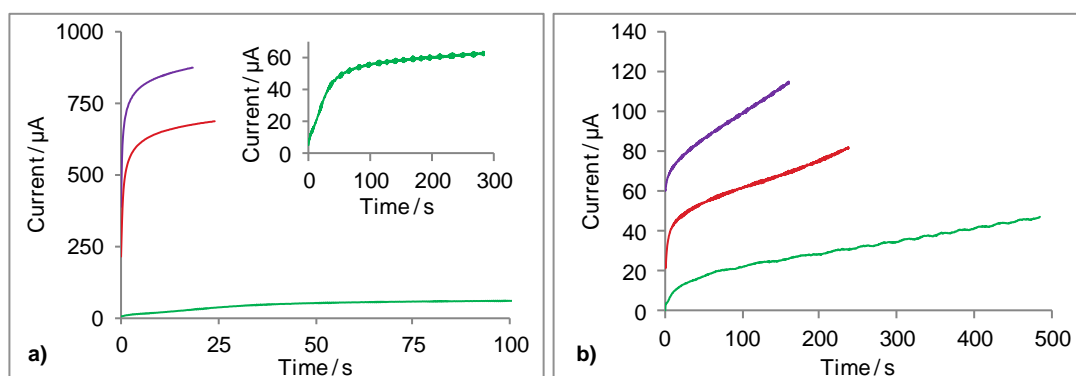


**Figure 4.6:** Current–time plots for the polymerisation of PpyPSS film; a) 0.20 M Ppy and 0.10 M PSS, applied potentials of 0.55 V (—), 0.70 V (—) or 0.80 V (—) vs. Ag/AgCl. Inset: Complete current–time plot for film formed at 0.55 V vs. SCE. b) 0.20 M Ppy and 0.002 M PSS, applied potentials of 0.55 V (—), 0.70 V (—) or 0.80 V (—) vs. Ag/AgCl. All films were formed until a charge of 15.0 mC was achieved.

Holzhauser *et al.* report a volume-to-charge ratio ( $K$ ) of  $3.0 \times 10^{-4} \text{ cm}^3 \text{ C}^{-1}$  for PpyPSS films formed potentiostatically at 0.75 V vs. SCE, from an aqueous solution of 0.10 M Ppy and 0.10 M PSS.<sup>36</sup> This value for  $K$  was calculated according to Equation 4.2, using the real thickness of the polymer film ( $\delta_{\text{film}}$ ) obtained from SEM micrographs and the charge consumed ( $Q$ ) during the polymerisation. The parameter  $A$  denotes the geometric area of the film.

$$\text{Equation 4.2} \quad \delta_{\text{film}} = K \frac{Q}{A}$$

Applying this volume-to-charge ratio to our films, which are formed to a charge of 15.0 mC (equivalent to a charge density of  $74 \text{ mC cm}^{-2}$ ), results in a thickness of approximately 220 nm. Veeco Dektak profilometry carried out by Fonner *et al.* of PpyPSS films formed to a charge density of  $80 \text{ mC cm}^{-2}$  estimate a film thickness of

< 300 nm.<sup>43</sup> Thus it is reasonable to assume that the PpyPSS films formed in this study are in the acoustically thin range.

The  $\Delta m$  vs.  $Q$  plots for PpyPSS films are shown in Figure 4.7. Films formed at both high and low PSS dopant concentrations appear to show two linear regions. This difference in the rate of change of film mass with charge supports the proposal that PSS anions adsorbed to the surface act as adsorption points for pyrrole monomers. This results in the initial fast rate of mass change, which proceeds until the polymer chains reach a length such that the potential drop along the chain prevents further chain growth. The rate of mass change then slows down as secondary polymer growth occurs on the remaining exposed electrode surface. This also elucidates the prolonged increase in current observed in Figure 4.6. The current will increase until the polymerisation becomes controlled by ion migration to the electrode surface. As this will not occur until all nucleation sites on the electrode are occupied with polymer, the continuing increase in current observed, particularly at low concentrations of PSS (Figure 4.6 b), suggests that once polymer nucleation has occurred at the adsorbed PSS polyanions, the process of secondary polymer growth is slower. Previous studies have indicated that since a linear relationship is observed for both the initial chain formation and subsequent secondary polymer growth processes, the films can be treated as rigid and free from viscoelastic effects.<sup>4, 12</sup>

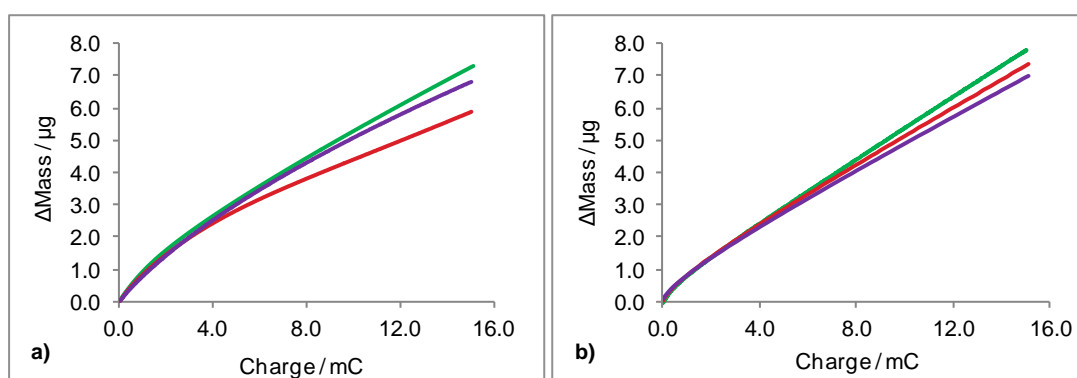


Figure 4.7: Mass change as a function of charge passed for the polymerisation of PpyPSS film; a) 0.20 M Ppy and 0.10 M PSS, applied potentials of 0.55 V (—), 0.70 V (—) or 0.80 V (—) vs. Ag/AgCl, b) 0.20 M Ppy and 0.002 M PSS, applied potentials of 0.55 V (—), 0.70 V (—) or 0.80 V (—) vs. Ag/AgCl.

## 4.2.1.3 Doping Level and Theoretical Film Thickness

The slope of the linear relationship  $\Delta m$  vs.  $Q$  allows for the calculation of the doping level ( $y$ ) of the polymer film according to a derivation of Faraday's Law of Electrolysis:

$$\text{Equation 4.3} \quad \frac{m}{Q} = \frac{(M_m) + (M_a)y}{(2 + y)F}$$

where  $m$  is the mass of the deposited polymer,  $Q$  is the amount of charged passed by the system during polymerisation,  $F$  is Faraday's constant ( $96485.34 \text{ C mol}^{-1}$ ),  $M_m$  is the molecular mass of the pyrrole monomer ( $65.07 \text{ g mol}^{-1}$ ) and  $M_a$  is the molecular mass of the dopant anion<sup>15</sup> ( $1016.79 \text{ g mol}^{-1}$  for C4S and  $183.21 \text{ g mol}^{-1}$  for PSS, which corresponds to the molecular weight of the PSS monomer unit). This relationship assumes that no neutral species or solvent are incorporated into the film during polymerisation and that the current efficiency is 100%. The results of this calculation are shown in Table 4.2 for a number of film preparations ( $n$  = number of films). The maximum possible doping level reported for Ppy films is 0.33,<sup>45</sup> which can occur when the Ppy backbone is doped with simple anions such as  $\text{Cl}^-$ . This value indicates that one anion will dope 3 pyrrole monomer units in order to neutralise the positive charge generated during polymer oxidation. The doping levels observed in this study are much less than the theoretical doping levels calculated by Bidan *et al.*, who calculated a doping level of 0.25 for polypyrrole doped with *p*-sulfonatocalix[4]arene and 0.3 calculated for polypyrrole doped with *p*-sulfonatocalix[6]arene, with both films being polymerised at an applied potential of 0.75 V vs. SCE to a charge of 7 mC on a glassy carbon electrode.<sup>22</sup> However lower than expected doping levels have been previously observed when using EQCM data<sup>46, 47</sup> and so the doping levels calculated here must be taken as indicative rather than definitive.

Theoretical doping levels calculated for PpyPSS films synthesised with high dopant concentrations of 0.10 M PSS are in keeping with the values of 0.20 - 0.22 reported for similar PpyPSS films studied by EQCM (Table 4.3).<sup>30, 44</sup> These low doping levels are expected with PpyPSS as steric hindrance will only permit a fraction of the charges on PSS to effectively dope the Ppy aromatic rings.<sup>43</sup> Thus, these films can be taken as qualitatively consistent with literature reports of PpyPSS ion exchange films. Doping levels calculated for PpyPSS formed at lower dopant concentrations of 0.002 M PSS also exhibit lower than expected values (Table 4.4). Baker *et al.* propose that this low

doping value may be due to the EQCM measuring more mass change than expected for a given charge. They suggest that this extra mass is due to a combination of solvent incorporation and non-stoichiometric usage of the PSS sulfonate site.<sup>44</sup> It has also been observed that thin films, which are generally more compact and rigid, yield lower theoretical doping levels.<sup>12</sup> In this study, the films are thin and are polymerised from a solution with a high ratio of solvent to dopant. Therefore it is very likely that the compact and rigid nature of the films, coupled with solvent incorporation are explanations for the lower than expected doping levels calculated for films formed at low dopant concentrations. Thus, as Equation 4.3 is based on the assumption that no solvent enters the film during polymerisation, the values calculated will be primarily for comparison of the films formed in this study rather than as representative of actual doping levels.

Theoretical thicknesses of dry polymer films were calculated according to Equation 4.4.

$$\text{Equation 4.4} \quad l = \left( \frac{QM_m}{nFA\rho} \right)$$

where  $l$  is the theoretical film thickness,  $Q$  is the amount of charged passed by the system during polymerisation,  $M_m$  is the molar mass of the pyrrole monomer,  $F$  is Faraday's constant (96485.34 C mol<sup>-1</sup>),  $A$  is the piezoelectrically active area of the electrode and  $\rho$  is the density of the film (where 1.27 g cm<sup>-3</sup> is the literature quoted value for PpyPSS<sup>44</sup> and 1 g cm<sup>-3</sup> is an approximation for PpyC4S as used by Akieh *et al.* for Ppy-C6S<sup>48</sup>). The parameter  $n$  is calculated from the number of electrons involved in the polymerisation added to the doping level ( $2e^- + y$ ). The thicknesses thus calculated, and displayed in Table 4.2, are close to the thickness of ~250 nm measured using Tencor profilometry for PpyC4S films formed in the same manner.<sup>21</sup> This suggests that the low doping levels calculated are reasonably accurate rather than anomalous. In contrast, when assuming the doping level to be 0.30 for *p*-sulfonatocalix[6]arene-polypyrrole, Akieh *et al.* calculated thickness values less than those they experimentally determined.<sup>48</sup> This suggests that 0.30 is a larger doping level than appropriate for this system. It must be noted however, that Equation 4.4 does not take into account any involvement of the dopant or solvent in the film thickness. It also assumes that any charge passed by the system is entirely polymerisation related, and does not take into account any charge that may be used for the formation of oligomers in solution.<sup>2</sup>

**Table 4.2:** Maximum current densities achieved during polymerisation of PpyC4S with different concentrations of dopant, at an applied potential of 0.55 V vs. Ag/AgCl. Slope and  $R^2$  values associated with  $\Delta m$  vs.  $Q$  plots and the theoretical doping levels and film thickness calculated from said plots,  $n$  = number of films formed.

C4S Dopant Conc. / g mol <sup>-1</sup>	Current Density / $\mu\text{A cm}^{-2}$	$\Delta m$ vs. $Q$ / $\mu\text{g mC}^{-1}$	Typical $R^2$	Theoretical Film Thickness / nm	Theoretical Doping Level	$n$
0.002	384 ± 10	0.423 ± 0.008	0.9999	256 ± 1.0	0.018 ± 0.002	6
0.01	313 ± 9	0.438 ± 0.005	1.0000	254 ± 0.1	0.021 ± 0.001	5
0.10	1469 ± 27	0.469 ± 0.018	0.9993	254 ± 0.6	0.028 ± 0.004	5

**Table 4.3:** Maximum current densities achieved during polymerisation of PpyPSS (0.20 M Ppy and 0.10 M PSS) at different applied potentials. Slope and  $R^2$  values associated with  $\Delta m$  vs.  $Q$  plots and the theoretical doping levels and film thickness calculated from said plots,  $n$  = number of films formed.

Applied Potential / V vs. Ag/AgCl	Current Density / $\mu\text{A cm}^{-2}$	$\Delta m$ vs. $Q$ / $\mu\text{g mC}^{-1}$	Typical $R^2$	Theoretical Film Thickness / nm	Theoretical Doping Level	$n$
0.55	307 ± 4	0.494 ± 0.006	0.9982	182 ± 0.8	0.22 ± 0.01	5
0.70	3358 ± 82	0.463 ± 0.003	0.9979	188 ± 0.8	0.17 ± 0.00	3
0.80	4345 ± 176	0.444 ± 0.006	0.9976	191 ± 0.4	0.15 ± 0.01	4

**Table 4.4:** Maximum current densities achieved during polymerisation of PpyPSS (0.20 M Ppy and 0.002 M PSS) at different applied potentials. Slope and  $R^2$  values associated with  $\Delta m$  vs.  $Q$  plots and the theoretical doping levels and film thickness calculated from said plots,  $n$  = number of films formed.

Applied Potential / V vs. Ag/AgCl	Current Density / $\mu\text{A cm}^{-2}$	$\Delta m$ vs. $Q$ / $\mu\text{g mC}^{-1}$	Typical $R^2$	Theoretical Film Thickness / nm	Theoretical Doping Level	$n$
0.55	210 ± 6	0.425 ± 0.014	0.9934	191 ± 1.6	0.12 ± 0.02	5
0.70	405 ± 5	0.384 ± 0.010	0.9786	196 ± 1.3	0.06 ± 0.01	3
0.80	552 ± 22	0.397 ± 0.014	0.9956	195 ± 1.9	0.08 ± 0.02	4

### 4.2.2 Cyclic Voltammetry and Ion Exchange Properties of PpyC4S

In order to investigate the ion exchange properties of the PpyC4S films, EQCM was employed to record the frequency change during cyclic voltammetry experiments. The films were cycled from positive to negative potentials, in 0.10 M aqueous solutions of the following salts; NaCl, CsCl, CaCl<sub>2</sub>, MgCl<sub>2</sub>, NiCl<sub>2</sub>, CrCl<sub>3</sub>, NaNO<sub>3</sub> and NaClO<sub>4</sub>, to examine the contribution of anions and cations in the electrolyte. Initially however, the effect of dopant concentration and scan rate were examined. The EQCM data were quantitatively interpreted by relating the change in mass of the polymer to the amount of charge passed, using Faraday's Law of Electrolysis (Equation 4.5):

$$\text{Equation 4.5} \quad \Delta m = \frac{M'}{zF} Q$$

where  $\Delta m$  is the change in mass of the polymer recorded during the EQCM experiment,  $M'$  is the apparent molar mass of the species moving into or out of the polymer and causing the change in mass,  $F$  is Faraday's constant,  $z$  is the charge on the ion which is being transferred and  $Q$  is the charge consumed during the process. Data were obtained from the linear regions of the mass change plotted as a function of charge.<sup>2</sup> A typical  $\Delta m$  vs.  $Q$  plot, with characteristic linear regions highlighted, is shown in Figure 4.8. Its corresponding cyclic voltammogram and massogram are shown in Figure 4.9. A massogram illustrates the observed change in film mass as a function of potential, as calculated from the change in oscillation frequency of the crystal measured by EQCM. Throughout this study, the mass changes depicted in the massograms have been normalised with respect to zero, such that each massogram is comparable.

As discussed in the introduction to this chapter, polypyrrole films can be employed as either anion or cation exchange materials, depending on the mobility of the incorporated dopant. As the film is reduced by cycling to more negative potentials, the polypyrrole backbone becomes neutral.<sup>2</sup> In order to maintain the electroneutrality of the polymer film, cations ( $C_e^+$ ) from the surrounding electrolyte are incorporated. Scheme 4.1 is the reaction expected to occur when an ideal cation exchange polymer, incorporating a large immobile dopant ( $A^-$ ), is cycled in an aqueous salt solution.



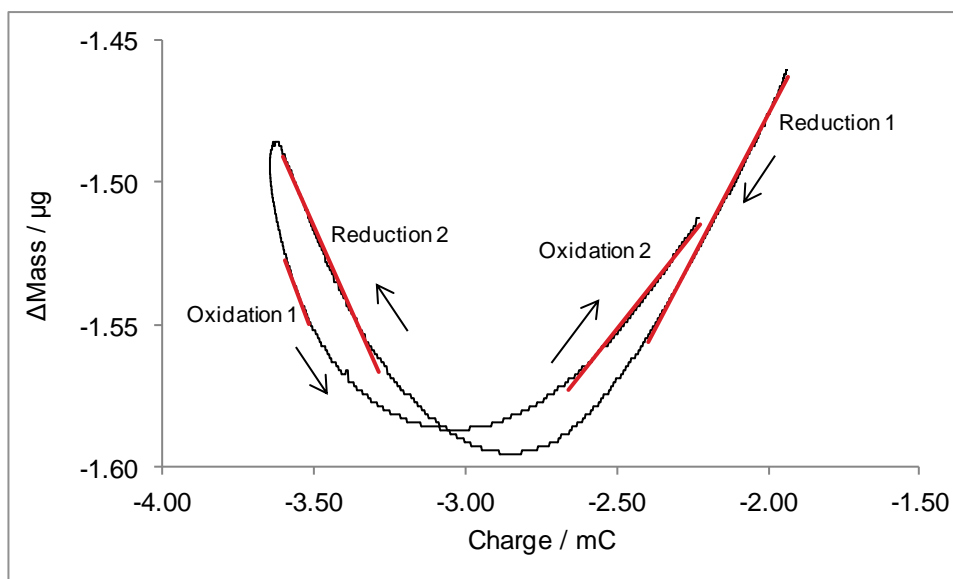


Figure 4.8: A typical  $\Delta m$  vs.  $Q$  plot of the data obtained during the cycling of PpyC4S film in 0.10 M aqueous salt solutions showing the typical linear regions which were analysed using Equation 4.5. The 5<sup>th</sup> cycle is shown.

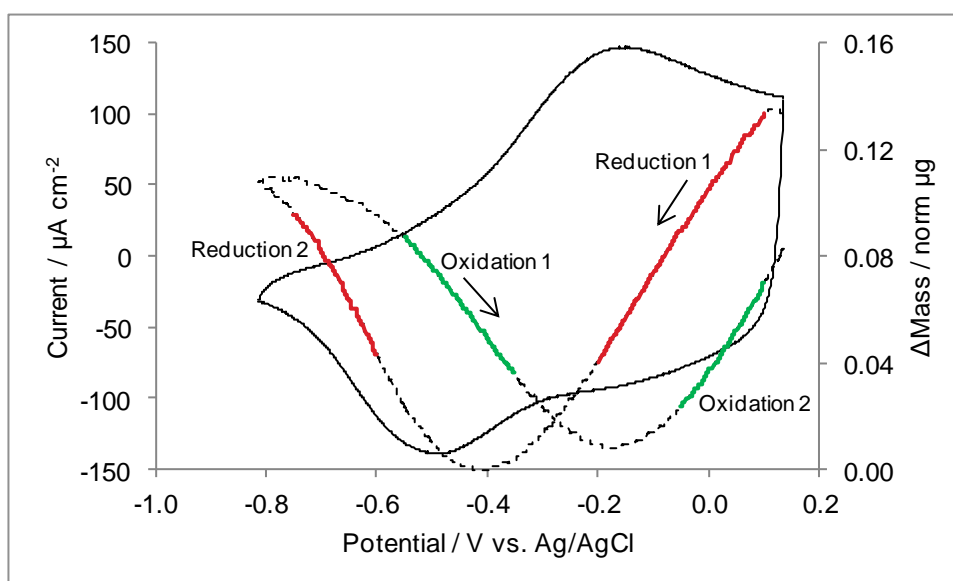
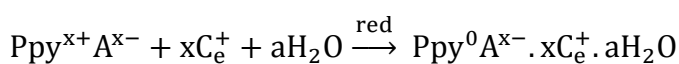


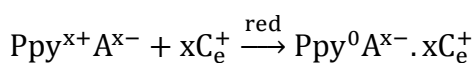
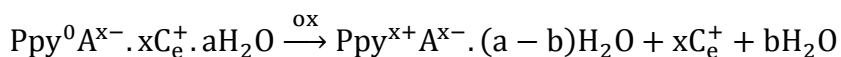
Figure 4.9: A typical cyclic voltammogram (—) and massogram (···) obtained during the cycling of a PpyC4S film in 0.10 M aqueous salt solutions showing the typical linear regions which correspond to those shown in Figure 4.7. The massogram data has been normalised with respect to zero. The 5<sup>th</sup> cycle is shown.

Figure 4.8 shows a typical  $\Delta m$  vs.  $Q$  plot obtained during this study, when a polypyrrole film, doped with a large, practically immobile dopant is cycled in an aqueous salt solution (Figure 4.9). A linear region with a negative slope is observed during the initial portion of the reduction cycle (Reduction 1) which indicates that the film is losing mass. This corresponds with the expulsion of mobile anions ( $A_e^-$ ) uptaken from the surrounding electrolyte. As the reduction step proceeds, the mass of the film begins to

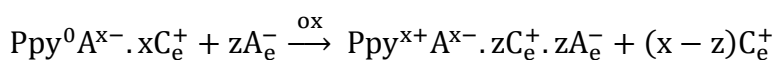
increase (Reduction 2) as cations from the electrolyte are uptaken to balance out the negative charge inferred upon the polymer by its immobilised dopant. The polymer is then cycled back up to more positive potentials which sees the expulsion of the electrolyte cations and a corresponding decrease in film mass (Oxidation 1). As the oxidation sweep continues an increase in film mass is seen, as anions from the surrounding solution are uptaken to balance the increasing positive charge on the polymer backbone. It will be shown in this chapter that the movement of ions into and out of the polymer film is most likely accompanied by solvent and that a gradual accumulation of salt in the film results. This more complex charge compensation mechanism which takes place within the studied films can be represented by Scheme 4.2 and 4.3.<sup>2</sup>



Scheme 4.2



Scheme 4.3



#### 4.2.2.1 Equilibration of PpyC4S Films

It has been observed that the first reduction cycle in the CV of a Ppy film is usually different to the subsequent cycles.<sup>49</sup> In the EQCM experiments, this large initial cathodic peak is typically accompanied by a corresponding frequency drop which equates to a substantial mass increase in the film. Often called the “break-in” period, it has been characterised as an irreversible uptake of solvent and/or cations and a restructuring of the morphology of the polymer chains.<sup>8, 44</sup> Thus it has been found that, in order to obtain a representative response of the polypyrrole film, it must be equilibrated. Steady state can be achieved either by applying a fixed potential for a set amount of time prior to CV, or by cycling for a number of cycles before utilising data from the CV.<sup>2-4, 7</sup> Figure 4.10 illustrates that although the CV of PpyC4S in 0.10 M NaCl changes over time, by cycle 5 the massogram has achieved an equilibrium response. The mass change observed during redox cycle 5 can therefore be taken as

representative of the mass changes occurring during the oxidation and reduction of the film. Thus, for all graphs in this study, cycle 5 will be plotted, unless otherwise stated. This will also preclude the need to consider dopant leaching, as at this early stage of redox cycling, it would be expected that the dopant remains in the polymer.<sup>9</sup>

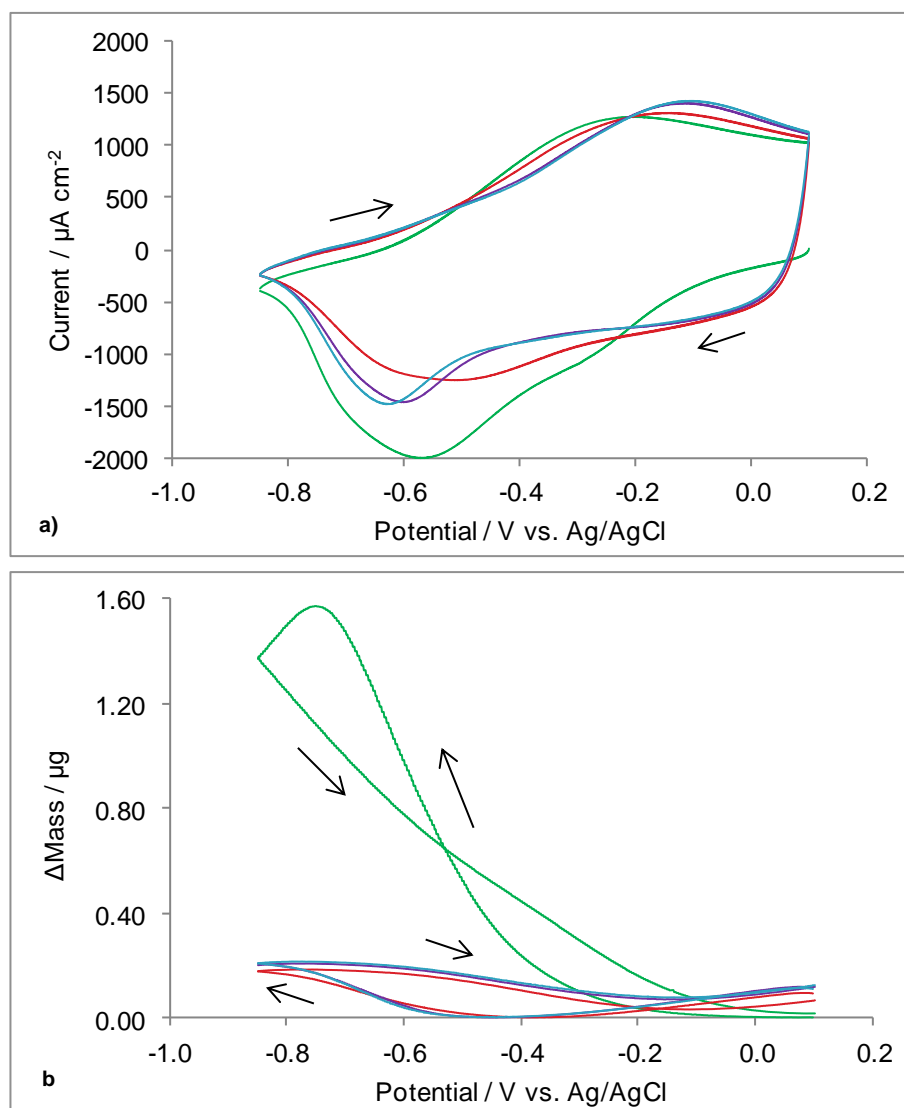


**Figure 4.100:** a) Cyclic voltammogram and b) massogram accompanying the cycling of PpyC4S films (0.20 M Ppy and 0.002 M C4S, formed to a charge of 15.0 mC) in 0.10 M NaCl solution. The potential was swept from positive to negative potentials at  $100 \text{ mV s}^{-1}$ . The following cycles are plotted: 1 (—), 5 (—), 10 (—) and 15 (—). Arrows indicate the direction of potential cycling and mass change.

#### 4.2.2.2 Effect of Film Thickness on the Redox Properties of PpyC4S

The effect of changing the charge to which the films were formed is shown using cyclic voltammetry, in Figure 4.11. Each PpyC4S film was formed at an applied potential of 0.55 V vs. Ag/AgCl in an aqueous solution of 0.20 M pyrrole and 0.002 M C4S. Films were formed to charges of 6.5, 10.0, 15.0 and 20.0 mC which are equivalent to charge densities of 32, 50, 74 and 98 mC cm<sup>-2</sup> respectively. Each film was then washed with deionised water and 0.10 M NaCl before cyclic voltammetry (CV) was carried out in an aqueous solution of 0.10 M NaCl. The data obtained for peak potential, peak separation and current density of formation for each PpyC4S film are displayed in Table 4.5.

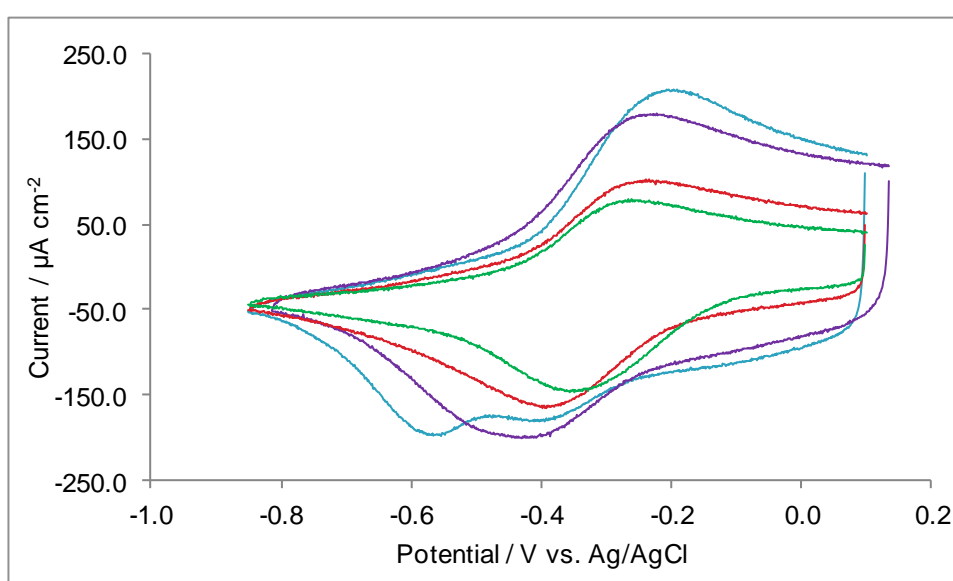


**Figure 4.11:** Cyclic voltammograms of PpyC4S films in 0.10 M NaCl solution. The potential was swept from positive to negative potentials at 10 mV s<sup>-1</sup>, cycle 5 is plotted. Each film was formed from a solution of 0.20 M Ppy and 0.002 M C4S at an applied potential of 0.55 V vs. Ag/AgCl until the following charges were achieved: 6.5 mC (—), 10.0 mC (—), 15.0 mC (—) and 20.0 mC (—).

The most apparent difference observed in the cyclic voltammogram when increasing the charge to which the film is formed, is the changing shape of the voltammogram. The reduction peak is observed to shift to more negative potentials and a second reduction peak becomes apparent for the PpyC4S film formed until a charge of 20.0 mC was achieved (Figure 4.10). It is possible that morphological changes in the PpyC4S film, with enhanced globular formation may affect the electroactivity of the polymer.<sup>50</sup> However, the emergence of a second reduction peak occurs for all PpyC4S films with repeated electrochemical cycling in aqueous 0.10 M NaCl at slow scan rates, but at later cycles for thinner films. This suggests that the additional peak is not related to the film

thickness. It is more likely related to the presence of different Ppy species, often referred to as Ppy(I) and Ppy(II), within the polymer matrix and the conversion between the two during cyclic voltammetry.<sup>51</sup> Ppy(II) tends to be short oligomeric chains, and is thought to result from hampered deprotonation of the  $\alpha$ - and  $\beta$ -positions of pyrrole in the polymerisation process.<sup>11</sup> Ppy(I) is characterised by longer chains which have a greater tendency to form  $\sigma$ -coupled chains and networks. Prolonged redox cycling of the polymer film results in the incorporation of solvent, which expands the polymer volume and results in Ppy(II) being fully or partially transformed to Ppy(I).<sup>51</sup> As the polymer is electrochemically switched between its oxidised and reduced states, the twisted polymeric chains are flattened, improving the conjugation and allowing for the formation of  $\sigma$ -bonds between chains, resulting in PPy(I).<sup>52</sup> Although C4S is known to be electroactive, its contribution to this second peak can be dismissed, as it is only oxidised at potentials above 0.7 V vs. SCE.<sup>38</sup> Moreover, the redox couple associated with the oxidation of C4S and observed for Ppy-C4S films cycled in Na<sub>2</sub>SO<sub>4</sub> is absent when the upper potential is less than 0.55 V vs. Ag/AgCl.<sup>21</sup> Thus, the potential window used in this study ensures that the electroactivity of the C4S can be ruled out. Interestingly, PpyPSS films do not exhibit a second cathodic peak, but this is most likely due to the different structural properties of the PpyPSS polymer. The PpyPSS polymer is thought to form helical Ppy chains coated with the PSS polyanion. This results in a highly structured and ordered film, with no indication of structural differences being observed with redox cycling.<sup>34</sup>

It can be clearly seen in Figure 4.11 that the peak current increases as the charge to which the film was formed increases. As charge and film thickness are connected, increasing the charge results in a thicker film and thus the higher polymer surface area explains the increase in current.<sup>53</sup> It can also be seen that there is a shift in both anodic ( $E_p^A$ ) and cathodic ( $E_p^C$ ) peak potentials, which is consistent with Nernstian behaviour and results in a larger peak separation with increasing film thickness (Table 4.5). The cathodic peak also appears sharper or more defined than the broad anodic peak which indicates that the rate of reduction of the PpyC4S films is faster than the rate of oxidation. This sharper cathodic peak is often seen for polypyrrole films doped with large immobile dopants,<sup>54</sup> and it suggests that the polymer is acting as a cation exchange material.<sup>55</sup> The sharp appearance of the cathodic peak has been

attributed to the immobility of the dopant anions and the dominance of the cations in solution in maintaining the electroneutrality of the polymer.<sup>55</sup>

**Table 4.5:** Maximum current densities achieved during polymerisation of PpyC4S (0.20 M Ppy and 0.002 M C4S) when grown to different charges. Peak potentials ( $E_p^C$  and  $E_p^A$ ) and peak separation ( $\Delta E_p$ ) recorded for these PpyC4S films cycled in 0.10 M NaCl at  $10 \text{ mV s}^{-1}$ . Increase in mass during reduction and associated  $\text{Na}^+$  uptake ( $\Delta m^C / \mu\text{g}$ ),  $n$  = number of films examined.

Charge of Growth / mC	Current Density / $\mu\text{A cm}^{-2}$	$E_p^C$ / V vs. Ag/AgCl	$E_p^A$ / V vs. Ag/AgCl	$\Delta E_p$ / V	$\Delta m^C$ / $\mu\text{g}$	$n$
6.5	$52 \pm 7$	$-0.33 \pm 0.02$	$-0.27 \pm 0.01$	0.06	$0.04 \pm 0.00$	3
10	$53 \pm 7$	$-0.39 \pm 0.01$	$-0.29 \pm 0.02$	0.10	$0.06 \pm 0.00$	3
15	$72 \pm 2$	$-0.42 \pm 0.01$	$-0.24 \pm 0.01$	0.18	$0.07 \pm 0.00$	3
20	$47 \pm 2$	$-0.40 \pm 0.00$ $-0.58 \pm 0.01$	$-0.19 \pm 0.02$	0.39	$0.11 \pm 0.01$	3

Figure 4.12 shows the massogram plots associated with the CVs in Figure 4.11. The ion exchange abilities of the PpyC4S films can be clearly observed, with the mass of the film changing with the reduction and oxidation of the PpyC4S films. As explained in Section 4.1 and 4.2.2, the reduction of a polymer doped with large dopant ions is accompanied by ingress of electrolyte cations, in order to maintain electroneutrality.<sup>15</sup> This can be seen in the increase in mass at negative potentials (the left hand side of the plot). It can also be seen in Figure 4.12, that the egress and ingress of solution anions ( $\text{Cl}^-$ ) which occur at more positive potentials (right hand side of plot) become more apparent as the film thickness increases. This may be due to the effect of film thickness on polymer morphology and porosity. Thicker films result in an increase in the density of the polymer matrix, which may slow down the movement of ions from the electrolyte, into and out of the polymer.<sup>56</sup> For the rest of this chapter, all polymers discussed were formed potentiostatically until a charge of 15.0 mC was achieved.

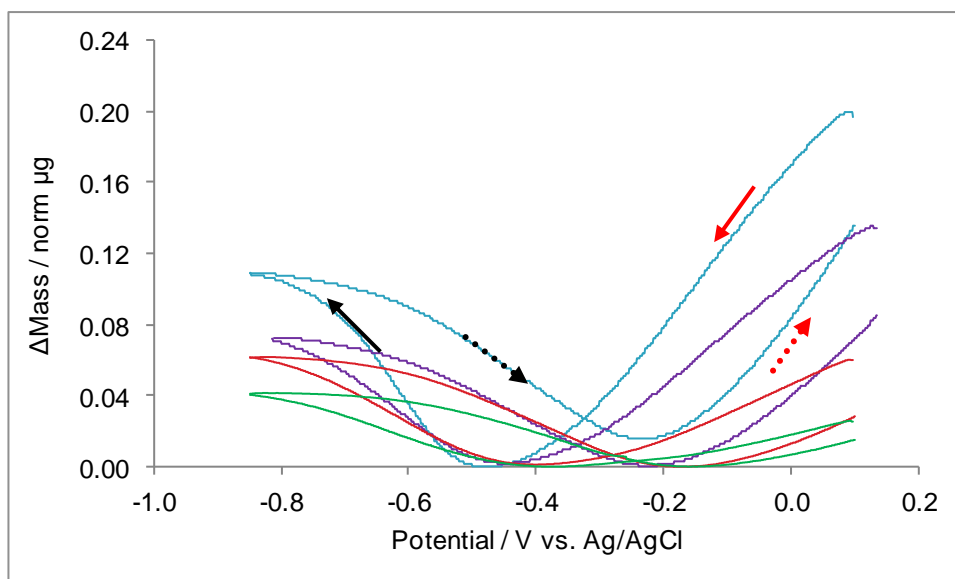
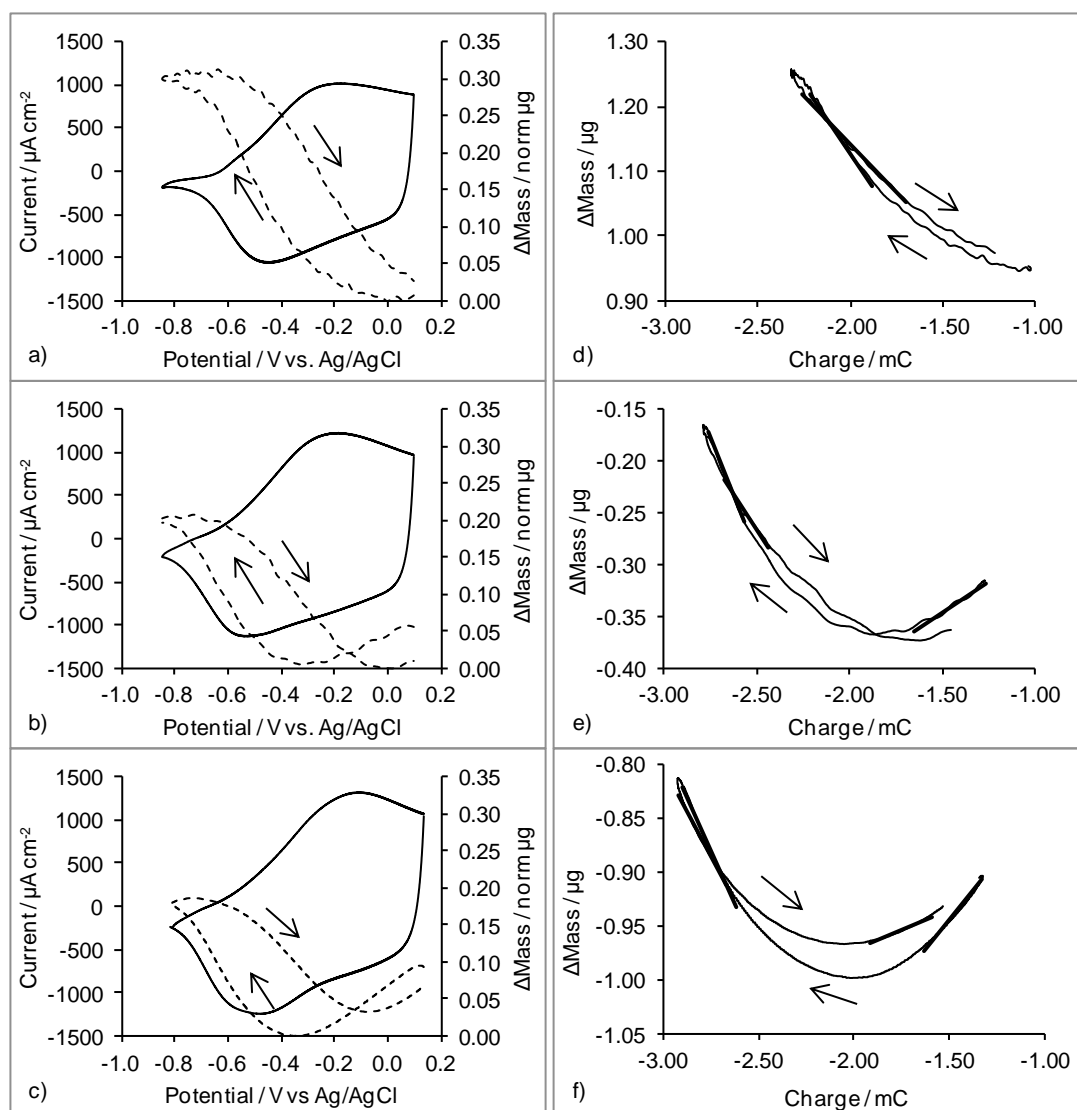


Figure 4.11: Massograms of PpyC4S films in an aqueous 0.10 M NaCl solution. The potential was swept from positive to negative potentials at  $10 \text{ mV s}^{-1}$ , cycle 5 is plotted. Each film was formed from a solution of 0.20 M Ppy and 0.002 M C4S at an applied potential of 0.55 V vs. Ag/AgCl until the following charges were achieved: 6.5 mC (—), 10.0 mC (—), 15.0 mC (—) and 20.0 mC (—).  $\text{Na}^+$  ingress  $\leftarrow$  and egress  $\cdots>$ ,  $\text{Cl}^-$  egress  $\leftarrow$  and ingress  $\cdots>$ .

## 4.2.2.3 Effect of Dopant Concentration

PpyC4S films were electropolymerised from three solutions, containing 0.20 M pyrrole and either 0.10 M, 0.01 M or 0.002 M C4S. These were formed to a charge of 15.0 mC ( $74 \text{ mC cm}^{-2}$ ) at an applied potential of 0.55 V vs. Ag/AgCl. The films were rinsed as described in Section 4.2.2.1 and cycled in 0.10 M NaCl aqueous solution. Figure 4.13 (a, b, c) show the CV and associated massograms for PpyC4S films formed at each dopant concentration, and plots of  $\Delta m$  as a function of charge during redox cycling for each film are depicted in Figure 4.13 (d, e, f).



**Figure 4.12:** Cyclic voltammogram (—) and massogram (---) of PpyC4S grown from an aqueous solution of 0.20 M Ppy and a) 0.10 M, b) 0.01 M and c) 0.002 M of C4S, to a charge of 15.0 mC. Scan rate  $100 \text{ mV s}^{-1}$  in 0.10 M NaCl aqueous solution. The  $\Delta m$  vs. Q plots corresponding to a, b and c are depicted in plots d, e and f respectively. Arrows indicate the direction of scan, cycle 5 is plotted.

The general features of the CVs are similar for each dopant concentration, yet the massograms and  $\Delta m$  vs.  $Q$  plots change gradually from depicting an ideal cation ingress/ egress (Figure 4.13 a/d) to an emergence of mixed cation/anion egress/ingress with decreasing dopant concentration (Figure 4.13 b/e and c/f). In Figure 4.13 (b) and (c), during the initial stages of the reduction (between + 0.10 V to - 0.16 / - 0.2 V vs. Ag/AgCl) a decrease in mass is observed which can be related to the simultaneous movement of cations ( $\text{Na}^+$ ) into and anions ( $\text{Cl}^-$ ) out of the polymer film. Once the polymer backbone is fully reduced (- 0.60 V to - 0.80 V vs. Ag/AgCl), the negative charges inferred upon the film by the incorporated C4S are compensated by the ingress of  $\text{Na}^+$  from the electrolyte. During the reverse anodic scan, the polymer becomes re-oxidised and  $\text{Na}^+$  ions are ejected from the film to maintain charge neutrality, resulting in a decrease in mass. A small increase in mass ( $0.035 \pm 0.001 \mu\text{g}$ ) is observed between the potentials of 0.0 V to + 0.1 V for PpyC4S formed with low dopant concentrations (Figure 4.13 c). As the theoretical doping levels are the lowest for this polymer, it is expected that the incorporated C4S is not sufficient to fully balance the positive charges on the oxidised polymer backbone, and so a small amount of  $\text{Cl}^-$  from the electrolyte is taken up.

Tables 4.6 and 4.7 detail the mass changes calculated from the measured change in frequency and the apparent molar mass calculated using Equation 4.5. It can be observed that the mass increase during the reduction cycle is greater for the polymer containing the higher amount of C4S dopant (0.10 M), indicating that an increase of dopant concentration does require a greater number of cations to enter the polymer for charge compensation. Similar results are observed for Ppy-sulfonated- $\beta$ -cyclodextrin ( $\beta$ -CD) systems, and the increase in cation exchange is explained by the greater number of negatively charged sulfate moieties present at higher concentrations of  $\beta$ -CD.<sup>57</sup> In comparing the apparent molar mass of incorporated ions to the expected molar mass, it is immediately obvious that  $\text{Na}^+$  ions are not solely responsible for the mass increase during film reduction (Table 4.6). It is generally accepted that ion bound solvent accompanies cation ingress<sup>7, 46</sup> and so it is estimated that 1  $\text{H}_2\text{O}$  molecule accompanies the insertion of  $\text{Na}^+$  ions at a scan rate of  $100 \text{ mV s}^{-1}$ . The apparent molar mass calculated for mass change during the initial stages of reduction correspond directly with neither  $\text{Na}^+$  ingress nor  $\text{Cl}^-$  egress, which suggest that these processes occur concurrently.

A similar trend is observed during the oxidation cycle in which a greater mass loss is observed for polymers containing the higher amount of C4S dopant (Table 4.7). It therefore appears that less solvent accompanies the egress of  $\text{Na}^+$  than during uptake, in films formed with higher dopant concentrations, but it has been reported that solvent expulsion is slower than its insertion.<sup>58</sup>

**Table 4.6:** The apparent molar mass of ions ( $M'$ ), calculated from the respective slopes ( $\Delta m$  vs.  $Q$ ) for the reduction sweep of PpyC4S films, formed with different dopant concentrations, cycled in 0.10 M NaCl at 100 mV  $s^{-1}$ . The mass change detected by EQCM is also listed. The + and – signs are employed to indicate mass increase and decrease respectively, n = number of films tested.

Dopant Conc. / M	Cycle Segment	$\Delta m$ vs. $Q$ / $\mu\text{g C}^{-1}$	$M'$ / $\text{g mol}^{-1}$	Expected $M'$ / $\text{g mol}^{-1}$ (dominant ion)	Measured $\Delta m$ / $\mu\text{g}$	n
0.10	Reduction	+ 423.9 ± 21.7	+ 40.9 ± 2.1	+ 23.0 ( $\text{Na}^+$ )	+ 0.34 ± 0.02	3
0.01	Reduction 1	– 126.4 ± 6.4	– 12.2 ± 0.6	– 35.5 ( $\text{Cl}^-$ )	– 0.06 ± 0.00	2
	Reduction 2	+ 340.1 ± 80.9	+ 32.8 ± 7.8	+ 23.0 ( $\text{Na}^+$ )	+ 0.20 ± 0.01	2
0.002	Reduction 1	– 208.9 ± 16.0	– 20.2 ± 1.6	– 35.5 ( $\text{Cl}^-$ )	– 0.10 ± 0.01	3
	Reduction 2	+ 420.1 ± 11.7	+ 40.5 ± 1.1	+ 23.0 ( $\text{Na}^+$ )	+ 0.18 ± 0.01	3

**Table 4.7:** The apparent molar mass of ions ( $M'$ ), calculated from the respective slopes ( $\Delta m$  vs.  $Q$ ) for the oxidation sweep of PpyC4S films, formed with different dopant concentrations, cycled in 0.10 M NaCl at 100 mV  $s^{-1}$ . The mass change detected by EQCM is also listed. The + and – signs are employed to indicate mass increase and decrease respectively, n = number of films tested.

Dopant Conc. / M	Cycle Segment	$\Delta m$ vs. $Q$ / $\mu\text{g C}^{-1}$	$M'$ / $\text{g mol}^{-1}$	Expected $M'$ / $\text{g mol}^{-1}$ (dominant ion)	Measured $\Delta m$ / $\mu\text{g}$	n
0.10	Oxidation	– 282.5 ± 21.1	– 27.3 ± 2.0	– 23.0 ( $\text{Na}^+$ )	– 0.30 ± 0.01	3
0.01	Oxidation	– 277.2 ± 4.8	– 26.7 ± 0.5	– 23.0 ( $\text{Na}^+$ )	– 0.21 ± 0.01	2
0.002	Oxidation 1	– 342.6 ± 12.5	– 33.1 ± 1.2	– 23.0 ( $\text{Na}^+$ )	– 0.16 ± 0.01	3
	Oxidation 2	+ 81.0 ± 4.6	+ 7.8 ± 0.4	+ 35.5 ( $\text{Cl}^-$ )	+ 0.04 ± 0.00	3

## 4.2.2.4 Effect of Scan Rate

PpyC4S films were electropolymerised from a solution containing 0.20 M pyrrole and 0.002 M C4S. These were formed to a charge of 15.0 mC ( $74 \text{ mC cm}^{-2}$ ) at an applied potential of 0.55 V vs. Ag/AgCl. The films were rinsed as described in Section 4.2.2.1 and cycled in 0.10 M NaCl aqueous solution at scan rates of 10, 50 and 100  $\text{mV s}^{-1}$ . It can be seen from Figure 4.14 that both the anodic and cathodic peak currents increase with increasing scan rates. From the massograms and analysis carried out using Faraday's Law of Electrolysis on data obtained at lower scan rates, it would appear that a more complicated ion/solvent exchange occurs at the lower scan rates of 50  $\text{mV s}^{-1}$  and 10  $\text{mV s}^{-1}$ .

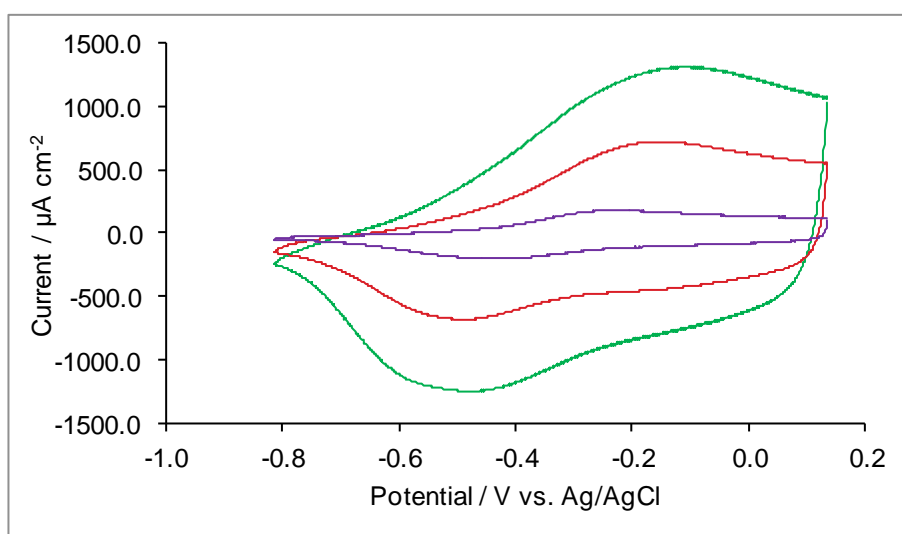
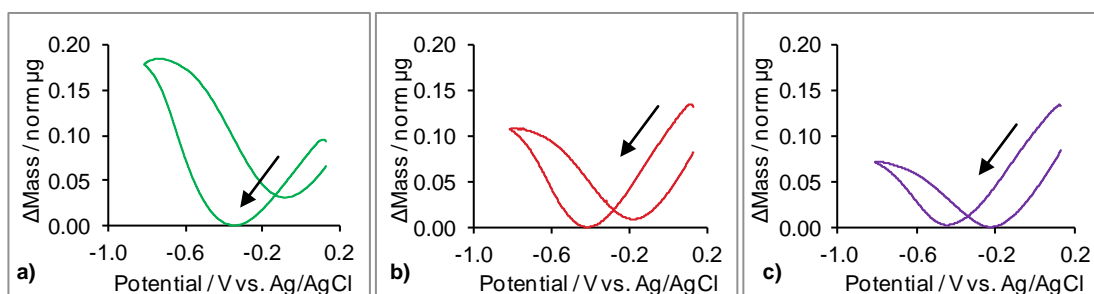


Figure 4.13: Cyclic voltammograms of PpyC4S grown from an aqueous solution of 0.20 M Ppy and 0.002 M C4S, to a charge of 15.0 mC. PpyC4S films were cycled in 0.10 M NaCl aqueous solution at scan rates of 100  $\text{mV s}^{-1}$  (—), 50  $\text{mV s}^{-1}$  (—) and 10  $\text{mV s}^{-1}$  (—). Cycle 5 is plotted.

Table 4.8: Peak potentials ( $E_p^C$  and  $E_p^A$ ) and peak separation ( $\Delta E_p$ ) recorded for PpyC4S films cycled in 0.10 M NaCl at 100  $\text{mV s}^{-1}$ , 50  $\text{mV s}^{-1}$  and 10  $\text{mV s}^{-1}$ , n = number of films tested.

Scan Rate / $\text{mV s}^{-1}$	$E_p^C$ / V vs. Ag/AgCl	$E_p^A$ / V vs. Ag/AgCl	$\Delta E_p$ / V	n
100	$-0.50 \pm 0.00$	$-0.14 \pm 0.02$	0.36	3
50	$-0.49 \pm 0.00$	$-0.19 \pm 0.01$	0.30	3
10	$-0.42 \pm 0.01$	$-0.24 \pm 0.01$	0.18	3

The massograms obtained at each scan rate are also reasonably similar in shape and resemble the response of a polymer doped with an immobile dopant<sup>2</sup> (Figure 4.15). The reduction cycle yields two linear regions in the  $\Delta m$  vs.  $Q$  plot. The first linear region (Reduction 1) occurs when reducing the potential from approximately 0.10 V to -0.30 V, -0.40V and -0.45 V vs. Ag/AgCl at scan rates of 100  $\text{mV s}^{-1}$ , 50  $\text{mV s}^{-1}$  and 10  $\text{mV s}^{-1}$  respectively. This linear region corresponds to a loss in film mass. This is consistent with the expulsion of  $\text{Cl}^-$  ions and associated water uptaken by the film during the previous oxidation sweep. Once the potential is swept beyond potentials -0.30 V, -0.40V and -0.45 V vs. Ag/AgCl at scan rates of 100  $\text{mV s}^{-1}$ , 50  $\text{mV s}^{-1}$  and 10  $\text{mV s}^{-1}$ , a second linear region emerges, between approximately -0.50 V and -0.80 V vs. Ag/AgCl, corresponding to an increase in film mass (Reduction 2). It is at this point that the polymer has become significantly reduced and  $\text{Na}^+$  ions and associated water molecules from the electrolyte solution are uptaken to balance the charge on the immobile anionic calixarene dopant. At each scan rate, mass lost during the first portion of the reduction sweep are comparable, but the mass increase measured during the second portion increases with increasing scan rate (Table 4.9), with twice as much mass being gained at 100  $\text{mV s}^{-1}$  compared to 10  $\text{mV s}^{-1}$  which suggests that cation exchange becomes more dominant at this higher scan rate.



**Figure 4.14:** Massograms of PpyC4S grown from an aqueous solution of 0.20 M Ppy and 0.002 M of C4S, to a charge of 15.0 mC. PpyC4S films were cycled in 0.10 M NaCl aqueous solution at scan rates of a) 100  $\text{mV s}^{-1}$ , b) 50  $\text{mV s}^{-1}$  and c) 10  $\text{mV s}^{-1}$ . Cycle 5 is plotted. Increasing complexity in the ion transfer processes is apparent with decreasing scan rate. Arrows indicate the direction of the initial reduction sweep.

**Table 4.9: Measured  $\Delta m$  and potential ranges of linear regions of the reduction sweep of  $\Delta m$  vs.  $Q$  plots for PpyC4S films (0.20 M Ppy / 0.002 M C4S) cycled in 0.10 M NaCl at scan rates of 100, 50 and 10  $\text{mV s}^{-1}$ .**

Scan Rate / $\text{mV s}^{-1}$	Cycle Segment	Potential Range / V vs. Ag/AgCl	Measured $\Delta m$ / $\mu\text{g}$	n
100	Reduction 1	+ 0.10 to - 0.16	- 0.10 $\pm$ 0.01	3
	Reduction 2	- 0.61 to - 0.82	+ 0.18 $\pm$ 0.01	3
50	Reduction 1	+ 0.10 to - 0.20	- 0.11 $\pm$ 0.01	4
	Reduction 2	- 0.60 to - 0.75	+ 0.12 $\pm$ 0.01	4
10	Reduction 1	+ 0.10 to - 0.19	- 0.12 $\pm$ 0.01	5
	Reduction 2	- 0.60 to - 0.80	+ 0.08 $\pm$ 0.00	5

The oxidation cycle similarly yields two linear regions in the  $\Delta m$  vs.  $Q$  plot at each scan rate. The potential ranges over which these occur are less similar than those of the reduction cycle (Table 4.10). The first linear region (Oxidation 1) follows on from the linear region denoted Reduction 2 and occurs as the potential is swept to more positive potentials, corresponding to a loss in film mass. This is the expulsion of  $\text{Na}^+$  cations and associated water. As expected, at higher scan rates, more mass loss is observed, since more ions and solvent were uptaken during the previous reduction sweep. Once the potential is swept as far as approximately - 0.10 V vs. Ag/AgCl, the polymer is significantly oxidised and the measured mass increases as  $\text{Cl}^-$  ions and associated water molecules are uptaken again from the electrolyte. This linear region (Oxidation 2) is observed for the potential range in the region of - 0.10 V to 0.10 V vs. Ag/AgCl. The mass lost during the initial oxidation sweep (Oxidation 1) increases with increasing scan rate, while the mass gained through the ingress of  $\text{Cl}^-$  ions and water molecules increases slightly at scan rates 50  $\text{mV s}^{-1}$  and 10  $\text{mV s}^{-1}$  (Oxidation 2). Interestingly, when comparing the mass gained during the reduction of the polymer (Reduction 2, Table 4.9) to the mass lost during its oxidation (Oxidation 1, Table 4.10), it can be observed that at lower scan rates, all mass uptaken is subsequently released, whereas at a scan rate of 100  $\text{mV s}^{-1}$ , some mass is retained by the film. This may be attributed to the slow rate at which solvent is expelled from the film.<sup>4</sup> At slow scan rates, more mass is uptaken by the film during the oxidation sweep (Oxidation 2, Table 4.10) than at higher scan rates. As the polymer is reduced again, more mass is lost than was uptaken during Oxidation 2 which suggests that solvent egress accompanies the expulsion of the  $\text{Cl}^-$  ions.

**Table 4.10:** Measured  $\Delta m$  and potential ranges of linear regions of the oxidation sweep of  $\Delta m$  vs.  $Q$  plots for PpyC4S films (0.20 M Ppy/0.002 M C4S) cycled in 0.10 M NaCl aqueous solution at scan rates 100, 50 and 10  $\text{mV s}^{-1}$ .

Scan Rate / $\text{mVs}^{-1}$	Cycle Segment	Potential Range / V vs. Ag/AgCl	Measured $\Delta m$ / $\mu\text{g}$	n
100	Oxidation 1	- 0.61 to - 0.34	- 0.16 $\pm$ 0.01	3
	Oxidation 2	+ 0.04 to + 0.10	+ 0.04 $\pm$ 0.00	3
50	Oxidation 1	- 0.55 to - 0.35	- 0.12 $\pm$ 0.02	4
	Oxidation 2	- 0.05 to + 0.10	+ 0.06 $\pm$ 0.01	4
10	Oxidation 1	- 0.75 to - 0.25	- 0.08 $\pm$ 0.00	5
	Oxidation 2	- 0.02 to + 0.10	+ 0.07 $\pm$ 0.01	5

The results of the quantitative analysis of the  $\Delta m$  vs.  $Q$  plot using Equation 4.5 are shown in Table 4.11. Through this analysis the difference in response of the PpyC4S films as a function of scan rate becomes more apparent. At high scan rates, and thus low experimental timescales, the cation exchange process becomes dominant and the largest mass change occurs at more negative potentials. The apparent molar mass of the species being uptaken during Reduction 2 (- 0.60 V to - 0.80 V vs. Ag/AgCl) were calculated to be 40.5, 23.3 and 12.4  $\text{g mol}^{-1}$  for scan rates 100, 50 and 10  $\text{mV s}^{-1}$  respectively. If  $\text{Na}^+$  ions were solely responsible for the mass increase during this stage of the reduction cycle, the molar mass would be 23.0  $\text{g mol}^{-1}$ . While the apparent molar mass calculated for 100  $\text{mV s}^{-1}$  is higher than expected, this can be explained by the solvation of the  $\text{Na}^+$  ions. This value would correspond with 1  $\text{H}_2\text{O}$  molecule being uptaken with the  $\text{Na}^+$ . Akieh *et al.* have also observed mass changes greater than the theoretical values for a PpyPSS film, which they also attributed to solvent molecule uptake.<sup>2</sup> Interestingly, at 10  $\text{mV s}^{-1}$ , the apparent molar mass calculated is less than that of  $\text{Na}^+$ . This is most likely due to the movement of neutral species such as salts or water out of the film in tandem with the ingress of  $\text{Na}^+$  ions. It has also been suggested that hydronium cations ( $\text{H}_3\text{O}^+$ ) in solution may compete with the metal cation in the cation exchange process.<sup>39</sup> This could explain the difference in the calculated molar mass of the exchanged species. It has also been observed that at higher scan rates, ion movement is kinetically favoured, and the involvement of neutral species is “frozen out” of the process.<sup>4</sup> At lower scan rates, the experimental time frame is much longer and so the movement of neutral and hydronium species competes with ion movement, often occurring in opposing

directions. This can be seen in both Figure 4.15 and Table 4.11, where the response of the film becomes more symmetrical at lower scan rates and the apparent molar mass uptaken and released during the reduction and oxidation of the polymer are more comparable. The apparent molar mass of the species uptaken during Oxidation 2 were calculated to be 7.8, 11.9 and 11.3  $\text{g mol}^{-1}$  for scan rates 100, 50 and 10  $\text{mV s}^{-1}$  respectively. These values are much lower than the expected molar mass of  $\text{Cl}^-$  ions, which suggests that neutral species and water also move out of the film in tandem with the uptake of the  $\text{Cl}^-$  ions.

**Table 4.11:** The apparent molar mass of ions ( $M'$ ), calculated from the respective slopes ( $\Delta m$  vs.  $Q$ ) of PpyC4S films (0.20 M Ppy/0.002 M C4S) in 0.10 M NaCl at scan rates of 100  $\text{mV s}^{-1}$ , 50  $\text{mV s}^{-1}$  and 10  $\text{mV s}^{-1}$ . Expected  $M'$  are listed, assuming that  $\text{Cl}^-$  is the dominant ion exchanged during sweep segments Reduction 1 and Oxidation 2 and  $\text{Na}^+$  is the dominant ion exchanged during the sweep segments Reduction 2 and Oxidation 1. The + and – signs are employed to indicate mass increase and decrease respectively, n = number of films tested.

Scan Rate / $\text{mV s}^{-1}$	Expected $M'$ / $\text{g mol}^{-1}$ (Cation)	$M'$ / $\text{g mol}^{-1}$ Reduction 2 Cation ingress	$M'$ / $\text{g mol}^{-1}$ Oxidation 1 Cation egress	Expected $M'$ / $\text{g mol}^{-1}$ (Anion)	$M'$ / $\text{g mol}^{-1}$ Reduction 1 Anion egress	$M'$ / $\text{g mol}^{-1}$ Oxidation 2 Anion ingress	n
100	23.0 ( $\text{Na}^+$ )	+ 40.5 $\pm$ 1.1	– 33.1 $\pm$ 1.2	35.5 ( $\text{Cl}^-$ )	– 20.2 $\pm$ 1.6	+ 7.8 $\pm$ 0.4	3
50	23.0 ( $\text{Na}^+$ )	+ 23.3 $\pm$ 0.3	– 26.9 $\pm$ 2.7	35.5 ( $\text{Cl}^-$ )	– 17.7 $\pm$ 1.5	+ 11.9 $\pm$ 1.0	4
10	23.0 ( $\text{Na}^+$ )	+ 12.4 $\pm$ 0.7	—	35.5 ( $\text{Cl}^-$ )	– 16.1 $\pm$ 0.8	+ 11.3 $\pm$ 0.7	5

In summary, it would appear that the ion exchange behaviour of the PpyC4S film is scan rate dependent. Cation exchange predominates at high scan rates and the calculated molar mass values suggest the solvation of the uptaken  $\text{Na}^+$ . At lower scan rates, neutral species and possibly hydronium cation movement begins to compete with the  $\text{Na}^+/\text{Cl}^-$  ion exchange and so the mass changes due to cation and anion movement become more symmetrical. This competition also results in calculated molar masses lower than expected, as neutral species transfer often occurs in the opposite direction to ion movement.

It was concluded in Section 4.2.2.3 that dopant concentration also had an impact on the ion exchange behaviour of the PpyC4S films. At higher dopant concentrations, cation exchange predominates. Therefore, the effect of scan rate was also investigated for PpyC4S films prepared with high concentrations of dopant. Figure 4.16 depicts cyclic voltammograms, massograms and  $\Delta m$  vs.  $Q$  plots obtained for films formed from a solution containing 0.20 M pyrrole and 0.10 M C4S. These were formed to a charge of 15.0 mC ( $74 \text{ mC cm}^{-2}$ ) at an applied potential of 0.55 V vs. Ag/AgCl and cycled in 0.10 M NaCl aqueous solution at scan rates of  $100 \text{ mV s}^{-1}$  and  $10 \text{ mV s}^{-1}$ . As observed for films formed at dopant concentrations of 0.002 M C4S, the anodic and cathodic peak currents observed for PpyC4S films formed at a dopant concentration of 0.10 M C4S decrease with a decrease in scan rates from  $100 \text{ mV s}^{-1}$  to  $10 \text{ mV s}^{-1}$  (Figure 4.16 a).

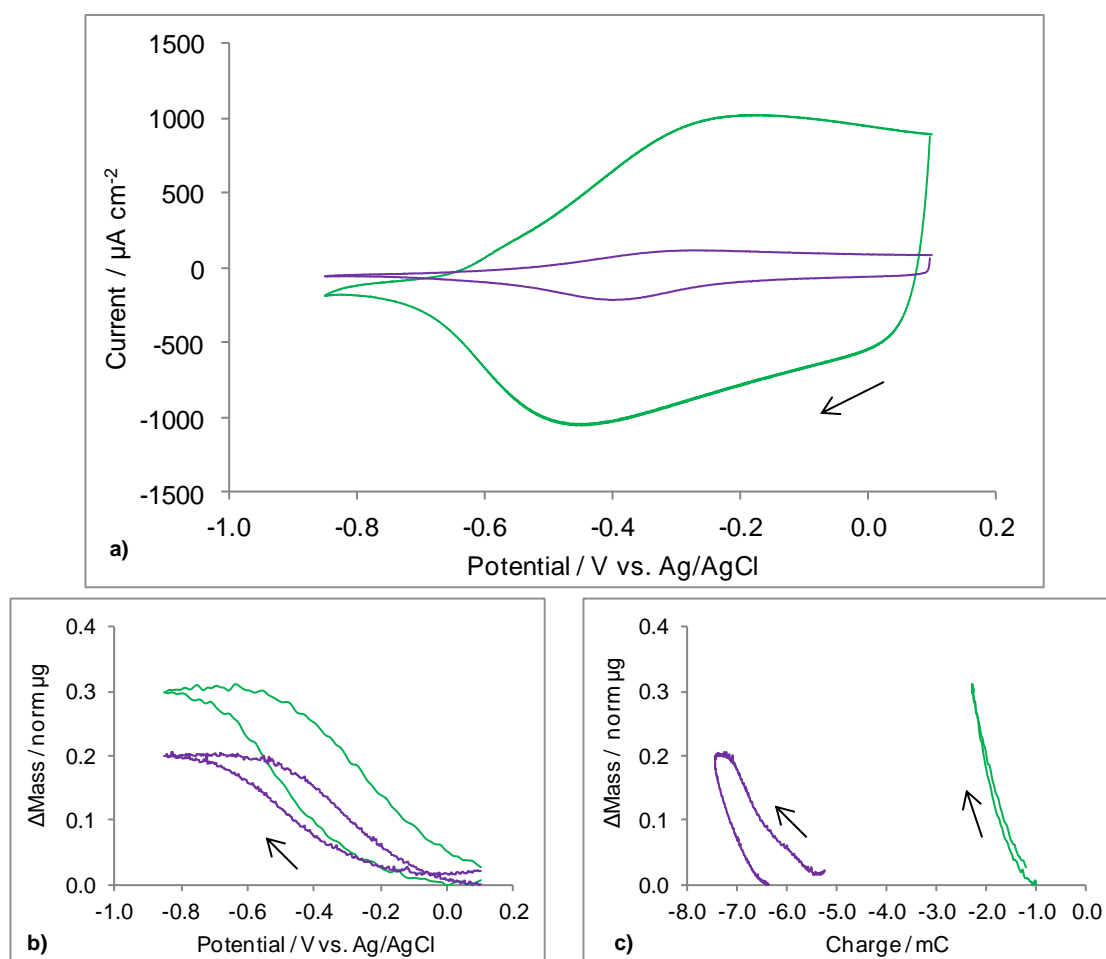


**Figure 4.15:** Cyclic voltammograms (a), massograms (b) and  $\Delta m$  vs.  $Q$  plots (c) of PpyC4S films grown from an aqueous solution of 0.20 M Ppy and 0.10 M of C4S, to a charge of 15.0 mC. and cycled in 0.10 M NaCl aqueous solution. PpyC4S films were cycled at scan rates of  $100 \text{ mV s}^{-1}$  (—) and  $10 \text{ mV s}^{-1}$  (—). Arrows indicate the direction of the initial reduction sweep, cycle 5 is plotted.

Similar to Figure 4.15, it can be seen that a greater mass change at negative potentials is measured at higher scan rates (Figure 4.16 b). The mass increase observed at a scan rate of  $100 \text{ mV s}^{-1}$  is approximately 80 percent higher than the mass increase observed at  $10 \text{ mV s}^{-1}$ . It is clear from the  $\Delta m$  vs.  $Q$  plot (Figure 4.16 c) that at  $100 \text{ mV s}^{-1}$  the response is more monotonic than that at  $10 \text{ mV s}^{-1}$  which may also be explained by the “freezing out” of neutral species movement. While the  $\Delta m$  vs.  $Q$  plots are quite different to those observed for PpyC4S films formed at dopant concentrations of  $0.002 \text{ M C4S}$  (Figure 4.13 f), the apparent molar masses calculated follow the same trend as that seen in Table 4.11. At higher scan rates, the uptaken  $\text{Na}^+$  is solvated with approximately 1  $\text{H}_2\text{O}$  molecule, and so the molar mass is higher than expected. At lower scan rates,  $\text{Na}^+$  ion egress occurs simultaneously with neutral species transfer and so the calculated molar mass is lower than expected. Table 4.12 summarises the mass changes measured, the potential ranges where linear regions were observed in the  $\Delta m$  vs.  $Q$  plots and the apparent molar masses calculated for those linear regions.

**Table 4.12: The apparent molar mass of ions ( $M'$ ), calculated from the respective slopes ( $\Delta m$  vs.  $Q$ ) of PpyC4S films ( $0.20 \text{ M Ppy}/0.100 \text{ M C4S}$ ) in  $0.10 \text{ M NaCl}$  at scan rates of  $100 \text{ mV s}^{-1}$  and  $10 \text{ mV s}^{-1}$ . Expected  $M'$  are also listed,  $\text{Na}^+$  is the dominant ion exchanged. The mass change detected by EQCM is also listed. The + and – signs are employed to indicate mass increase and decrease respectively.**

Scan Rate / $\text{mV s}^{-1}$	Cycle Segment	Potential Range / V vs. Ag/AgCl	$M'$ / $\text{g mol}^{-1}$	Expected $M'$ / $\text{g mol}^{-1}$ (dominant ion)	Measured $\Delta m$ / $\mu\text{g}$
100	Reduction	– 0.45 to – 0.65	+ $40.9 \pm 2.1$	+ 23.0 ( $\text{Na}^+$ )	+ $0.34 \pm 0.02$
	Oxidation	– 0.39 to – 0.10	– $27.3 \pm 2.0$	– 23.0 ( $\text{Na}^+$ )	– $0.30 \pm 0.01$
10	Reduction	– 0.46 to – 0.68	+ $16.3 \pm 1.8$	+ 23.0 ( $\text{Na}^+$ )	+ $0.19 \pm 0.01$
	Oxidation	– 0.39 to – 0.23	– $21.4 \pm 2.0$	– 23.0 ( $\text{Na}^+$ )	– $0.21 \pm 0.01$

## 4.2.2.5 Metal Cation Exchange Properties of PpyC4S

PpyC4S films were electropolymerised from a solution containing 0.20 M pyrrole and 0.002 M C4S. A few studies were also carried out on films formed from a solution containing 0.10 M C4S. The PpyC4S films were formed to a charge of 15.0 mC ( $74 \text{ mC cm}^{-2}$ ) at an applied potential of 0.55 V vs. Ag/AgCl. The films were rinsed first with water and then with the relevant aqueous salt solution before cycling in 0.10 M aqueous solutions of CsCl, CaCl<sub>2</sub>, MgCl<sub>2</sub>, NiCl<sub>2</sub> or CrCl<sub>3</sub> at scan rates of  $10 \text{ mV s}^{-1}$  and  $100 \text{ mV s}^{-1}$ . Table 4.13 summarises the peak potentials ( $E_p^C$  and  $E_p^A$ ) and peak separation ( $\Delta E_p$ ) recorded for PpyC4S films cycled in each solution. It is shown in Figure 4.19 that no anodic or cathodic peaks were distinguishable in the cyclic voltammograms obtained when the films were cycled in 0.10 M CrCl<sub>3</sub>.

**Table 4.13: Peak potentials ( $E_p^C$  and  $E_p^A$ ) and peak separation ( $\Delta E_p$ ) recorded for PpyC4S (0.2 M Ppy/0.002 M C4S) cycled in 0.10 M aqueous metal chloride solutions.**

Metal Chloride (0.10 M)	$E_p^C / \text{V vs. Ag/AgCl}$	$E_p^A / \text{V vs. Ag/AgCl}$	$\Delta E_p / \text{V}$	n
NaCl	$-0.42 \pm 0.01$	$-0.24 \pm 0.01$	0.18	3
CsCl	$-0.40 \pm 0.01$	$-0.28 \pm 0.00$	0.12	2
CaCl <sub>2</sub>	$-0.41 \pm 0.01$	$-0.30 \pm 0.01$	0.11	3
MgCl <sub>2</sub>	$-0.36 \pm 0.00$	$-0.28 \pm 0.00$	0.09	2
NiCl <sub>2</sub>	$-0.63 \pm 0.03$	$-0.20 \pm 0.01$	0.43	4
CrCl <sub>3</sub>	—	—	—	3

It can be seen that as the metal cation is changed, a shift in the peak potential of the PpyC4S film is observed. This shift has been explained by interactions between the polymer film and the metal cations in the electrolyte.<sup>59</sup> The peak potentials for the s-block metal cations are reasonably similar and it can be seen from Figure 4.17 that the corresponding cyclic voltammograms and massograms display similar behaviour. In particular, the massograms for NaCl, CaCl<sub>2</sub> and MgCl<sub>2</sub> have similar features, with a loss in mass observed during the reduction cycle until a potential of approximately  $-0.30 \text{ V vs. Ag/AgCl}$  is reached. This occurs as the polymer is reduced and any uptaken anions and neutral species are ejected from the film. As the reduction potential reaches approximately  $-0.40 \text{ V vs. Ag/AgCl}$ , the polymer backbone has become sufficiently reduced such that cations must be uptaken from the electrolyte to balance

the negative charge imparted upon the polymer by the practically immobilised C4S dopant. This results in the mass increase seen in this region of the massogram. Oxidation of the PpyC4S during the first stage of the oxidation sweep sees the expulsion of uptaken cations and associated solvent. This is followed by a small increase in mass as anions and neutral species enter the film again.

It has been suggested that the uptake of anions during the oxidation of the film may be a result of complexation of the metal cations in the cavity of the C4S.<sup>39</sup> It can be seen from Table 4.1 that C4S has a moderate binding affinity for  $\text{Cs}^+$ ,  $\text{Ca}^{2+}$  and  $\text{Mg}^{2+}$  ions but no binding affinity for  $\text{Na}^+$  ions. Thus it would be expected that anion exchange would occur to a greater extent in films cycled in solutions of  $\text{CsCl}$ ,  $\text{CaCl}_2$ ,  $\text{MgCl}_2$ , as the ingress of anions would be necessary to compensate for the positive charge imparted on the film by the complexed cation. It can be observed from Figure 4.17 and Table 4.14 that there is little difference in the contribution of anion exchange between the films cycled in  $\text{NaCl}$ ,  $\text{CaCl}_2$  or  $\text{MgCl}_2$ , and no anion exchange is observed for films cycled in  $\text{CsCl}$ . Thus it can be concluded that complexation of the metal cations is not a significant process.

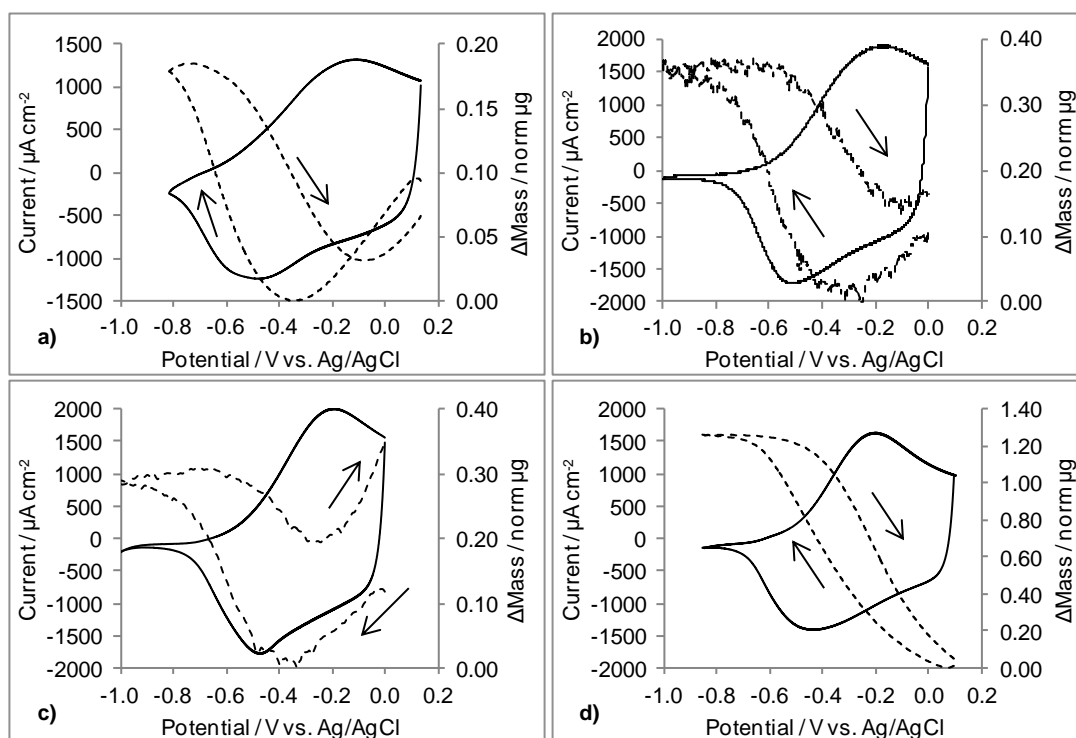


Figure 4.16: Cyclic voltammograms (—) and massograms (---) of PpyC4S films grown from an aqueous solution of 0.20 M Ppy and 0.002 M of C4S, to a charge of 15.0 mC. Films were cycled at a scan rate of  $100 \text{ mV s}^{-1}$  in 0.10 M aqueous solutions of a)  $\text{NaCl}$ , b)  $\text{CaCl}_2$ , c)  $\text{MgCl}_2$  and d)  $\text{CsCl}$ . Cycle 5 is plotted.

The mass loss and increase attributed to anion and solvent species, in the region between 0.10 V and  $-0.40$  V vs. Ag/AgCl are not observed for the PpyC4S film cycled in 0.10 M CsCl. This may reflect the higher mobility of the  $\text{Cs}^+$  ion compared to  $\text{Na}^+$ ,  $\text{Ca}^{2+}$  or  $\text{Mg}^{2+}$  ions, as it has been observed that  $\text{Cs}^+$  ions are only weakly hydrated in comparison, and often exhibit greater transport in and through polypyrrole polymers doped with large dopant anions.<sup>60, 61</sup> It can also be observed that the mass increase in the region of  $-0.40$  V to  $-0.80$  V vs. Ag/AgCl is substantially larger for the film cycled in CsCl, which may obscure any small change in mass in the region between 0.10 V and  $-0.40$  V vs. Ag/AgCl. Table 4.14 details the change in mass measured for films cycled in each metal chloride solution at scan rates of  $100 \text{ mV s}^{-1}$  and  $10 \text{ mV s}^{-1}$ . As seen for NaCl in Section 4.2.2.4, there is a greater uptake of mass observed during the second segment of the reduction sweep (Reduction 2) at higher scan rates. This corresponds to charge compensation through the uptake of cations and solvent.

**Table 4.14: The  $\Delta m / \mu\text{g}$  measured during the cycling of PpyC4S films (0.20 M Ppy/0.002 M C4S) in 0.10 M metal chloride solutions at scan rates of  $100 \text{ mV s}^{-1}$  and  $10 \text{ mV s}^{-1}$ . The + and – signs are employed to indicate mass increase and decrease respectively, n = number of films tested.**

Metal Chloride (0.10 M)	Scan Rate / $\text{mV s}^{-1}$	$\Delta m / \mu\text{g}$ Reduction 2 Cation ingress	$\Delta m / \mu\text{g}$ Oxidation 1 Cation egress	$\Delta m / \mu\text{g}$ Reduction 1 Anion egress	$\Delta m / \mu\text{g}$ Oxidation 2 Anion ingress	n
NaCl						
	100	$+0.18 \pm 0.01$	$-0.16 \pm 0.01$	$-0.10 \pm 0.01$	$+0.04 \pm 0.00$	3
	10	$+0.08 \pm 0.00$	$-0.08 \pm 0.00$	$-0.12 \pm 0.01$	$+0.07 \pm 0.01$	5
CsCl						
	100	$+1.26 \pm 0.01$	$-1.21 \pm 0.01$	—	—	3
	10	$+1.17 \pm 0.00$	$-1.14 \pm 0.00$	—	—	2
CaCl <sub>2</sub>						
	100	$+0.31 \pm 0.05$	$-0.20 \pm 0.03$	$-0.11 \pm 0.01$	—	2
	10	$+0.05 \pm 0.00$	$-0.02 \pm 0.01$	$-0.16 \pm 0.02$	$+0.13 \pm 0.01$	3
MgCl <sub>2</sub>						
	100	$+0.28 \pm 0.01$	$-0.18 \pm 0.06$	$-0.16 \pm 0.03$	$+0.14 \pm 0.02$	2
	10	$+0.12 \pm 0.02$	$-0.11 \pm 0.03$	$-0.17 \pm 0.00$	$+0.09 \pm 0.00$	2
NiCl <sub>2</sub>						
	10	$+0.44 \pm 0.03$	$-0.05 \pm 0.01$	$-0.09 \pm 0.01$	—	4
CrCl <sub>3</sub>						
	10	$+0.05 \pm 0.03$	$+0.02 \pm 0.00$	—	—	3

Figure 4.18 depicts the  $\Delta m$  vs.  $Q$  plots resulting from the cyclic voltammograms illustrated in Figure 4.17. The monotonic response of the PpyC4S film cycled in CsCl is very apparent, and Table 4.15 lists the figures obtained when using Equation 4.5 to analyse the straight line portions of the  $\Delta m$  vs.  $Q$  plots. It can be observed, that as with PpyC4S cycled in 0.10 M NaCl, at high scan rates the apparent molar mass of the exchanged ion is larger than expected with the exception of when the films are cycled in CsCl. As before this large calculated molar mass at higher scan rates is most likely due to solvation of the metal cation. In the case of  $\text{Cs}^+$ , the lower than expected molar mass is most likely due to neutral species transport in the opposite direction to cation uptake. At the lower scan rate competition between neutral species movement and ion exchange predominates and charge compensation is no longer exclusively achieved through cation exchange for films cycled in NaCl,  $\text{CaCl}_2$  or  $\text{MgCl}_2$ , which also results in lower than expected calculated molar masses.

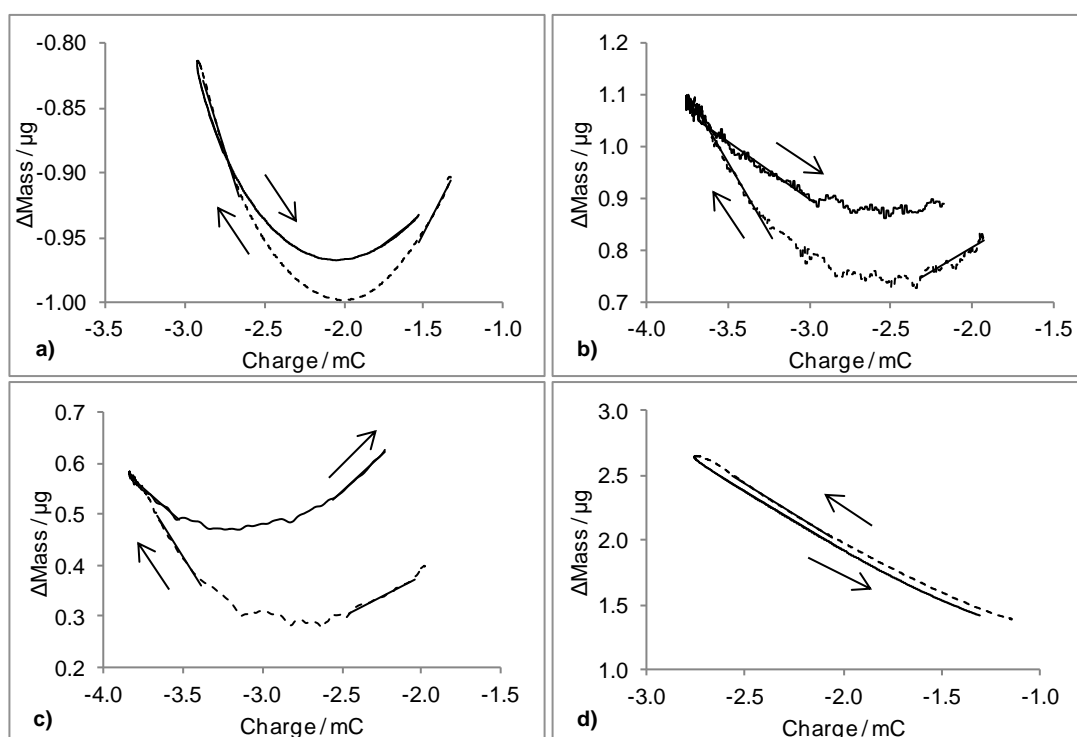


Figure 4.17:  $\Delta m$  vs.  $Q$  plots for PpyC4S films grown from an aqueous solution of 0.20 M Ppy and 0.002 M of C4S, to a charge of 15.0 mC. Films were cycled at a scan rate of  $100 \text{ mV s}^{-1}$  in 0.10 M aqueous solutions of a) NaCl, b)  $\text{CaCl}_2$ , c)  $\text{MgCl}_2$  and d) CsCl. Cycle 5 is plotted.

**Table 4.15:** The apparent molar mass of ions ( $M'$ ), calculated from the respective slopes ( $\Delta m$  vs.  $Q$ ) of PpyC4S films (0.20 M Ppy/0.002 M C4S) cycled in various metal chloride solutions at  $100 \text{ mV s}^{-1}$  and  $10 \text{ mV s}^{-1}$ . Expected  $M'$  are also listed, the + and - signs are employed to indicate mass increase and decrease respectively.

Metal Chloride (0.10 M)	Scan Rate / $\text{mV s}^{-1}$	Expected $M'$ / $\text{g mol}^{-1}$ (Cation)	$M' / \text{g mol}^{-1}$ Reduction 2 Cation ingress	$M' / \text{g mol}^{-1}$ Oxidation 1 Cation egress	Expected $M'$ / $\text{g mol}^{-1}$ (Anion)	$M' / \text{g mol}^{-1}$ Reduction 1 Anion egress	$M' / \text{g mol}^{-1}$ Oxidation 2 Anion ingress	n
NaCl	100	23.0 ( $\text{Na}^+$ )	+ 40.5 $\pm$ 1.1	- 33.1 $\pm$ 1.2	35.5 ( $\text{Cl}^-$ )	- 20.2 $\pm$ 1.6	+ 7.8 $\pm$ 0.4	3
	10	23.0 ( $\text{Na}^+$ )	+ 12.4 $\pm$ 0.7	—	35.5 ( $\text{Cl}^-$ )	- 16.1 $\pm$ 0.8	+ 11.3 $\pm$ 0.7	5
CsCl	100	132.9 ( $\text{Cs}^+$ )	+ 90.7 $\pm$ 1.3	- 87.7 $\pm$ 0.6	35.5 ( $\text{Cl}^-$ )	—	—	3
	10	132.9 ( $\text{Cs}^+$ )	+ 69.5 $\pm$ 8.5	- 80.3 $\pm$ 1.9	35.5 ( $\text{Cl}^-$ )	—	—	2
$\text{CaCl}_2$	100	40.1 ( $\text{Ca}^{2+}$ )	+ 89.6 $\pm$ 1.4	- 44.8 $\pm$ 2.4	35.5 ( $\text{Cl}^-$ )	- 20.4 $\pm$ 2.3	—	2
	10	40.1 ( $\text{Ca}^{2+}$ )	+ 15.0 $\pm$ 1.9	—	35.5 ( $\text{Cl}^-$ )	- 22.1 $\pm$ 6.2	+ 22.7 $\pm$ 7.1	3
$\text{MgCl}_2$	100	24.3 ( $\text{Mg}^{2+}$ )	+ 76.7 $\pm$ 15.0	- 49.2 $\pm$ 3.1	35.5 ( $\text{Cl}^-$ )	- 16.4 $\pm$ 1.4	+ 22.1 $\pm$ 6.2	2
	10	24.3 ( $\text{Mg}^{2+}$ )	+ 42.0 $\pm$ 5.6	- 36.1 $\pm$ 11.0	35.5 ( $\text{Cl}^-$ )	- 19.4 $\pm$ 0.3	+ 24.4 $\pm$ 0.9	2
$\text{NiCl}_2$	100	58.7 ( $\text{Ni}^{2+}$ )	+ 86.6 $\pm$ 5.3	- 32.8 $\pm$ 7.8	35.5 ( $\text{Cl}^-$ )	- 25.4 $\pm$ 1.3	—	4
	10	58.7 ( $\text{Ni}^{2+}$ )	+ 86.6 $\pm$ 5.3	- 32.8 $\pm$ 7.8	35.5 ( $\text{Cl}^-$ )	- 25.4 $\pm$ 1.3	—	4
$\text{CrCl}_3$	100	52.0 ( $\text{Cr}^{3+}$ )	+ 1.9 $\pm$ 0.9	+ 0.5 $\pm$ 0.2	35.5 ( $\text{Cl}^-$ )	—	—	3
	10	52.0 ( $\text{Cr}^{3+}$ )	+ 1.9 $\pm$ 0.9	+ 0.5 $\pm$ 0.2	35.5 ( $\text{Cl}^-$ )	—	—	3

The transition metal chlorides,  $\text{NiCl}_2$  and  $\text{CrCl}_3$ , present quite different results. The cyclic voltammograms and massograms for PpyC4S films cycled at a scan rate of  $10 \text{ mV s}^{-1}$  in 0.10 M aqueous solutions of  $\text{NiCl}_2$  and  $\text{CrCl}_3$  are depicted in Figure 4.19. It can be seen from the massograms, and from the values in Table 4.15 that the species uptaken by the polymer film are predominantly retained, causing a marked increase in film mass with repeated cycling. This indicates that the metal cation is becoming trapped within the polymer. The standard electrode potential for the reduction of  $\text{Ni}^{2+}$  to  $\text{Ni}^0$  is  $-0.27 \text{ V}$  vs. standard hydrogen electrode (SHE).<sup>62, 63</sup> This corresponds to a standard potential of  $-0.47 \text{ V}$  vs.  $\text{Ag}/\text{AgCl}$  and as the experimental potential range encompasses this, it is most likely that the increase in film mass with repeated cycling is due to nickel metal deposition.<sup>64</sup> This is not the case for the  $\text{Cr}^{3+}$ , as the standard electrode potential for the reduction of  $\text{Cr}^{3+}$  to  $\text{Cr}^0$  is  $-0.74 \text{ V}$  vs. SHE.<sup>63</sup> As this corresponds to a standard potential of  $-0.94 \text{ V}$  vs.  $\text{Ag}/\text{AgCl}$ , the potential range of this experiment will not be sufficient to reduce the  $\text{Cr}^{3+}$  to  $\text{Cr}^0$  metal. Akieh *et al.* proposed that, in the case of trivalent metal cations, the triply charge  $\text{Cr}^{3+}$  would have a greater

electrostatic interaction with a sulfonated dopant, retarding cation expulsion<sup>2</sup> or, in this case complexation of the ion by the C4S may be occurring. This, in conjunction with the higher concentration of  $\text{Cl}^-$  ions in comparison to an equimolar solution of NaCl for example, results in a complex charge compensation mechanism, involving competitive movement of anions, cations and neutral species. This could also explain the discrepancy between estimated molar mass and expected molar mass of  $\text{Cr}^{3+}$  as shown in Table 4.15.

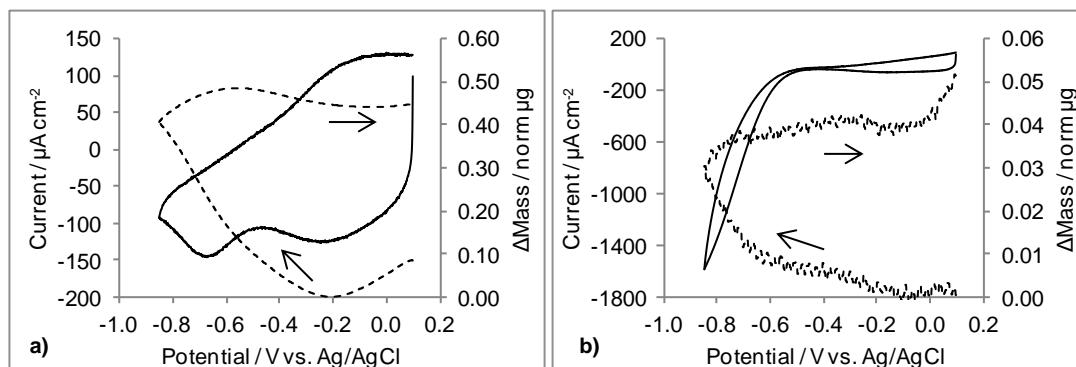


**Figure 4.18:** Cyclic voltammograms (—) and massograms (....) of PpyC4S films grown from an aqueous solution of 0.20 M Ppy and 0.002 M of C4S, to a charge of 15.0 mC. Films were cycled in 0.10 M aqueous solutions of a)  $\text{NiCl}_2$  and b)  $\text{CrCl}_3$  at a scan rate of  $10 \text{ mV s}^{-1}$ . Cycle 5 is plotted.

The effect of changing the concentration of C4S dopant was investigated for PpyC4S films cycled in 0.10 M aqueous solutions of  $\text{CaCl}_2$  and  $\text{MgCl}_2$ . Films formed with 0.10 M and 0.002 M C4S were compared at a scan rate of  $100 \text{ mV s}^{-1}$ . Similar to that found in Section 4.2.2.3,  $\Delta m$  vs.  $Q$  plots for films formed at higher dopant concentrations exhibit more monotonic behaviour than for those films formed with the lower dopant concentration. The apparent molar masses calculated from the straight line segments of these  $\Delta m$  vs.  $Q$  plots also show a similar trend to that seen for NaCl (Table 4.16). A larger than expected molar mass is calculated for segments Reduction 2 and Oxidation 1, which should correspond to the ingress and egress of cations. This is explained by the solvation of the cations. When the actual mass change of the film is investigated however, it differs somewhat to that seen for NaCl in Section 4.2.2.3. In that case, a greater mass increase was observed for films formed with high dopant concentrations (Table 4.17). For films cycled in  $\text{CaCl}_2$  and  $\text{MgCl}_2$ , it appears that similar mass is uptaken and released during segments Reduction 2 and Oxidation 1 for films formed with both 0.10 M C4S and 0.002 M C4S. cation exchange predominates in films formed with the higher dopant concentration. Thus, the similar mass changes may be due to the slow release of uptaken solvent which competes with the cation exchange, making the net mass increase/decrease difficult to separate out into purely cation based. The effect of changing the concentration of C4S dopant was also investigated for PpyC4S films cycled in 0.10 M aqueous solutions of CsCl. CsCl is a more mobile cation than  $\text{Ca}^{2+}$  and  $\text{Mg}^{2+}$ , and as such has demonstrated a more cation dominated response. Cyclic voltammograms, massograms and  $\Delta m$  vs.  $Q$  plots obtained for films formed from 0.10 M C4S and 0.002 M C4S are consistent with those seen in Figure 4.17 (d) and Figure 4.18 (d). The mass change experienced by the film is comparable to PpyC4S films formed with both 0.002 M and 0.10 M concentrations of dopant, with the mass increase during Reduction 2 almost mirroring that released during Oxidation 1. As before, the ingress and egress of anions is not apparent from the massogram, but any anion contribution may be masked by the large mass change observed. The apparent molar masses of contributing ions, calculated from the  $\Delta m$  vs.  $Q$  plots, are lower than expected at both C4S dopant concentrations. However, the apparent molar masses calculated for ion ingress and egress are comparable and so it is most likely that neutral species transfer is occurring in the opposite direction to cation exchange.

**Table 4.16:** The apparent molar mass of ions ( $M'$ ), calculated from the respective slopes ( $\Delta m$  vs.  $Q$ ) of PpyC4S films (0.20 M Ppy/0.10 M C4S or 0.002 M C4S) cycled in various metal chloride solutions at 100 mV s<sup>-1</sup>. Expected  $M'$  are also listed, the + and – signs are employed to indicate mass increase and decrease respectively.

Metal Chloride (0.10 M)	Dopant Conc / M	Expected $M'$ / g mol <sup>-1</sup> (Cation)	$M'$ / g mol <sup>-1</sup> Reduction 2 Cation ingress	$M'$ / g mol <sup>-1</sup> Oxidation 1 Cation egress	Expected $M'$ / g mol <sup>-1</sup> (Anion)	$M'$ / g mol <sup>-1</sup> Reduction 1 Anion egress	$M'$ / g mol <sup>-1</sup> Oxidation 2 Anion ingress	n
NaCl	0.10	23.0 (Na <sup>+</sup> )	+ 40.9 ± 2.1	- 27.3 ± 2.0	35.5 (Cl <sup>-</sup> )	—	—	3
	0.002	23.0 (Na <sup>+</sup> )	+ 40.5 ± 1.1	- 33.1 ± 1.2	35.5 (Cl <sup>-</sup> )	- 20.2 ± 1.6	+ 7.8 ± 0.4	3
CsCl	0.10	132.9 (Cs <sup>+</sup> )	+ 81.7 ± 0.95	- 83.7 ± 2.4	35.5 (Cl <sup>-</sup> )	—	—	3
	0.002	132.9 (Cs <sup>+</sup> )	+ 90.7 ± 1.3	- 87.7 ± 0.6	35.5 (Cl <sup>-</sup> )	—	—	3
CaCl <sub>2</sub>	0.10	40.1 (Ca <sup>2+</sup> )	+ 45.9 ± 1.2	- 45.99 ± 2.3	35.5 (Cl <sup>-</sup> )	—	—	3
	0.002	40.1 (Ca <sup>2+</sup> )	+ 89.6 ± 1.4	- 44.8 ± 2.4	35.5 (Cl <sup>-</sup> )	- 20.4 ± 2.3	—	2
MgCl <sub>2</sub>	0.10	24.3 (Mg <sup>2+</sup> )	+ 48.4 ± 0.2	- 48.4 ± 1.1	35.5 (Cl <sup>-</sup> )	—	—	2
	0.002	24.3 (Mg <sup>2+</sup> )	+ 76.7 ± 15.0	- 49.2 ± 3.1	35.5 (Cl <sup>-</sup> )	- 16.4 ± 1.4	+ 22.1 ± 6.2	2

**Table 4.17:** The  $\Delta m$  /  $\mu\text{g}$  measured during the cycling of PpyC4S films formed from 0.20 M Ppy and either 0.10 M C4S or 0.002 M C4S) in 0.10 M metal chloride solutions at scan rates of 100 mV s<sup>-1</sup> and 10 mV s<sup>-1</sup>. The + and – signs are employed to indicate mass increase and decrease respectively, n = number of films tested.

Metal Chloride (0.10 M)	Dopant Conc / M	$\Delta m$ / $\mu\text{g}$ Reduction 2 Cation ingress	$\Delta m$ / $\mu\text{g}$ Oxidation 1 Cation egress	$\Delta m$ / $\mu\text{g}$ Reduction 1 Anion egress	$\Delta m$ / $\mu\text{g}$ Oxidation 2 Anion ingress	n
NaCl	0.10	+ 0.34 ± 0.02	- 0.30 ± 0.01	—	—	3
	0.002	+ 0.18 ± 0.01	- 0.16 ± 0.01	- 0.10 ± 0.01	+ 0.04 ± 0.00	3
CaCl <sub>2</sub>	0.10	+ 0.31 ± 0.02	- 0.26 ± 0.01	—	—	3
	0.002	+ 0.31 ± 0.05	- 0.20 ± 0.03	- 0.11 ± 0.01	—	2
MgCl <sub>2</sub>	0.10	+ 0.28 ± 0.01	- 0.24 ± 0.00	—	—	2
	0.002	+ 0.28 ± 0.01	- 0.18 ± 0.06	- 0.16 ± 0.03	+ 0.14 ± 0.02	2
CsCl	0.10	+ 1.00 ± 0.01	- 0.96 ± 0.01	—	—	3
	0.002	+ 1.26 ± 0.01	- 1.21 ± 0.01	—	—	3

## 4.2.2.6 Anion Exchange Properties of PpyC4S

It can be seen that the PpyC4S film is not permselective i.e. it does not act exclusively as a cation exchange material and anion and neutral species have a role in the charge compensation mechanism. It can also be noted that non-permselectivity is more pronounced at lower scan rates, where anion interaction is more apparent in both the massograms and in the apparent molar mass values calculated from the  $\Delta m$  vs.  $Q$  plots. Therefore a study was carried out to investigate the anion exchange behaviour of the film. The PpyC4S films were electropolymerised from a solution containing 0.20 M pyrrole and 0.002 M C4S. The PpyC4S films were formed to a charge of 15.0 mC ( $74 \text{ mC cm}^{-2}$ ) at an applied potential of 0.55 V vs. Ag/AgCl. The films were rinsed first with water and then with the relevant aqueous salt solution before cycling in 0.10 M aqueous solutions at scan rates of  $10 \text{ mV s}^{-1}$  and  $100 \text{ mV s}^{-1}$ . Three anions were used for this study; nitrate, perchlorate and chloride and the peak potential for the redox processes of PpyC4S polymer recorded in 0.10 M solution of each of these ions is given in Table 4.18.

**Table 4.18: Peak potentials ( $E_p^C$  and  $E_p^A$ ) and peak separation ( $\Delta E_p$ ) recorded for PpyC4S (0.2 M Ppy/0.002 M C4S) cycled in 0.10 M sodium salt solutions.**

Metal Chloride (0.10 M)	$E_p^C$ / V vs. Ag/AgCl	$E_p^A$ / V vs. Ag/AgCl	$\Delta E_p$ / V	n
NaCl	$-0.42 \pm 0.01$	$-0.24 \pm 0.01$	0.18	3
NaNO <sub>3</sub>	$-0.46 \pm 0.00$	$-0.14 \pm 0.01$	0.32	3
NaClO <sub>4</sub>	$-0.48 \pm 0.01$	$-0.09 \pm 0.00$	0.39	3

The shift in peak potentials suggests an interaction between each PpyC4S film and the metal cation solution it is cycled in. This could result in different film morphologies developing during the redox cycling process, which may account for the differing responses observed during EQCM analysis.<sup>59</sup> Tables 4.19 and 4.20 summarise the mass changes measured during the redox process and the apparent molar mass of the involved ions calculated using Equation 4.5. Each film follows the scan rate dependence seen for NaCl in which a greater mass change is measured at negative potentials (Reduction 2 and Oxidation 1) at scan rates of  $100 \text{ mV s}^{-1}$  than at  $10 \text{ mV s}^{-1}$ . This is the range in which cation movement occurs. At more positive potentials, (Reduction 1 and Oxidation 2), anion movement occurs and it can be seen in Table 4.19 that the mass increase due to anion ingress is greater at the low scan rate. This is in keeping with the

“freezing out” of anion and neutral species involvement which is seen at higher scan rates. The ingress and egress of the perchlorate anion does not appear to have a significant dependence on scan rate.

**Table 4.19: The  $\Delta m / \mu\text{g}$  measured during the cycling of PpyC4S films (0.20 M Ppy/0.002 M C4S) in 0.10 M metal chloride solutions at scan rates of  $100 \text{ mV s}^{-1}$  and  $10 \text{ mV s}^{-1}$ . The + and – signs are employed to indicate mass increase and decrease respectively, n = number of films tested.**

Metal Chloride (0.10 M)	Scan Rate / $\text{mV s}^{-1}$	$\Delta m / \mu\text{g}$ Oxidation 2 Anion ingress	$\Delta m / \mu\text{g}$ Reduction 1 Anion egress	$\Delta m / \mu\text{g}$ Reduction 2 Cation ingress	$\Delta m / \mu\text{g}$ Oxidation 1 Cation egress	n
NaCl	100	+ 0.04 ± 0.00	– 0.10 ± 0.01	+ 0.18 ± 0.01	– 0.16 ± 0.01	3
	10	+ 0.07 ± 0.01	– 0.12 ± 0.01	+ 0.08 ± 0.00	– 0.08 ± 0.00	5
NaNO <sub>3</sub>	100	+ 0.11 ± 0.01	– 0.19 ± 0.01	+ 0.12 ± 0.01	– 0.10 ± 0.00	3
	10	+ 0.17 ± 0.01	– 0.23 ± 0.02	+ 0.08 ± 0.01	– 0.04 ± 0.00	2
NaClO <sub>4</sub>	100	+ 0.34 ± 0.00	– 0.40 ± 0.01	+ 0.06 ± 0.00	– 0.07 ± 0.00	3
	10	+ 0.34 ± 0.01	– 0.36 ± 0.00	+ 0.02 ± 0.00	– 0.06 ± 0.01	2

Interestingly, changing the anion appears to change the predominance of which species assists in charge compensation (Figure 4.20). It can be seen from Table 4.19, at high scan rates, the response of PpyC4S in NaCl is cation dominated, in NaNO<sub>3</sub> mass changes relating to both anion and cation movement are very similar, whereas the response for PpyC4S cycled in NaClO<sub>4</sub> is anion dominated. This can be attributed to the mobility of the studied anions ( $\text{ClO}_4^- < \text{Cl}^- < \text{NO}_3^-$ ) and their different ionic radii.<sup>3, 65</sup> As seen before, neutral species and solvent often accompany ion exchange and so the different solvent affinities of these anions will also cause different trends.<sup>7</sup> Thus, although previously it was concluded that the PpyC4S films exhibit mixed ion exchange behaviour depending on the dopant concentration and scan rate used, when the PpyC4S film is cycled in a solution containing perchlorate anions, anion exchange becomes the more dominant process. This can be clearly observed in Figure 4.20.

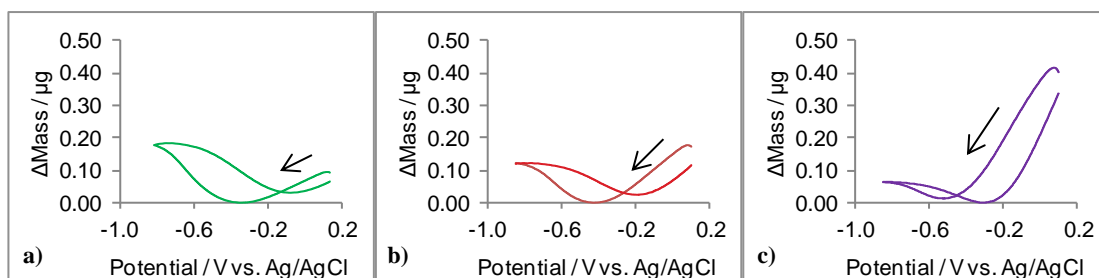


**Figure 4.19:** Massograms of PpyC4S grown from an aqueous solution of 0.20 M Ppy and 0.002 M of C4S, to a charge of 15.0 mC. PpyC4S films were cycled at a scan rate of  $100 \text{ mV s}^{-1}$  in 0.10 M aqueous solutions of a) NaCl, b) NaNO<sub>3</sub> and c) NaClO<sub>4</sub>. Cycle 5 is plotted. The change in which ion dominates charge compensation can clearly be seen to change from cation for NaCl, to mixed cation/anion for NaNO<sub>3</sub> and to predominantly anion for NaClO<sub>4</sub>.

The apparent molar mass of exchanged ions is depicted in Table 4.20. The molar mass values calculated for anion ingress and egress are much lower than the values expected. This is most likely due to expulsion of water molecules during the ingress of anions. It has been found that up to four water molecules are ejected from a Ppy-dodecylbenzene sulfonate film when ClO<sub>4</sub><sup>-</sup> is uptaken.<sup>58</sup> The molar masses calculated for cation involvement follows the same trend previously seen in which a greater molar mass is calculated at high scan rates and a lower than expected value is calculated at lower scan rates. This again is due to the neutral species movement in tandem with ion movement.

**Table 4.20:** The apparent molar mass of ions ( $M'$ ), calculated from the respective slopes ( $\Delta m$  vs.  $Q$ ) of PpyC4S films (0.20 M Ppy/0.002 M C4S) cycled in various metal chloride solutions at scan rates of  $100 \text{ mV s}^{-1}$  and  $10 \text{ mV s}^{-1}$ . Expected  $M'$  are also listed, the + and - signs are employed to indicate mass increase and decrease respectively.

Metal Chloride	Scan Rate ( $\text{mV s}^{-1}$ )	Expected $M'$ / $\text{g mol}^{-1}$ (Anion)	$M' / \text{g mol}^{-1}$ Oxidation 2 Anion ingress	$M' / \text{g mol}^{-1}$ Reduction 1 Anion egress	Expected $M'$ / $\text{g mol}^{-1}$ (Cation)	$M' / \text{g mol}^{-1}$ Reduction 2 Cation ingress	$M' / \text{g mol}^{-1}$ Oxidation 1 Cation egress	$n$
NaCl	100	35.5 (Cl <sup>-</sup> )	+ 7.8 ± 0.4	- 20.2 ± 1.6	23.0 (Na <sup>+</sup> )	+ 40.5 ± 1.1	- 33.1 ± 1.2	3
	10	35.5 (Cl <sup>-</sup> )	+ 11.3 ± 0.7	- 16.1 ± 10.8	23.0 (Na <sup>+</sup> )	+ 12.4 ± 0.7	—	3
NaNO <sub>3</sub>	100	62.0 (NO <sub>3</sub> <sup>-</sup> )	+ 23.1 ± 1.3	- 30.3 ± 1.3	23.0 (Na <sup>+</sup> )	+ 35.9 ± 1.8	- 40.5 ± 0.4	3
	10	62.0 (NO <sub>3</sub> <sup>-</sup> )	+ 26.1 ± 2.1	- 29.8 ± 0.6	23.0 (Na <sup>+</sup> )	+ 12.5 ± 1.7	—	2
NaClO <sub>4</sub>	100	99.5 (ClO <sub>4</sub> <sup>-</sup> )	+ 48.0 ± 1.0	- 56.9 ± 2.5	23.0 (Na <sup>+</sup> )	+ 22.6 ± 1.9	—	3
	10	99.5 (ClO <sub>4</sub> <sup>-</sup> )	+ 42.4 ± 1.8	- 52.8 ± 1.4	23.0 (Na <sup>+</sup> )	+ 10.4 ± 0.8	—	2

### 4.2.3 Cyclic Voltammetry and Ion Exchange Properties of PpyPSS

#### 4.2.3.1 Effect of Applied Growth Potential

PpyPSS films were formed at applied potentials of 0.55 V, 0.70 V and 0.80 V vs. Ag/AgCl in aqueous solutions of 0.20 M pyrrole and 0.002 M PSS to a charge of 15.0 mC ( $74 \text{ mC cm}^{-2}$ ). While these films are not directly comparable to the PpyC4S films, due to the larger number of negatively charged groups on PSS, the data obtained from the PpyPSS study will allow for the establishment of a link between trends found for PpyC4S films and the wide range of published studies on immobilised and practically immobilised dopant ions. The formed films were rinsed with deionised water, and then 0.10 M NaCl aqueous solution, before being cycled at a scan rate of  $100 \text{ mV s}^{-1}$  in 0.10 M NaCl aqueous solution. As before, cycle five will be represented in all graphs.

It can be seen from Figure 4.21 that while the cyclic voltammograms are comparable for each film formed at a different applied potential, the massograms of films formed at a lower applied potential of 0.55 V vs. Ag/AgCl, are quite different. Each film appears to act as an ideal cation exchange material, however the mass change observed for films formed at 0.55 V vs. Ag/AgCl is substantially greater than that of films formed at applied potentials of 0.70 V and 0.80 V vs. Ag/AgCl (Table 4.21). In fact, the mass change observed in films formed at an applied potential of 0.55 V vs. Ag/AgCl, during the segment of the redox cycle denoted Reduction 2, is almost double that of mass change observed during the same segment of the redox cycle for films formed at higher polymerisation potentials. It was shown in Section 4.2.1.2 that PpyPSS films formed at applied potentials of 0.55 V vs. Ag/AgCl grow much slower and the theoretical doping level calculated is much higher than for films formed at applied potentials of 0.70 V and 0.80 V vs. Ag/AgCl (Table 4.3). This slow film formation results in a more compact and conductive film.<sup>66</sup> Although the doping levels calculated are merely for comparative purposes, the greater amount of dopant in films formed at 0.55 V vs. Ag/AgCl may account for the greater mass increase illustrated in Figure 4.21 (b).

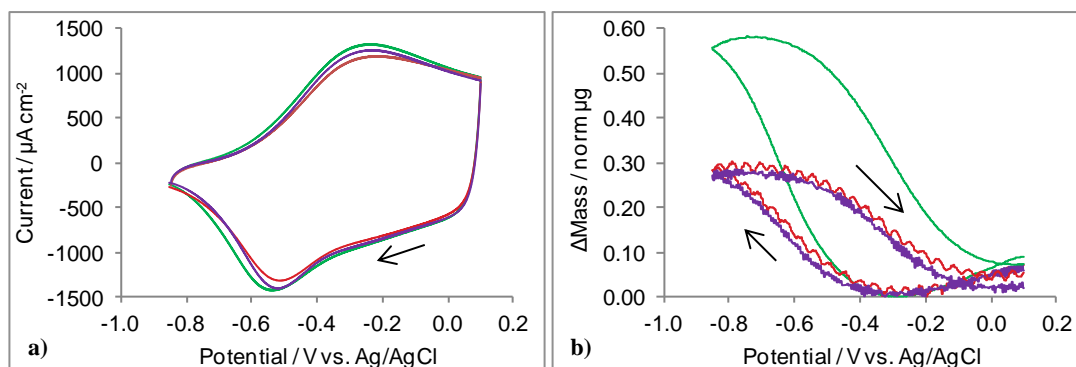


Figure 4.20: Cyclic voltammograms (a) and Massograms (b) of PpyPSS films grown at applied potentials of 0.55 V (—), 0.70 V (—) and 0.80 V (—) from an aqueous solution of 0.20 M Ppy and 0.002 M of, to a charge of 15.0 mC. PpyPSS films were cycled in 0.10 M NaCl aqueous solution at scan rate of  $100 \text{ mV s}^{-1}$ , cycle 5 is plotted.

Table 4.21: The  $\Delta m / \mu\text{g}$  measured during the cycling of PpyPSS films (0.20 M Ppy/0.002 M C4S) in 0.10 M metal chloride solutions at scan rates of  $100 \text{ mV s}^{-1}$ . The + and – signs are employed to indicate mass increase and decrease respectively, n = number of films tested.

Growth Potential / V vs. Ag/AgCl	Cycle Segment	Potential Range / V vs. Ag/AgCl	Measured $\Delta m / \mu\text{g}$	n
0.55	Reduction 1	+ 0.10 to – 0.20	– 0.08 ± 0.01	2
	Reduction 2	– 0.60 to – 0.85	+ 0.46 ± 0.10	2
	Oxidation	– 0.60 to – 0.25	– 0.41 ± 0.10	2
0.70	Reduction 1	+ 0.10 to – 0.16	– 0.08 ± 0.01	2
	Reduction 2	– 0.60 to – 0.85	+ 0.23 ± 0.05	2
	Oxidation	– 0.47 to – 0.15	– 0.18 ± 0.04	2
0.80	Reduction 1	+ 0.10 to – 0.13	– 0.06 ± 0.01	2
	Reduction 2	– 0.60 to – 0.85	+ 0.24 ± 0.04	2
	Oxidation	– 0.41 to – 0.26	– 0.22 ± 0.04	2

Table 4.22 shows the apparent molar mass of exchanged ions, calculated from  $\Delta m$  vs. Q plots for films formed at applied potentials of 0.55 V, 0.70 V and 0.80 V vs. Ag/AgCl. It can be seen that for PpyPSS films formed at 0.70 V and 0.80 V vs. Ag/AgCl, the molar masses calculated for the uptaken cation correspond to a  $\text{Na}^+$  ion with approximately one associated water molecule. The apparent molar masses calculated for the PpyPSS films formed at 0.55 V vs. Ag/AgCl are much higher than the expected molar mass of  $23.0 \text{ g mol}^{-1}$  and thus it can be concluded that substantial amounts of

solvent is incorporated along with the cation. The apparent molar mass calculated for the first segment of the reduction sweep (Reduction 1) is comparable for each film, and with a value much closer to that of H<sub>2</sub>O than to the molar mass of the chloride ion, the mass loss observed for this segment of the massogram may be due to the slow release of solvent from the film.

**Table 4.22: The apparent molar mass of ions ( $M'$ ), calculated from the respective slopes ( $\Delta m$  vs.  $Q$ ) of PpyPSS films (0.20 M Ppy/0.002 M PSS) cycled in 0.10 M NaCl at a scan rate of 100 mV s<sup>-1</sup>. Expected  $M'$  are also listed, the + and - signs are employed to indicate mass increase and decrease respectively.**

Growth Potential / V vs. Ag/AgCl	Expected $M'$ / g mol <sup>-1</sup> (Cation)	$M'$ / g mol <sup>-1</sup> Reduction 2 Cation ingress	$M'$ / g mol <sup>-1</sup> Oxidation 1 Cation egress	Expected $M'$ / g mol <sup>-1</sup> (Anion)	$M'$ / g mol <sup>-1</sup> Reduction 1 Anion egress	$M'$ / g mol <sup>-1</sup> Oxidation 2 Anion ingress	n
0.55	23.0 (Na <sup>+</sup> )	+ 82.0 ± 27.5	- 44.6 ± 7.4	35.5 (Cl <sup>-</sup> )	- 16.1 ± 4.2	—	2
0.70	23.0 (Na <sup>+</sup> )	+ 40.5 ± 8.9	- 19.9 ± 4.4	35.5 (Cl <sup>-</sup> )	- 15.6 ± 0.1	—	2
0.80	23.0 (Na <sup>+</sup> )	+ 49.7 ± 5.8	- 25.0 ± 2.5	35.5 (Cl <sup>-</sup> )	- 14.2 ± 1.1	—	2

## 4.2.3.2 Effect of Dopant Concentration

PpyPSS films were electropolymerised from two solutions, containing 0.20 M pyrrole and a dopant concentration of either 0.10 M or 0.002 M PSS. The PpyPSS films were formed at an applied potential of 0.55 V vs. Ag/AgCl. The films were rinsed as before and cycled in 0.10 M NaCl aqueous solution at a scan rate of  $100 \text{ mV s}^{-1}$ . The resulting cyclic voltammograms, massograms and associated  $\Delta m$  vs. Q plots are shown in Figure 4.22. As seen with the PpyC4S films formed at different dopant concentrations, the cyclic voltammograms are similar for PpyPSS films formed with a high dopant concentration (0.10 M PSS) and with a low dopant concentration (0.002 M PSS). The massograms and  $\Delta m$  vs. Q plots recorded for each film are also comparable, although it can be seen that films formed with a higher dopant concentration are more ideal cation exchangers. At the lower dopant concentration, cation exchange is not solely responsible for maintaining film neutrality and a small egress of species is observed during the first segment of the reduction sweep (Reduction 1).

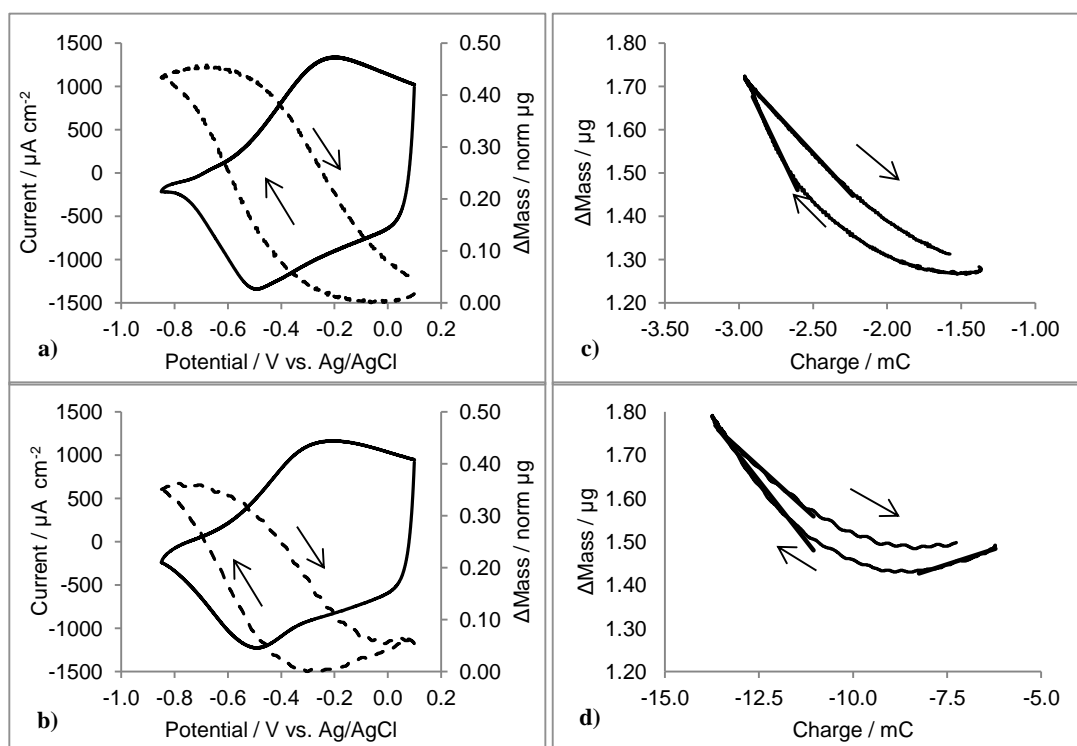


**Figure 4.21:** Cyclic voltammogram (—) and massogram (---) of PpyPSS films grown from an aqueous solution of 0.20 M Ppy and a) 0.10 M or, b) 0.002 M of PSS, to a charge of 15.0 mC. Scan rate  $100 \text{ mV s}^{-1}$  in 0.10 M NaCl aqueous solution. The  $\Delta m$  vs. Q plots corresponding to plots a and b are depicted in plots c and d respectively. Arrows indicate the direction of scan, cycle 5 is plotted.

Tables 4.23 and 4.24 list the  $\Delta m$ ,  $M'$  and expected  $M'$  values obtained from analysis of the data from the EQCM. The mass change due to cation ingress and egress is very similar for each film, in contrast to the results seen for the PpyC4S films where a greater increase in mass was observed in films formed with a high dopant concentration during the reduction cycle. This difference between the PpyPSS films and the PpyC4S films may be due to the large number of negative charges on the PSS dopant compared to on C4S. As with the PpyC4S films, there is no trend evident in the apparent molar mass values calculated, except that they are higher than the expected values, indicating that solvent transport may be taking place in the same or opposite direction to ion transport.

**Table 4.23:** The  $\Delta m$  /  $\mu\text{g}$  measured during the cycling of PpyPSS films formed from 0.20 M Ppy and either 0.10 M or 0.002 M PSS at an applied potential of 0.55 V vs. Ag/AgCl to a charge of 15.0 mC. PpyPSS films were cycled in 0.10 M NaCl aqueous solutions at a scan rate of 100 mV s<sup>-1</sup>. The + and - signs are employed to indicate mass increase and decrease respectively, n = number of films tested.

Dopant Conc. / M	Cycle Segment	Potential Range / V vs. Ag/AgCl	Measured $\Delta m$ / $\mu\text{g}$	n
0.100	Reduction	-0.53 to -0.80	+ 0.43 $\pm$ 0.02	3
	Oxidation	-0.50 to -0.16	- 0.39 $\pm$ 0.02	3
0.002	Reduction 1	+ 0.10 to -0.20	- 0.08 $\pm$ 0.01	2
	Reduction 2	-0.60 to -0.85	+ 0.46 $\pm$ 0.10	2
	Oxidation	-0.60 to -0.25	- 0.41 $\pm$ 0.10	2

**Table 4.24:** The apparent molar mass of ions ( $M'$ ), calculated from the respective slopes ( $\Delta m$  vs.  $Q$ ) of PpyPSS films (0.20 M Ppy and 0.10 M PSS or 0.002 M PSS) cycled in 0.10 M NaCl at a scan rate of 100 mV s<sup>-1</sup>. Expected  $M'$  are also listed, the + and - signs are employed to indicate mass increase and decrease respectively.

Dopant Conc. / M	Expected $M'$ / g mol <sup>-1</sup> (Cation)	$M'$ / g mol <sup>-1</sup> Reduction 2 Cation ingress	$M'$ / g mol <sup>-1</sup> Oxidation 1 Cation egress	Expected $M'$ / g mol <sup>-1</sup> (Anion)	$M'$ / g mol <sup>-1</sup> Reduction 1 Anion egress	$M'$ / g mol <sup>-1</sup> Oxidation 2 Anion ingress	n
0.100	23.0 (Na <sup>+</sup> )	+ 60.1 $\pm$ 6.2	- 33.7 $\pm$ 1.4	35.5 (Cl <sup>-</sup> )	—	—	3
0.002	23.0 (Na <sup>+</sup> )	+ 82.0 $\pm$ 27.5	- 44.6 $\pm$ 7.4	35.5 (Cl <sup>-</sup> )	- 16.1 $\pm$ 4.2	—	2

## 4.2.3.3 Effect of Scan Rate

PpyPSS films were electropolymerised from a solution containing 0.20 M pyrrole and 0.002 M PSS. These were formed to a charge of 15.0 mC ( $74 \text{ mC cm}^{-2}$ ) at an applied potential of 0.55 V vs. Ag/AgCl. The films were rinsed as described in Section 4.2.2.1 and cycled in 0.10 M NaCl aqueous solution at scan rates of 10 and 100  $\text{mV s}^{-1}$ . Figure 4.23 depicts the cyclic voltammograms recorded. As with PpyC4S films, both the anodic and cathodic peak currents in the cyclic voltammograms recorded increase with increasing scan rates and the peak separation ( $\Delta E_p$ ) decreases with decreasing scan rate which indicates that electron transfer is more facile at the lower scan rate of 10  $\text{mV s}^{-1}$  (Table 4.25). The cathodic peak observed is also sharper than the broad anodic peak at both scan rates, which suggests that cation exchange is occurring during the redox cycling.<sup>55</sup>

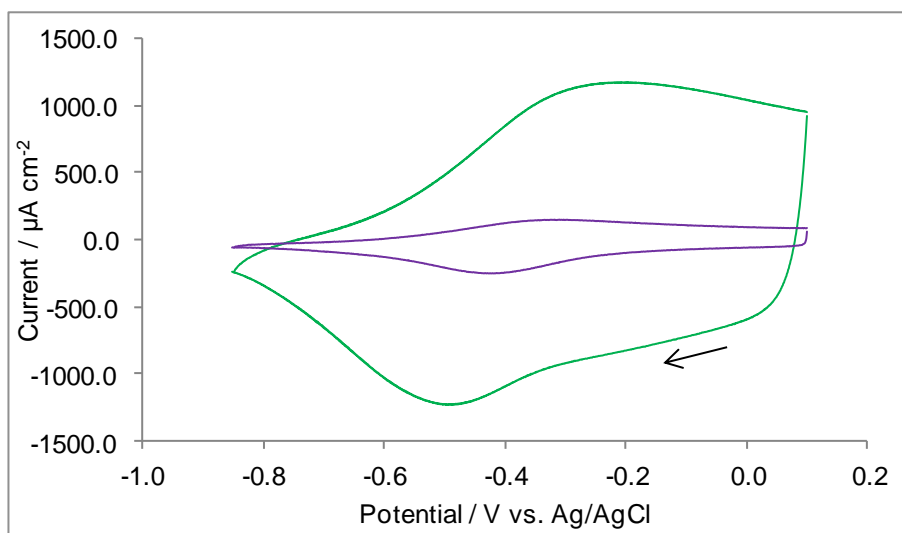


Figure 4.22: Cyclic voltammograms of PpyPSS films grown at an applied potential of 0.55 V vs. SCE, from an aqueous solution of 0.20 M Ppy and 0.002 M of PSS, to a charge of 15.0 mC. PpyPSS films were cycled in 0.10 M NaCl aqueous solution at scan rates of 100  $\text{mV s}^{-1}$  (—) and 10  $\text{mV s}^{-1}$  (—). The arrow indicates the direction of the initial reduction sweep, cycle 5 is plotted.

Table 4.25: Peak potentials ( $E_p^C$  and  $E_p^A$ ) and peak separation ( $\Delta E_p$ ) recorded for PpyPSS films cycled in 0.10 M NaCl at 100  $\text{mV s}^{-1}$  and 10  $\text{mV s}^{-1}$ , n = number of films tested.

Scan Rate / $\text{mV s}^{-1}$	$E_p^C$ / V vs. Ag/AgCl	$E_p^A$ / V vs. Ag/AgCl	$\Delta E_p$ / V	n
100	$-0.51 \pm 0.03$	$-0.23 \pm 0.02$	0.28	3
10	$-0.41 \pm 0.00$	$-0.32 \pm 0.00$	0.09	3

Figure 4.24 illustrates the massograms and  $\Delta m$  vs.  $Q$  plots corresponding to the cyclic voltammograms shown in Figure 4.23. It can be seen that the massograms recorded for the PpyPSS films, exhibit more cation orientated ion exchange than the PpyC4S films formed with a dopant concentration of 0.002 M C4S (Figure 4.15). This is to be expected as PSS is a much bulkier and more highly charged immobilised dopant than C4S and will impart a greater negative charge upon the neutral reduced Ppy backbone.

Table 4.26 and 4.27 list the measured  $\Delta m$ , calculated  $M'$  and expected  $M'$  for the PpyPSS films cycled at each scan rate. Similar trends to those observed with PpyC4S films are again evident (Table 4.9, 4.10 and 4.11). The mass changes due to cation ingress and egress (Reduction 2 and Oxidation 1 segments) are larger at higher scan rates. It would appear that a certain amount of mass is retained at both scan rates, as not all of the mass uptaken during Reduction 2 is released during the following oxidation. This is most likely due to the greater number of negatively charged sites on the PSS dopant. Calculated apparent molar masses are larger than the expected molar mass for  $\text{Na}^+$  ( $23.0 \text{ g mol}^{-1}$ ) and it can be estimated that 3  $\text{H}_2\text{O}$  molecules accompany each  $\text{Na}^+$  at a scan rate of  $100 \text{ mV s}^{-1}$ . This is in keeping with the observations of Akieh *et al.* who estimated that 1 – 4  $\text{H}_2\text{O}$  molecules would be inserted into the PpyPSS film with each cation.<sup>2</sup> At  $10 \text{ mV s}^{-1}$ , the calculated molar masses for cation ingress and egress are more comparable, and thus it appears that less solvent is retained by the film at slower scan rates. This was also observed for the PpyC4S films and was attributed to the slow transport of solvent compared to ion transport at higher scan rates. The values calculated for the species egressing from the film during the initial segment of the reduction cycle are much lower than the expected molar mass of  $\text{Cl}^-$  ions, which suggests movement of neutral species and water are responsible for the mass lost by the film during this part of the reduction cycle.

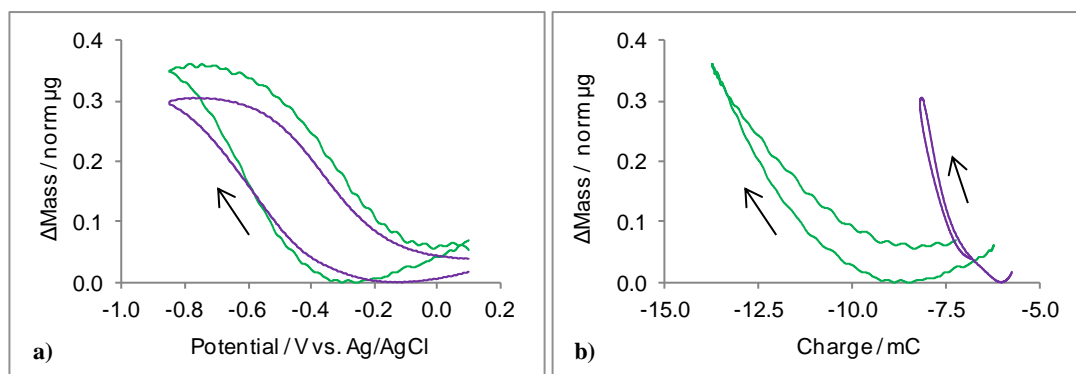


Figure 4.23: Massograms (a) and  $\Delta m$  vs.  $Q$  plots (b) of PpyPSS films grown from an aqueous solution of 0.20 M Ppy and 0.002 M of PSS, to a charge of 15.0 mC, cycled in 0.10 M NaCl aqueous solution. PpyPSS films were cycled at scan rates of  $100 \text{ mV s}^{-1}$  (—) and  $10 \text{ mV s}^{-1}$  (—). Arrows indicate the direction of the initial reduction sweep, cycle 5 is plotted.

Table 4.26: The  $\Delta m / \mu\text{g}$  measured during the cycling of PpyPSS films (0.20 M Ppy/0.002 M PSS) at an applied potential of 0.55 V vs. Ag/AgCl. PpyC4S films were cycled in 0.10 M NaCl aqueous solutions at scan rates of  $100 \text{ mV s}^{-1}$  and  $10 \text{ mV s}^{-1}$ . The + and – signs are employed to indicate mass increase and decrease respectively,  $n$  = number of films tested.

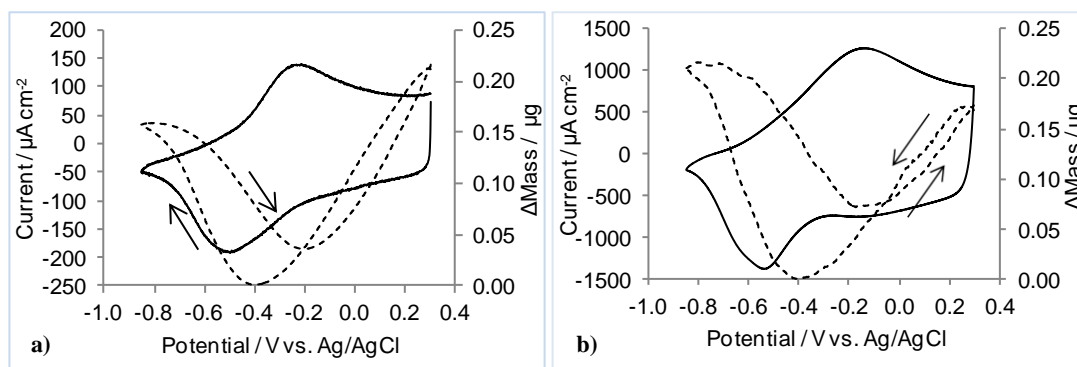
Scan Rate / $\text{mVs}^{-1}$	Cycle Segment	Potential Range / V vs. Ag/AgCl	Measured $\Delta m / \mu\text{g}$	$n$
100	Reduction 1	+ 0.10 to – 0.20	– $0.08 \pm 0.01$	2
	Reduction 2	– 0.60 to – 0.85	+ $0.46 \pm 0.10$	2
	Oxidation	– 0.60 to – 0.25	– $0.41 \pm 0.10$	2
10	Reduction 1	+ 0.10 to 0.00	– $0.04 \pm 0.03$	2
	Reduction 2	– 0.60 to – 0.85	+ $0.30 \pm 0.01$	2
	Oxidation	– 0.41 to – 0.26	– $0.26 \pm 0.01$	2

Table 4.27: The apparent molar mass of ions ( $M'$ ), calculated from the respective slopes ( $\Delta m$  vs.  $Q$ ) of PpyPSS films (0.20 M Ppy/0.002 M PSS) cycled in 0.10 M NaCl at scan rates of  $100 \text{ mV s}^{-1}$  and  $10 \text{ mV s}^{-1}$ . Expected  $M'$  are also listed, the + and – signs are employed to indicate mass increase and decrease respectively.

Scan Rate / $\text{mV s}^{-1}$	Expected $M'$ / $\text{g mol}^{-1}$ (Cation)	$M' / \text{g mol}^{-1}$ Reduction 2 Cation ingress	$M' / \text{g mol}^{-1}$ Oxidation 1 Cation egress	Expected $M'$ / $\text{g mol}^{-1}$ (Anion)	$M' / \text{g mol}^{-1}$ Reduction 1 Anion egress	$M' / \text{g mol}^{-1}$ Oxidation 2 Anion ingress	$n$
100	23.0 (Na+)	+ $82.0 \pm 27.5$	– $44.6 \pm 7.4$	35.5 (Cl–)	– $16.1 \pm 4.2$	—	2
10	23.0 (Na+)	+ $31.5 \pm 0.7$	– $23.0 \pm 0.4$	35.5 (Cl–)	– $9.0 \pm 2.0$	—	2

#### 4.2.4 Influence of Potential Window on Ion Exchange Properties of PpyC4S

Throughout this research, the polymer films were cycled to a maximum potential of 0.10 V vs. Ag/AgCl. In order to investigate the effect of increasing this potential window, a preliminary study was carried out in which PpyC4S films were cycled in 0.10 M NaCl, up to a potential greater than 0.10 V vs. Ag/AgCl. These films were formed to a charge of 15.0 mC ( $74 \text{ mC cm}^{-2}$ ) at an applied potential of 0.55 V vs. Ag/AgCl, from a solution containing either 0.002 M C4S or 0.10 M C4S. These experiments were carried out at scan rates of  $10 \text{ mV s}^{-1}$  or  $100 \text{ mV s}^{-1}$  and the cyclic voltammograms and massograms for films formed at a dopant concentration of 0.002 M C4S are displayed in Figure 4.24.



**Figure 4.24:** Cyclic voltammogram (—) and massogram (---) of PpyC4S films grown from an aqueous solution of 0.20 M Ppy and 0.002 M of C4S, to a charge of 15.0 mC. Scan rate a)  $10 \text{ mV s}^{-1}$  or b)  $100 \text{ mV s}^{-1}$  in 0.10 M NaCl aqueous solution, to a potential of 0.30 V vs. Ag/AgCl. Cycle 5 is plotted for each.

It can be observed that the cyclic voltammograms recorded are similar to those seen in Figure 4.13. The massograms are quite different however, when compared to those obtained using a smaller potential window (Figure 4.14), with more mixed anion-cation exchange behaviour apparent at both low and high scan rates. Table 4.28 details the mass changes calculated from the measured change in frequency during cycle 5. Similar to the results discussed in Section 4.2.2.4, a greater mass increase during the reduction cycle is measured at higher scan rates. During the subsequent oxidation cycle, a greater increase in mass is observed at a scan rate of  $10 \text{ mV s}^{-1}$ , corresponding to the uptake of anions and solvent. This is also similar to the results obtained at a smaller potential window. Some mass is retained by the film during the reduction and oxidation cycles at both scan rates. Table 4.29 compares the calculated apparent molar mass of incorporated ions to the expected molar mass. The values calculated indicate that  $\text{Na}^+$  and  $\text{Cl}^-$  ions are not the only species moving into and out of the film during the

reduction and oxidation. This is in keeping with the suggestion that solvent molecules are also uptaken and released by the polymer film.

**Table 4.28:** Measured  $\Delta m$  and potential ranges of linear regions of the reduction and oxidation sweeps of  $\Delta m$  vs.  $Q$  plots for PpyC4S films (0.20 M Ppy / 0.002 M C4S) cycled in 0.10 M NaCl up to 0.30 V vs. Ag/AgCl, at scan rates of 100 and 10  $\text{mV s}^{-1}$ .

Scan Rate / $\text{mV s}^{-1}$	Cycle Segment	Potential Range / V vs. Ag/AgCl	Measured $\Delta m$ / $\mu\text{g}$
100	Reduction 1	+ 0.27 to - 0.15	- 0.17
	Reduction 2	- 0.65 to - 0.85	+ 0.21
	Oxidation 1	- 0.53 to - 0.33	- 0.14
	Oxidation 2	+ 0.08 to + 0.30	+ 0.10
10	Reduction 1	+ 0.30 to - 0.12	- 0.21
	Reduction 2	- 0.59 to - 0.85	+ 0.16
	Oxidation 1	- 0.43 to - 0.34	- 0.12
	Oxidation 2	+ 0.10 to + 0.30	+ 0.18

**Table 4.29:** The apparent molar mass of ions ( $M'$ ), calculated from the respective slopes ( $\Delta m$  vs.  $Q$ ) of PpyC4S films (0.20 M Ppy/0.002 M C4S) in 0.10 M NaCl at scan rates of 100  $\text{mV s}^{-1}$  and 10  $\text{mV s}^{-1}$ . Expected  $M'$  are listed, assuming that  $\text{Cl}^-$  is the dominant ion exchanged during sweep segments Reduction 1 and Oxidation 2 and  $\text{Na}^+$  is the dominant ion exchanged during the sweep segments Reduction 2 and Oxidation 1. The + and - signs are employed to indicate mass increase and decrease respectively.

Scan Rate / $\text{mV s}^{-1}$	Expected $M'$ / $\text{g mol}^{-1}$ (Cation)	$M'$ / $\text{g mol}^{-1}$ Reduction 2 Cation ingress	$M'$ / $\text{g mol}^{-1}$ Oxidation 1 Cation egress	Expected $M'$ / $\text{g mol}^{-1}$ (Anion)	$M'$ / $\text{g mol}^{-1}$ Reduction 1 Anion egress	$M'$ / $\text{g mol}^{-1}$ Oxidation 2 Anion ingress
100	23.0 ( $\text{Na}^+$ )	+ 45.2	- 29.2	35.5 ( $\text{Cl}^-$ )	- 23.5	+ 18.0
10	23.0 ( $\text{Na}^+$ )	+ 20.7	- 22.8	35.5 ( $\text{Cl}^-$ )	- 25.4	+ 27.5

The cyclic voltammograms and massograms obtained for PpyC4S films formed at high dopant concentrations are illustrated in Figure 4.25. As observed for films formed at dopant concentrations of 0.002 M C4S, the anodic and cathodic peak currents recorded decrease with a decrease in scan rate from  $100 \text{ mV s}^{-1}$  to  $10 \text{ mV s}^{-1}$ . Also similar to the results observed at a smaller potential window is the predominance of cation exchange behaviour, with only a small influence of anion exchange seen at low scan rates (Figure 4.25 a).

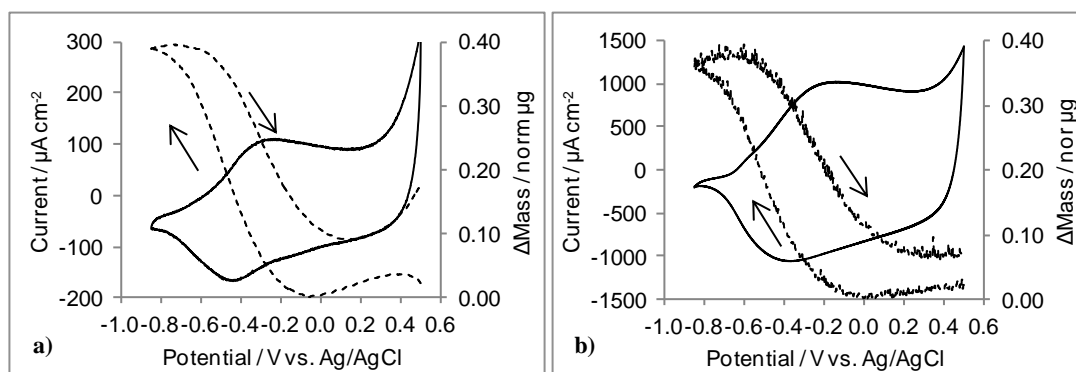


**Figure 4.25:** Cyclic voltammogram (—) and massogram (····) of PpyC4S films grown from an aqueous solution of 0.20 M Ppy and 0.10 M of C4S, to a charge of 15.0 mC. Scan rate a)  $10 \text{ mV s}^{-1}$  or b)  $100 \text{ mV s}^{-1}$  in 0.10 M NaCl aqueous solution, to a potential of 0.50 V vs. Ag/AgCl. Cycle 5 is plotted for each.

Tables 4.30 and 4.31 detail the mass changes calculated from the measured change in frequency and the apparent molar mass calculated using Equation 4.5. It can be observed that similar mass changes due to cation ingress and egress are recorded at both high and low scan rates. At a scan rate of  $10 \text{ mV s}^{-1}$ , a small mass change is apparent at more positive potentials, which may be due to the uptake and release of anions. It can also be noted that both films cycled at  $100 \text{ mV s}^{-1}$  and  $10 \text{ mV s}^{-1}$  retain some mass. It can be seen in Table 4.31 that the apparent molar mass values calculated do not correspond to the expected molar masses. Thus it is possible that the process of charge compensation is not solely due to ion exchange, and that solvent movement is also occurring.

**Table 4.30: Measured  $\Delta m$  and potential ranges of linear regions of the reduction and oxidation sweeps of  $\Delta m$  vs.  $Q$  plots for PpyC4S films (0.20 M Ppy / 0.10 M C4S) cycled in 0.10 M NaCl up to 0.50 V vs. Ag/AgCl, at scan rates of 100 and 10  $\text{mV s}^{-1}$ .**

Scan Rate / $\text{mVs}^{-1}$	Cycle Segment	Potential Range / V vs. Ag/AgCl	Measured $\Delta m$ / $\mu\text{g}$	n
100	Reduction	- 0.39 to - 0.65	+ 0.35 $\pm$ 0.01	2
	Oxidation 2	- 0.36 to + 0.08	- 0.29 $\pm$ 0.01	2
10	Reduction 1	+ 0.32 to + 0.20	- 0.04	-
	Reduction 2	- 0.40 to - 0.63	+ 0.39	-
	Oxidation 1	- 0.48 to - 0.19	- 0.30	-
	Oxidation 2	+ 0.28 to + 0.50	+ 0.09	-

**Table 4.31: The apparent molar mass of ions ( $M'$ ), calculated from the respective slopes ( $\Delta m$  vs.  $Q$ ) of PpyC4S films (0.20 M Ppy/0.10 M C4S) in 0.10 M NaCl at scan rates of 100  $\text{mV s}^{-1}$  and 10  $\text{mV s}^{-1}$ . Expected  $M'$  are listed, assuming that  $\text{Cl}^-$  is the dominant ion exchanged during sweep segments Reduction 1 and Oxidation 2 and  $\text{Na}^+$  is the dominant ion exchanged during the sweep segments Reduction 2 and Oxidation 1. The + and - signs are employed to indicate mass increase and decrease respectively.**

Scan Rate / $\text{mV s}^{-1}$	Expected $M'$ / $\text{g mol}^{-1}$ (Cation)	$M' / \text{g mol}^{-1}$ Reduction 2 Cation ingress	$M' / \text{g mol}^{-1}$ Oxidation 1 Cation egress	Expected $M'$ / $\text{g mol}^{-1}$ (Anion)	$M' / \text{g mol}^{-1}$ Reduction 1 Anion egress	$M' / \text{g mol}^{-1}$ Oxidation 2 Anion ingress
100	23.0 ( $\text{Na}^+$ )	+ 40.7 $\pm$ 5.1	- 26.2 $\pm$ 4.3	35.5 ( $\text{Cl}^-$ )	—	—
10	23.0 ( $\text{Na}^+$ )	+ 26.6	- 27.7	35.5 ( $\text{Cl}^-$ )	- 5.8	+ 9.3

### 4.3 Conclusions

The results of the study carried out with *p*-sulfonatocalix[4]arene-polypyrrole films (PpyC4S) would indicate that the moderately sized penta-anionic *p*-sulfonatocalix[4]arene acts like an immobile dopant during the early cycles of the potential cycling experiments in ionic salt solutions. It can be seen that the measured massograms remain stable over potential cycles 3 to 15, which indicates that no C4S is being removed from the film over this period. This is consistent with the observations made by Latonen *et al.* for polypyrrole films doped with *p*-sulfonatocalix[6]arene (C6S).<sup>9</sup> Their study found a small decrease in the amount of C6S present in the polymer film after 100 potential cycles and so all EQCM analysis they carried out was on data obtained at early potential cycles (cycle 3). In this study, the analysis was carried out using data recorded during cycle 5.

The results obtained for the PpyC4S film were compared to analogous experiments carried out on PpyPSS films. In general it was found that the polypyrrole doped with the large highly charged PSS dopant exhibited cation exchange behaviour, whereas the PpyC4S films exhibited mixed cation-anion behaviour and the pre-dominance of each process is dependent on the experimental conditions. The PpyC4S film was grown at different concentrations of C4S (0.002, 0.01 and 0.10 M). Theoretical calculations determined that there was an increase in doping level with the increasing concentration of calixarene in the polymerisation solution. Consequently it was shown that the dopant concentration was found to affect the ion exchange properties with the polymer grown from the highest dopant concentration acting most like an ideal cation exchanger. This is clearly shown in Figure 4.13 (a), which depicts the cyclic voltammogram and massogram obtained when cycling a PpyC4S film, polymerised from a solution of 0.20 M pyrrole and 0.10 M C4S, in 0.10 M NaCl at a scan rate of 100 mV s<sup>-1</sup>. The effect of scan rate was investigated on the polymer grown from both the lowest and highest concentration of C4S (0.002 M and 0.100 M). For the PpyC4S film formed at the lowest concentration of dopant, the ion exchange behaviour was mixed at all scan rates and the anion exchange became to dominate at the lowest scan rate. In contrast the polymer grown from the higher concentration of C4S behaved like a cation exchange material at all scan rates studied.

A study was carried out to investigate the role of the electrolyte salt on the ion exchange properties of the PpyC4S film and it is clear that both the nature of the anion and cation in solution can significantly affect the shape of the massogram. For example the massogram shown for the PpyC4S polymer cycled in CsCl at  $100 \text{ mV s}^{-1}$ , is the shape of a classic cation exchange polymer (Figure 4.17 d). The same polymer which was grown under analogous conditions and cycled in  $\text{NaClO}_4$  displays a massogram which is the shape of a classic anion exchange polymer (Figure 4.20 c).

Analysis of the data using Faraday's Law of Electrolysis showed that the exchange behaviour of the PpyC4S was even more complicated, with solvent and ion-pairs moving into and out of the polymer. It would appear that these species moved in opposite directions to the ions so that the analysis of the data gave a calculated molar mass which was smaller in magnitude than the known molar mass for the ion in question.

#### 4.4 References

1. Y. Pei, J. Travas-Sejdic and D. E. Williams, *Langmuir*, 2012, **28**, 8072-8083.
2. M. N. Akieh, W. E. Price, J. Bobacka, A. Ivaska and S. F. Ralph, *Synthetic Metals*, 2009, **159**, 2590-2598.
3. C. Weidlich, K. M. Mangold and K. Jüttner, *Electrochimica Acta*, 2005, **50**, 1547-1552.
4. S. Bruckenstein, K. Brzezinska and A. R. Hillman, *Physical Chemistry Chemical Physics*, 2000, **2**, 1221-1229.
5. J. Y. Lim, W.-K. Paik and I.-H. Yeo, *Synthetic Metals*, 1995, **69**, 451-454.
6. E. Andreoli, Ph.D., NUI Maynooth, 2010.
7. S. Bruckenstein, J. H. Chen, I. Jureviciute and A. R. Hillman, *Electrochimica Acta*, 2009, **54**, 3516-3525.
8. Y. Velmurugu and S. Skaarup, *Ionics*, 2005, **11**, 370-374.
9. R.-M. Latonen, M. N. Akieh, K. Vavra, J. Bobacka and A. Ivaska, *Electroanalysis*, 2013, **25**, 991-1004.
10. K. Kontturi, L. Murtomaki, P. Pentti and G. Sundholm, *Synthetic Metals*, 1998, **92**, 179-185.
11. P. M. Dziewonski and M. Grzeszczuk, *Journal of Physical Chemistry B*, 2010, **114**, 7158-7171.
12. K. Naoi, M. Lien and W. H. Smyrl, *Journal of The Electrochemical Society*, 1991, **138**, 440-445.
13. C. Weidlich, K. M. Mangold and K. Jüttner, *Electrochimica Acta*, 2005, **50**, 5247-5254.
14. S. Skaarup, L. Bay, K. Vidanapathirana, S. Thybo, P. Tofte and K. West, *Solid State Ionics*, 2003, **159**, 143-147.
15. V. Syritski, A. Opik and O. Forsen, *Electrochimica Acta*, 2003, **48**, 1409-1417.
16. P. Kubat, J. Sebera, S. Zalis, J. Langmaier, M. Fuciman, T. Polivka and K. Lang, *Physical Chemistry Chemical Physics*, 2011, **13**, 6947-6954.
17. J. Szejtli, *Cyclodextrins and Their Inclusion Complexes*, Akademiai Kiado, 1982.

18. D.-S. Guo, K. Wang and Y. Liu, *Journal of Inclusion Phenomena and Macrocyclic Chemistry*, 2008, **62**, 1-21.
19. S. J. Dalgarno, J. L. Atwood and C. L. Raston, *Crystal Growth and Design*, 2006, **6**, 174-180.
20. I. Yoshida, N. Yamamoto, F. Sagara, D. Ishii, K. Ueno and S. Shinkai, *Bulletin of the Chemical Society of Japan*, 1992, **65**, 1012-1015.
21. R. Doyle, C. B. Breslin, O. Power and A. D. Rooney, *Electroanalysis*, 2012, **24**, 293-302.
22. G. Bidan and M.-A. Niel, *Synthetic Metals*, 1997, **85**, 1387-1388.
23. Z. Mousavi, J. Bobacka and A. Ivaska, *Electroanalysis*, 2005, **17**, 1609-1615.
24. C. Bonal, Y. Israeli, J.-P. Morel and N. Morel-Desrosiers, *Journal of the Chemical Society, Perkin Transactions 2*, 2001, 1075-1078.
25. J.-P. Morel and N. Morel-Desrosiers, *Organic and Biomolecular Chemistry*, 2006, **4**, 462-465.
26. G. Sauerbrey, *Zeitschrift Fur Physik*, 1959, **155**, 206-222.
27. S. Bruckenstein and M. Shay, *Electrochimica Acta*, 1985, **30**, 1295-1300.
28. C. Fruboese and K. Doblhofer, *Synthetic Metals*, 1993, **55**, 1329-1334.
29. R. M. Torresi, S. I. Córdoba de Torresi, T. Matencio and M. A. De Paoli, *Synthetic Metals*, 1995, **72**, 283-287.
30. K. M. Mangold, C. Weidlich, J. Schuster and K. Juettner, *Journal of Applied Electrochemistry*, 2005, **35**, 1293-1301.
31. C. Debiemme-Chouvy, A. Rubin, H. Perrot, C. Deslouis and H. Cachet, *Electrochimica Acta*, 2008, **53**, 3836-3843.
32. A. R. Hillman, *Journal of Solid State Electrochemistry*, 2011, **15**, 1647-1660.
33. W. Plieth, A. Bund, U. Rammelt, S. Neudeck and L. Duc, *Electrochimica Acta*, 2006, **51**, 2366-2372.
34. R. Yang, K. Naoi, D. F. Evans, W. H. Smyrl and W. A. Hendrickson, *Langmuir*, 1991, **7**, 556-558.
35. D. A. Reece, S. F. Ralph and G. G. Wallace, *Journal of Membrane Science*, 2005, **249**, 9-20.

36. P. Holzhauser and K. Bouzek, *Journal of Applied Electrochemistry*, 2006, **36**, 703-710.
37. V. Annibaldi, Ph.D., NUI Maynooth, 2010.
38. G. Diao and W. Zhou, *Journal of Electroanalytical Chemistry*, 2004, **567**, 325-330.
39. L. T. T. Kim, C. Gabrielli, A. Pailleret and H. Perrot, *Electrochimica Acta*, 2011, **56**, 3516-3525.
40. R. Schrebler, P. Grez, P. Cury, C. Veas, M. Merino, H. Gómez, R. Córdova and M. A. del Valle, *Journal of Electroanalytical Chemistry*, 1997, **430**, 77-90.
41. R. Rajagopalan and J. O. Iroh, *Electrochimica Acta*, 2002, **47**, 1847-1855.
42. S. McDermott, Ph.D., NUI Maynooth, 2010.
43. J. M. Fonner, L. Forciniti, H. Nguyen, J. D. Byrne, Y.-F. Kou, J. Syeda-Nawaz and C. E. Schmidt, *Biomedical Materials*, 2008, **3**, 034124.
44. C. K. Baker, Y. J. Qiu and J. R. Reynolds, *Journal of Physical Chemistry*, 1991, **95**, 4446-4452.
45. P. R. Teasdale, L. A. P. Kane-Maguire, G. G. Wallace and G. M. Spinks, *Conductive Electroactive Polymers: Intelligent Materials Systems*, CRC Press, 2002.
46. Q. J. Xie, S. Kuwabata and H. Yoneyama, *Journal of Electroanalytical Chemistry*, 1997, **420**, 219-225.
47. C. S. C. Bose, S. Basak and K. Rajeshwar, *J. Phys. Chem.*, 1992, **96**, 9899-9906.
48. M. N. Akieh, S. F. Ralph, J. Bobacka and A. Ivaska, *Journal of Membrane Science*, 2010, **354**, 162-170.
49. Y. Li, *Electrochimica Acta*, 1996, **42**, 203-210.
50. T. V. Vernitskaya and O. N. Efimov, *Uspekhi Khimii*, 1997, **66**, 489-505.
51. C. C. B. Bufon, J. Vollmer, T. Heinzl, P. Espindola, H. John and J. Heinze, *Journal of Physical Chemistry B*, 2005, **109**, 19191-19199.
52. M. Zhou, M. Pagels, B. Geschke and J. Heinze, *Journal of Physical Chemistry B*, 2002, **106**, 10065-10073.
53. A. A. A. Almario and R. L. T. Caceres, *Journal of the Chilean Chemical Society*, 2009, **54**, 14-19.

54. K. R. Ansari, *Russian Journal of Electrochemistry*, 2005, **41**, 950-955.
55. T. Raudsepp, M. Marandi, T. Tamm, V. Sammelselg and J. Tamm, *Electrochimica Acta*, 2008, **53**, 3828-3835.
56. G. Garcia-Belmonte, *Electrochemical Communications*, 2003, **5**, 236-240.
57. K. R. Temsamani, O. Ceylan, B. J. Yates, S. Oztemiz, T. P. Gbatu, A. M. Stalcup, H. B. Mark, Jr. and W. Kutner, *Journal of Solid State Electrochemistry*, 2002, **6**, 494-497.
58. K. P. Vidanapathirana, M. A. Careem, S. Skaarup and K. West, *Solid State Ionics*, 2002, **154-155**, 331-335.
59. G. Inzelt, V. Kertesz and A.-S. Nyback, *Journal of Solid State Electrochemistry*, 1999, **3**, 251-257.
60. S. Skaarup, M. J. M. Jafeen and M. A. Careem, *Solid State Ionics*, 2010, **181**, 1245-1250.
61. A. C. Partridge, C. Milestone, C. O. Too and G. G. Wallace, *Journal of Membrane Science*, 1997, **132**, 245-253.
62. A. J. Bard and L. R. Faulkner, *Electrochemical Methods. Fundamentals and Applications*, John Wiley and Sons Inc., New York, 2001.
63. P. C. Hayes and S. H. Algie, *Process Principles in Minerals and Materials Production*, Hayes Publishing, 1993.
64. M. Hepel, Y.-M. Chen and R. Stephenson, *Journal of the Electrochemical Society*, 1996, **143**, 498-505.
65. T. Raudsepp, M. Marandi, T. Tamm, V. Sammelselg and J. Tamm, *Electrochimica Acta*, 2013, Ahead of Print.
66. B. C. C. Bof, T. Heinzl, P. Espindola and J. Heinze, *Journal of Physical Chemistry B*, 2010, **114**, 714-718.

## Chapter 5

---

Remediation of Hexavalent Chromium  
using Polypyrrole Nanowires on  
Conventional Electrodes and Polyamide  
Membranes; and Polypyrrole-Sodium  
Alginate Particles

---

## 5.1 Introduction

Chromium is a naturally occurring metal which exists primarily in its trivalent state, Cr(III). However, hexavalent chromium Cr(VI), a known carcinogen and mutagen, is released into the environment as a waste product of industrial processes such as chrome plating, pigment manufacture and leather tanning. Treatment methods for removing Cr(VI) from industrial wastewaters include chemical and electrochemical reduction, electrocoagulation, ion exchange, membrane separation and adsorption.<sup>1-6</sup> While these methods of remediation are often very effective many produce Cr(VI) impregnated secondary waste products which are difficult to dispose of or recycle.<sup>7, 8</sup> This problem of post removal processing, in addition to the high costs associated with many of these methods gives rise to the need for an efficient, environmentally friendly removal method for Cr(VI).

In this chapter, two different methods of Cr(VI) remediation by nanostructures of the conducting polymer polypyrrole will be examined. The first method is the development of a polypyrrole nanowire coated porous electrode, using a polyamide filtration membrane as the base material, for the electrochemical remediation of Cr(VI). It has been found that polypyrrole coated electrodes can effectively reduce Cr(VI) to the less toxic Cr(III) with a removal efficiency of almost 100 percent over short periods of time.<sup>9-11</sup> These electrochemical treatment strategies employ the application of a reduction potential, prior to immersion of the polypyrrole in a solution containing Cr(VI).<sup>11-15</sup> As polypyrrole is in its oxidised form after electropolymerisation, this ensures that the polymer is in its reduced state.<sup>13</sup> It is reported that the reduction of Cr(VI) to Cr(III) is the result of two phenomena; a) the spontaneous electron transfer from the polypyrrole to Cr(VI) present in solution and b) anion exchange which occurs to maintain the electroneutrality of the polypyrrole film as it is oxidised by the Cr(VI).<sup>14, 15</sup> Polypyrrole nanowires (PpyNW) can have advantages over bulk polypyrrole, such as a larger surface area with increased access to surface access sites, while formation on a large porous electroactive membrane offers the potential for electrochemical regeneration of the polymer for further Cr(VI) remediation.<sup>12</sup> During the course of this study, it was discovered that the remediation of Cr(VI) was not as straightforward as described in the literature. Thus, this chapter includes an examination of the mechanism of Cr(VI) removal from solution by the polypyrrole nanowires and an investigation of

the efficacy of the electrochemical pre-reduction step. It will be shown that although the pre-reduction step does influence the kinetics during the initial stages of Cr(VI) removal, adsorption and spontaneous electron transport at the polymer interface are the more dominant processes in the removal of Cr(VI) from solution.

The second approach which is discussed in Section 5.7, is the development of a polypyrrole/sodium alginate composite for the adsorption of Cr(VI) from solution. There is great interest currently being shown in the use of conducting polymer based materials for the adsorption of Cr(VI) from solution. Polyaniline and polypyrrole particles and micro- and nanocomposites of polypyrrole and iron oxides have been investigated as adsorbents for Cr(VI) and often exhibit higher removal capacities for Cr(VI) than commercially available adsorbents.<sup>16-20</sup> Polypyrrole coated on organic supports such as cellulose or sawdust have also shown an improvement in removal capacity compared to the uncoated substrates.<sup>21, 22</sup> While acting as adsorbents, these polypyrrole coated supports also have the potential to chemically reduce Cr(VI) to the less toxic Cr(III). Conducting/biopolymer composites are inexpensive, environmentally friendly and relatively easy to prepare. Polypyrrole/sodium alginate composites (PpySA) have been investigated for use in the fields of biomedical materials and devices and in energy conversion and storage.<sup>23-25</sup> Thus far their ability to remediate Cr(VI) has not been studied, although other conducting/biopolymer systems have been examined. For example, polyaniline/chitosan composites were found to effectively adsorb Cr(III) and Cr(VI) over a 30 minute period<sup>26</sup> while most recently alginate-montmorillonite/polyaniline nanocomposites were prepared, exhibiting *pseudo*-second-order adsorption kinetics for Cr(VI) adsorption.<sup>27</sup> This chapter demonstrates the ability of the PpySA composites to remove Cr(VI) from solution and investigates the effect of solution pH, solution temperature and initial concentration of the Cr(VI) solution. The adsorption kinetics of the removal process are also examined using the Morris-Weber, Lagergren and *pseudo*-second-order equations.

## 5.2 Polypyrrole Nanowires – Preliminary Studies

### 5.2.1 Cr(VI) Speciation

Chromium can exist in oxidation states ranging from 0 to VI, however, only trivalent and hexavalent chromium are sufficiently stable to exist in the environment.<sup>28</sup> It has been discovered that the remediation of Cr(VI) is dependent on solution pH.<sup>9, 29</sup> Cr(VI) in acidic solutions has a very high, positive redox potential ( $E^\circ$  between 1.195 and 1.33 V)<sup>30, 31</sup> which indicates that it is very strongly oxidising.<sup>28</sup> As the reduction of Cr(VI) to Cr(III) is thermodynamically favoured at low pH the studies carried out in this chapter were all performed in acidic solutions of 0.10 M  $H_2SO_4$ . The speciation of Cr(VI) in solution is dependant both on solution pH and on total Cr(VI) concentration. Based on the findings of Tandon *et al.*, the diagram shown in Figure 5.1 was developed illustrating the abundance of Cr(VI) species in aqueous solution over a pH range of 0-14.<sup>28, 32</sup> It can be observed that between pH 1 and 6  $HCrO_4^-$  is the main species of Cr(VI) up to a Cr(VI) concentration of 0.01 M at which point it will begin to condense and form  $Cr_2O_7^{2-}$ , the dichromate ion.<sup>28</sup> Therefore, as the pH of the 0.1 mM Cr(VI) solution used in this study is pH 1 and the concentration of Cr(VI) in solution is below 0.01 M, the predominant species of interest will be the  $HCrO_4^-$  ion.

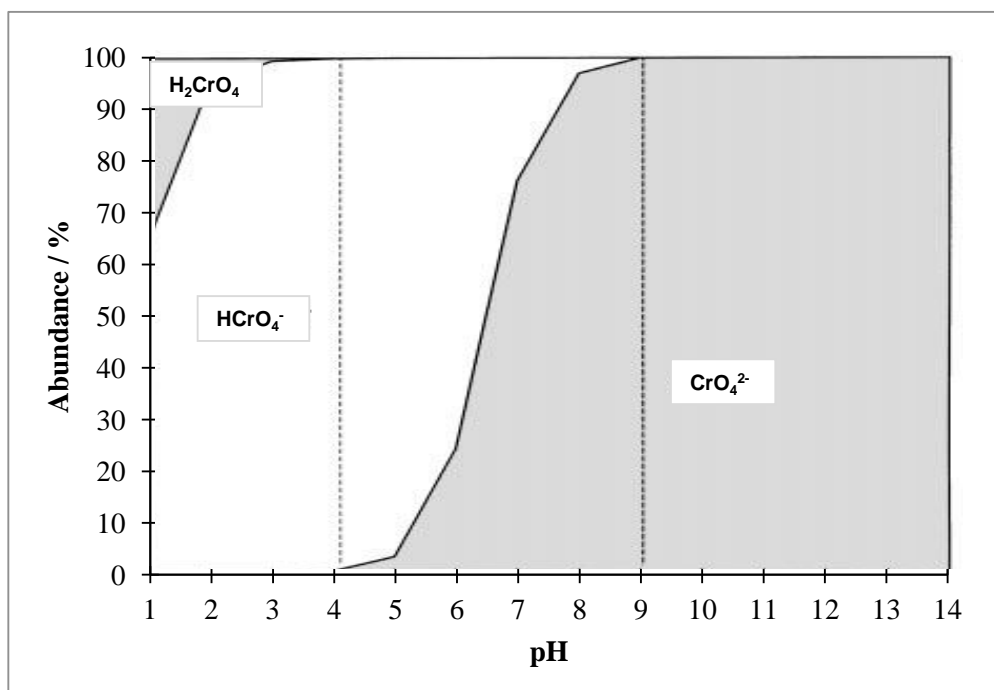


Figure 5.1: Calculated abundance of Cr(VI) species in aqueous solution at total Cr(VI) concentration of 1  $\mu$ M within a pH range of 1-14.<sup>28</sup>

### 5.2.2 Removal of Cr(VI) by Polypyrrole Nanowires

Hexavalent chromium is a strongly coloured species, with a characteristic absorption spectrum in the visible-ultraviolet region. A typical UV-Vis spectrum of Cr(VI) displays peaks at 350 nm and 260 nm. Throughout this study, the exact concentration of the  $\text{Na}_2\text{Cr}_2\text{O}_7 \cdot 2\text{H}_2\text{O}$  in 0.10 M  $\text{H}_2\text{SO}_4$  was obtained by relating the absorbance observed at 350 nm to the calibration curve prepared according to the Beer-Lambert Law, for various concentrations of  $\text{Na}_2\text{Cr}_2\text{O}_7 \cdot 2\text{H}_2\text{O}$  in 0.10 M  $\text{H}_2\text{SO}_4$  (Section 2.2.8.1). All chromium solutions were kept at a temperature of  $20 \pm 2$  °C unless otherwise stated.

In order to determine the mechanism by which polypyrrole nanowires (PpyNW) interact with Cr(VI) it was imperative to first establish whether or not PpyNW could remove Cr(VI) from an aqueous solution. The parameters for formation of polymer films in this chapter are summarised in Table 5.1. Studies were carried out using polypyrrole films formed on a conventional gold electrode, unless otherwise stated.

**Table 5.1: Summary of the parameters and aqueous solution formulations used to fabricate Ppy films.**

Polymer Film	Monomer Concentration / M	Dopant Concentration / M	Applied Potential / V vs. SCE	Charge Density / $\text{mC cm}^{-2}$
Polypyrrole Nanowires (PpyNW)	0.15	$\text{Na}_2\text{H}_2\text{PO}_4$ : 0.20 $\text{LiClO}_4$ : 0.001	0.80	400
Polypyrrole Chloride (PpyCl)	0.15	$\text{NaCl}$ : 0.10	0.70	400

PpyNW were potentiostatically formed on a gold wire electrode of surface area  $1.2 \text{ cm}^2$ . A potential of 0.80 V vs. SCE was applied until a charge density of  $400 \text{ mC cm}^{-2}$  was achieved. After growth, the PpyNW were rinsed with distilled  $\text{H}_2\text{O}$  and then reduced in 0.10 M  $\text{H}_2\text{SO}_4$  at an applied potential of  $-0.80$  V vs. SCE for 30 minutes to ensure the polymer was in its reduced state.<sup>13</sup> The PpyNW coated Au wire was then transferred to a quartz crystal cuvette containing  $3 \text{ cm}^3$  0.10 mM  $\text{Na}_2\text{Cr}_2\text{O}_7 \cdot 2\text{H}_2\text{O}$  in 0.10 M  $\text{H}_2\text{SO}_4$  (acidified 0.10 mM  $\text{Na}_2\text{Cr}_2\text{O}_7 \cdot 2\text{H}_2\text{O}$ ). This solution is strongly coloured yellow and so the absorbance bands of Cr(VI) could be monitored by UV-Vis absorption spectroscopy. Figure 5.2 depicts the UV-Vis spectra showing the removal of Cr(VI) from solution during contact with the PpyNW coated Au electrode for a period of 24 hours. The peak at 350 nm is a characteristic charge transfer band for the  $\text{HCrO}_4^-$  species.<sup>33</sup>

Bulk polypyrrole (PpyCl) was formed (Table 5.1) on an Au wire electrode for comparison with the PpyNW films. After growth, the PpyCl was rinsed with distilled H<sub>2</sub>O and then reduced in 0.10 M H<sub>2</sub>SO<sub>4</sub> at an applied potential of  $-0.80$  V vs. SCE for 30 minutes before being transferred to a quartz crystal cuvette containing 3 cm<sup>3</sup> acidified 0.10 mM Na<sub>2</sub>Cr<sub>2</sub>O<sub>7</sub>·2H<sub>2</sub>O solution and the resulting UV-Vis spectra are depicted in Figure 5.3. It can clearly be seen that the Cr(VI) band at 350 nm decreases in intensity, similar to that seen in Figure 5.2, as a function of exposure time to the PpyCl coated electrode.

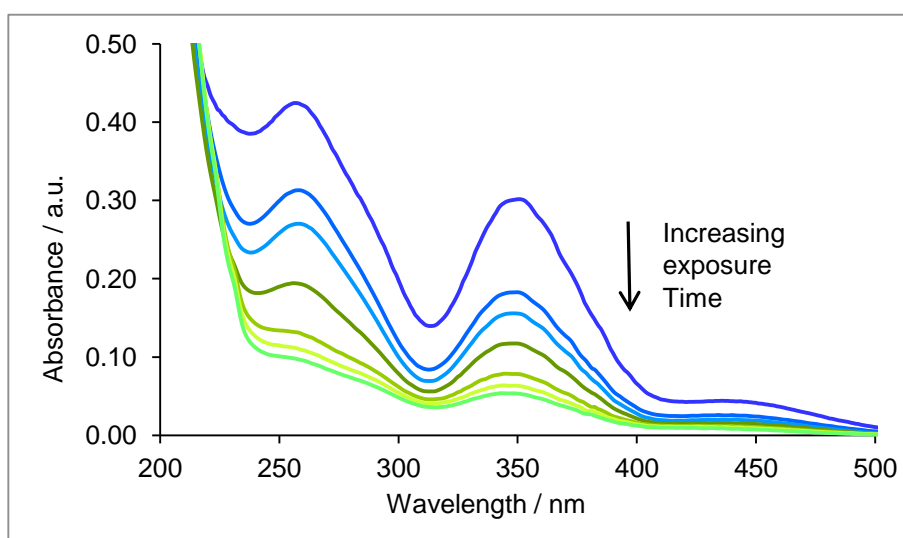


**Figure 5.2:** UV-Vis spectra recorded for 0.10 mM Na<sub>2</sub>Cr<sub>2</sub>O<sub>7</sub>·2H<sub>2</sub>O in 0.10 M H<sub>2</sub>SO<sub>4</sub> as a function of exposure time to the PpyNW coated Au wire electrode. Spectra were recorded at time intervals of 0 (—), 60 (—), 120 (—), 300 (—), 900 (—), 1200 (—) and 1440 (—) minutes.

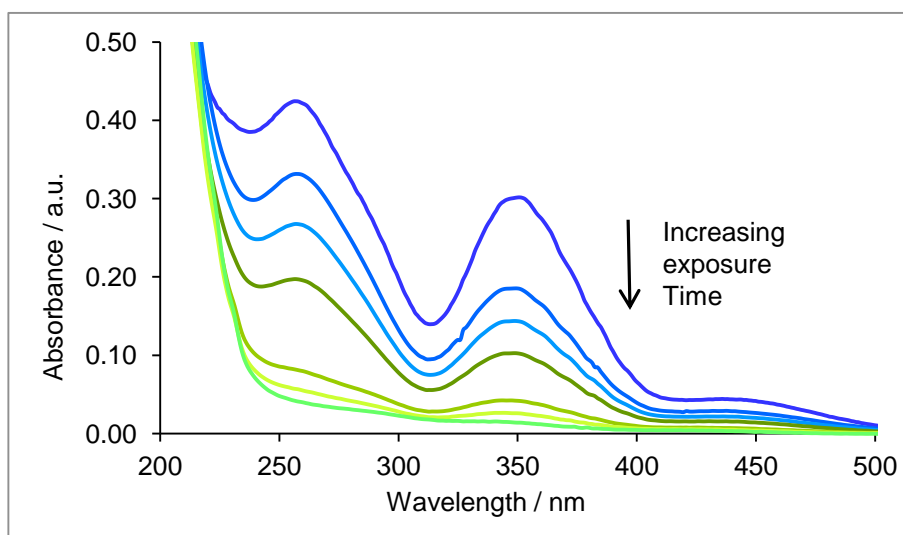


**Figure 5.3:** UV-Vis spectra recorded for 0.10 mM Na<sub>2</sub>Cr<sub>2</sub>O<sub>7</sub>·2H<sub>2</sub>O in 0.10 M H<sub>2</sub>SO<sub>4</sub> as a function of exposure time to the PpyCl coated Au wire electrode. Spectra were recorded at time intervals of 0 (—), 60 (—), 120 (—), 300 (—), 900 (—), 1200 (—) and 1440 (—) minutes.

The similar decrease in the absorbance band at 350 nm which is seen for the acidified 0.10 mM  $\text{Na}_2\text{Cr}_2\text{O}_7 \cdot 2\text{H}_2\text{O}$  exposed to both PpyNW and PpyCl films confirms the abilities of the PpyNW and PpyCl films to remove Cr(VI) from solution. Thus, the mechanism by which the removal of Cr(VI) occurs was investigated. The following studies were all carried out with PpyNW and PpyCl coated on a conventional gold electrode, before the applications of a PpyNW coated porous membrane electrode were examined.

### 5.3 Mechanism of Chromium Remediation

Literature reports on the use of electrochemically reduced polypyrrole films vary on the mechanism by which the polypyrrole films remove Cr(VI) from solution. By applying a negative reduction potential to the polypyrrole coated electrode, prior to immersion in a Cr(VI) solution, it has been found that polypyrrole coated electrodes can effectively reduce Cr(VI) to the less toxic Cr(III) with a removal efficiency of almost 100 percent over short periods of time.<sup>9-11</sup> A number of theories as to the primary mechanism of Cr(VI) removal by polypyrrole abound. These include a) the spontaneous electron transfer from the polypyrrole to Cr(VI) present in solution, b) anion exchange which occurs to maintain the electroneutrality of the polypyrrole film as it is oxidised by the Cr(VI) and c) adsorption of the resulting Cr(III).<sup>14, 33, 34</sup> Thus, in investigating the mechanism by which Cr(VI) is removed from solution by the Ppy films, three possible modes of Cr(VI) removal were examined in this study.

The first potential mechanism discussed will be adsorption of Cr(VI) through anion exchange. This could occur, as the mobile phosphate and perchlorate anions which dope the polypyrrole nanowires during electropolymerisation may be expelled from the polymer during the application of the reduction potential of  $-0.80$  V vs. SCE in  $0.10$  M  $\text{H}_2\text{SO}_4$ . When placed in an acidified solution of  $\text{Na}_2\text{Cr}_2\text{O}_7 \cdot 2\text{H}_2\text{O}$ , the polymer may take in mobile anions such as  $\text{HCrO}_4^-$  from solution, in order to balance the charge on the polypyrrole backbone, as it is oxidised. In this way, Cr(VI) is removed from solution.<sup>11</sup> The second possible adsorption process is the attraction of the  $\text{HCrO}_4^-$  to the positively charged protonated polypyrrole backbone. It has been reported that at a  $\text{pH} < 3$ , the nitrogen atoms of the polypyrrole backbone become protonated, which causes the polymer to carry a positive charge, even when in its reduced state.<sup>35</sup> The final mode of Cr(VI) remediation investigated was the reduction of Cr(VI) to Cr(III) through spontaneous electron transfer. These processes are summarised in Figure 5.4.

Tests were also carried out to determine the fate of the chromium; whether it was adsorbed onto the polypyrrole film as Cr(VI) or Cr(III) or whether it was released into solution as Cr(III). This will be discussed in Section 5.3.4.

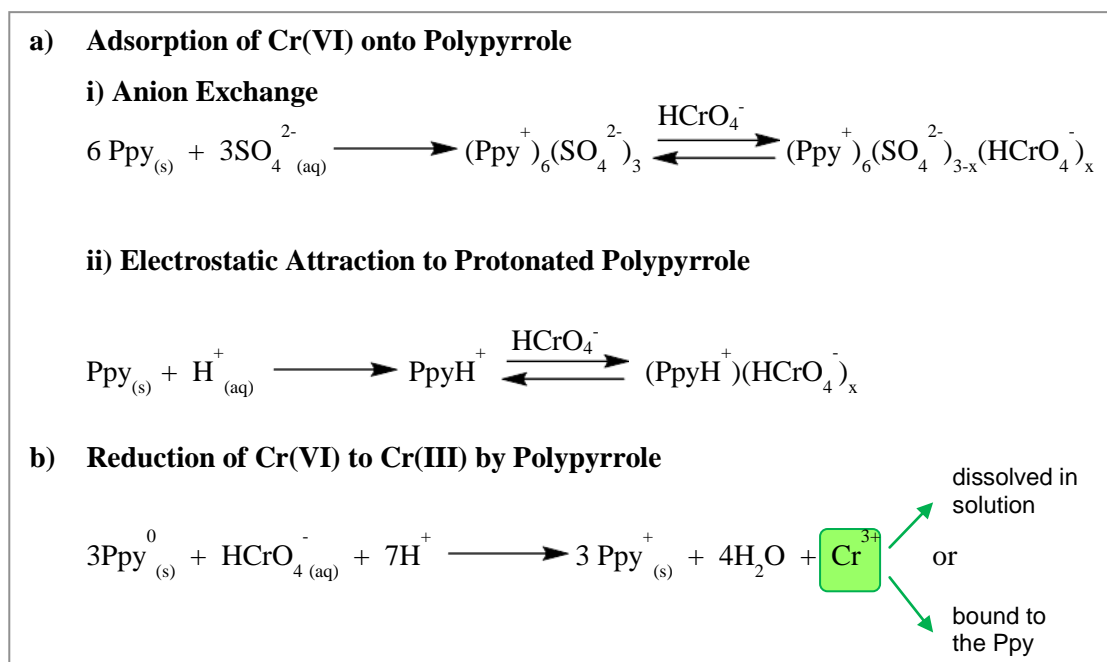


Figure 5.4: Possible processes which could occur during the remediation of Cr(VI) by polypyrrole films.

### 5.3.1 Adsorption of Cr(VI) onto Polypyrrole – Anion Exchange

As illustrated in Chapter 4, Figure 4.1, polypyrrole doped with small, mobile anions can undergo ion exchange with ions in solution. As the polypyrrole nanowires are doped with  $\text{ClO}_4^-$ ,  $\text{PO}_4^{3-}$  and  $\text{SO}_4^{2-}$  post reduction in sulfuric acid, and Cr(VI) exists as  $\text{HCrO}_4^-$  in 0.10 M  $\text{H}_2\text{SO}_4$ ,<sup>29</sup> it is possible that ion exchange is the predominate process by which chromium is removed from solution. If anion exchange is occurring, replacing the small, mobile dopants with a large, immobile species should reduce the efficiency of the Cr(VI) removal. The immobile dopant chosen was sodium dodecyl sulfate (SDS) which is depicted in Figure 5.5. Its large size causes it to be entrapped within the polymer and it will not undergo ion exchange.<sup>36</sup>

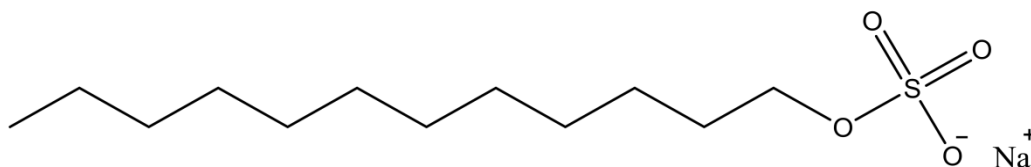


Figure 5.5: Structure of dodecyl sulfate sodium salt (SDS).

PpySDS films were formed potentiostatically on an Au wire electrode of surface area  $1.2 \text{ cm}^2$ , by the application of a potential of  $0.70 \text{ V vs. SCE}$ , in an aqueous solution containing  $0.15 \text{ M}$  pyrrole and  $0.10 \text{ M}$  sodium dodecyl sulfate until a charge density of  $400 \text{ mC cm}^{-2}$  was achieved. As with the PpyNW and PpyCl films, the PpySDS film was rinsed with distilled  $\text{H}_2\text{O}$  and then reduced in  $0.10 \text{ M H}_2\text{SO}_4$  at  $-0.80 \text{ V vs. SCE}$  for 30 minutes before being transferred to a quartz crystal cuvette containing  $3 \text{ cm}^3$  acidified solution of  $0.10 \text{ mM Na}_2\text{Cr}_2\text{O}_7 \cdot 2\text{H}_2\text{O}$ . UV-Vis spectroscopy was used to follow the decrease in the Cr(VI) absorbance band at  $350 \text{ nm}$  over 24 hours and the data were compared to the data obtained for the removal of Cr(VI) from solution by PpyNW and PpyCl films, which can be seen in Figures 5.2 and 5.3.

It can be clearly observed from Figure 5.6 that there is little difference in the extent of removal of Cr(VI) from solution by PpyCl and PpySDS films. This indicates that the nature of the dopant, whether mobile or immobile, does not play an essential role in the removal of Cr(VI) from solution. Interestingly, it can be seen that the PpyNW film removes Cr(VI) from the solution at a slower rate than the other films. It has been reported that polypyrrole doped with chloride anions, which have a smaller hydrated radius, are better at reducing Cr(VI) than polypyrrole doped with the larger perchlorate anions. This is attributed to different porosity of the polymer film when the dopant anions are expelled.<sup>37</sup> Rajeshwar *et al.* conducted X-ray photoelectron spectroscopy (XPS) on PpyCl films which were immersed in an acidified solution containing  $2 \text{ mM}$  Cr(VI), until UV-Vis spectroscopy indicated complete Cr(VI) removal. While some uptake of Cr(VI) was observed, this only accounted for approximately 6 percent of the Cr(VI) removed from solution.<sup>9, 11</sup> Thus it can be concluded that while some ion exchange occurs, it is not the primary mechanism by which Cr(VI) is removed from solution.

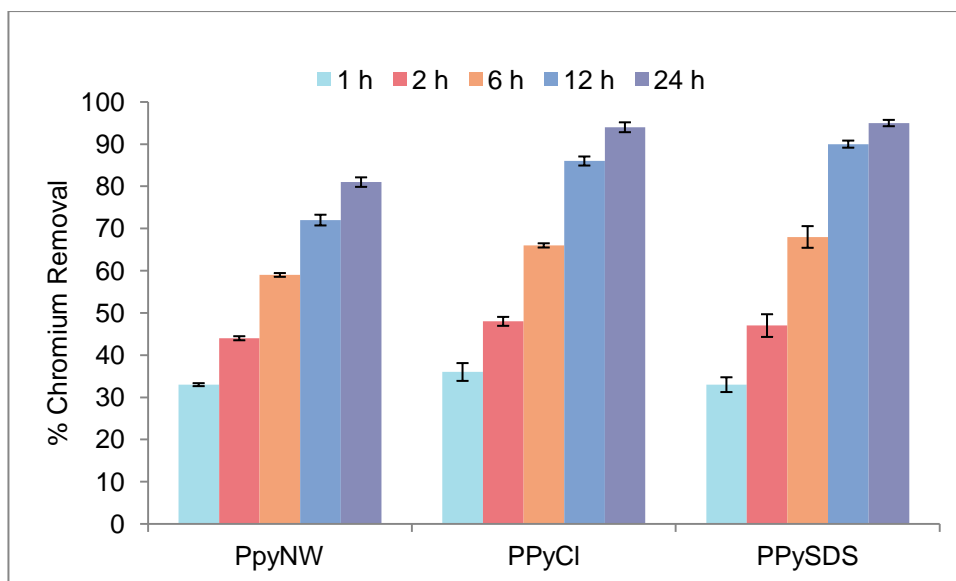
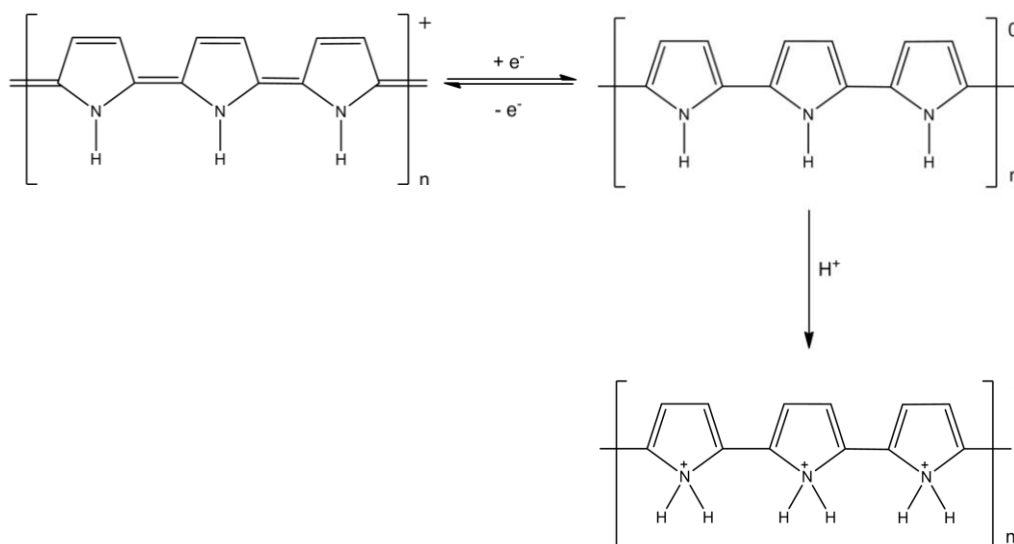


Figure 5.6: The percentage of chromium removed from an acidified 0.1 mM Cr(VI) solution, in contact with polypyrrole nanowires (PpyNW), polypyrrole doped with chloride ions (PPyCl) and polypyrrole doped with dodecyl sulfate ions (PPySDS),  $n = 3$ .

### 5.3.2 Protonation of Polypyrrole

It has been long established that the reduction of Cr(VI) is dependent on solution pH.<sup>9, 29</sup> This is because the reduction of Cr(VI) to Cr(III) is thermodynamically favoured at low pH; as  $H^+$  ion concentration in solution increases, the standard potential of the reduction of Cr(VI) to Cr(III) increases and  $\Delta G^\circ$  becomes more negative.<sup>8</sup> At  $pH > 3$  the  $H^+$  ion concentration may not be sufficient for the stoichiometry of the reduction reaction of Cr(VI) to Cr(III)<sup>38</sup> (Figure 5.4 b), and as the standard potential of the reduction of Cr(VI) to Cr(III) becomes less positive at increasing pH values,  $\Delta G^\circ$  becomes less negative. This results in the reduction of Cr(VI) to Cr(III) becoming less thermodynamically favoured. Higher pH values may also promote the formation of insoluble Cr(III) hydroxides at the polymer surface, which will hamper electron transfer.<sup>8</sup> It has also been observed that the nitrogen atoms of polypyrrole are protonated at pH values below pH 3 (Scheme 5.1) which infers a positive charge upon the polypyrrole backbone, even when in its reduced form. This was observed through the increased conductivity of the reduced polypyrrole film after immersion in a de-aerated solution at pH 3.<sup>39</sup> This positive charge enhances the adsorption of anions in solution by the polypyrrole film, through electrostatic interactions.<sup>35</sup>



**Scheme 5.1:** The positively charged electropolymerised polypyrrole film is reduced by the application of a negative reduction potential. The nitrogen atoms in the reduced film become protonated in an acidic solution, which in this study is 0.10 mM Na<sub>2</sub>Cr<sub>2</sub>O<sub>7</sub>·2H<sub>2</sub>O in 0.10 M H<sub>2</sub>SO<sub>4</sub>.

Therefore a study was carried out to investigate the efficiency of Cr(VI) removal by PpyNW as a function of pH. PpyNW were potentiostatically formed as described in Section 5.2, rinsed with distilled H<sub>2</sub>O and then reduced in 0.10 M H<sub>2</sub>SO<sub>4</sub> at -0.80 V vs. SCE for 30 minutes to ensure the polymer was in its reduced state.<sup>13</sup> After rinsing, the PpyNW coated electrodes were immersed in an aqueous solution of 0.10 mM Na<sub>2</sub>Cr<sub>2</sub>O<sub>7</sub>·2H<sub>2</sub>O, held at pH 1, pH 3.5 and pH 6 respectively by the addition of H<sub>2</sub>SO<sub>4</sub> to distilled water. The initial absorbance spectrum of the solution at pH 6 was different to those at pH 1 and pH 3.5 (Figure 5.7) as at this pH, chromium is predominantly in the form CrO<sub>4</sub><sup>2-</sup>. The speciation of chromium is highly pH dependent; it can be seen in Figure 5.1 that while CrO<sub>4</sub><sup>2-</sup> and HCrO<sub>4</sub><sup>-</sup> ions exist in a pH dependent equilibrium between pH 2 – pH 6,<sup>40</sup> at pH 1 HCrO<sub>4</sub><sup>-</sup> predominates.

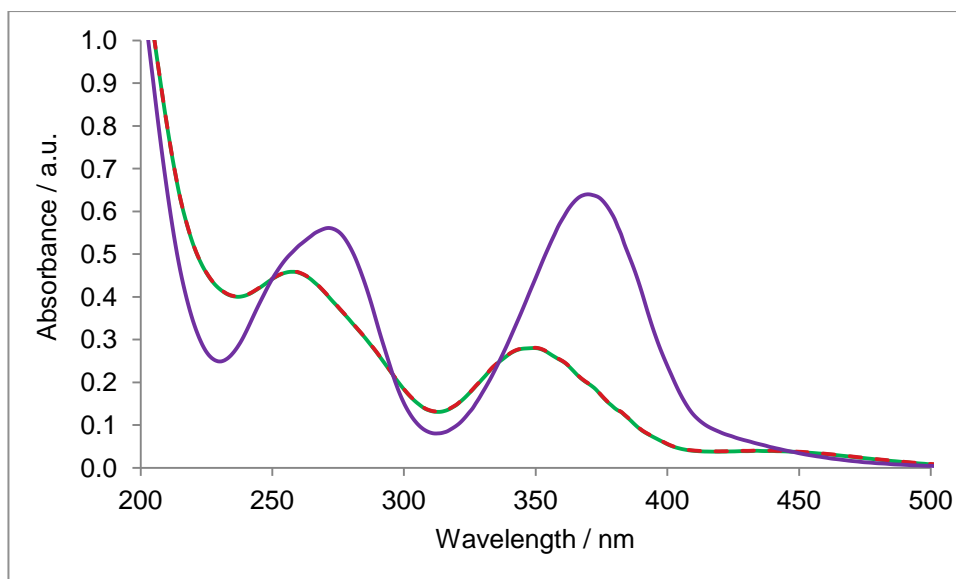


Figure 5.7: Absorbance spectra of 0.10 mM  $\text{Na}_2\text{Cr}_2\text{O}_7 \cdot 2\text{H}_2\text{O}$ , held at pH 1 (—), pH 3.5 (---) and pH 6 (—) respectively, by the addition of  $\text{H}_2\text{SO}_4$ .

The absorbance spectrum of each solution was monitored using UV-Vis spectroscopy over a period of 10 hours, and the percentage of chromium remaining in solution was calculated according to:

$$\text{Equation 5.1} \quad \% \text{ Cr in solution} = \text{Initial Cr \%} - \left[ \left( \frac{C_0 - C_t}{C_0} \right) \times 100 \right]$$

where  $C_0$  is the initial absorbance at 350 nm and  $C_t$  is the absorbance at a given time. The absorbance of the Cr(VI) solutions was monitored at a wavelength of at 350 nm for each trace. It can be seen in Figure 5.8 that there is only a significant decrease in the amount of chromium in the solution held at pH 1. This implies that Cr(VI) removal from solution only occurs effectively at very low pH values. This is in keeping with the findings of other research groups, who have observed efficient removal of chromium by polypyrrole films, which were electrochemically reduced prior to immersion in solutions of Cr(VI) prepared with 0.10 M  $\text{H}_2\text{SO}_4$ .<sup>9, 11, 13</sup> However, efficient chromium removal has been observed up to pH 6 for polypyrrole nanostructures when they are utilised as adsorbents rather than coated on electrodes.<sup>41, 42</sup> The oxidative power of Cr(VI) increases as pH decreases, and the standard potential of the  $\text{Cr}^{6+}/\text{Cr}^{3+}$  redox couple increases, making the reduction of Cr(VI) to Cr(III) thermodynamically most favourable. The results shown here therefore suggest that while electrostatic adsorption

of the Cr(VI) may occur due to the positive charge inferred upon the PpyNW by the protonated nitrogen atoms of the polypyrrole backbone, there is a further step than just adsorption involved in the removal of Cr(VI) from solution: its reduction to Cr(III).

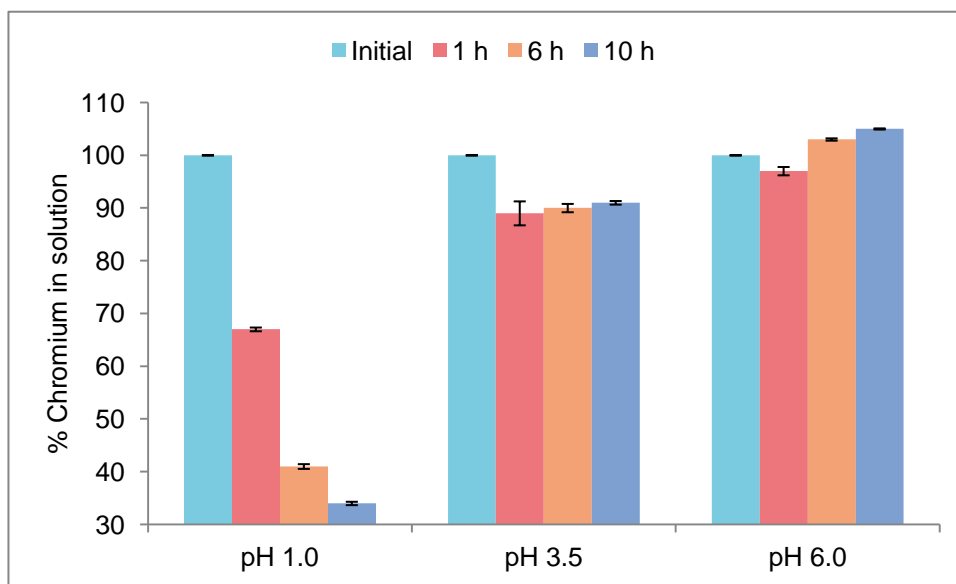


**Figure 5.8:** Percentage of Cr(VI) remaining in solution exposed to PpyNW. PpyNW formed to  $400 \text{ mCcm}^{-2}$  on an Au wire and reduced at  $-0.80 \text{ V}$  vs. SCE in  $0.10 \text{ M H}_2\text{SO}_4$  for 30 minutes, prior to immersion in  $0.10 \text{ mM Na}_2\text{Cr}_2\text{O}_7 \cdot 2\text{H}_2\text{O}$  at various pHs,  $n = 2$ .

There is a discrepancy observed in Figure 5.8 in which the percentage chromium in solution appears to increase over time in the Cr(VI) solution held at pH 6. This is due to the polypyrrole degrading at higher pH values, which may leach into the Cr(VI) solution. This unfortunately compromises the results. It can still be observed that the removal of Cr(VI) from solution over the first hour (before the Ppy degradation can occur) is still most effective at a solution pH of 1.0.

### 5.3.3 Oxidation of Polypyrrole: Cr(VI) $\rightarrow$ Cr(III)

In order to determine whether a chemical reaction was occurring between the polymer film and the Cr(VI), to reduce it to Cr(III), the open-circuit potential (OCP) of the polymers was measured under a number of conditions. OCP is the potential of the working electrode relative to the reference electrode when no external potential or current is being applied to the system. Thus an increase in the OCP of the polymer coated electrode will indicate polymer oxidation. This technique has been previously used to demonstrate the oxidation by Cr(VI) of polypyrrole films deposited on carbon substrates<sup>14</sup> and the effect of solution agitation on the reduction of chromium by

polypyrrole-oxalic acid films.<sup>12</sup> Initial control experiments were carried out on the gold electrode substrate and its OCP was measured as a function of time as it was immersed in 0.10 M H<sub>2</sub>SO<sub>4</sub> and in 0.10 mM Na<sub>2</sub>Cr<sub>2</sub>O<sub>7</sub>·2H<sub>2</sub>O/0.10 M H<sub>2</sub>SO<sub>4</sub>. The resulting traces and associated potentials are depicted in Figure 5.9 and Table 5.2. It can be observed that there is little change in the OCP of gold in sulfuric acid (0.10 M), indicating that no reaction is occurring. A small increase in the OCP is seen for gold in 0.10 mM Na<sub>2</sub>Cr<sub>2</sub>O<sub>7</sub>·2H<sub>2</sub>O/0.10 M H<sub>2</sub>SO<sub>4</sub>, which reveals that the chromium solution does have some ability to oxidise the gold substrate. This is also observed in the difference of approximately 0.2 V vs. SCE in the open circuit potential of the gold electrode in 0.10 M H<sub>2</sub>SO<sub>4</sub> and in 0.10 mM Na<sub>2</sub>Cr<sub>2</sub>O<sub>7</sub>·2H<sub>2</sub>O/0.10 M H<sub>2</sub>SO<sub>4</sub>.

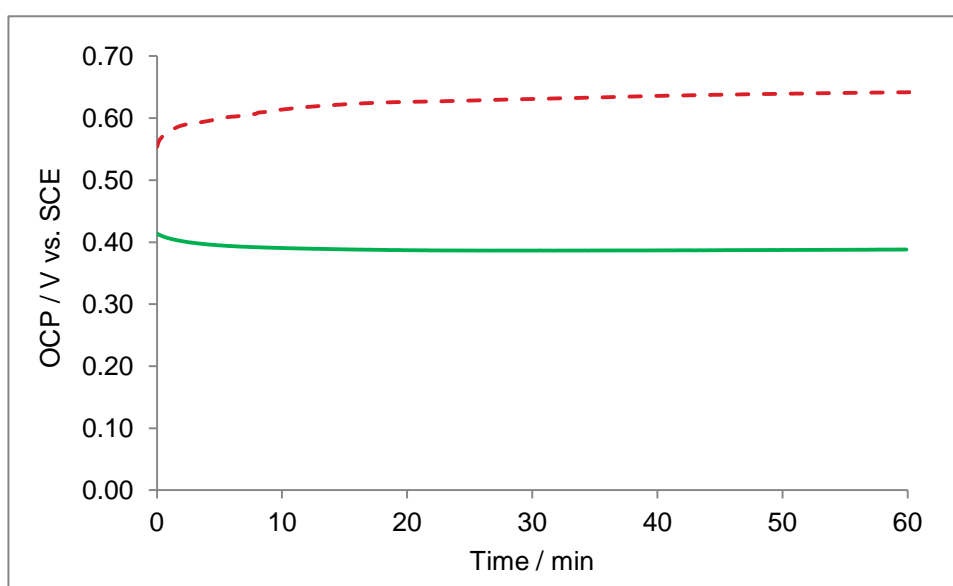


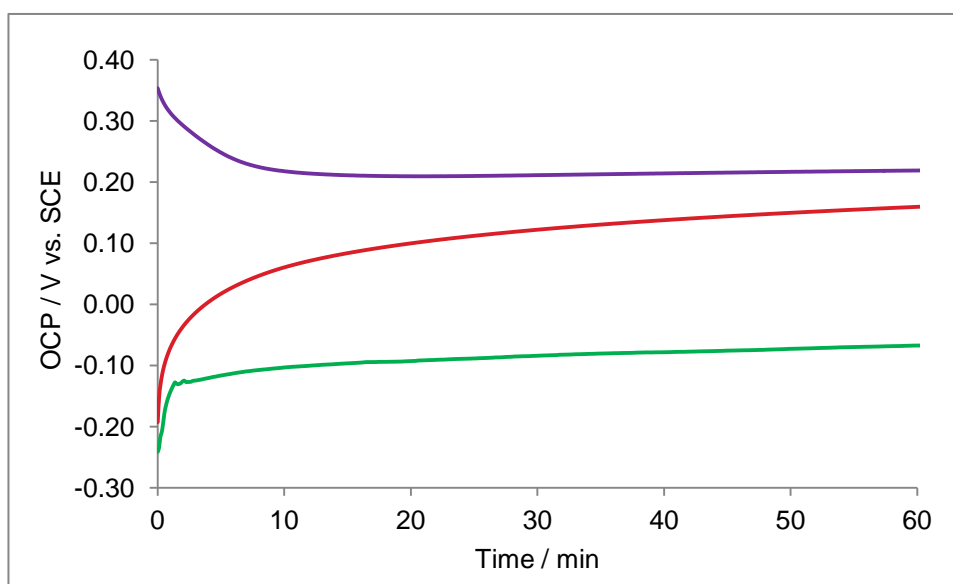
Figure 5.9: Open circuit potential as a function of time of a bare gold electrode immersed in 0.10 mM Cr(VI)/0.10 M H<sub>2</sub>SO<sub>4</sub> (---) and in 0.10 M H<sub>2</sub>SO<sub>4</sub> (—) with stirring.

Table 5.2: OCP / V vs. SCE, at time 0 and at 60 minutes, of bare gold electrodes immersed in 0.10 mM Na<sub>2</sub>Cr<sub>2</sub>O<sub>7</sub>·2H<sub>2</sub>O/0.10 M H<sub>2</sub>SO<sub>4</sub> with stirring. Standard error of potential at 60 minutes is calculated for 3 repetitions of each experiment.

Substrate	Solution	Initial Potential / V	Potential at 60 min / V	Potential Difference / V	Standard Error
Bare Au	0.10 M H <sub>2</sub> SO <sub>4</sub>	0.38	0.37	0.01	0.02
Bare Au	0.10 mM Na <sub>2</sub> Cr <sub>2</sub> O <sub>7</sub> / 0.10 M H <sub>2</sub> SO <sub>4</sub>	0.52	0.60	0.08	0.01

### 5.3.3.1 Open Circuit Potential of Bulk Polypyrrole (PpyCl)

Preliminary investigations were carried out using a PpyCl coated gold electrode in sulfuric acid. Figure 5.10 depicts the OCP vs. time plots of PpyCl films either untreated or reduced at  $-0.80$  V vs. SCE, prior to OCP being recorded during immersion of the films in  $0.10$  M  $\text{H}_2\text{SO}_4$ . It can be observed that the reduced film undergoes oxidation while the non-reduced PpyCl film undergoes a slight reduction. The extent of oxidation/reduction is detailed in Table 5.3. In order to investigate whether dissolved oxygen was influencing the oxidation of the PpyCl film, the OCP of the PpyCl film was also recorded during immersion in de-aerated  $0.10$  M  $\text{H}_2\text{SO}_4$ . The sulfuric acid ( $0.10$  M) was de-aerated with nitrogen for 30 minutes prior to immersion of the reduced PpyCl film, and nitrogen was bubbled over the surface of the  $0.10$  M  $\text{H}_2\text{SO}_4$  solution for the duration of the OCP experiments. It can be seen from Figure 5.10 that the polymer remains in its reduced state when immersed in the de-aerated solution, which suggests that the oxygen present in the sulfuric acid is contributing to the oxidation of the polymer.



**Figure 5.10:** OCP as a function of time for PpyCl film; not reduced prior to immersion in  $0.10$  M  $\text{H}_2\text{SO}_4$  (—), reduced prior to immersion in  $0.10$  M  $\text{H}_2\text{SO}_4$  (—) and reduced prior to immersion in de-aerated  $0.10$  M  $\text{H}_2\text{SO}_4$  (—) with stirring.

Figure 5.11 shows a plot of the OCP over time for PpyCl films either reduced at an applied potential of  $-0.80$  V vs. SCE (in  $0.10$  M  $\text{H}_2\text{SO}_4$ ) or not reduced prior to immersion in  $0.10$  mM  $\text{Na}_2\text{Cr}_2\text{O}_7 \cdot 2\text{H}_2\text{O} / 0.10$  M  $\text{H}_2\text{SO}_4$ . Unlike the OCP traces recorded in  $0.10$  M  $\text{H}_2\text{SO}_4$  (Figure 5.10), both reduced and non-reduced polymers are oxidised.

This is manifested in the increase of the open circuit potential of the films. This increase in OCP has been observed previously for poly(1,8-diaminonaphthalene) films in a solution of 0.073 mM  $\text{K}_2\text{Cr}_2\text{O}_7/0.1 \text{ M HClO}_4$  and was attributed to the presence of the  $\text{Cr}^{6+}/\text{Cr}^{3+}$  redox couple in solution.<sup>43</sup> The PpyCl films in the current study are all oxidised before achieving an open circuit potential of approximately 0.6 V vs. SCE during immersion in 0.10 mM  $\text{Na}_2\text{Cr}_2\text{O}_7 \cdot 2\text{H}_2\text{O}/0.10 \text{ M H}_2\text{SO}_4$  solution. The non-reduced PpyCl film reaches an OCP of approximately 0.6 V vs. SCE very quickly ( $\sim 30$  seconds), while the reduced PpyCl films take longer to achieve an open circuit potential of approximately 0.6 V vs. SCE. This can be seen more clearly in Figure 5.11 (b) which focuses on the initial 5 minutes of the immersion of the PpyCl films in 0.10 mM  $\text{Na}_2\text{Cr}_2\text{O}_7 \cdot 2\text{H}_2\text{O}/0.10 \text{ M H}_2\text{SO}_4$ .

The OCP trace of the reduced PpyCl film in de-aerated acidified 0.10 mM  $\text{Na}_2\text{Cr}_2\text{O}_7 \cdot 2\text{H}_2\text{O}$  is also plotted in Figure 5.11 and it can be observed that while it takes longer, the film is oxidised and the same open circuit potential is recorded as for non-reduced and reduced PpyCl films in acidified 0.10 mM  $\text{Na}_2\text{Cr}_2\text{O}_7 \cdot 2\text{H}_2\text{O}$ . This is in keeping with the finding that dissolved oxygen contributes to oxidation of the polymer. However, the open circuit potential of  $\sim 0.6 \text{ V vs. SCE}$  achieved by the PpyCl films in acidified 0.10 mM  $\text{Na}_2\text{Cr}_2\text{O}_7 \cdot 2\text{H}_2\text{O}$  is much higher than the open circuit potential of  $\sim 0.2 \text{ V vs. SCE}$  that is achieved in 0.10 M sulfuric acid. This difference in OCP confirms that it is not just the acid or dissolved oxygen which is oxidising the polymer, but the strongly oxidising dichromate in solution. Table 5.4 details the extent of polymer oxidation recorded.

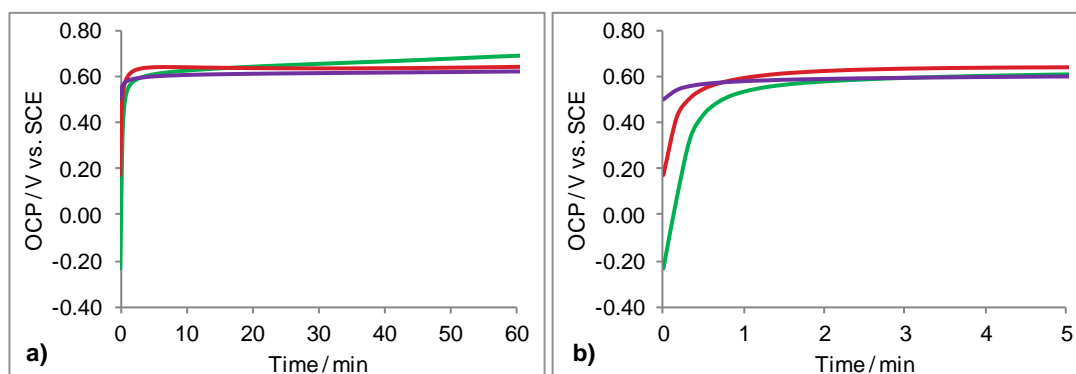


Figure 5.11: a) OCP as a function of time for PpyCl film; not reduced prior to immersion in acidified 0.10 mM  $\text{Na}_2\text{Cr}_2\text{O}_7 \cdot 2\text{H}_2\text{O}$  (—), reduced prior to immersion in acidified 0.10 mM  $\text{Na}_2\text{Cr}_2\text{O}_7 \cdot 2\text{H}_2\text{O}$  (—) and reduced prior to immersion in de-aerated acidified 0.10 mM  $\text{Na}_2\text{Cr}_2\text{O}_7 \cdot 2\text{H}_2\text{O}$  (—) with stirring, b) initial 5 minutes of OCP vs. time plot.

**Table 5.3: Open Circuit Potential / V vs. SCE, at time 0 and at 60 minutes for PpyCl films; not reduced or reduced prior to immersion in 0.10 M H<sub>2</sub>SO<sub>4</sub>, and reduced prior to immersion in de-aerated 0.10 M H<sub>2</sub>SO<sub>4</sub>. Standard error of potential at 60 minutes calculated for 3 repetitions of each experiment.**

Substrate	Solution	Initial Potential / V	Potential at 60 min / V	Potential Difference / V	Standard Error
PpyCl Not reduced	0.10 M H <sub>2</sub> SO <sub>4</sub>	0.27	0.22	- 0.05	0.04
PpyCl reduced	0.10 M H <sub>2</sub> SO <sub>4</sub>	- 0.19	0.17	0.36	0.02
PpyCl reduced	De-aerated 0.10 M H <sub>2</sub> SO <sub>4</sub>	- 0.26	- 0.03	0.12	0.09

**Table 5.4: Open Circuit Potential / V vs. SCE, at time 0 and at 60 minutes for PpyCl films; not reduced prior to immersion in acidified 0.10 mM Na<sub>2</sub>Cr<sub>2</sub>O<sub>7</sub>·2H<sub>2</sub>O, reduced prior to immersion in acidified 0.10 mM Na<sub>2</sub>Cr<sub>2</sub>O<sub>7</sub>·2H<sub>2</sub>O and reduced prior to immersion in de-aerated acidified 0.10 mM Na<sub>2</sub>Cr<sub>2</sub>O<sub>7</sub>·2H<sub>2</sub>O. Standard error of potential at 60 minutes calculated for 2 repetitions of each experiment.**

Substrate	Solution	Initial Potential / V	Potential at 60 min / V	Potential Difference / V	Standard Error
PpyCl Not reduced	0.10 mM Na <sub>2</sub> Cr <sub>2</sub> O <sub>7</sub> / 0.10 M H <sub>2</sub> SO <sub>4</sub>	0.52	0.62	0.10	0.02
PpyCl reduced	0.10 mM Na <sub>2</sub> Cr <sub>2</sub> O <sub>7</sub> / 0.10 M H <sub>2</sub> SO <sub>4</sub>	0.15	0.62	0.47	0.00
PpyCl reduced	De-aerated 0.10 mM Na <sub>2</sub> Cr <sub>2</sub> O <sub>7</sub> / 0.10 M H <sub>2</sub> SO <sub>4</sub>	- 0.24	0.65	0.90	0.03

Thus it can be concluded that the bulk polypyrrole chloride films, whether pre-reduced or not reduced, are oxidised by acidified dichromate solution, which in turn implies that reduction of the chromium is occurring. However, it can be seen from Figure 5.11 that the open circuit potential plateaus at ~ 0.6 V vs. SCE for each PpyCl film after approximately 2 minutes, suggesting that the oxidation of PpyCl is no longer occurring. Figure 5.12 depicts the OCP of a reduced PpyCl film in 0.10 mM acidified Na<sub>2</sub>Cr<sub>2</sub>O<sub>7</sub>·2H<sub>2</sub>O, overlaid with the UV-Vis data obtained for the decrease in the absorbance band observed at 350 nm for the Cr(VI) over a 24 hour period. The decrease in the concentration of the Cr(VI) occurs quite rapidly during initial stages, with up to 35 percent reduction in the Cr(VI) absorbance peak observed in the first hour. This decrease in the Cr(VI) concentration after the initial hour continues gradually, even though the OCP appears to have reached a plateau. Figure 5.12 (b) shows an expanded plot of the plateau region of the OCP and it can be observed that the OCP continues to increase. Thus the polymer is being oxidised very slowly during this time and it is most

likely that this occurs due to a reaction between the PPyCl film and the Cr(VI) in solution.

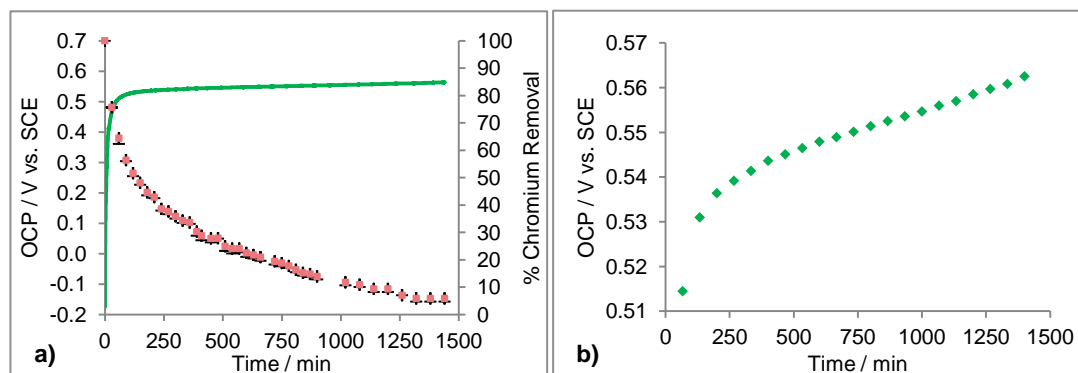


**Figure 5.12:** OCP (—) compared to the absorbance (■), recorded for the immersion of a reduced PPyCl film in 0.1 mM acidified Cr over 24 hours. b) An expanded plot of the OCP vs. Time, showing that oxidation of PPyCl continues slowly.

### 5.3.3.2 Open Circuit Potential of Polypyrrole Nanowires (PpyNW)

As with the bulk polymer PPyCl, preliminary studies were carried out to investigate the OCP of PpyNW in 0.10 M sulfuric acid, the results of which are depicted in Figure 5.13 and detailed in Table 5.5. The PpyNW films were either not reduced or reduced at  $-0.80$  V vs. SCE in 0.10 M  $\text{H}_2\text{SO}_4$ , prior to OCP being recorded during immersion in 0.10 M  $\text{H}_2\text{SO}_4$  or de-aerated 0.10 M  $\text{H}_2\text{SO}_4$ . Similar to the results seen for the PPyCl films immersed in 0.10 M  $\text{H}_2\text{SO}_4$ , it can be observed that the reduced PpyNW film undergoes oxidation while the non-reduced PpyNW film undergoes a slight reduction in sulfuric acid (0.10 M). It can also be observed that the PpyNW film immersed in de-aerated 0.10 M  $\text{H}_2\text{SO}_4$  achieves an OCP of 0.10 V vs. SCE, which is greater than the OCP of  $-0.03$  V vs. SCE achieved by the PPyCl film immersed in de-aerated 0.10 M  $\text{H}_2\text{SO}_4$ . This is most likely due to the greater surface area upon which the sulfuric acid can act upon in the PpyNW film. The difference between the OCP observed for PPyCl films in 0.10 M  $\text{H}_2\text{SO}_4$  and in 0.10 M de-aerated  $\text{H}_2\text{SO}_4$  is 0.20 V. The difference between the OCP observed for PpyNW films in 0.10 M  $\text{H}_2\text{SO}_4$  and in 0.10 M de-aerated  $\text{H}_2\text{SO}_4$  is only 0.07 V. This implies that for the PpyNW films, the oxygen in solution has less of an impact on the OCP of the film than on the OCP of the PPyCl films.

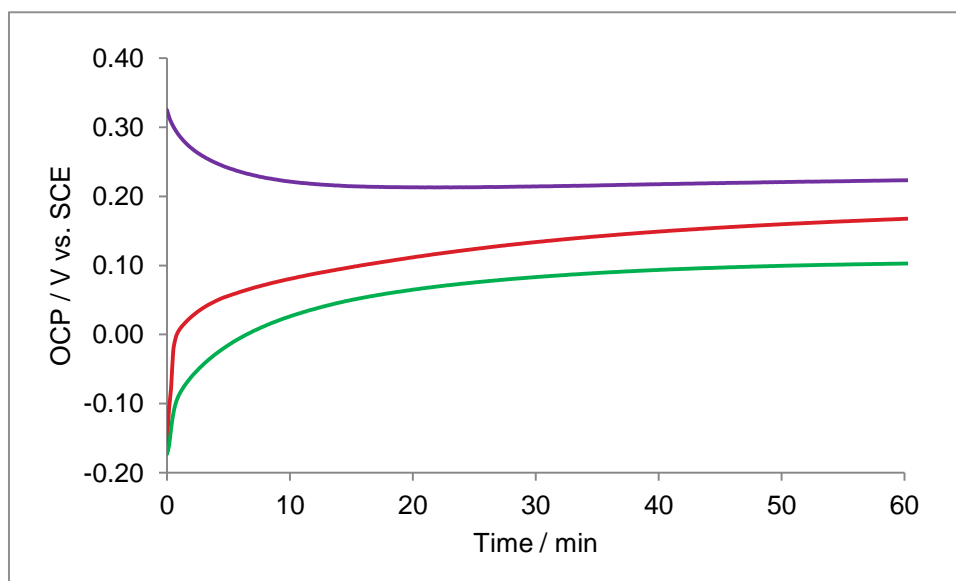


Figure 5.13: OCP as a function of time for PpyNW film; not reduced prior to immersion in 0.10 M  $\text{H}_2\text{SO}_4$  (—), reduced prior to immersion in 0.10 M  $\text{H}_2\text{SO}_4$  (—) and reduced prior to immersion in de-aerated 0.10 M  $\text{H}_2\text{SO}_4$  (—) with stirring.

Table 5.5: Open Circuit Potential / V vs. SCE, at time 0 and at 60 minutes for PpyNW films; not reduced prior to immersion in 0.10 M  $\text{H}_2\text{SO}_4$ , reduced prior to immersion in 0.10 M  $\text{H}_2\text{SO}_4$  and reduced prior to immersion in de-aerated  $\text{H}_2\text{SO}_4$  (0.10 M). Standard error of potential at 60 minutes calculated for 2-3 repetitions of each experiment.

Substrate	Electrolyte	Initial Potential / V	Potential at 60 min / V	Potential Difference / V	Standard Error
PpyNW Not reduced	0.10 M $\text{H}_2\text{SO}_4$	0.32	0.22	- 0.10	0.03
PpyNW reduced	0.10 M $\text{H}_2\text{SO}_4$	- 0.16	0.17	0.33	0.06
PpyNW reduced	De-aerated 0.10 M $\text{H}_2\text{SO}_4$	- 0.17	0.10	0.28	0.03

The PpyNW films were either reduced at an applied potential of  $-0.80$  V vs. SCE (in 0.10 M  $\text{H}_2\text{SO}_4$ ) or not reduced prior to immersion in 0.10 mM  $\text{Na}_2\text{Cr}_2\text{O}_7 \cdot 2\text{H}_2\text{O}$ /0.10 M  $\text{H}_2\text{SO}_4$ . Figure 5.14 depicts the OCP recorded of these reduced and non-reduced PpyNW films in acidified 0.10 mM  $\text{Na}_2\text{Cr}_2\text{O}_7 \cdot 2\text{H}_2\text{O}$ , and reduced PpyNW in de-aerated acidified 0.10 mM  $\text{Na}_2\text{Cr}_2\text{O}_7 \cdot 2\text{H}_2\text{O}$ . The non-reduced PpyNW film achieves a potential of 0.5 V vs. SCE after approximately 3 minutes, while the reduced PpyNW film is slower to achieve an OCP of 0.5 V vs. SCE, taking approximately 10 minutes. This is similar to the results observed for the PpyCl films immersed in acidified 0.10 mM  $\text{Na}_2\text{Cr}_2\text{O}_7 \cdot 2\text{H}_2\text{O}$ , and can be observed more clearly in Figure 5.14 (b) which shows an

expanded plot of the initial 10 minutes of the immersion of the PpyNW films in 0.10 mM  $\text{Na}_2\text{Cr}_2\text{O}_7 \cdot 2\text{H}_2\text{O}$ /0.10 M  $\text{H}_2\text{SO}_4$ .

Unlike the results observed for the PpyCl films immersed in 0.10 mM acidified  $\text{Na}_2\text{Cr}_2\text{O}_7 \cdot 2\text{H}_2\text{O}$ , the reduced PpyNW films in de-aerated 0.10 mM acidified  $\text{Na}_2\text{Cr}_2\text{O}_7 \cdot 2\text{H}_2\text{O}$  achieve an OCP of 0.5 V vs. SCE slightly quicker than the reduced PpyNW in the aerated 0.10 mM acidified  $\text{Na}_2\text{Cr}_2\text{O}_7 \cdot 2\text{H}_2\text{O}$ . However, the rate at which the reduced PpyNW film reach an OCP of 0.5 V vs. SCE in 0.10 mM acidified  $\text{Na}_2\text{Cr}_2\text{O}_7 \cdot 2\text{H}_2\text{O}$ , whether de-aerated or not, is very similar, which suggests that it is predominantly the Cr(VI) in solution that is oxidising the polymers, and that the dissolved oxygen does not have a great effect. This is in agreement with the results observed for the OCP of the PpyNW films in 0.10 M  $\text{H}_2\text{SO}_4$  with a difference of only 0.10 V being observed between the OCP recorded for the reduced PpyNW films in either 0.10 M  $\text{H}_2\text{SO}_4$  or de-aerated 0.10 M  $\text{H}_2\text{SO}_4$ . It can also be observed, as previously seen with the PpyCl films, that the OCP achieved by the PpyNW in 0.10 mM acidified  $\text{Na}_2\text{Cr}_2\text{O}_7 \cdot 2\text{H}_2\text{O}$  is greater than that reached in 0.10 M  $\text{H}_2\text{SO}_4$  and so again the conclusion may be drawn that it is the Cr(VI) in solution oxidising the PpyNW films, which will result in the Cr(VI) itself being reduced. Table 5.6 details the extent of the oxidation of the PpyNW.

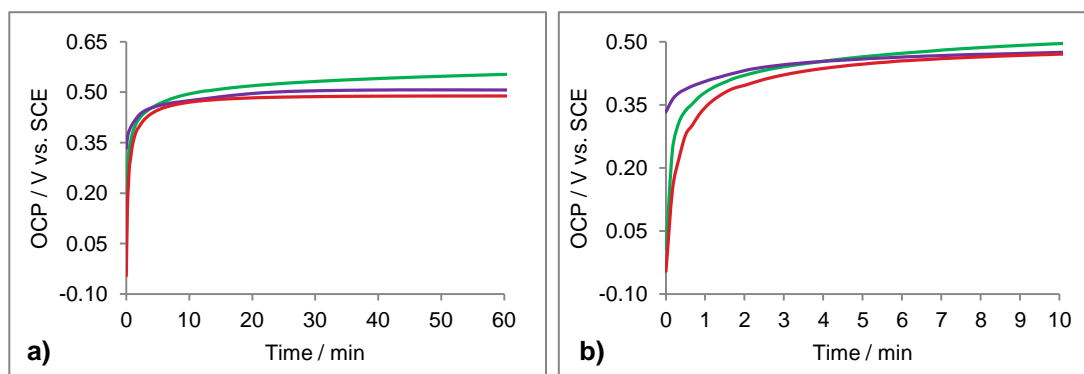


**Figure 5.14:** a) OCP as a function of time for PpyNW film; not reduced prior to immersion in 0.10 mM acidified  $\text{Na}_2\text{Cr}_2\text{O}_7 \cdot 2\text{H}_2\text{O}$  (—), reduced prior to immersion in 0.10 mM acidified  $\text{Na}_2\text{Cr}_2\text{O}_7 \cdot 2\text{H}_2\text{O}$  (—) and reduced prior to immersion in de-aerated 0.10 mM acidified  $\text{Na}_2\text{Cr}_2\text{O}_7 \cdot 2\text{H}_2\text{O}$  (—) with stirring, b) initial 10 minutes of OCP vs. time plot.

**Table 5.6: Open Circuit Potential / V vs. SCE, at time 0 and at 60 minutes for PpyNW films; not reduced prior to immersion in 0.10 mM acidified  $\text{Na}_2\text{Cr}_2\text{O}_7 \cdot 2\text{H}_2\text{O}$ , reduced prior to immersion in 0.10 mM acidified  $\text{Na}_2\text{Cr}_2\text{O}_7 \cdot 2\text{H}_2\text{O}$  and reduced prior to immersion in de-aerated 0.10 mM acidified  $\text{Na}_2\text{Cr}_2\text{O}_7 \cdot 2\text{H}_2\text{O}$ . Standard error of potential at 60 minutes calculated for 2-3 repetitions of each.**

Substrate	Electrolyte	Initial Potential / V	Potential at 60 min / V	Potential Difference / V	Standard Error
PpyNW Not reduced	0.10 mM $\text{Na}_2\text{Cr}_2\text{O}_7$ / 0.10 M $\text{H}_2\text{SO}_4$	0.33	0.51	0.17	0.02
PpyNW reduced	0.10 mM $\text{Na}_2\text{Cr}_2\text{O}_7$ / 0.10 M $\text{H}_2\text{SO}_4$	- 0.05	0.49	0.53	0.02
PpyNW reduced	De-aerated 0.10 mM $\text{Na}_2\text{Cr}_2\text{O}_7$ / 0.10 M $\text{H}_2\text{SO}_4$	0.01	0.55	0.55	0.06

The OCP traces for the PpyNW in 0.10 mM acidified  $\text{Na}_2\text{Cr}_2\text{O}_7 \cdot 2\text{H}_2\text{O}$  also achieve a plateau; however, this takes longer than for PpyCl films. Comparing Figure 5.11 and Figure 5.14, the open circuit potentials of the PpyNW films only reach a plateau value of 0.5 V vs. SCE after immersion in the 0.10 mM acidified  $\text{Na}_2\text{Cr}_2\text{O}_7 \cdot 2\text{H}_2\text{O}$  for almost 10 minutes. Having reached this plateau value, the oxidation of the PpyNW films continues slowly, which is also observed for the PpyCl films (Figure 5.12 b). This can be seen in Figure 5.15 which depicts the OCP of a reduced PpyNW film in 0.10 mM acidified  $\text{Na}_2\text{Cr}_2\text{O}_7 \cdot 2\text{H}_2\text{O}$ , overlaid with the UV-Vis data obtained for the decrease in the absorbance band observed at 350 nm for the Cr(VI) over a 24 hour period. Again, a 35 percent reduction in the concentration of Cr(VI) occurs over the first hour, and Figure 5.15 (b) reveals that the OCP continues to increase over the 24 hour period. The rate of oxidation of the PpyNW film is slightly slower than that observed for the PpyCl films immersed in 0.10 mM acidified  $\text{Na}_2\text{Cr}_2\text{O}_7 \cdot 2\text{H}_2\text{O}$ , which may explain why the PpyNW films take longer to reduce the same amount of Cr(VI) as the PpyCl films (Section 5.3.1). It can also be observed that the PpyCl films achieve an OCP of approximately 0.6 V vs. SCE, whereas the PpyNW films achieve an OCP of approximately 0.5 V vs. SCE. Thus it appears that the PpyNW are not as easily oxidised as the bulk PpyCl films. This is most likely due to the lower conductivity of the polypyrrole nanowires films compared to the bulk polypyrrole chloride films. Electrochemical Impedance Spectroscopy (EIS) studies carried out by our group have shown that PpyNW of the type used in the present study, are usually less conducting than polypyrrole in the bulk morphology. This is due to the greater number of carbonyl

defects in the polypyrrole backbone. Evidence for this can also be observed in the appearance of a medium intensity band at  $1695\text{ cm}^{-1}$  in the FTIR spectrum of the polypyrrole nanowires. This band is the result of carbonyl groups present along the polypyrrole backbone which can interrupt the conjugation and therefore the conductivity.<sup>44</sup>

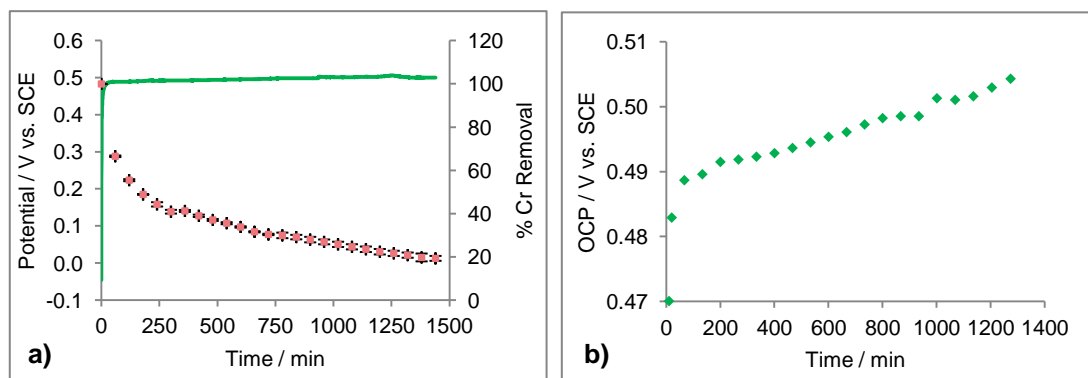


**Figure 5.15:** OCP (—) compared to the absorbance (■), recorded for the immersion of a reduced PpyNW film in 0.10 mM acidified Cr over 24 hours. b) Expansion of the OCP, shows that oxidation of PPyNW continues, slower than the PpyCl films.

It has therefore been established that the process of Cr(VI) removal from solution occurs as follows. First, the  $\text{HCrO}_4^-$  is electrostatically adsorbed onto the polypyrrole surface, which is positively charged due to protonation of the nitrogen atoms of the polypyrrole backbone in the acidic solution. The Cr(VI) is then reduced to Cr(III), oxidising the polypyrrole in the process. Having thus established that the Cr(VI) in solution was oxidising the polymer films, and being reduced to Cr(III), the whereabouts of this Cr(III) was investigated.

### 5.3.4 Fate of Chromium

Energy-dispersive X-ray spectroscopy (EDX) was carried out on the polymer samples post immersion in 0.10 mM acidified  $\text{Na}_2\text{Cr}_2\text{O}_7 \cdot 2\text{H}_2\text{O}$  to determine if chromium had adsorbed on the polymer surface (Figure 5.16). EDX is not an accurate quantitative technique and is unable to distinguish between Cr(VI) and Cr(III) and so will just indicate the presence of chromium on the polymer. Polypyrrole is known as an effective adsorbent for chromium.<sup>41</sup>

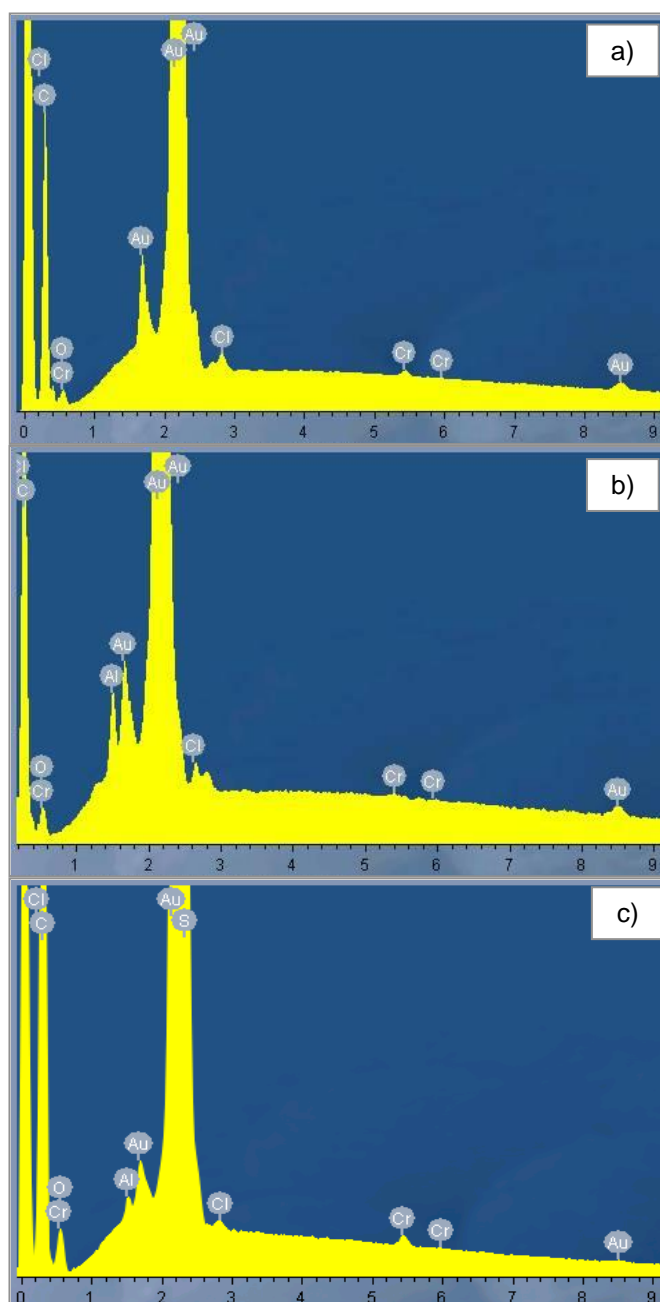


Figure 5.16: EDX spectra of a) PpyNW, b) PpyCl and c) PpySDS films post immersion in 0.10 mM acidified  $\text{Na}_2\text{Cr}_2\text{O}_7 \cdot 2\text{H}_2\text{O}$  for 24 hours. The x-axis is measured in keV.

The characteristic X-ray peaks for chromium are  $K_{\alpha} = 5.4117$  keV and  $L_{\alpha} = 0.5729$  keV and it can be seen in Figure 5.16 that chromium is present in the spectrum of each polymer. However, and although EDX is not quantitative, the small intensity of the peaks does indicate that only a small amount of chromium is present in the polymer films. The low intensity of the X-ray peaks appear to support this and so two colorimetric tests were carried out to determine the amount of chromium remaining in solution as Cr(III) after the immersion of polypyrrole films. This was necessary as UV-Vis spectroscopy is not sensitive enough to detect Cr(III) in the form of  $\text{Cr}_2(\text{SO}_4)_3$  in the small quantities present in this study. The 0.10 mM acidified  $\text{Na}_2\text{Cr}_2\text{O}_7 \cdot 2\text{H}_2\text{O}$  solutions appear colourless after exposure to the polypyrrole nanowires for an extended period of time.

#### 5.3.4.1 Hydrogen Peroxide / Potassium Peroxydisulfate Oxidation of Cr(III)

A preliminary colorimetric test was designed to oxidise any Cr(III) present in solution to Cr(VI) which could then be analysed using UV-Vis due to its strong yellow colour. The procedure used to carry out this test is described in Section 2.2.8.2(i) and the calibration curve prepared is shown in Chapter 2, Figure 2.5.

Films of PpyNW, PpyCl and PpySDS were formed as previously described on standard gold wire electrodes. Each polymer was then electrochemically reduced at an applied potential of  $-0.80$  V vs. SCE in 0.10 M  $\text{H}_2\text{SO}_4$  before immersion in acidified  $\text{Na}_2\text{Cr}_2\text{O}_7 \cdot 2\text{H}_2\text{O}$ . The concentration of Cr(VI) in solution was monitored with UV-Vis spectroscopy, and the polymer films remained immersed until Cr(VI) was no longer detected by UV-Vis. The solutions, which were now expected to contain Cr(III), were treated with hydrogen peroxide and potassium peroxydisulfate as described in Section 2.2.8.2(i). Control experiments were also carried out on acidified  $\text{Na}_2\text{Cr}_2\text{O}_7 \cdot 2\text{H}_2\text{O}$  which was not exposed to the polymer films and on sulfuric acid (0.10 M) in which polymer films were immersed for 24 hours. These were also treated with hydrogen peroxide and potassium peroxydisulfate as described in Section 2.2.8.2(i). As expected, the sulfuric acid samples which were exposed to each polymer film for 24 hours exhibited no UV-Vis spectrum after oxidation treatment: however, the original 0.10 mM  $\text{Na}_2\text{Cr}_2\text{O}_7 \cdot 2\text{H}_2\text{O}$  solution which was expected to contain 0.20 mM Cr(VI) was calculated to contain 0.27 mM Cr(VI) according to the calibration curve. This is very likely due to the error in the calibration curve as seen by the very large error bars in Figure 2.5

(Chapter 2). Table 5.7 details the concentration of chromium calculated to be in solution after exposure to reduced PpyNW, PpyCl and PpySDS films.

**Table 5.7: Concentration of chromium calculated to be in an acidified 0.10 mM Na<sub>2</sub>Cr<sub>2</sub>O<sub>7</sub>·2H<sub>2</sub>O solution after exposure to reduced PpyNW, PpyCl and PpySDS films until no Cr(VI) was detectable by UV-Vis. The concentration of chromium was obtained by oxidising Cr(III) back to Cr(VI) using hydrogen peroxide and potassium peroxydisulfate in order to obtain a UV-Vis response. The results obtained for a solution with no polymer immersed and for 0.10 M H<sub>2</sub>SO<sub>4</sub> in which a PpyNW film was immersed for 24 hours are also shown, n = the number of repetitions carried out.**

Polymer immersed	Immersion Solution	Calculated Chromium in solution / mM	% of original Cr in solution as Cr(III)	n
PpyNW reduced	0.10 M H <sub>2</sub> SO <sub>4</sub>	0.00	-	-
No Polymer	0.10 mM Na <sub>2</sub> Cr <sub>2</sub> O <sub>7</sub> ·2H <sub>2</sub> O	0.27	-	-
PpyNW reduced	0.10 mM Na <sub>2</sub> Cr <sub>2</sub> O <sub>7</sub> ·2H <sub>2</sub> O	0.26 ± 0.01	93-100	4
PpyCl reduced	0.10 mM Na <sub>2</sub> Cr <sub>2</sub> O <sub>7</sub> ·2H <sub>2</sub> O	0.24 ± 0.02	81-96	2
PpySDS reduced	0.10 mM Na <sub>2</sub> Cr <sub>2</sub> O <sub>7</sub> ·2H <sub>2</sub> O	0.22 ± 0.02	74-89	3

Taking from the colorimetric test that the original solution contained 0.27 mM Cr(VI), the percentage of chromium remaining in solution after exposure to the polymer films was determined (Table 5.7). It can be observed that in the case of the acidified Na<sub>2</sub>Cr<sub>2</sub>O<sub>7</sub>·2H<sub>2</sub>O exposed to reduced PpyNW, between 93-100 percent of the original chromium in solution remains in solution post immersion of the PPyNW film. In the case of PpyCl and PpySDS films immersed in acidified Na<sub>2</sub>Cr<sub>2</sub>O<sub>7</sub>·2H<sub>2</sub>O, between 81-96 percent and 74-89 percent respectively, of the original chromium remains in solution as Cr(III). While these figures cannot be taken as being accurate, due to the error in the calibration curve, it was concluded that a substantial amount of the original Cr(VI) is reduced to Cr(III) when exposed to the polymer films, and this Cr(III) is then expelled back into solution. In order to confirm this, a more rigorous colorimetric test was carried out on solutions exposed to the PpyNW films.

#### 5.3.4.2 Formation of a Chromophore Complex of Cr(VI) and 1,5-diphenylcarbazide

An alternative colorimetric test is US EPA Method 7196A in which all chromium species in solution are oxidised to Cr(VI) which then forms a red-violet chromophore

complex with 1,5-diphenylcarbazide (Figure 5.17), a colour chelating agent.<sup>45</sup> The structure of this diphenylcarbazide/Cr(VI) complex is unknown,<sup>45</sup> but it has been shown to exist as a cationic species in aqueous solution, and the stoichiometry of the interaction of the 1,5-diphenylcarbazide with the Cr(VI) requires 3 moles of the 1,5 diphenylcarbazide for every 2 moles of Cr(VI).<sup>46</sup> This complex produces a characteristic UV-Vis absorption peak at 540 nm.

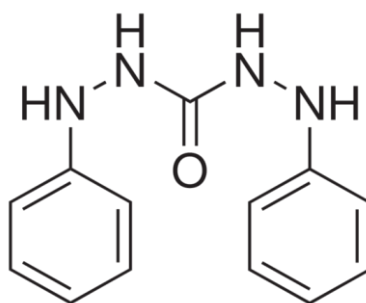


Figure 5.17: The structure of 1,5-diphenylcarbazide.

This test was carried out only on samples which were exposed to PpyNW films. A calibration curve was made as described in Section 2.2.8.2(ii) and is shown in Figure 2.6 (Chapter 2).

PpyNW films were formed as previously described on standard gold wire electrodes. The PpyNW film was then electrochemically reduced at an applied potential of -0.80 V vs. SCE in 0.10 M H<sub>2</sub>SO<sub>4</sub> before immersion in acidified Na<sub>2</sub>Cr<sub>2</sub>O<sub>7</sub>·2H<sub>2</sub>O. The concentration of Cr(VI) in solution was monitored with UV-Vis spectroscopy, and the PpyNW films remained immersed in the Cr(VI) solution until Cr(VI) was no longer detected by UV-Vis. 1,5-diphenylcarbazide in acetone (0.5 cm<sup>3</sup>, 0.02 M) was added to a portion of each of the resulting solutions, to complex with any Cr(VI) which may remain in solution, undetectable by UV-Vis spectroscopy. This data allowed the amount of chromium remaining as Cr(VI) in solution to be calculated.

The remaining portion of the solutions resulting from the immersion of PpyNW films in acidified Na<sub>2</sub>Cr<sub>2</sub>O<sub>7</sub>·2H<sub>2</sub>O were then treated as described in Section 2.2.8.2(ii) to determine the total amount of chromium in solution. This was achieved by oxidising all chromium species in the solution to Cr(VI) prior to addition of 1,5-diphenylcarbazide which will only form a coloured complex with Cr(VI).<sup>46</sup> The corresponding calibration curve for known concentrations of Cr(VI), prepared from a stock solution of 1.0 mM

$\text{Na}_2\text{Cr}_2\text{O}_7 \cdot 2\text{H}_2\text{O}$  in 0.10 M  $\text{H}_2\text{SO}_4$  is shown in Chapter 2, Figure 2.7. Using the values obtained for the total amount of chromium in solution, and the amount of chromium in solution as Cr(VI), the amount of Cr(III) in solution was calculated as follows.

$$\text{Equation 5.2} \quad \text{Cr(III)} = \text{Total Chromium} - \text{Cr(VI)}$$

It can be seen in Table 5.8 that no Cr(VI) is detected in solution post immersion of PpyNW films in acidified  $\text{Na}_2\text{Cr}_2\text{O}_7 \cdot 2\text{H}_2\text{O}$  which implies that any chromium remaining in solution is in the form of Cr(III). It was calculated that there was  $0.24 \pm 0.01$  mM of chromium as Cr(III) in solution after the exposure to PpyNW, while in the original solution there was a total of 0.25 mM chromium. This indicates that between 92-100 percent of the Cr(VI) reduced to Cr(III) by the PpyNW film is repelled back into the solution, suggesting that up to 8 percent of the chromium in solution may be retained by the PpyNW film. This is in keeping with the results observed by Senthurchelvan *et al.* who, using XPS, found that up to 6 percent of the Cr(VI) in solution was retained in their polypyrrole film.<sup>11</sup>

**Table 5.8: Concentration of total chromium and Cr(VI) calculated to be in an acidified  $\text{Na}_2\text{Cr}_2\text{O}_7 \cdot 2\text{H}_2\text{O}$  solution after exposure to reduced PpyNW films until no Cr(VI) was detectable by UV-Vis. Cr(VI) concentration was determined by the addition of 1,5-diphenylcarbazide. Total chromium was determined by oxidising all chromium in solution using potassium permanganate before the addition of 1,5-diphenylcarbazide. The results obtained for a solution of acidified 0.125 mM  $\text{Na}_2\text{Cr}_2\text{O}_7 \cdot 2\text{H}_2\text{O}$  with no polymer immersed are also shown, n = the number of repetitions carried out.**

Polymer Immersed	Immersion Solution	Calculated Total Cr in solution post immersion / mM	Cr as Cr(VI) in solution post immersion / mM	Calculated Cr(III) in solution post immersion / mM	n
No Polymer	Acidified $\text{Na}_2\text{Cr}_2\text{O}_7 \cdot 2\text{H}_2\text{O}$	0.25	0.25	-	-
PpyNW reduced	Acidified $\text{Na}_2\text{Cr}_2\text{O}_7 \cdot 2\text{H}_2\text{O}$	0.24	0.00	$0.24 \pm 0.01$	2

The mechanism by which Cr(VI) is removed from solution by the reduced PpyNW films can thus be summarised as follows. First, the Cr(VI), in the form of  $\text{HCrO}_4^-$  is adsorbed by the PpyNW film through the electrostatic attraction of the  $\text{HCrO}_4^-$  to the positively charged polypyrrole backbone. The Ppy backbone is positively charged, even in its reduced state, due to protonation of the nitrogen atoms which occurs in solutions at  $\text{pH} < 3$ .<sup>35, 39</sup> The polypyrrole backbone is oxidised by the Cr(VI) which in turn means that the Cr(VI) is reduced to Cr(III). This can be observed through the increase in the open circuit potential measured for the PpyNW films immersed in 0.10 mM acidified  $\text{Na}_2\text{Cr}_2\text{O}_7 \cdot 2\text{H}_2\text{O}$ . The remaining positive charges on the PpyNW repel between 92-100 percent of the Cr(III) back into solution, but EDX shows that some chromium is retained by the PPyNW film. It is unknown whether this retained chromium is in the form of Cr(VI) or Cr(III).

## 5.4 Removal Efficiency: Pre-reduction of the Polymer

As previously described, each polymer in this study was pre-treated by applying a reduction potential of -0.80 V vs. SCE for 30 minutes in 0.10 M H<sub>2</sub>SO<sub>4</sub>. Previous studies have found that this ensures the polypyrrole is in its fully reduced state, promoting reduction of Cr(VI) to Cr(III).<sup>13</sup> Interestingly, to the best of our knowledge, none of the literature reports which employ this reduction step have investigated the remediation ability of the polymer if it is not reduced prior to immersion in the Cr(VI) solution.<sup>9, 11, 12</sup> Thus, the efficacy of this reduction step will now be compared to non-reduced polypyrrole films. The impact of the reduction step on the removal abilities of PpyNW, PpyCl and PpySDS films will be discussed.

### 5.4.1 Rate of Chromium Removal

In order to contrast the reduced and non-reduced polypyrrole films, the efficiency with which they reduce Cr(VI) in solution was calculated as a percentage.

$$\text{Equation 5.3} \quad \% \text{ Removal Efficiency} = \left( \frac{C_0 - C_t}{C_0} \right) \times 100$$

where  $C_0$  is the initial absorbance observed at 350 nm and  $C_t$  is the absorbance at a given time. When the percentage removal efficiency is plotted against immersion time, it is immediately apparent that the films which have been reduced at an applied potential of - 0.8 V vs. SCE prior to immersion in 0.10 mM acidified Na<sub>2</sub>Cr<sub>2</sub>O<sub>7</sub>·2H<sub>2</sub>O, reduce Cr(VI) at a faster rate than the not reduced Ppy films. The removal efficiency of Cr(VI) by reduced and non-reduced PpyNW films over time is plotted in Figure 5.18. Reduced and non-reduced PpyCl and PpySDS films produce analogous traces to those seen here. While reduced films have a removal efficiency of up to 37 percent per hour for the first 60 minutes of immersion, the non-reduced films display a rate of approximately 20 percent removal efficiency over the same period of time (Table 5.9). The rate at which both sets of polymer films reduce Cr(VI) in solution decreases dramatically over the next 4 hours, until the rate at which the reduced and non-reduced films remove Cr(VI) are similar at 1-3 percent Cr(VI) removal per hour. This is to be expected as the progress of the reaction becomes limited by the mass transport of the Cr(VI) into the

polymer matrix once the exterior surfaces of the polymer have been oxidised by the Cr(VI).<sup>9</sup> Interestingly, the reduced PpyCl films show the greatest removal efficiency and the largest difference in rate of Cr(VI) remediation between the reduced and non-reduced PpyCl films during the first hour of immersion. This is in keeping with the results of the open-circuit potential measurements which show that the PpyCl films are more easily oxidised by Cr(VI) than the PpyNW films.

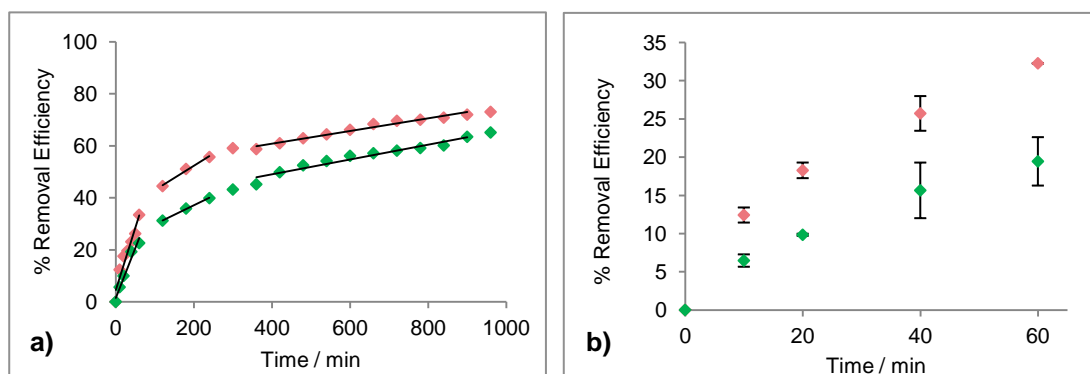


Figure 5.18: Percentage removal efficiency of PpyNW immersed in 0.10 mM acidified  $\text{Na}_2\text{Cr}_2\text{O}_7 \cdot 2\text{H}_2\text{O}$  over 15 hours, with stirring; (♦) PpyNW pre-reduced at  $-0.80$  V vs. SCE in 0.10 M  $\text{H}_2\text{SO}_4$ , (◆) PpyNW not treated before immersion, b) expansion of plot (a) showing the first 60 minutes of immersion.

Table 5.9: Comparison of the rate of change of percentage removal efficiency for reduced and non-reduced polymer films immersed in 0.10 mM acidified  $\text{Na}_2\text{Cr}_2\text{O}_7 \cdot 2\text{H}_2\text{O}$  solution. The reaction rate is measured as percentage removal of Cr(VI) per hour and is calculated from the slope of the relevant trendline as seen in Figure 5.18,  $n = 3$ .

Polymer	Pre-treatment	Reaction rate / % per hr 0 – 1 hr	Reaction rate / % per hr 1.5 – 4 hr	Reaction rate / % per hr 6 – 15 hr
PpyCl	Reduced	37	7	2
	Not reduced	19	7	3
PpyNW	Reduced	29	6	1
	Not reduced	23	4	2
PpySDS	Reduced	30	8	2
	Not reduced	21	5	3

The PpyNW and PpySDS films display comparable reaction rates for both reduced and non-reduced films, with the reduced films being 20–30 percent more efficient than the non-reduced films during the first hour of exposure. The reaction rates for all three non-reduced films are also similar over the first hour, exhibiting a rate of Cr(VI) removal of approximately 20 percent. It was thought that the PpyNW would be most efficient due to the larger surface area exposed to the Cr(VI) in solution. However, this

was clearly not the case. The loss in conductivity of the PpyNW films compared to the conductivity of the bulk PpyCl films may offset the effects of the increased surface area. As previously mentioned, EIS carried out by our group indicate that the PpyNW films formed by a template-free approach are less conducting than bulk polypyrrole films and this is consistent with the appearance of a carbonyl stretch in the FTIR spectra obtained for the PpyNW films in this study. This lower conductivity may also account for the small difference observed in the removal rate between the reduced PpyNW and the non-reduced PpyNW over the first hour of immersion in 0.10 mM acidified  $\text{Na}_2\text{Cr}_2\text{O}_7 \cdot 2\text{H}_2\text{O}$ . After the first hour of immersion, it can be seen that there is little difference between the three films whether reduced or not reduced. Thus it can be seen that while reduction of the polymer does increase the rate of Cr(VI) reduction in the initial stages of immersion, there is very little difference between the reduced and non-reduced films over time. Therefore, depending on the speed of Cr(VI) remediation required, the appropriate pre-treatment can be chosen, with no treatment required for remediation that will take place over long periods of time.

#### 5.4.2 Recyclability of the PpyNW films

The primary reason for using conducting polymers in Cr(VI) remediation is their ability to switch from one redox state to another in a reversible manner. This is achieved by applying either a cathodic or anodic potential to reduce or oxidise the polymer as required.<sup>13</sup> Thus, there is potential for the regeneration and re-use of the polymer film, which will now be considered.<sup>10, 37</sup> Immersion in the Cr(VI) results in the reduction of the Cr(VI) to Cr(III) and the concomitant oxidation of the polypyrrole. As discussed in Section 5.4.1, the initial reduction of the polymer does not have a significant effect on the removal efficiency over extended periods of time, however, if this reduction step is carried out after immersion in the acidified Cr solution, it was hoped that the polymer would be regenerated. It was also hoped that the application of the reduction step would increase the recyclability of the PpyNW films.

PpyNW films were electrochemically formed as before on conventional gold wire electrodes and either reduced by applying a reduction potential of  $-0.80$  V vs. SCE in 0.10 M  $\text{H}_2\text{SO}_4$  or rinsed with 0.10 M  $\text{H}_2\text{SO}_4$  prior to immersion in 0.10 mM acidified  $\text{Na}_2\text{Cr}_2\text{O}_7 \cdot 2\text{H}_2\text{O}$  with gentle agitation. The Cr(VI) reduction was monitored using UV-Vis spectroscopy over a 5 hour period. The PpyNW films were then removed and

rinsed and then either reduced again at an applied potential of  $-0.80$  V vs. SCE in  $0.10$  M  $\text{H}_2\text{SO}_4$  or rinsed with  $0.10$  M  $\text{H}_2\text{SO}_4$  before being immersed in a fresh  $0.10$  mM acidified  $\text{Na}_2\text{Cr}_2\text{O}_7 \cdot 2\text{H}_2\text{O}$  solution. These 5 hour immersions were repeated up to five times in a fresh  $0.10$  mM acidified  $\text{Na}_2\text{Cr}_2\text{O}_7 \cdot 2\text{H}_2\text{O}$  solution for each PpyNW film and the results are depicted in Figure 5.19. It can be observed that, upon immersion in  $0.10$  mM acidified  $\text{Na}_2\text{Cr}_2\text{O}_7 \cdot 2\text{H}_2\text{O}$  for the first time; the reduced films have a removal efficiency which is almost 50 percent greater than that observed for the non-reduced PpyNW films. The removal efficiency of the reduced PPyNW films decreases by approximately 15 percent with each subsequent immersion in  $0.10$  mM acidified  $\text{Na}_2\text{Cr}_2\text{O}_7 \cdot 2\text{H}_2\text{O}$ . The removal efficiency of the non-reduced PpyNW films decreases by 60 percent upon the second immersion and a further 10 percent with a third subsequent immersion in  $0.10$  mM acidified  $\text{Na}_2\text{Cr}_2\text{O}_7 \cdot 2\text{H}_2\text{O}$ . The removal efficiency of the non-reduced PpyNW films appears to hold steady at approximately 10 percent for the third and subsequent immersions of the non-reduced PpyNW films in  $0.10$  mM acidified  $\text{Na}_2\text{Cr}_2\text{O}_7 \cdot 2\text{H}_2\text{O}$ . This represents a removal efficiency that is 50 percent less efficient than the removal efficiency observed for the reduced PpyNW films immersed in  $0.10$  mM acidified  $\text{Na}_2\text{Cr}_2\text{O}_7 \cdot 2\text{H}_2\text{O}$  for the fifth time. This loss in removal efficiency after a number of immersion cycles has also been observed by Ruotolo *et al.* who also observed a small loss in the electrochemical activity of their polypyrrole films with repeated exposure to acidified Cr(VI).<sup>47</sup>

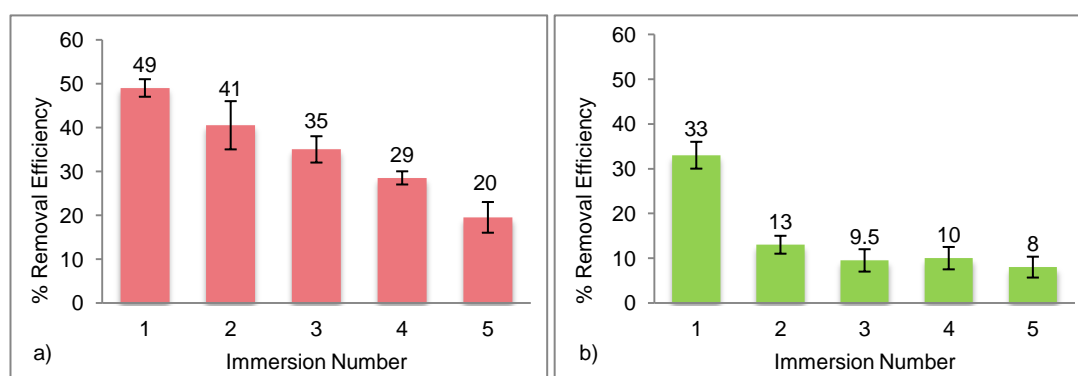


**Figure 5.19:** Percentage removal efficiency for PpyNW immersed in  $0.10$  mM acidified  $\text{Na}_2\text{Cr}_2\text{O}_7 \cdot 2\text{H}_2\text{O}$  with gentle agitation. Each experiment was carried out for 5 hours. a) Each PpyNW film was reduced before each immersion by applying a potential of  $-0.80$  V vs. SCE in  $0.10$  M  $\text{H}_2\text{SO}_4$  and b) each PpyNW film was rinsed with  $0.10$  M  $\text{H}_2\text{SO}_4$  before each immersion in  $0.10$  mM acidified  $\text{Na}_2\text{Cr}_2\text{O}_7 \cdot 2\text{H}_2\text{O}$ ,  $n = 2$ .

Thus it can be concluded that the application of a reduction step is able to regenerate the PpyNW films, and while they lose efficiency with repeated immersions, they are still more effective than the non-reduced films for immersion durations of 5 hours. It has been reported that immersing polypyrrole films for a longer duration with each repeated experiment can result in an increase in the amount of Cr(VI) remediated.<sup>12</sup> This was not investigated in this study and therefore it must be noted that if the PpyNW films were immersed in 0.10 mM acidified  $\text{Na}_2\text{Cr}_2\text{O}_7 \cdot 2\text{H}_2\text{O}$  solution until 100 percent of the Cr(VI) had been removed, it is very possible that there would be little difference observed between the recyclability of the reduced PpyNW films and the non-reduced PpyNW films.

## 5.5 Applications of PPyNW on a Porous Support

There is currently considerable interest in the use of polypyrrole coated on solid supports for the remediation or adsorption of heavy metals from wastewater. In particular the use of polypyrrole on sawdust or cellulose wires has been posited.<sup>48, 49</sup> Although very efficient, these materials cannot be used under the acidic conditions at which maximum Cr(VI) remediation can occur. Therefore, in this study a polyamide porous membrane, of surface area  $4.9 \text{ cm}^2$ , is employed as the solid support upon which polypyrrole nanowires are electrodeposited. The gold sputter-coating employed to infer conductivity on the membranes make this process uneconomical. Future work could be carried out on porous carbon substrates which have also been shown to successfully remediate heavy metals when impregnated with polypyrrole.<sup>50</sup>

### 5.5.1 Nanowire Formation on Polyamide Membranes

The membranes were sputter coated with gold as described in Chapter 3 and the polypyrrole nanowires were electrochemically grown using the conditions detailed in Table 5.1 until a charge density of  $300 \text{ mC cm}^{-2}$  was achieved (Figure 5.20).

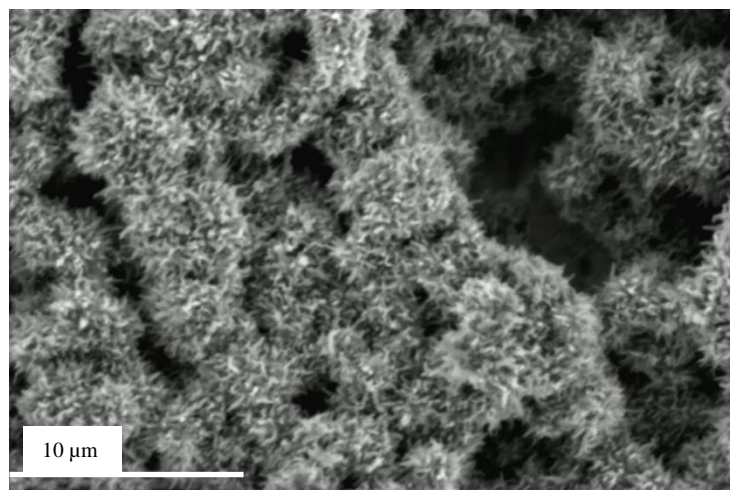


**Figure 5.20:** SEM micrograph of PPyNW formed electrochemically at 0.80 V vs. SCE, on a gold sputter coated polyamide membrane, to a charge density of  $300 \text{ mC cm}^{-2}$ .

Initial studies were carried out by stirring the PPyNW coated membranes in 0.10 mM acidified  $\text{Na}_2\text{Cr}_2\text{O}_7 \cdot 2\text{H}_2\text{O}$  to establish efficiency rates and recyclability. The membranes were then tested to determine whether they were best employed as electrochemically controlled membrane filters or as membrane filters in a flow-through system.

### 5.5.2 Rate of Chromium Removal at a PPyNW Modified Membrane

PPyNW coated membranes were either reduced for 30 minutes by applying a reduction potential of  $-0.80\text{ V vs. SCE}$  in  $0.10\text{ M H}_2\text{SO}_4$ , or rinsed with  $0.10\text{ M H}_2\text{SO}_4$  before being immersed with stirring in  $20\text{ cm}^3$  of  $0.10\text{ mM}$  acidified  $\text{Na}_2\text{Cr}_2\text{O}_7 \cdot 2\text{H}_2\text{O}$  solution. Aliquots were extracted periodically for UV-Vis spectroscopic measurements before returning to the vessel. Figure 5.21 shows the percentage removal efficiency of reduced and non-reduced PPyNW coated membranes over an 8 hour period, calculated according to Equation 5.3. As with the PPyNW films formed on a gold electrode, it can be observed that the initial removal rate is faster for PPyNW coated membranes which were reduced prior to immersion in  $0.10\text{ mM}$  acidified  $\text{Na}_2\text{Cr}_2\text{O}_7 \cdot 2\text{H}_2\text{O}$ . Table 5.10 details the rate of removal efficiency of the reduced and not-reduced PPyNW coated membranes and it can be seen that the PPyNW coated membranes have a removal efficiency of 23 percent, compared to 15 percent removal efficiency for the non-reduced membranes, during the first 60 minutes of immersion in  $0.10\text{ mM}$  acidified  $\text{Na}_2\text{Cr}_2\text{O}_7 \cdot 2\text{H}_2\text{O}$ . The rate of change of removal efficiency drops considerably for both the reduced and non-reduced PPyNW coated membranes after the first hour of immersion. This is similar to the results observed for PPyNW films formed on a standard gold electrode. After 2 hours immersion in  $0.10\text{ mM}$  acidified  $\text{Na}_2\text{Cr}_2\text{O}_7 \cdot 2\text{H}_2\text{O}$ , both the reduced and non-reduced PPyNW coated membranes exhibit the same rate of percentage removal efficiency. It can therefore be seen that both reduced and non-reduced PPyNW coated membranes have the ability to remediate chromium and that while the reduction step is useful in speeding up the initial remediation, it is not essential to the remediation process.

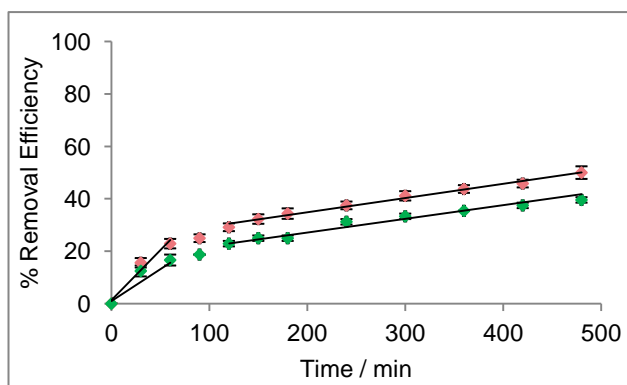


Figure 5.21: Percentage removal efficiency of PPyNW coated membranes immersed in  $0.10\text{ mM}$  acidified  $\text{Na}_2\text{Cr}_2\text{O}_7 \cdot 2\text{H}_2\text{O}$  over 8 hours, with stirring; (♦) PPyNW modified membranes reduced at  $-0.80\text{ V vs. SCE}$  in  $0.10\text{ M H}_2\text{SO}_4$ ,  $n = 4$ , (♦) PPyNW modified membranes not treated before immersion,  $n = 2$ .

**Table 5.10:** Comparison of the rate of change of percentage removal efficiency for reduced and non-reduced PpyNW coated membranes immersed in 0.10 mM acidified  $\text{Na}_2\text{Cr}_2\text{O}_7 \cdot 2\text{H}_2\text{O}$  over 8 hours. The reaction rate is measured in percentage removal per hour which is calculated from the slope of the relevant trendline as seen in Figure 5.21,  $n = 2$ .

Polymer	Immersion Solution	Reaction rate / % per hour 0 – 1 hr	Reaction Rate / % per hour 2 – 8 hr
Reduced PpyNW Coated membrane	0.10 mM $\text{Na}_2\text{Cr}_2\text{O}_7$ / 0.10 M $\text{H}_2\text{SO}_4$	23	3
Not reduced PpyNW coated membrane	0.10 mM $\text{Na}_2\text{Cr}_2\text{O}_7$ / 0.10 M $\text{H}_2\text{SO}_4$	15	3

### 5.5.3 Recyclability of Membranes

The recyclability of the PpyNW membranes was studied in the same manner applied to the PPyNW films formed on conventional gold electrodes. Each PpyNW coated membrane was either reduced at  $-0.80$  V vs. SCE in  $0.10$  M  $\text{H}_2\text{SO}_4$ , or rinsed with  $0.10$  M  $\text{H}_2\text{SO}_4$  prior to immersion in  $0.10$  mM acidified  $\text{Na}_2\text{Cr}_2\text{O}_7 \cdot 2\text{H}_2\text{O}$  with gentle agitation. The decreasing concentration of Cr(VI) was monitored using UV-Vis spectroscopy for a 3 hour period. The PpyNW coated membranes were removed from solution and rinsed and then either reduced again or rinsed with  $0.10$  M  $\text{H}_2\text{SO}_4$  prior to immersion in a fresh  $0.10$  mM acidified  $\text{Na}_2\text{Cr}_2\text{O}_7 \cdot 2\text{H}_2\text{O}$  solution. This was repeated three times for each membrane and the results are depicted in Figure 5.22.

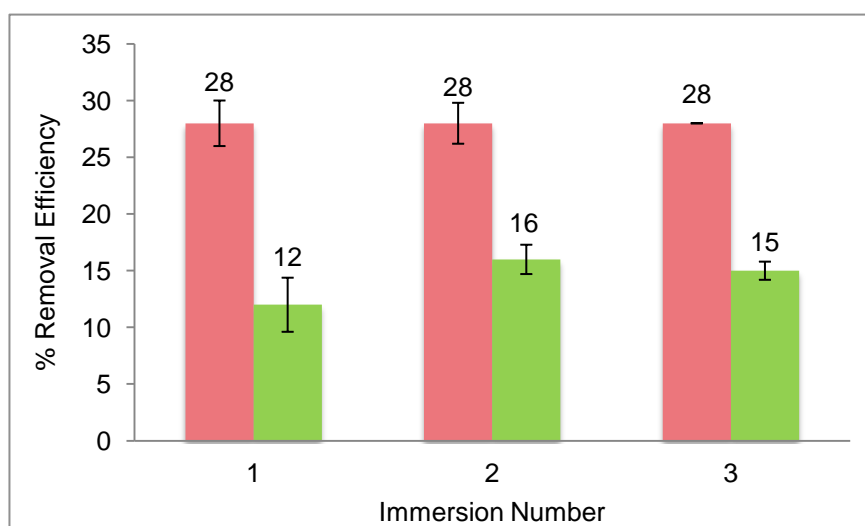


**Figure 5.22:** Percentage removal efficiency for PpyNW coated membranes immersed in  $0.10$  mM acidified  $\text{Na}_2\text{Cr}_2\text{O}_7 \cdot 2\text{H}_2\text{O}$  solution with gentle agitation. Each experiment was carried out for 3 hours. (■) PpyNW coated membranes reduced at  $-0.80$  V vs. SCE in  $0.10$  M  $\text{H}_2\text{SO}_4$ ,  $n = 3$ , (■) PpyNW modified membranes not reduced before immersion,  $n = 2$ .

It can be observed that the PPyNW coated membranes have inferior percentage removal efficiencies compared with the PpyNW films electropolymerised on conventional gold electrodes. For example, after 3 hours immersion, the PpyNW films on an electrode exhibit a percentage removal efficiency of 42 percent for reduced films and 30 percent for non-reduced PpyNW films. In comparison, after the first 3 hour immersion in 0.10 mM acidified  $\text{Na}_2\text{Cr}_2\text{O}_7 \cdot 2\text{H}_2\text{O}$ , the PpyNW coated membranes have percentage removal efficiencies of 28 percent and 12 percent respectively, for the reduced and non-reduced membranes. This discrepancy can be attributed to the larger immersion volume of the PpyNW coated membranes ( $3 \text{ cm}^3$  for PpyNW modified electrodes compared to  $20 \text{ cm}^3$  for PpyNW modified membranes) as this increases the ratio of polymer surface area to solution volume for the PpyNW coated membranes.

The advantage of the PpyNW coated membrane over the PPyNW films on an electrode can be seen with the second and subsequent immersions. The percentage removal efficiency for the reduced PPyNW coated membranes remains constant at 28 percent, compared to the reduced PpyNW films on electrodes, whose percentage removal efficiency has dropped by up to 30 percent by the third immersion. This difference is most likely due to the much larger surface area of the PpyNW coated membranes, which is  $4.9 \text{ cm}^2$  compared to  $1.2 \text{ cm}^2$  for the PpyNW films on gold electrodes. The PpyNW coated membranes were also only immersed for 3 hours in each fresh solution of 0.10 mM acidified  $\text{Na}_2\text{Cr}_2\text{O}_7 \cdot 2\text{H}_2\text{O}$ , compared to an immersion time of 5 hours for the PpyNW films formed on gold electrodes. Interestingly, the percentage removal efficiency of the non-reduced PpyNW coated membranes improves with the second immersion. This can be attributed to the adsorption of Cr(VI) in the form of  $\text{HCrO}_4^-$ , which will not be fully removed by the  $\text{H}_2\text{SO}_4$  wash. This increases the negative charge on the membrane, favouring the adsorption and concomitant reduction of Cr(VI), due to enhanced electrostatic attraction.<sup>51</sup> Thus, it can be concluded that the reduction step very effectively regenerates the PPyNW modified membrane, with no decline observed in percentage removal efficiency after three immersions for 3 hours. As with the PpyNW films formed on conventional gold electrodes, the recyclability of the PpyNW coated membranes was not investigated for immersion of the membranes until complete removal of the Cr(VI) was achieved. Therefore, it can only be concluded that the PpyNW coated membranes are recyclable through the application of the reduction potential over immersions that are 3 hours in duration.

#### 5.5.4 Electrochemically Enhanced Chromium Remediation – Pulse technique

It has been established that reducing the polymer nanowires with the application of a reduction potential is successful in regenerating their remediation properties. Reduction of the polypyrrole coated membrane in 0.10 M sulfuric acid between immersions means that the membrane must be removed from solution, which would not be practical on a large scale. Thus, the application of a pulsed reduction potential, during immersion in the acidified chromium solution was investigated as a regeneration process. The PpyNW coated membranes were prepared as before, and rinsed prior to immersion in 30 cm<sup>3</sup> of 0.10 mM acidified Na<sub>2</sub>Cr<sub>2</sub>O<sub>7</sub>·2H<sub>2</sub>O. The PpyNW coated membrane was employed as the working electrode in a conventional three electrode cell. A reduction potential of - 0.80 V vs. SCE was applied for 30 seconds every 10 minutes. This was carried out for 1 hour before the solution was changed for fresh acidified Na<sub>2</sub>Cr<sub>2</sub>O<sub>7</sub>·2H<sub>2</sub>O. Aliquots were removed for UV-Vis spectroscopic analysis prior to and after each reduction potential was applied. Each aliquot was immediately returned to solution. The experiment was repeated for three fresh solutions of 0.10 mM acidified Na<sub>2</sub>Cr<sub>2</sub>O<sub>7</sub>·2H<sub>2</sub>O.

The percentage removal efficiency, at 60 minutes, for the pulsed PpyNW coated membranes immersed in three consecutive solutions of 0.10 mM acidified Na<sub>2</sub>Cr<sub>2</sub>O<sub>7</sub>·2H<sub>2</sub>O is shown in Figure 5.23. These results are compared to PpyNW coated membranes which were reduced and PpyNW coated membranes which were not reduced prior to immersion in each fresh 0.10 mM acidified Na<sub>2</sub>Cr<sub>2</sub>O<sub>7</sub>·2H<sub>2</sub>O solution. It can be seen immediately that the pulse technique is not as successful as the reduction step carried out in 0.10 M H<sub>2</sub>SO<sub>4</sub>, exhibiting percentage removal efficiencies approximately 50 percent less than that seen for the reduced membrane after three immersions. As the pulsed PpyNW coated membranes were not reduced for 30 minutes prior to immersion, it is more accurate to compare their removal efficiency to the results obtained for non-reduced PpyNW coated membranes. In this case, an improvement in the percentage removal efficiency is evident for each immersion of the pulsed PpyNW coated membranes, though not to a great extent. For example, after 1 hour, the percentage removal efficiency of the pulsed PpyNW coated membranes is 15 percent, compared to a removal efficiency of 10 percent for the non-reduced PpyNW modified membranes.

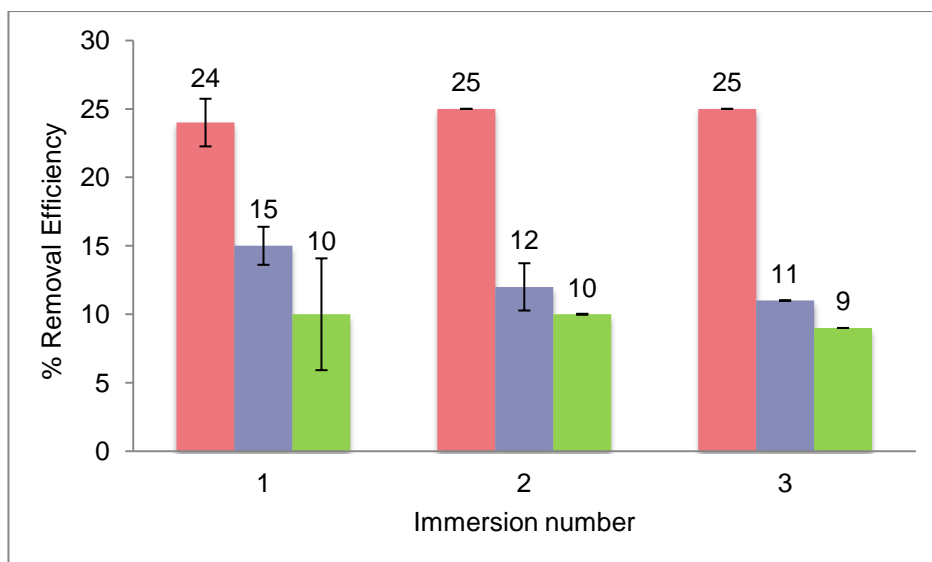


**Figure 5.23:** Percentage removal efficiency for PpyNW coated membranes immersed in 0.10 mM acidified Cr solution with gentle agitation for 1 hour, for three immersions. (■) PpyNW modified membranes reduced at -0.80 V vs. SCE in 0.10 M H<sub>2</sub>SO<sub>4</sub>, n = 3, (■) PpyNW modified membrane, not reduced prior to immersion, reduction potential of -0.80 V vs. SCE applied every 10 minutes for 30 seconds, n = 2, (■) PpyNW modified membranes not treated before immersion, n = 2.

The beneficial effect of applying a reduction potential to the PpyNW coated membranes every 10 minutes is more apparent in Figure 5.24 in which the percentage removal efficiency of the PpyNW coated membranes is plotted over time. This allows for the rate of change of removal efficiency to be calculated from the relevant trendline slopes. It can be observed that there is a rapid increase in removal efficiency in the first 10 minutes of exposure to the PpyNW coated membranes which are not reduced prior to immersion. This fast removal efficiency decreases and only a slight increase is observed over the remaining 50 minutes of the experiment. Applying a reduction potential every 10 minutes drives the removal of Cr(VI) from solution and prevents the rate of reaction from slowing down. The rate of change of removal efficiency was determined over the final 50 minutes of the experiments. Table 5.11 details the rate of change of removal efficiency calculated for the non-reduced PpyNW coated membranes and the pulsed PpyNW coated membranes immersed three separate times in acidified Na<sub>2</sub>Cr<sub>2</sub>O<sub>7</sub>·2H<sub>2</sub>O, for 1 hour each time. It can be seen that the non-reduced PpyNW coated membranes only exhibit a rate of change of removal efficiency of 3 percent per hour over the final 50 minutes of each immersion, compared to 12 percent per hour for the pulsed membranes during the first immersion (Table 5.11).

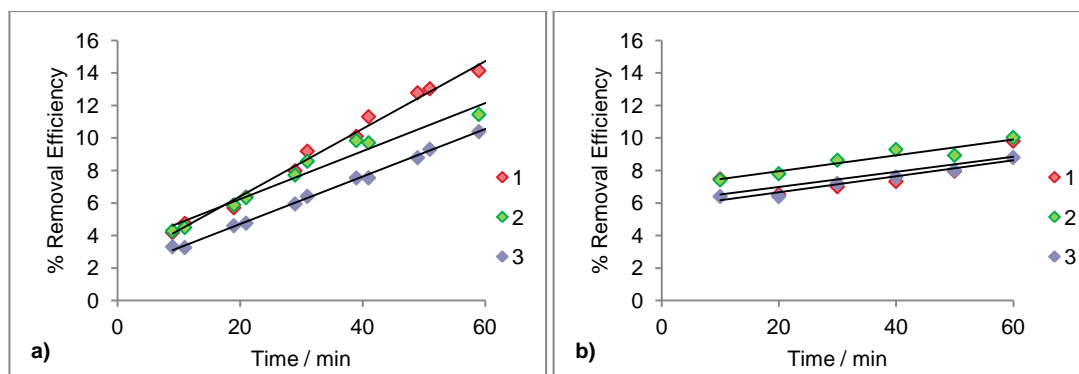


**Figure 5.24:** Percentage removal efficiency over time for a) PpyNW coated membranes, not reduced prior to immersion, a reduction potential of  $-0.80$  V vs. SCE applied every 10 minutes for 30 seconds, b) PpyNW modified membranes not reduced before immersion. Each membrane was immersed in three fresh solutions of  $0.10$  mM acidified  $\text{Na}_2\text{Cr}_2\text{O}_7 \cdot 2\text{H}_2\text{O}$  for 1 hour, the immersion number is indicated in the legend. Trendlines were applied to values obtained between 10 and 60 minutes of immersion time.

**Table 5.11:** Comparison of the rate of change of percentage removal efficiency for non-reduced PpyNW coated membranes and pulsed PpyNW coated membranes immersed in  $0.10$  mM acidified  $\text{Na}_2\text{Cr}_2\text{O}_7 \cdot 2\text{H}_2\text{O}$  for 1 hour. The reaction rate is measured in percentage removal per hour and is calculated from the slope of the relevant trendlines for data obtained between 10 and 60 minutes of immersion, as seen in Figure 5.24.

Polymer	Pre-treatment	Immersion Number	Reaction Rate / % Removal per hour
PpyNW coated membrane	Not reduced prior to immersions	1	3
		2	3
		3	3
PpyNW coated membrane	Potential pulsed $-0.80$ V vs. SCE for 30 seconds every 10 minutes	1	12
		2	9
		3	9

The conclusion can therefore be drawn that the reduction step is most effective at regenerating the PpyNW coated membranes between immersions of 3 hours duration. Also, applying a reduction potential in pulses during the immersion does improve the percentage reduction efficiency of the membrane, but not to a great extent. However, it may be a more efficient method of regeneration of the PpyNW coated membranes for a large scale system.

### 5.5.5 Chromium Remediation in a Stirred Filtration Cell

The PPyNW films were formed as before on the polyamide membranes. The PPyNW coated membranes were rinsed and electrochemically reduced at an applied potential of - 0.80 V vs. SCE in 0.10 M H<sub>2</sub>SO<sub>4</sub>. The membrane was then loaded into a stirred filtration cell, as depicted in Figure 5.25, in order to carry out dead-end filtration in which the 0.10 mM acidified Na<sub>2</sub>Cr<sub>2</sub>O<sub>7</sub>·2H<sub>2</sub>O solution flows through the PPyNW coated membrane under gravity. 10 cm<sup>3</sup> of 0.10 mM acidified Na<sub>2</sub>Cr<sub>2</sub>O<sub>7</sub>·2H<sub>2</sub>O solution was passed through the PPyNW coated membrane and retained. UV-Vis analysis was carried out on the filtrate and the same 0.10 mM acidified Na<sub>2</sub>Cr<sub>2</sub>O<sub>7</sub>·2H<sub>2</sub>O solution was passed through the PPyNW coated membrane nine more times. This was to investigate whether repeated exposure to the PPyNW coated membranes would increase the amount of chromium remediated from the 0.10 mM acidified Na<sub>2</sub>Cr<sub>2</sub>O<sub>7</sub>·2H<sub>2</sub>O solution. Wastewater treatment plants often employ flat sheet membrane modules which consist of a number of membranes layered with spacers or spiral membrane configurations in which one or more membranes are wrapped around a perforated central tube which collects the permeate.<sup>52</sup> This allows the solution greater time in contact with the membrane surface. It can be seen from Figure 5.26 that the greatest amount of Cr(VI) is remediated during the first exposure of the solution to the PPyNW coated membrane, but this is followed by a gradual decrease in the percentage of chromium left in solution, with repeated exposures. This large initial decrease, followed by the gradual chromium removal with repeated exposures suggests that the PPyNW coated membranes may be effective if a large number of PPyNW coated membranes were placed in series in a flat sheet membrane module.<sup>9</sup>

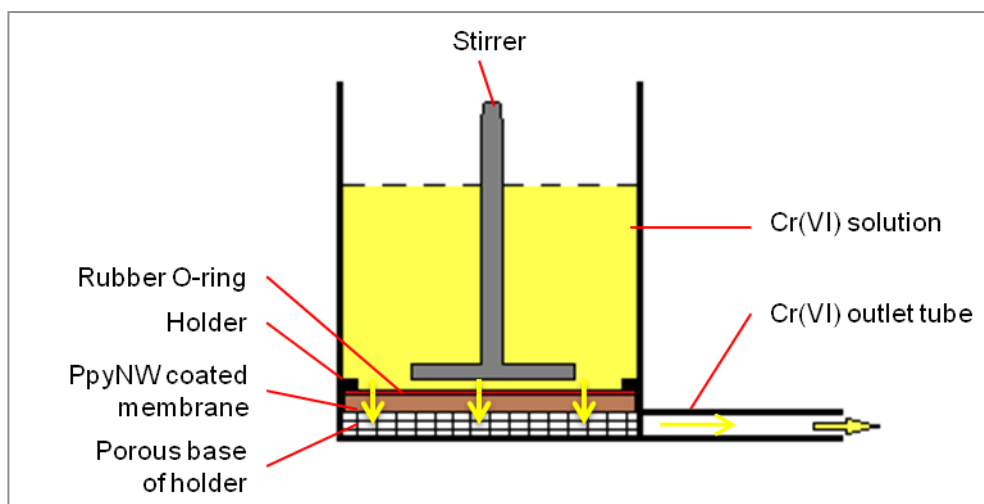


Figure 5.25: The PpyNW coated membrane is loaded into a stirred filtration cell and held in place with a rubber O-ring. The 0.10 mM acidified  $\text{Na}_2\text{Cr}_2\text{O}_7 \cdot 2\text{H}_2\text{O}$  solution can flow through the PpyNW coated membrane under gravity, and is collected at the Cr(VI) outlet tube in order to be passed through the membrane again.

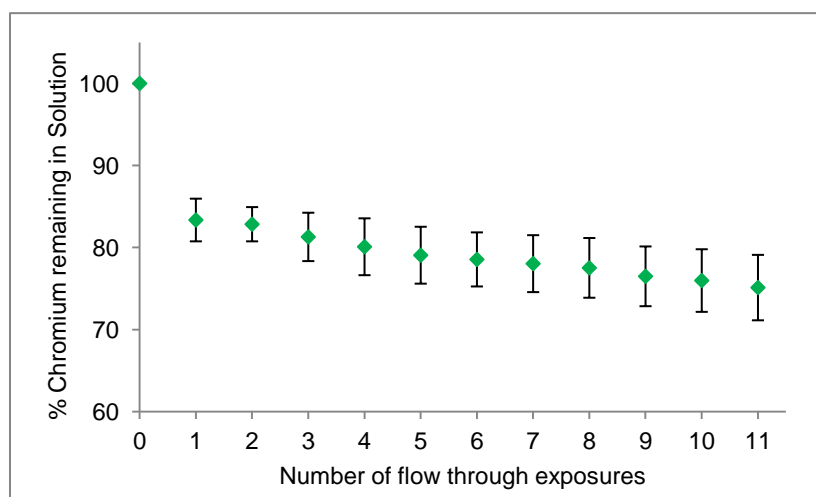


Figure 5.26: Percentage of chromium remaining in solution after 0.10 mM acidified  $\text{Na}_2\text{Cr}_2\text{O}_7 \cdot 2\text{H}_2\text{O}$  is flowed through the PpyNW coated membrane a number of times.

## 5.6 Summary of Polypyrrole Nanowires

The mechanism by which the PpyNW films remove Cr(VI) from solution was investigated using PpyNW films coated on conventional gold electrodes. The removal mechanism of Cr(VI) by PpyNW was found to be most effective at pH 1.0 and occurs in two steps. First, the nitrogen atoms on the polypyrrole backbone become protonated in the acidic solution.<sup>39, 53</sup> This infers a positive charge on the PpyNW film, attracting the Cr(VI) anions which exist in the acidic solution as  $\text{HCrO}_4^-$  anions.<sup>28</sup> The strongly oxidising Cr(VI) solution oxidises the polypyrrole nanowires and is in turn reduced to Cr(III). This can be observed through the increase in the open circuit potential measured for the PpyNW films immersed in 0.10 mM acidified  $\text{Na}_2\text{Cr}_2\text{O}_7 \cdot 2\text{H}_2\text{O}$ . The PpyNW films are less easily oxidised than bulk PpyCl films and this is thought to be due to the loss of conductivity experienced by the PpyNW films, due to carbonyl defects along the PpyNW backbone. The Cr(III) produced by the reduction of Cr(VI) at the PpyNW film surface is repelled back into solution. EDX analysis indicates that some chromium is retained by the PpyNW film. A colorimetric test in which 1,5-diphenylcarbazide complexes with Cr(VI) to produce a red/violet complex shows that between 92-100 percent of the Cr(VI) is repelled back into solution as Cr(III). The speciation of the 8 percent of chromium retained by the PpyNW films was not investigated in the course of this work.

The effect of the reduction step, in which a reduction potential of  $-0.80$  V vs. SCE is applied to the PpyNW films in 0.10 M  $\text{H}_2\text{SO}_4$ , was also examined. This reduction step is employed by the majority of groups using electrochemically polymerised polypyrrole for the remediation of Cr(VI).<sup>9, 11-14, 33, 37</sup> It was shown in Section 5.4 that the reduction of the PpyNW films prior to immersion in 0.10 mM acidified  $\text{Na}_2\text{Cr}_2\text{O}_7 \cdot 2\text{H}_2\text{O}$  resulted in a faster rate of Cr(VI) removal over the first hour of immersion. When compared to non-reduced PpyNW films, after the first hour had elapsed there was very little difference observed in the rate of Cr(VI) removal by the reduced and non-reduced PpyNW films. It was also observed that the application of a reduction step is able to regenerate the PpyNW films, and while they lose efficiency with repeated immersions in 0.10 mM acidified  $\text{Na}_2\text{Cr}_2\text{O}_7 \cdot 2\text{H}_2\text{O}$ , they are still more effective than the non-reduced PpyNW films after immersion durations of 5 hours. This efficiency may decrease if the immersion time was increased until all of the Cr(VI) in solution was remediated.

The PpyNW coated on porous polyamide membrane supports displayed similar results to those found for the PpyNW films on conventional gold electrodes. The reduced PpyNW coated membranes demonstrate a greater rate of Cr(VI) removal over the first hour of immersion when compared to non-reduced PpyNW coated membranes. After the initial hour however, both the reduced and non-reduced PpyNW coated membranes show a slow rate of Cr(VI) removal, which is similar to the rate observed for PpyNW films both reduced and non-reduced on gold electrodes. The reduced PpyNW coated membranes also exhibit good recyclability properties, with no decrease observed in the percentage removal efficiency of Cr(VI) for repeated immersions in 0.10 mM acidified  $\text{Na}_2\text{Cr}_2\text{O}_7 \cdot 2\text{H}_2\text{O}$  for 3 hours. This is most likely due to the increased surface area of the PpyNW coated membrane in comparison to the surface area of the PpyNW films on gold electrodes, and also due to the shorter immersion time of 3 hours compared to the 5 hours for which the PpyNW films on gold electrodes were immersed in 0.10 mM acidified  $\text{Na}_2\text{Cr}_2\text{O}_7 \cdot 2\text{H}_2\text{O}$ .

In order to put the PpyNW coated membranes in context with the polypyrrole films used for the removal of Cr(VI) reported in the literature, Table 5.12 compiles the results of a number of studies in which the prepared polypyrrole film is reduced prior to immersion in a Cr(VI) solution. All of the studies detailed have immersed the polypyrrole films in an acidic Cr(VI) solution. The most efficient removal of Cr(VI) is reported by Wei *et al.* with 100 percent of the Cr(VI) from an initial solution of 0.77 mM Cr(VI) being removed in 60 minutes.<sup>9</sup> The results obtained in the current study for the PpyNW coated membranes do not appear to compare favourably to the removal efficiencies observed in the literature. While it was hoped that the increased surface area of the polypyrrole nanowires would provide increased removal efficiency, it appears that the loss in conductivity of the PpyNW when compared to the bulk polypyrrole films has impacted negatively on the polypyrrole nanowires ability to remove Cr(VI) from solution. However, the degree of agitation applied to the systems and the quantity of polypyrrole that is deposited on the electrodes is not clearly defined in these literature reports and the observed results vary quite a bit. Thus it may not be correct to apply a direct comparison to the PpyNW coated membranes. The removal efficiency may be improved by more vigorous agitation of the Cr(VI) solution while in contact with the PpyNW coated membranes. This approach was successfully used by Earley *et al.* to improve the removal efficiency of their Ppy/oxalate films from

35 percent removal efficiency with gentle agitation, to 96 percent removal efficiency with vigorous agitation over 2 hours exposure to 0.25 mM Cr(VI) in 0.10 M H<sub>2</sub>SO<sub>4</sub>.<sup>12</sup>

**Table 5.12: Comparison of the percentage of Cr(VI) removed from solution by the reduced and non-reduced PpyNW coated membranes to the values presented in various studies reported in the literature.**

Study	Polymer	pH	Initial Cr(VI) concentration / mM	% of Cr(VI) removed from solution	Duration of Experiment / min
Wei <i>et al.</i> (1993) <sup>9</sup>	PpyCl on 4 cm <sup>2</sup> Pt mesh	Aqueous H <sub>2</sub> SO <sub>4</sub>	0.77	100	60
Senthurchelvan <i>et al.</i> (1996) <sup>11</sup>	PpyCl on glassy carbon	1.0	0.39	50	45
Wampler <i>et al.</i> (1996) <sup>10</sup>	Ppy/carbon black composite	0.10 M H <sub>2</sub> SO <sub>4</sub>	2.0	80	60
Alatorre <i>et al.</i> (1998) <sup>14</sup>	PpyCl on a graphite felt, 1 cm <sup>2</sup>	0.10 M H <sub>2</sub> SO <sub>4</sub>	2.0	80	120
Rodriguez <i>et al.</i> (2007) <sup>33</sup>	PpyCl on reticulated vitreous carbon, 1 cm <sup>2</sup>	0.10 M H <sub>2</sub> SO <sub>4</sub>	0.2 2.0	100 91	120 120
Earley <i>et al.</i> (2009) <sup>12</sup>	Ppy/oxalate on titanium	0.10 M H <sub>2</sub> SO <sub>4</sub>	0.25	96	120 with vigorous stirring
Krishnani <i>et al.</i> (2013) <sup>34</sup>	PpyClO <sub>4</sub> on gold	1.8	0.1	74	1440
Present	PpyNW coated membrane, 4.9 cm <sup>2</sup> , reduced	1.0	0.2	50	480
Present	PpyNW coated membrane, 4.9 cm <sup>2</sup> , not reduced	1.0	0.2	40	480

## 5.7 Polypyrrole-Sodium Alginate Particles

It can be seen from the results obtained for the PpyNW coated membranes that immobilising the PpyNW on a porous support does not improve the removal efficiency of Cr(VI) from solution. It is thought that coating the nanowires on the membrane was restricting the access of the Cr(VI) to the full surface of the polypyrrole, negating the benefits of forming the polypyrrole in a nanosized structure. It was also thought that greater agitation of the Cr(VI) solution would increase the removal efficiency of the PpyNW. Thus a second synthesis approach was developed in which a conducting/biopolymer composite was formed using a soft template mediated chemical polymerisation process. This composite material is composed of polypyrrole and the biopolymer of sodium alginate in the form of particles. Using the particles as standalone Cr(VI) adsorbents will allow for greater agitation of the Cr(VI) solution and improved access for the Cr(VI) to the increased surface area of the polymer.<sup>54</sup> The following sections of this Chapter will investigate the use of polypyrrole-sodium alginate (PpySA) structures as adsorbents for Cr(VI).

As discussed in the Introduction to this Chapter, micro and nanostructures of conducting polymers such as polyaniline and polypyrrole have been investigated as adsorbents for Cr(VI) and in a laboratory setting often exhibit higher removal capacities for Cr(VI) than commercially available adsorbents.<sup>16-20</sup> Polypyrrole coated on organic supports such as cellulose or sawdust have also shown an improvement in removal capacity for Cr(VI) compared to the uncoated substrates.<sup>21, 22</sup> It has been observed that polypyrrole, when used as an adsorbent, will remove Cr(VI) from solution through a process of ion exchange and reduction of the adsorbed Cr(VI) to the less toxic Cr(III).<sup>42, 55</sup> Polypyrrole-sodium alginate composites have been investigated for use in the fields of biomedical materials and devices, and in energy conversion and storage.<sup>23-25</sup> Thus far their ability to remediate Cr(VI) has not been studied, although other conducting-biopolymer such as polyaniline-chitosan composites have been examined and were found to effectively adsorb Cr(III) and Cr(VI) over a 30 minute period.<sup>26</sup> Initial experiments were therefore carried out on the PpySA particles to investigate whether they were suitable for the removal of Cr(VI) from solution. This Chapter will demonstrate the ability of the PpySA particles to remove Cr(VI) from solution. The effect of solution pH, solution temperature and initial concentration of the Cr(VI)

solution on the removal of Cr(VI) will also be discussed. The adsorption kinetics of the removal process are also examined using the Morris-Weber, Lagergren (*pseudo*-first-order) and *pseudo*-second-order equations.

### 5.7.1 Preliminary Investigation of the Cr(VI) Removal by PpySA Particles

The polypyrrole-sodium alginate (PpySA) particles were prepared as described in Chapter 2, Section 2.2.3. Initial experiments were carried out to determine whether the PpySA would remove Cr(VI) from solution. Dried PpySA particles (0.025 g) were added to a 0.10 mM acidified  $\text{Na}_2\text{Cr}_2\text{O}_7 \cdot 2\text{H}_2\text{O}$  solution (50 cm<sup>3</sup>), which was gently agitated in a water bath at  $35 \pm 2$  °C for 2 hours. The concentration of Cr(VI) was monitored using UV-Vis spectroscopy to follow the decrease in the Cr(VI) peak at 350 nm. It can be observed in Figure 5.27 that almost 60 percent of the chromium in solution has been removed after just 2 hours contact with the PpySA particles. This removal efficiency increases to  $82 \pm 0.43$  percent removal of the original Cr(VI) in solution after 24 hours contact with the PpySA particles. Rather than using percentage removal efficiency to examine the efficacy of the PpySA particles, the removal capacity of the PpySA particles was calculated using Equation 5.4.

Equation 5.4

$$\text{Removal Capacity} = \frac{(C_0 - C_t)V}{m}$$

Removal capacity is measured in millimoles of Cr(VI) removed per gram of PpySA,  $m$  is the mass of PpySA in grams,  $V$  is the solution volume in litres, while  $C_0$  and  $C_t$  (mmol/L) are the concentration of Cr(VI) in the original solution, and in solution at time  $t$  respectively.<sup>19</sup> Figure 5.28 displays the plot obtained when this calculation was applied to the data used to produce Figure 5.27.

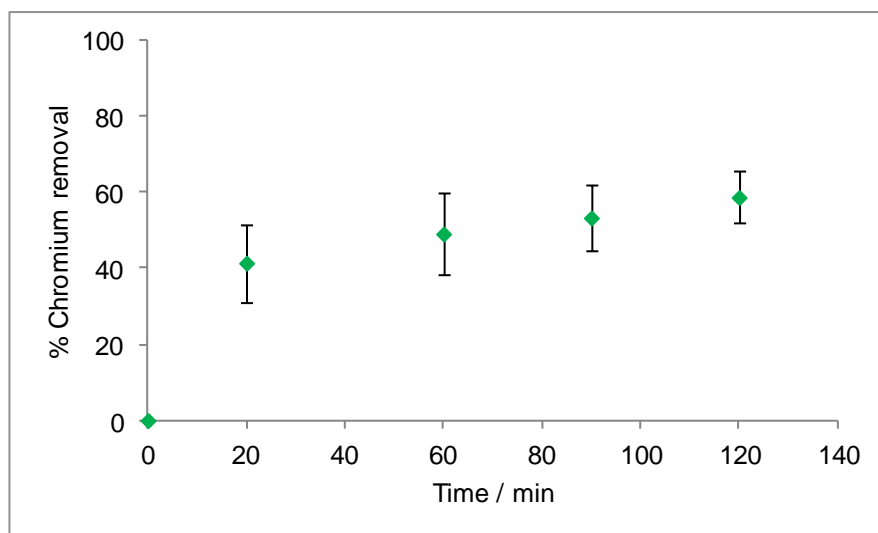


Figure 5.27: Percentage removal of chromium from a 0.10 mM acidified  $\text{Na}_2\text{Cr}_2\text{O}_7 \cdot 2\text{H}_2\text{O}$  solution ( $50 \text{ cm}^3$ ), using PpySA particles (0.025 g). The solution was gently agitated at  $35^\circ\text{C}$  for 2 hours.

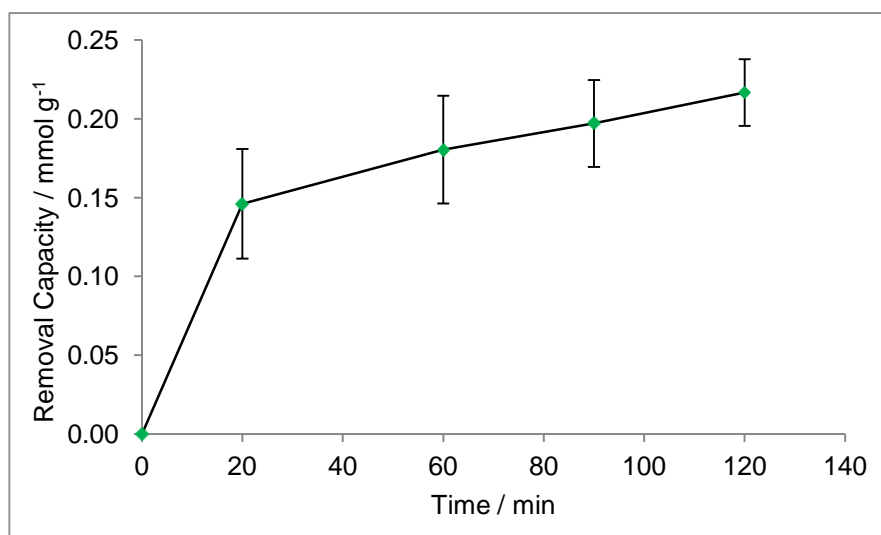
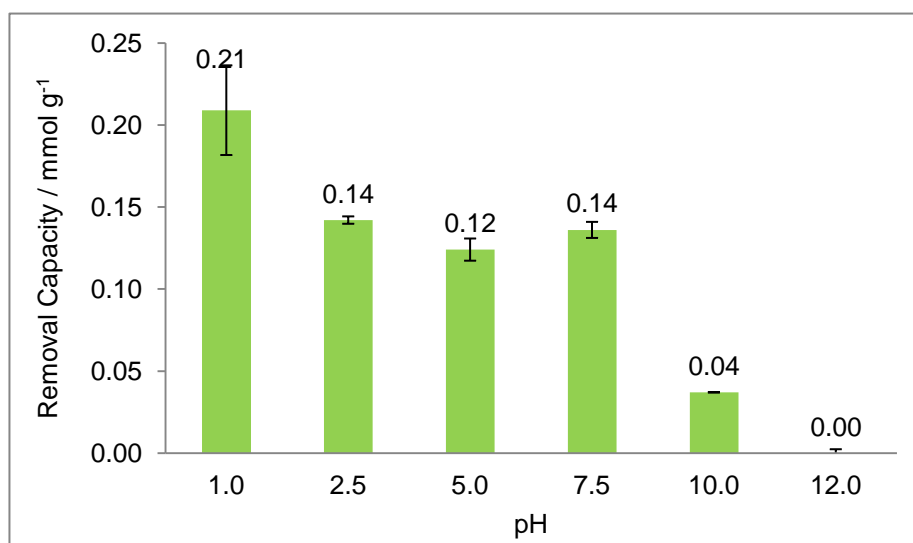


Figure 5.28: The removal capacity of PpySA particles over time of chromium from a 0.10 mM acidified  $\text{Na}_2\text{Cr}_2\text{O}_7 \cdot 2\text{H}_2\text{O}$  solution ( $50 \text{ cm}^3$ ), by PpySA particles. The solution was gently agitated at  $35^\circ\text{C}$  for 2 hours.

### 5.7.2 Effect of Solution pH

The importance of solution pH on the remediation of Cr(VI) by polypyrrole was discussed in Section 5.3.2. The pH value will affect not only the speciation of chromium in the solution,<sup>28</sup> but also the surface charge on the adsorbent.<sup>41</sup> It is known that both polypyrrole and sodium alginate become protonated at low pH values,<sup>39, 56</sup> and this should enhance the electrostatic attractions between the chromium species in solution and the PpySA adsorbent.<sup>55</sup> Solutions of 0.10 mM Na<sub>2</sub>Cr<sub>2</sub>O<sub>7</sub>·2H<sub>2</sub>O were prepared in distilled water, which was adjusted to the required pH using 1.0 M H<sub>2</sub>SO<sub>4</sub> and 1.0 M NaOH. Each solution (50 cm<sup>3</sup>) was placed in a water bath at 35 ± 2 °C to equilibrate before 0.025 g of dried PpySA particles were added. The solutions were subjected to gentle agitation for a period of 2 hours during which aliquots were extracted for UV-Vis spectroscopic examination. Figure 5.29 displays the removal capacity of the PpySA particles calculated after 2 hours contact time with the Cr(VI) solutions (0.10 mM), for each solution pH. It is immediately apparent that a solution pH of 1.0 confers the greatest removal capacity, with a decrease in removal capacity being observed for increasing solution pH values.



**Figure 5.29:** Effect of solution pH on percentage removal capacity. Solution concentration of 0.10 mM (50 cm<sup>3</sup>) in contact with 0.025 g PpySA particles at 35 °C for 2 hours, with agitation, n = 2.

The decrease in removal capacity with the decrease in solution acidity has been previously reported for polypyrrole particles, polypyrrole-Fe<sub>3</sub>O<sub>4</sub> nanocomposites and polypyrrole-polyaniline nanowires in aqueous Cr(VI) solutions.<sup>41, 54, 55</sup> Interestingly, the removal capacity exhibited by the PpySA particles in Cr(VI) solutions at pH 2.5, 5.0

and 7.5 are very similar and so the pH of the solution after each experiment was tested. It was found that while the Cr(VI) solutions at pH 1.0 and 2.5 stay stable, the Cr(VI) solutions at pH 5.0 and 7.5 decrease to pH 3.3 – 3.5. It therefore appears that the PpySA particles may be degrading in the Cr(VI) solutions at mid range pH values, changing the pH of the Cr(VI) solution during the course of the experiment. The decrease in solution pH from pH 7.5 to a pH value of 3.5 changes the speciation of the chromium in solution which may promote the reduction of Cr(VI) to Cr(III). It has also been observed that at lower solution pH values, increased removal capacity can be attributed to the ion exchange of the  $\text{HCrO}_4^-$  ions in solution with the dopant ions in the polypyrrole matrix.<sup>54</sup>

The Cr(VI) solutions which originally had pH values of 10.0 and 12.0 also experienced a decrease in solution pH during exposure to the PpySA particles. The Cr(VI) solution which originally had a pH value of 10.0 experienced a decrease in pH to a value of 7.2. The Cr(VI) solution of pH 12.0 decreased only slightly to a pH value of 11.9. This decrease in pH may affect the speciation of Cr(VI) in solution, but the solutions are still not sufficiently acidic to affect the charge on the PpySA particles. In addition to this, sodium alginate is composed of monomers of mannuronic and guluronic acid which have  $\text{pK}_a$  values of 3.38 and 3.65 respectively.<sup>57</sup> This renders the alginate negatively charged at near neutral pH and above, which will repel the anions in solution. The competition between  $\text{CrO}_4^{2-}$  and  $\text{OH}^-$  ions for the anion exchange sites of the Ppy adsorbent have also been credited with the decrease in removal capacity observed in Cr(VI) solutions at alkaline pH values.<sup>40, 54</sup>

As the PpySA particles demonstrated the greatest removal capacity in Cr(VI) solutions at pH 1.0, all further experiments in this study were carried out using  $\text{Na}_2\text{Cr}_2\text{O}_7 \cdot 2\text{H}_2\text{O}$  solutions at pH 1.0. This result was expected, as at a low pH both elements of the mixed composite are protonated.<sup>39, 56</sup> Moreover, if the removal of the Cr(VI) from solution involved its reduction to Cr(III), this process will become more favourable at lower pH, as discussed in Section 5.3.

### 5.7.3 Effect of Solution Temperature

Solution temperature is another important parameter in adsorption experiments. Previous work has shown that the adsorption of Cr(VI) by polypyrrole nanocomposites,

such as Ppy-polyaniline<sup>54</sup>, Ppy-polyacrylonitrile nanowires<sup>40</sup> or polypyrrole particles grafted in silica gel<sup>58</sup> is endothermic in nature. This implies that the removal capacity of the adsorbent should increase with increasing solution temperature. Therefore, sodium dichromate solutions (0.10 mM, pH 1.0, 50 cm<sup>3</sup>) were allowed to equilibrate in a water bath at 35 °C, 45 °C or 55 °C ( $\pm 2$  °C) before the addition of dried PpySA particles (0.025 g). After the addition of the PpySA particles, the Cr(VI) solutions were gently agitated for 2 hours, during which time aliquots were removed regularly for UV-Vis spectroscopic measurements. The concentration of Cr(VI) in solution was monitored by observing the absorbance of the aliquots at a wavelength of 350 nm. Figure 5.30 shows the removal capacity over time of the PpySA particles in Cr(VI) solutions at each temperature. The PpySA particles have the greatest removal capacity for Cr(VI) at a solution temperature of 35 °C. A lesser removal capacity is observed for PpySA particles at higher solution temperatures of 45 °C and 55 °C, though the removal capacities exhibited by the PpySA particles at higher temperatures are similar. It has been reported that at increased temperatures sodium alginate beads swell, which may allow for leaching of alginate fragments.<sup>56</sup> Thus the decrease in removal capacity exhibited by the PpySA particles at solution temperatures of 45 °C and 55 °C may be due to degradation of the PpySA particles.

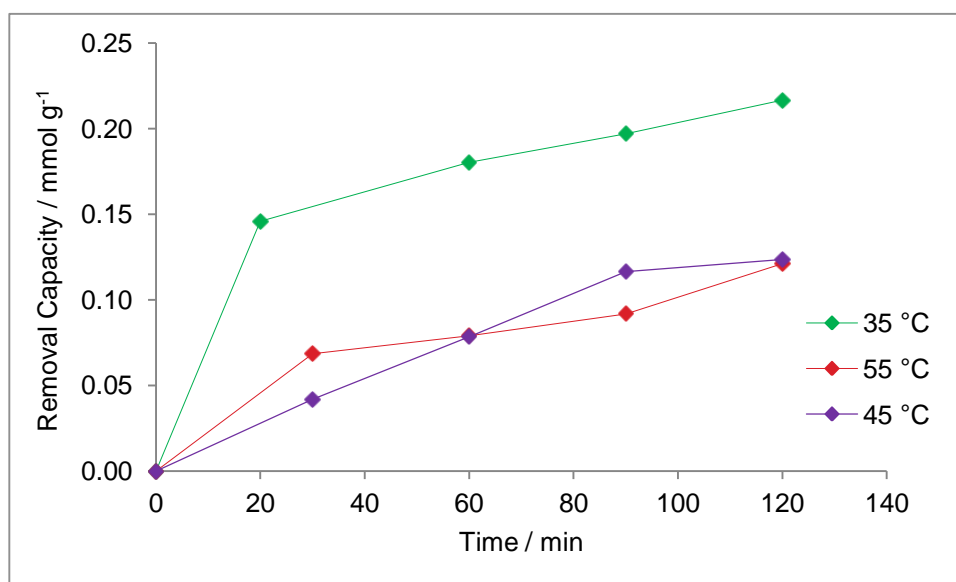


**Figure 5.30:** Effect of solution temperature on removal capacity. Results shown for PpySA particles (0.025 g) in 0.10 mM acidified Na<sub>2</sub>Cr<sub>2</sub>O<sub>7</sub>·2H<sub>2</sub>O solution maintained at various temperatures in a water bath, for 2 hours with agitation. The temperature of the solutions is detailed in the legend.

### 5.7.4 Effect of Initial Cr(VI) Concentration

In order to fully investigate the efficiency of the PpySA particles as an adsorbent for Cr(VI) from solution, it was important to examine the effect of the initial concentration ( $C_0$ ) of Cr(VI) on the adsorption capacity of the PpySA particles. The acidified  $\text{Na}_2\text{Cr}_2\text{O}_7 \cdot 2\text{H}_2\text{O}$  solutions were prepared at initial concentrations of 0.50 mM, 0.10 mM and 0.05 mM. Each solution ( $50 \text{ cm}^3$ ) was placed in a water bath at  $35 \text{ }^\circ\text{C}$  and allowed to equilibrate before the addition of dried PpySA particles (0.025 g). The solutions were gently agitated for 2 hours, during which time aliquots were removed regularly for UV-Vis spectroscopic measurements. The concentration of Cr(VI) in solution was monitored by observing the absorbance of the aliquots at a wavelength of 350 nm. The effect of initial chromium solution concentration on the removal capacity of the PpySA particles is shown in Figure 5.31.

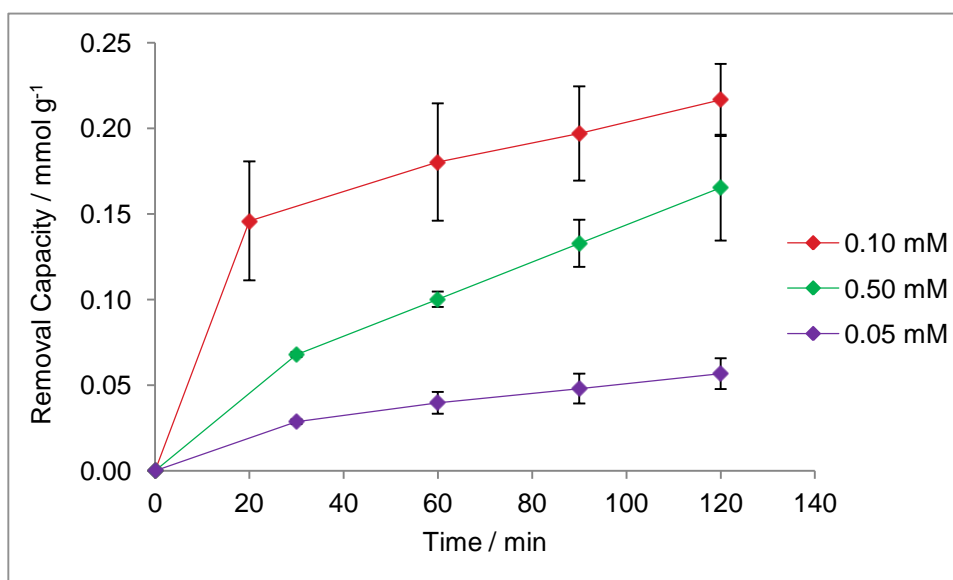


Figure 5.31: Effect of initial Cr(VI) concentration on the removal capacity of PpySA particles. The solutions were kept at a temperature of  $35 \text{ }^\circ\text{C}$ ; with a solution pH 1.0 and solution volume  $50 \text{ cm}^3$ ; in contact with 0.025 g PpySA particles for 2 hours, with agitation.

The initial rapid uptake is due to the large surface area and easily accessible adsorption sites on the PpySA particles. This is followed by a steady increase in removal capacity over time until equilibrium between the PpySA particles and the Cr(VI) solution is approached. As the initial  $\text{Na}_2\text{Cr}_2\text{O}_7 \cdot 2\text{H}_2\text{O}$  concentration increases from 0.05 mM to 0.10 mM, the removal capacity of the PpySA particles also increases. Over the time scale of this experiment, only PpySA particles in a solution with an initial concentration

of 0.05 mM  $\text{Na}_2\text{Cr}_2\text{O}_7 \cdot 2\text{H}_2\text{O}$  reach this equilibrium and display an equilibrium adsorption capacity of 0.06 mmol Cr(VI) per gram of PpySA.

Interestingly, PpySA particles exposed to a sodium dichromate solution with an initial concentration of 0.50 mM exhibit a lower removal capacity than that seen for PpySA particles in 0.10 mM sodium dichromate. This may be due to saturation of the adsorption sites upon first exposure to the 0.50 mM sodium dichromate solution. The PpySA particles in a solution of 0.50 mM Cr(VI) continue to display increasing removal capacities, with no equilibrium between the adsorbent and the Cr(VI) achieved during the 2 hour experiment duration. The rapid initial increase in removal capacity, which increases with increasing contact time, is widely observed for Ppy particles and nanocomposites.<sup>40, 42, 55</sup> In order to further understand the adsorption performance of the PpySA particles in Cr(VI) solutions, kinetic models were employed and are discussed in the next section.

### 5.7.5 Adsorption Kinetics

A total of three kinetic models were employed to scrutinise the kinetic mechanism of Cr(VI) adsorption by the PpySA particles. These were the Lagergren or *pseudo*-first-order (Equation 5.5), *pseudo*-second-order (Equation 5.6) and the Weber-Morris or intraparticle diffusion model (Equation 5.7).<sup>54, 59</sup> These models are linearly expressed as follows:

$$\text{Equation 5.5} \quad \log(q_e - q_t) = \log q_e - \frac{k_1}{2.303} t$$

$$\text{Equation 5.6} \quad \frac{t}{q_t} = \frac{1}{k_2 q_e^2} + \frac{1}{q_e} t$$

$$\text{Equation 5.7} \quad q_t = k_{ip} t^{1/2} + C$$

where  $q_e$  and  $q_t$  are removal capacity at equilibrium and at time  $t$  respectively,  $k_1$  ( $\text{min}^{-1}$ ) is the *pseudo*-first-order rate constant,  $k_2$  ( $\text{g mmol}^{-1} \text{min}^{-1}$ ) is the *pseudo*-second-order rate constant,  $k_{ip}$  is the intraparticle diffusion rate constant ( $\text{mmol g}^{-1} \text{min}^{-1/2}$ ) and  $C$  is the intercept which relates to the thickness of the boundary layer. Table 5.13 details the

kinetic parameters calculated from the plots shown in Figure 5.32. Figure 5.32 depicts the plots of the linearised forms of the three models, for PpySA particles (0.025 g) in 0.05 mM sodium dichromate (pH 1.0, 50 cm<sup>3</sup>) at various temperatures as this is the only initial concentration of sodium dichromate in which an equilibrium was achieved between the adsorbent and the Cr(VI) during the 2 hour experiment duration.

Table 5.13 details the kinetic parameters for Cr(VI) adsorption on PpySA particles in an initial sodium dichromate concentration of 0.05 mM at different solution temperatures. The validity of each model can be ascertained from the correlation coefficient,  $R^2$ , with the magnitude of the correlation coefficient indicating the suitability of the model. It can be seen from the results listed in Table 5.13 that both the *pseudo*-first-order model and *pseudo*-second-order model describe the kinetics for the adsorption process of Cr(VI) at PpySA particles. The calculated values for  $q_e$  for the *pseudo*-second-order model however, are in good agreement with experimentally obtained values of  $q_e$ . This suggests that the *pseudo*-second-order model is the more appropriate kinetic model for the adsorption process of Cr(VI) at PpySA particles. This demonstrates that the primary rate controlling step is the chemical sorption between the Cr(VI) and PpySA, influenced by the intraparticle diffusion layer.<sup>41, 59, 60</sup>

The Morris-Weber or intraparticle diffusion model further elucidates the rate-controlling step. The correlation coefficient  $R^2$  is close to unity for the modelled data recorded for solutions at 35 °C, whereas at higher solution temperatures there appears to be two linear regions in the plot. The initial linear region observed when modelling the data obtained at higher solution temperatures may be due to intraparticle pore diffusion, which is slow due to the possible leaching of alginate fragments from the PpySA particles. The second linear region may be due to the chemical reaction between the Cr(VI) and the PpySA particles.<sup>59</sup> The dual nature of the adsorption process is supported by the fact that the straight line graphs of the Morris-Weber model do not pass through the origin which indicates that intraparticle diffusion is not the only rate controlling step.

It must be noted that polypyrrole, when used as an adsorbent, will remove Cr(VI) from solution through a process of ion exchange or electrostatic attraction and reduction of the adsorbed Cr(VI) to the less toxic Cr(III).<sup>42, 55</sup> This subsequent reduction of Cr(VI) to Cr(III) which is then released back into solution may make the modelling of the

adsorption kinetic models inaccurate. It is particularly difficult to model the adsorption of Cr(VI) with simple kinetics models as the effects of ion transport and the chemical reaction between the Cr(VI) and the PpySA particles may be experimentally inseparable.<sup>60</sup> The results observed here seem to support this. The initial adsorption process of Cr(VI) by PpySA particles most closely fits the *pseudo*-second-order model which indicates that the primary rate controlling step may be the chemisorptions of the Cr(VI). The Morris-Weber model further indicates that intraparticle diffusion may also play a role.

**Table 5.13: Kinetics parameters for Cr(VI) adsorption onto PpySA particles (0.025 g) from a solution of 0.05 mM sodium dichromate (pH 1.0, 50 cm<sup>3</sup>).**

		<u>Pseudo-first-order-model</u>		
Solution Temperature	$q_{e,exp}$ (mmol g <sup>-1</sup> )	R <sup>2</sup>	$k_1$ (min <sup>-1</sup> )	$q_e$ (mmol g <sup>-1</sup> )
35 °C	0.06	0.9692	0.0193	19.93
45 °C	0.05	0.9915	0.0175	19.67
55 °C	0.11	0.9892	0.0364	8.15
		<u>Pseudo-second-order model</u>		
Solution Temperature	$q_{e,exp}$ (mmol g <sup>-1</sup> )	R <sup>2</sup>	$k_2$ (g mmol min <sup>-1</sup> )	$q_e$ (mmol g <sup>-1</sup> )
35 °C	0.06	0.9580	0.38	0.07
45 °C	0.05	0.9315	0.31	0.07
55 °C	0.11	0.9660	0.05	0.20
		<u>Intraparticle Diffusion Model</u>		
Solution Temperature	$q_{e,exp}$ (mmol g <sup>-1</sup> )	R <sup>2</sup>	$k_{ip}$ (mmol g <sup>-1</sup> min <sup>-1/2</sup> )	$C$
35 °C	0.06	0.9824	0.0043	0.008
45 °C	0.05	0.8638	0.0047	0.003
55 °C	0.11	0.9738	0.0118	-0.018

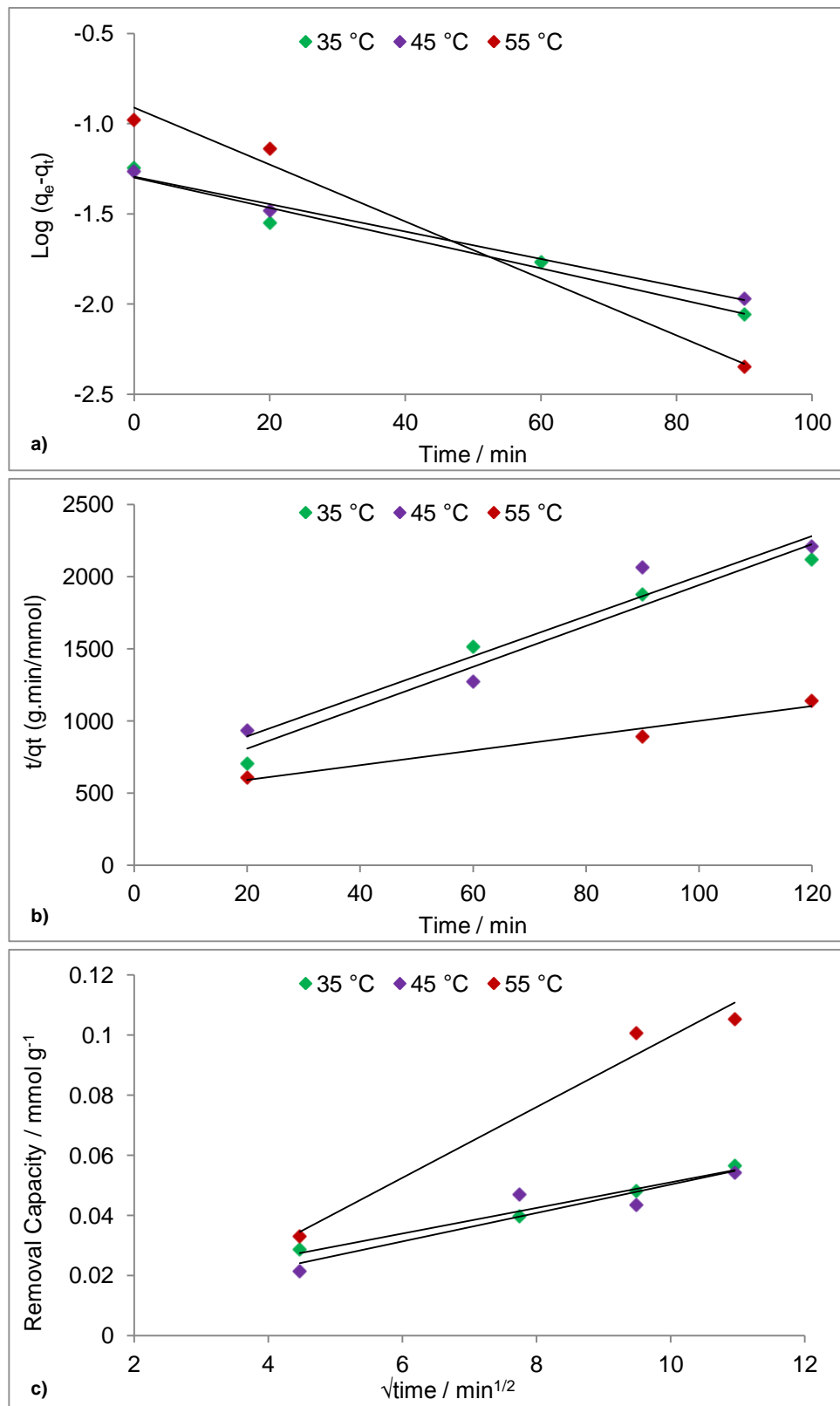


Figure 5.32: a) *Pseudo-first-order* kinetic model, b) *pseudo-second-order* kinetic model and c) intraparticle diffusion model for adsorption of Cr(VI) on PpySA particles. Initial solution concentration was 0.05 mM; solution pH 1.0.

## 5.8 Summary of PpySA Particles

This preliminary screening of polypyrrole-sodium alginate particles was carried out with a view to developing an adsorbent for Cr(VI) remediation. It was observed that the most efficient removal of Cr(VI) occurred at a solution pH of 1.0. While it has been reported that the protonation of both polypyrrole and sodium alginate at low pH values may enhance the electrostatic attractions between the chromium species in solution and the PpySA adsorbent,<sup>55</sup> at a pH of 1.0 it is very possible that adsorption through ion exchange is not the only mechanism by which Cr(VI) remediation occurs.<sup>42, 55</sup> As discussed in Section 5.3, spontaneous electron transfer between the conducting polymer and the Cr(VI) can result in the reduction of Cr(VI) to Cr(III)<sup>14, 54</sup> which at very low pH may be repelled into solution due to electrostatic repulsion by the positive charges on the Ppy backbone. Preliminary experiments carried out in which the solutions exposed to PpySA particles were treated with 1,5-diphenylcarbazide (as described in Section 2.2.8.2 ii), indicate that  $67 \pm 2$  percent of Cr(VI) is reduced to Cr(III) which is released into solution. These initial tests also show that  $18 \pm 9$  percent of chromium in solution remains adsorbed on the particles. The particles were exposed to 0.10 mM  $\text{Na}_2\text{Cr}_2\text{O}_7 \cdot 2\text{H}_2\text{O}$  (pH 1.0), at 35 °C for 2 hours with gentle agitation.

While PpySA particles exposed to a sodium dichromate solution at pH 1.0 exhibit the greatest removal capacity, Cr(VI) remediation was also observed in solutions at higher pH. This suggests that adsorption does play a role and therefore three kinetics models were employed to investigate the adsorption aspect of the remediation process. The adsorption process of Cr(VI) by PpySA particles appears to fit most closely to the *pseudo*-second-order kinetic model which suggests that the primary rate controlling step in the adsorption process may be the chemisorption of the Cr(VI). The Morris-Weber model further indicates that intraparticle diffusion may play a role in this initial step of the Cr(VI) remediation by PpySA particles.

Table 5.14 summarises a number of studies in which nanoscale polypyrrole materials were used for the adsorption of Cr(VI) from solution. Unfortunately, it is difficult to make a direct comparison between the current study of PpySA particles and the reported adsorption capacities because, at a solution pH of 1.0, adsorption does not appear to be the sole mechanism by which Cr(VI) is removed by the PpySA particles. The way in which the Cr(VI) solution is agitated while in contact with the polypyrrole materials

also varies. Many literature studies use a stirred batch method, in which a magnetic stirrer is used to agitate the Cr(VI) solution,<sup>20, 42, 54</sup> while others employ a fixed bed column, packed with the polypyrrole materials.<sup>18, 21</sup> In this study, the Cr(VI) solutions were only gently agitated using a shaker, and so the full surface area of the particles were not exposed to the Cr(VI) solution. It is believed that these low levels of agitation are the main limiting factor in PpySA particle system and that this hinders access of the Cr(VI) to the full extent of the polymer surface area. Thus, a more extensive investigation is required, not only to establish the optimum agitation, but also to determine the adsorption properties of the PpySA particles at higher solution pH, at which it is expected that adsorption will dominate.

**Table 5.14: Comparison of adsorption capacity of PpySA particles for Cr(VI) removed from solution, to the values presented in various studies reported in the literature.**

Polymer	Optimum pH	Solution temperature / °C	Initial Cr(VI) concentration / mM	Adsorbent (g) / Solution volume (ml)	$Q_e$ / mmol g <sup>-1</sup>
Ppy nanoparticles <sup>20</sup>	5	Room temp.	3.4	0.01 g / 20 ml	1.14
Ppy nanoclusters <sup>20</sup>	5	Room temp.	3.4	0.01 g / 20 ml	3.47
Ppy nanotubes <sup>42</sup>	3	Not specified	1.95	0.003 g / 20 ml	8.32
Ppy/polyaniline nanowires <sup>54</sup>	2	25	1.92	0.05 / 50 ml	4.36
Ppy/Fe <sub>3</sub> O <sub>4</sub> nanocomposite <sup>18</sup>	2	Not specified	1.92	2 g / 3 ml	3.26
Ppy/sawdust <sup>21</sup>	5.0	Room temp.	0.96	1g / 25 ml	0.07
Ppy/SA particles	1.0	35	0.05	0.025 g / 50 ml	0.06

### 5.9 References

1. C. Fabiani, F. Ruscio, M. Spadoni and M. Pizzichini, *Desalination*, 1997, **108**, 183-191.
2. Y. Xie, X. Li and F. Li, *Zhongguo Huanjing Kexue*, 2009, **29**, 1260-1265.
3. G. Mahajan and D. Sud, *Applied Water Science*, 2012, **2**, 299-308.
4. Y. S. Dzyazko, A. Mahmoud, F. Lopicque and V. N. Belyakov, *Journal of Applied Electrochemistry*, 2007, **37**, 209-217.
5. M. S. Bhatti, A. S. Reddy and A. K. Thukral, *Journal of Hazardous Materials*, 2009, **172**, 839-846.
6. Y.-X. Liu, D.-X. Yuan, J.-M. Yan, Q.-L. Li and T. Ouyang, *Journal of Hazardous Materials*, 2011, **186**, 473-480.
7. A. Olad and R. Nabavi, *Journal of Hazardous Materials*, 2007, **147**, 845-851.
8. F. Rodriguez-Valadez, C. Ortiz-Exiga, J. G. Ibanez, A. Alatorre-Ordaz and S. Gutierrez-Granados, *Environmental Science and Technology*, 2005, **39**, 1875-1879.
9. C. Wei, S. German, S. Basak and K. Rajeshwar, *Journal of the Electrochemical Society*, 1993, **140**, L60-L62.
10. W. A. Wampler, S. Basak and K. Rajeshwar, *Carbon*, 1996, **34**, 747-755.
11. R. Senthurchelvan, Y. Wang, S. Basak and K. Rajeshwar, *Journal of the Electrochemical Society*, 1996, **143**, 44-51.
12. S. T. Earley, B. E. Alcock, J. P. Lowry and C. B. Breslin, *Journal of Applied Electrochemistry*, 2009, **39**, 1251-1257.
13. K. G. Conroy and C. B. Breslin, *Journal of Applied Electrochemistry*, 2004, **34**, 191-195.
14. M. A. Alatorre, S. Gutierrez, U. Paramo and J. G. Ibanez, *Journal of Applied Electrochemistry*, 1998, **28**, 551-557.
15. F. J. Rodriguez, L. A. de la Rosa-Garcia, A. Alatorre, J. Ibanez, L. Godinez, S. Gutierrez and P. Herrasti, *Progress in Organic Coatings*, 2007, **60**, 297-302.
16. K. Roy, P. Mondal, S. P. Bayen and P. Chowdhury, *Journal of Macromolecular Science, Part A: Pure and Applied Chemistry*, 2012, **49**, 931-935.

17. Y. Wang, B. Zou, T. Gao, X. Wu, S. Lou and S. Zhou, *Journal of Materials Chemistry*, 2012, **22**, 9034-9040.
18. M. Bhaumik, K. Setshedi, A. Maity and M. S. Onyango, *Separation and Purification Technology*, 2013, **110**, 11-19.
19. X. Guo, G. T. Fei, H. Su and L. D. Zhang, *Journal of Physical Chemistry C*, 2011, **115**, 1608-1613.
20. T. Yao, T. Cui, J. Wu, Q. Chen, S. Lu and K. Sun, *Polymer Chemistry*, 2011, **2**, 2893-2899.
21. R. Ansari and N. Khoshbakht Fahim, *Reactive and Functional Polymers*, 2007, **67**, 367-374.
22. Y. Lei, X. Qian, J. Shen and X. An, *Industrial & Engineering Chemistry Research*, 2012, **51**, 10408-10415.
23. J. Foroughi, G. M. Spinks and G. G. Wallace, *Journal of Materials Chemistry*, 2011, **21**, 6421-6426.
24. C. Yore and T. W. Hanks, *Extrusion of Alginate and Electronically Conducting Polymers: Methods for Preparing Nanostructured Fibers for Bionic Devices*, 2009.
25. S. Sahoo, S. Dhibar and C. K. Das, *eXPRESS Polymer Letters*, 2012, **6**, 965-974.
26. A. G. Yavuz, E. D. Atalay, A. Uygun and F. Gode, *Polymer Preprints*, 2010, **51**, 474-475.
27. A. Olad and A. F. Farshi, *Desalination and Water Treatment*, 2013, Ahead of Print.
28. J. Kotas and Z. Stasicka, *Environmental Pollution*, 2000, **107**, 263-283.
29. Y. Tian, L. Huang, X. Zhou and C. Wu, *Journal of Hazardous Materials*, 2012, **225-226**, 15-20.
30. S. A. Durban and D. J. Brown, *Journal of Physical Chemistry*, 1939, **43**, 491-493.
31. J. W. Ball and D. K. Nordstrom, *Journal of Chemical and Engineering Data*, 1998, **43**, 895-918.
32. R. K. Tandon, P. T. Crisp, J. Ellis and R. S. Baker, *Talanta*, 1984, **31**, 227-228.
33. F. J. Rodriguez, d. I. R. L. A. Garcia, A. Alatorre, J. Ibanez, L. Godinez, S. Gutierrez and P. Herrasti, *Progress in Organic Coatings*, 2007, **60**, 297-302.

34. K. K. Krishnani, S. Srinives, B. C. Mohapatra, V. M. Boddu, J. Hao, X. Meng and A. Mulchandani, *Journal of Hazardous Materials*, 2013, **252–253**, 99-106.
35. R. Bai and X. Zhang, *Journal of Colloid and Interface Science*, 2001, **243**, 52-60.
36. C. Weidlich, K. M. Mangold and K. Jüttner, *Electrochimica Acta*, 2005, **50**, 1547-1552.
37. F. J. Rodriguez, S. Gutierrez, J. G. Ibanez, J. L. Bravo and N. Batina, *Environmental Science and Technology*, 2000, **34**, 2018-2023.
38. L. A. M. Ruotolo, D. S. Santos-Junior and J. C. Gublin, *Water Research*, 2006, **40**, 1555-1560.
39. R. Qian, Q. Pei and Y. Li, *Synthetic Metals*, 1993, **61**, 275-278.
40. J. Wang, K. Pan, Q. He and B. Cao, *Journal of Hazardous Materials*, 2013, **244-245**, 121-129.
41. R. Katal, M. Ghiass and H. Esfandian, *Journal of Vinyl and Additive Technology*, 2011, 222-230.
42. S. Li, X. Lu, X. Li, Y. Xue, C. Zhang, J. Lei and C. Wang, *Journal of Colloid and Interface Science*, 2012, **378**, 30-35.
43. A. Nasalska and M. Skompska, *Journal of Applied Electrochemistry*, 2003, **33**, 113-119.
44. I. Rodriguez, B. R. Scharifker and J. Mostany, *Journal of Electroanalytical Chemistry*, 2000, **491**, 117-125.
45. E. P. Agency, *US EPA Method 7196A*, 1992.
46. R. T. Pflaum and L. C. Howick, *Journal of the American Chemical Society*, 1956, **78**, 4862-4866.
47. L. A. M. Ruotolo, A. A. Liao and J. C. Gubulin, *Journal of Applied Electrochemistry*, 2004, **34**, 1259-1263.
48. M. Ghorbani, H. Esfandian, N. Taghipour and R. Katal, *Desalination*, 2010, **263**, 279-284.
49. Y. Lei, X. Qian, J. Shen and X. An, *Industrial & Engineering Chemistry Research*, 2012, **51**, 10408-10415.
50. M. Choi and J. Jang, *Journal of Colloid and Interface Science*, 2008, **325**, 287-289.

51. G.-R. Xu, J.-N. Wang and C.-J. Li, *Chemical Engineering Journal*, 2012, **198-199**, 310-317.
52. I. Bodik, A. Blst'akova, L. Dancova and S. Sedlacek, *Polish Journal of Environmental Studies*, 2009, **18**, 331-340.
53. Q. Pei and R. Qian, *Synthetic Metals*, 1991, **45**, 35-48.
54. M. Bhaumik, A. Maity, V. V. Srinivasu and M. S. Onyango, *Chemical Engineering Journal*, 2012, **181-182**, 323-333.
55. M. Bhaumik, A. Maity, V. V. Srinivasu and M. S. Onyango, *Journal of Hazardous Materials*, 2011, **190**, 381-390.
56. K. I. Draget, G. Skjaak-Braek, B. E. Christensen, O. Gaaseroed and O. Smidsroed, *Carbohydrate Polymers*, 1996, **29**, 209-215.
57. K. A. J. De and M. Elimelech, *Macromolecules*, 2006, **39**, 6558-6564.
58. P. Mondal, K. Roy, S. P. Bayen and P. Chowdhury, *Talanta*, 2011, **83**, 1482-1486.
59. Z. Wu, S. Li, J. Wan and Y. Wang, *Journal of Molecular Liquids*, 2012, **170**, 25-29.
60. Y. S. Ho and G. McKay, *Process Biochemistry*, 1999, **34**, 451-465.

## Chapter 6

---

### Conclusions

---

## 6.1 Conclusions

The work presented in this thesis looked at the development of a number of polypyrrole particles and nanomaterials for the removal of metals from water. Polypyrrole (Ppy) has the potential to act as an electrochemically switchable ion exchange material as well as an adsorbent. The removal of chromium in particular was investigated as a model environmental pollutant, as its removal from water samples can be monitored with UV-Vis spectroscopy.

In Chapter 3, the growth of Ppy particles and nanowires, via chemical and electrochemical methods, was discussed. Three distinct approaches were presented. The first approach involved the chemical oxidation of pyrrole, on a membrane support, for the formation of a polypyrrole nanowire network. It was found that a combination of two chemical oxidation methods formed a mesh of nanowires across the surface of the polyamide membrane support, with diameters ranging from 100 nm to 400 nm. Unfortunately, methyl orange, which was utilised as a reactive self-degraded template, was found to leach from the nanowire structures and so this method of nanowire formation was not pursued.

The second approach described in Chapter 3 employed the biopolymer sodium alginate as a soft-template for the formation of Ppy-sodium alginate particles. The particles formed were spherical in shape, with a diameter of  $225 \pm 15$  nm. This was established using SEM analysis. The particles were further characterised using Raman and FTIR spectroscopy. Similar spectra to those reported in literature were observed, with characteristic Ppy bands evident at  $1559\text{ cm}^{-1}$ ,  $1470\text{ cm}^{-1}$ ,  $1199\text{ cm}^{-1}$  and  $1043\text{ cm}^{-1}$  in the FTIR spectra. The incorporation of alginate into the particles was confirmed by the presence of a peak at  $1716\text{ cm}^{-1}$ , which is attributed to the  $-\text{COO}$  stretch in alginate.<sup>1</sup> In the Raman spectra, two bands at  $665\text{ cm}^{-1}$  and  $881\text{ cm}^{-1}$  further confirmed this. These bands have been ascribed to the symmetric C-O-C glycosidic linkage and to symmetric C-O-C 1,4-glycosidic linkage in the alginate biopolymer.<sup>2</sup>

Electrochemical polymerisation was the main method investigated in this work, for the formation of polypyrrole nanowires (PpyNW). This was the third approach reported in Chapter 3. The electrochemical deposition of PpyNW from a solution of phosphate and

the dopant perchlorate has been reported by a number of research groups.<sup>3-6</sup> In order to investigate the influence of changing the applied potential, polymerisation duration and the electrolyte system, the deposition of PpyNW was monitored using the current density-time ( $j$ - $t$ ) plots, generated during the polymerisation, and SEM. SEM analysis indicated that PpyNW formation occurred at applied potentials of 0.75 V vs. SCE and 0.80 V vs. SCE. The PpyNW formed at 0.80 V vs. SCE were most clearly defined and uniform. The  $j$ - $t$  plot recorded for this polymerisation also exhibited the greatest maximum current density, compared to the  $j$ - $t$  plots recorded at other applied potentials. An applied potential of 0.80 V vs. SCE was thus used for the remainder of the research.

In order to examine the effect of polymerisation duration on the PpyNW morphology, a number of experiments were carried out where PpyNW were grown, at 0.80 V vs. SCE, to different charge densities. SEM analysis showed the initial nucleation of the polymer occurred before a charge density of  $10 \text{ mC cm}^{-2}$  was achieved. As the charge density reached  $30 \text{ mC cm}^{-2}$ , initial nanowire nodules were apparent. Clearly defined PpyNW were evident as the polymerisation was continued until charge densities of  $300 \text{ mC cm}^{-2}$  and  $400 \text{ mC cm}^{-2}$  were attained. When polymerisation was carried out for extended periods of time, small nodules were observed to form on the PpyNW. This branching was not further investigated, as homogeneous, defined PpyNW were favoured. Further investigation of this branching could show an increased surface area, and may result in higher conductivity.<sup>7</sup>

These PpyNW were polymerised from a solution containing disodium hydrogen phosphate (bulk electrolyte) and lithium perchlorate (seed electrolyte). The influence of these electrolyte components on PpyNW formation was investigated by altering their concentration in solution. No polymer formation was discernible for polymerisations carried out in a solution containing only  $\text{HPO}_4^{2-}$  and so it was concluded that that  $\text{HPO}_4^{2-}$  alone does not efficiently support the electropolymerisation of polypyrrole. Polypyrrole in the typical cauliflower morphology was evident when the polymerisation was carried out in a solution containing a high concentration of  $\text{LiClO}_4^-$  and no phosphate, with thick Ppy nodules visible on the surface. While nanowires were formed from solutions containing  $\text{HPO}_4^{2-}$  and medium and low concentrations of  $\text{ClO}_4^-$ , the PpyNW formed from a solution with low  $\text{ClO}_4^-$  concentrations were clearly defined, and a “hills and valleys” morphology<sup>8</sup> was less pronounced. This morphology was thought

to occur as the polymer lost adherence to the electrode surface. It was therefore apparent that both phosphate and a low concentration of perchlorate were necessary for the formation of adherent PpyNW films. This electrolyte system was used for the formation of PpyNW throughout the remainder of the research, and PpyNW were also successfully polymerised at the surface of polyamide membranes.

In order to further investigate the effect of the seed electrolyte on PpyNW morphology, polymerisations were carried out in electrolytes containing lithium chloride, lithium sulfate, lithium tetrafluoroborate, lithium bis(trifluoromethane)sulfonimide (LiTFSI), sodium perchlorate or potassium perchlorate as substitutes for lithium perchlorate. Changing the seed electrolyte anion resulted in differing  $j-t$  plots and nanowires of varying diameter, length and base layer thickness were observed with SEM analysis. A pronounced “hills and valleys” morphology was evident for films formed in the presence of  $\text{LiBF}_4$ , while solutions containing LiTFSI formed very long PpyNW with the thinnest polymer base layer. Changing the seed electrolyte cation also produced differing  $j-t$  plots and although nanowires were again successfully formed from each solution, the morphologies varied. PpyNW formed in the presence of  $\text{KClO}_4$  were long and intertwined. PpyNW formed in the presence of  $\text{NaClO}_4$  exhibited a marked “hills and valleys” morphology, with very long nanowires apparent in the “valleys” and very short nanowires formed on the “hills”. This was attributed to the loss of adherence of the polymer during the polymerisation process. No correlation between the ionic properties of the various salts and the morphology of the polymers formed could be determined.

Attempts were also made to replace the seed electrolyte with the large bulky anion *p*-sulfonatocalix[4]arene. It was hoped that PpyNW with cation exchange properties would form, however this was not the case. No polymer formation occurred and so an alternative approach was followed. PpyNW were polymerised from a solution of pyrrole,  $\text{HPO}_4^{2-}$  and  $\text{ClO}_4^-$  and then a layer of polypyrrole doped with C4S (PpyC4S) was polymerised as a coating on the nanowires. This was also carried out to form PpyNW coated with a layer of polypyrrole–polystyrene sulfonate (PpyPSS). EDX analysis was carried out and confirmed the incorporation of the C4S and PSS into the polymer coating. SEM analysis showed that the average diameter of the PpyNW

increased when coated, and that the coated PpyNW had a rougher surface morphology than the uncoated PpyNW.

FTIR and Raman spectroscopy, and water contact angle measurements were used to compare the PpyNW; PpyNW coated with PpyC4S and PpyPSS; and PpyCl which forms polypyrrole in the bulk morphology. The spectra obtained indicated that PpyNW may be less conducting than bulk PpyCl films due to the shorter conjugation lengths in the Ppy chains. Coating the PpyNW with PpyC4S and PpyPSS films appeared to improve the conjugation in the polymer film. Water contact angle measurements indicated that PpyNW films were more hydrophilic than PpyCl films. A coating of PpyC4S on the nanowires caused the material to become less hydrophilic, while coating the nanowires with a PpyPSS film caused the PpyNW film to become superhydrophilic. To the best of our knowledge, this is the first example of the template-less electrochemical deposition of nanowires containing an immobile dopant. It was a facile method and could be used in a range of systems in the future.

The ion exchange properties of the PpyC4S and PpyPSS films were investigated using EQCM, the results of which were reported in Chapter 4. The influence of various parameters on the growth of the films was studied, including the applied potential and dopant concentration. Theoretical doping levels and film thicknesses were also calculated but were taken as indicative rather than definitive, as discrepancies have been reported when using EQCM data for these calculations.<sup>9, 10</sup> Initial experiments were carried out by electrochemically cycling the films in 0.10 M NaCl. In general it was found that the PpyPSS films behaved as cation exchange materials, while the PpyC4S films exhibited mixed ion exchange behaviour. Increasing the dopant concentration for polymerisation of the PpyC4S films resulted in an increase in the calculated doping level, and films formed with the highest concentration of C4S dopant were found to exhibit more cation exchange dominated behaviours. The scan rate at which the PpyC4S film was cycled in NaCl also affected the ion exchange properties of the film, with cation exchange most evident at high scan rates, and anion exchange dominating at low scan rates. A study was carried out to investigate the role of the electrolyte salt on the ion exchange properties of the PpyC4S film and it was clear that both the nature of the anion and cation in solution was significant. The PpyC4S films were cycled in 0.10 M aqueous solutions of CsCl, CaCl<sub>2</sub>, MgCl<sub>2</sub>, NiCl<sub>3</sub>, CrCl<sub>3</sub>, NaCl, NaNO<sub>3</sub> or NaClO<sub>4</sub>.

While mixed cation-anion exchange was evident for films cycled in NaCl, CaCl<sub>2</sub>, and MgCl<sub>2</sub>, cation exchange predominated for films cycled in CsCl. This was attributed to the greater mobility of Cs<sup>+</sup> ions as they are only weakly hydrated in comparison to the other ions studied.<sup>11, 12</sup> Unfortunately, no evidence for complexation of the metal ions by C4S was observed. The transition metal chlorides presented different results in which the mass uptaken by the film was retained, suggesting that the Ni<sup>2+</sup> and Cr<sup>3+</sup> ions were becoming trapped in the film. It was suggested that Ni<sup>2+</sup> was reduced to Ni<sup>0</sup> and deposited as metallic nickel, while Cr<sup>3+</sup> may have a strong electrostatic interaction with the sulfonated dopant. The electrolyte anion was also investigated and it was observed that the response of PpyC4S films cycled in NaCl was cation dominated, in NaNO<sub>3</sub> mixed ion exchange was apparent, whereas the response for PpyC4S cycled in NaClO<sub>4</sub> was anion dominated. This was also attributed to the mobility of the studied anions and their different ionic radii.<sup>13, 14</sup> Analysis of the data using Faraday's Law of Electrolysis showed that the exchange behaviour of the PpyC4S was complex, involving solvent and ion pair movement into and out of the polymer film. A preliminary investigation of the potential window indicated that if the PpyC4S films were cycled between 0.30 V and 0.85 V vs. SCE, mixed anion exchange was apparent at both low and high scan rates.

Chromium remediation was the focus of Chapter 5, in which the PpyNW and the PpySA particles were employed for the removal of hexavalent chromium from solution. The removal mechanism of Cr(VI) by PpyNW was found to be most effective at pH 1.0 and to consist of two steps. Protonation of the nitrogen atoms on the polypyrrole backbone attracted the Cr(VI) anions which exist in an acidic solution as HCrO<sub>4</sub><sup>-</sup> anions. Open circuit potential measurements showed that the strongly oxidising Cr(VI) solution oxidised the PpyNW, and was thus reduced itself to Cr(III). Colorimetric testing of the solution indicated that the majority of Cr(III) was repelled back into solution, while EDX analysis revealed that some chromium was retained by the PpyNW film. A pre-reduction step is employed by the majority of groups using electrochemically polymerised polypyrrole for the remediation of Cr(VI).<sup>15-21</sup> Thus its effect on the removal efficiency of the PpyNW was investigated. It was found that a pre-reduced PpyNW film removed Cr(VI) faster over the first hour of the immersion, but for the rest of the experimental duration, little difference was observed between reduced and non-reduced PpyNW films. An advantage of the pre-reduction step was its use in the regeneration of the PpyNW films. All PpyNW films lose efficiency with

repeated immersions, but the reduced PpyNW films were more effective than non-reduced PpyNW after immersion durations of 5 hours. PpyNW coated on polyamide films exhibited similar results. The PpyNW prepared in this study were not as efficient as the polypyrrole based remediation methods reported in literature. However, it was proposed that a greater degree of solution agitation would increase the removal efficacy of the PpyNW films.

The polypyrrole-sodium alginate particles (PpySA) were investigated as an adsorbent for Cr(VI) remediation. The most efficient removal of Cr(VI) occurred at a solution pH of 1.0 however, Cr(VI) remediation was also observed in solutions at higher pH. The removal method was not fully elucidated though it was proposed that adsorption through ion exchange may be accompanied by the reduction of Cr(VI) to Cr(III). Preliminary colorimetric tests indicated that  $67 \pm 2$  percent of Cr(VI) was reduced to Cr(III) and released back into solution. These initial tests also showed that chromium was retained by the particles. Three kinetics models were employed to investigate the adsorption aspect of the removal process. The adsorption process of Cr(VI) by PpySA particles appeared to fit most closely to the *pseudo*-second-order kinetic model which suggested that the primary rate controlling step in the adsorption process may be the chemisorption of the Cr(VI). The Morris-Weber model further indicated that intraparticle diffusion may play a role in the adsorption of the Cr(VI). AS with the PpyNW films, it is believed that more vigorous solution agitation would greatly improve the Cr(VI) remediation by the PpySA particles.

In summary, the growth of polypyrrole based particles and nanomaterials was investigated, and each material was characterised. The application of the PpyC4S and PpyPSS films for the removal of metal ions was investigated with EQCM. The data obtained indicated that while the PpyPSS films exhibited cation exchange properties, the ion exchange process of the PpyC4S films was much more complex. These films were successfully coated on PpyNW, a technique which could be further investigated for use in different systems. Finally, two polypyrrole materials were investigated for the remediation of Cr(VI). Both the PpyNW and PpySA particles exhibited efficient removal of Cr(VI) but it is proposed that more vigorous solution agitation would improve these results.

## 6.2 References

1. Y. Yu, Z. Si, S. Chen, C. Bian, W. Chen and G. Xue, *Langmuir*, 2006, **22**, 3899-3905.
2. M. M. Campos-Vallette, N. P. Chandia, E. Clavijo, D. Leal, B. Matsuhira, I. O. Osorio-Roman and S. Torres, *Journal of Raman Spectroscopy*, 2010, **41**, 758-763.
3. J. Zang, C. M. Li, S. J. Bao, X. Cui, Q. Bao and C. Q. Sun, *Macromolecules*, 2008, **41**, 7053-7057.
4. C. Debiemme-Chouvy, *Electrochemistry Communications*, 2009, **11**, 298-301.
5. L. Al-Mashat, C. Debiemme-Chouvy, S. Borensztajn and W. Wlodarski, *Journal of Physical Chemistry C*, 2012, **116**, 13388-13394.
6. C. P. McCarthy, N. B. McGuinness, P. B. Carolan, C. M. Fox, B. E. Alcock-Earley, C. B. Breslin and A. D. Rooney, *Macromolecules*, 2013, **46**, 1008-1016.
7. K. Xue, Y. Xu and W. Song, *Electrochimica Acta*, 2012, **60**, 71-77.
8. D. T. Ge, S. Q. Huang, R. C. Qi, J. Mu, Y. Q. Shen and W. Shi, *ChemPhysChem*, 2009, **10**, 1916-1921.
9. Q. J. Xie, S. Kuwabata and H. Yoneyama, *Journal of Electroanalytical Chemistry*, 1997, **420**, 219-225.
10. C. S. C. Bose, S. Basak and K. Rajeshwar, *J. Phys. Chem.*, 1992, **96**, 9899-9906.
11. S. Skaarup, M. J. M. Jafeen and M. A. Careem, *Solid State Ionics*, 2010, **181**, 1245-1250.
12. A. C. Partridge, C. Milestone, C. O. Too and G. G. Wallace, *Journal of Membrane Science*, 1997, **132**, 245-253.
13. C. Weidlich, K. M. Mangold and K. Jüttner, *Electrochimica Acta*, 2005, **50**, 1547-1552.
14. T. Raudsepp, M. Marandi, T. Tamm, V. Sammelselg and J. Tamm, *Electrochimica Acta*, 2013, Ahead of Print.
15. C. Wei, S. German, S. Basak and K. Rajeshwar, *Journal of the Electrochemical Society*, 1993, **140**, L60-L62.
16. R. Senthurchelvan, Y. Wang, S. Basak and K. Rajeshwar, *Journal of the Electrochemical Society*, 1996, **143**, 44-51.

17. F. J. Rodriguez, S. Gutierrez, J. G. Ibanez, J. L. Bravo and N. Batina, *Environmental Science and Technology*, 2000, **34**, 2018-2023.
18. K. G. Conroy and C. B. Breslin, *Journal of Applied Electrochemistry*, 2004, **34**, 191-195.
19. S. T. Earley, B. E. Alcock, J. P. Lowry and C. B. Breslin, *Journal of Applied Electrochemistry*, 2009, **39**, 1251-1257.
20. F. J. Rodriguez, d. I. R. L. A. Garcia, A. Alatorre, J. Ibanez, L. Godinez, S. Gutierrez and P. Herrasti, *Progress in Organic Coatings*, 2007, **60**, 297-302.
21. M. A. Alatorre, S. Gutierrez, U. Paramo and J. G. Ibanez, *Journal of Applied Electrochemistry*, 1998, **28**, 551-557.

## Appendix

---

### Conference Presentations and Publications

---

---

### Conference Presentations and Publications

R. Doyle, C. Breslin, O. Power, D. Rooney, “Electrochemical Characterisation of Polypyrrole Doped with p-Sulfonatocalix[4]arene”, *Electroanalysis*, 2012, **24**, 293-302.

23rd Irish Environmental Researchers' Colloquium – Environ 2012, University College Dublin, March 2012.

“Remediating Hexavalent Chromium with Polymer Modified Membranes”, Orla Power [Oral Presentation].

EPA Environment and Health Conference, Athlone, May 2012.

“Modified Electrodes for Sensing and Remediation of Pollutants”, Orla Power [Oral Presentation].

Electrochem 2012: RSC Electrochemical Horizons, Trinity College Dublin, September 2012.

“Polypyrrole Nanowire Modified Membranes: Remediation of Hexavalent Chromium”, Orla Power, Carmel Breslin, Denise Rooney [Poster Presentation].

63rd Irish Chemistry Colloquium, University College Dublin, June 2011.

“Reduction of Hexavalent Chromium at a Polypyrrole Nanofibre Modified Membrane”, Orla Power, Denise Rooney, Carmel Breslin [Poster Presentation].

3rd Eirelec Conference – “Electrochemistry- the future?”, Adare, Co. Limerick, May 2011.

“Formation of Polypyrrole Nanofibres at a Membrane Surface for the Extraction of Metal Ions from Water”, Orla Power, Catherine Fox, Denise Rooney, Carmel Breslin [Poster Presentation].

61st Annual Meeting of the International Society of Electrochemistry, Nice, France, September 2010.

“The Modification of Nylon Membranes, using Polypyrrole Nanofibres, for the Remediation of Heavy Metals or Nitrates from Water”, Orla Power, Catherine Fox, Denise Rooney, Carmel Breslin [Poster Presentation].

EPA National Research Conference 2010 – “Science into Action for a Sustainable Ireland”, Dublin, June 2010.

“The modification of nylon membranes using conducting polymer nanowires for the remediation of heavy metals and nitrates from water”, Orla Power, Catherine Fox, Denise Rooney, Carmel Breslin [Poster Presentation].

20th Irish Environmental Researchers' Colloquium – Environ 2010, Limerick Institute of Technology, Limerick, February 2010.

“The modification of nylon membranes using conducting polymer nanowires for the remediation of heavy metals and nitrates from water”, Orla Power, Catherine Fox, Denise Rooney, Carmel Breslin [Poster Presentation].

---

“They've done studies, you know. Sixty percent of the time, it works every time.”

*Brian Fantana*

---